Title
Indium Phosphide Photonic Integrated Circuits for Remote Sensing

Author
SANG, FENGQIAO

Publication Date
2022

University of California
Santa Barbara

Indium Phosphide Photonic Integrated Circuits for Remote Sensing

A dissertation submitted in partial satisfaction
of the requirements for the degree

Doctor of Philosophy
in
Electrical and Computer Engineering

by

Fengqiao Sang

Committee in charge:

Professor Jonathan Klamkin, Chair
Professor Larry A. Coldren
Professor John E. Bowers
Professor Jon A. Schuller

March 2022

The dissertation of Fengqiao Sang is approved.

Professor Larry A. Coldren

Professor John E. Bowers

Professor Jon A. Schuller

Professor Jonathan Klamkin, Committee Chair

March 2022

Indium Phosphide Photonic Integrated Circuits for Remote Sensing

Fengqiao Sang

This dissertation is dedicated to my parents,
Quan Sang and Chunlan Zhao,
for their love and support.

Acknowledgements

This work would not have been possible without a great deal of support and guidance from a great number of people. I would like to acknowledge them for their support and guidance both directly and indirectly.

I would first like to thank my advisor Professor Jonathan Klamkin, for giving me the opportunity to join his research group at University of California, Santa Barbara. I thank him for his vision, for sharing his knowledge and experience with me, for the guidance and support, and also for his patience and understanding. I have learned lots of essential things from him, and it has been a great pleasure and privilege to work with him.

I would like to thank Professor Larry Coldren. I am impressed by his broad knowledge and experience in photonics. He has given me lots of advice and suggestions in the past six years, especially in the Integrated Micro-Photonics for Remote Earth Science Sensing Lidar (IMPRESS) project.

I would also like to thank other committee members Professor John Bowers and Professor Jon Schuller, they have shared their vast knowledge throughout my graduate studies and provided many helpful suggestions for my thesis.

I also thank all the members of the IMPRESS team. Without the effort of Victoria Rosborough, Joseph Fridlander, Fabrizio Gambini, Mark Stephen, none of those works would have been possible. Victoria Rosborough and Fabrizio Gambini, who worked with me together in the UCSB NanoFab, we helped and encouraged each other to solve those hard fabrication problems and successfully fabricated working devices. Joseph Fridlander, who took care of most of the complicated system measurements while we were doing fabrication in the NanoFab. Mark Stephen, who gave us a lot of help and support from NASA Goddard space flight center. Also other NASA folks Jeffrey Chen, Kenji Numata, Randy Kawa for their help and support. This is a great team, I am very happy I can work in such a wonderful team.

I would like to give a special thanks to Keisuke Kojima. He was my mentor during my internship at Mitsubishi Electric Research Laboratories (MERL), who was also one of our collaborator for many years. He is very nice and patient. I appreciate his work attitude. He have taught me numerous thing both inside and outside the work.

I would like to thank all the members of IPL group. They have provided a positive and friendly research environment and helped me in many ways; in particular, Hongwei Zhao, who was my cleanroom mentor; Yuan Liu and Sergio Pinna, who were my lab testing mentors. I have learned all those valuable fabrication skills from Hongwei. Yuan Liu and Sergio Pinna, they both have a solid background in physics and circuits, and they were always willing to help me. Simone Tommaso Šuran Brunelli, who was our MOCVD expert, did the high-quality MOCVD regrowth for us. Without the high quality regrowth, those devices would not have worked so well. To other members in the IPL group : Bowen Song, Bei Shi, Si Zhu, Thomas Meissner, Lei Wang, Paul Verrinder, Michael Nickerson, Diya Hu, Brandon Isaac, Sarvagya Dwivedi, Ludovico Megalini, Yu-Ning Lo, thank you all for your kindness and help in the past few years. In addition, a special thanks to Elisa Drelie Gelasca and Amanda Miller for taking care of the paperwork and keeping everything on track.

I am very fortune to have the chance to work in the UCSB NanoFab. It is a very special place for me. I have spent almost one third of my Ph.D. time there. I would like to thank all the NanoFab staff: Brian Thibeault, Aidan Hopkins, Don Freeborn, Bill Mitchell, Ning Cao, Demis John, Brian Lingg, Mike Silva, Lee Sawyer, Tony Bosch, Biljana Stamenic, Mike Day, Dan Read. They all are highly-skilled and doing a wonderful job on maintaining the tools, especially Aidan Hopkins and Don Freeborn. Aidan is always nice and helpful, I can almost report any problems to him and he can always find a way to solve it; Don helped me a lot during the pandemic, where we only have limited access to the NanoFab, and he was the main staff on duty at my access time.

During my study in past six years at UCSB, I also received many help from other group members. I would like to thank many people from other groups. Weiqiang Xie used to be a postdoc at Bowers group and now an associate professor at SJTU. With a strong background in fabrication, he guided and helped me a lot on the fabrication process. Yujie Xia and Takako Hirokawa from Schow's group and also my office mates, they brought a lot of happiness to our office. Yujie also helped me in solving some hard physics problems. Haojun Zhang from Denbaars group, Jiawei Wang from Blumenthal group, Wenjian Liu and Weiyi Li from Mishra group, discuss process problem with them can always help me thinking it through.

In addition, many mental support from my college and graduate buddies, Shi Fang, Xuhao Wang, Leilai Shao, Yuyang Wang, Zhenlin Su, Jianfeng Wang, Yitian Shao. They have brought lots of happiness to my ph.D. life. I also would like to give a special thanks to my roommate Yu-Hsuan Lee, being so nice and supportive for the past couple years.

At last, I would like to thank my family members. Especially my parents, Quan and Chunlan, they are always my strongest supporter. They have supported me in every aspect of my life, and I would be nowhere without thier support. Also, My grandparents who are always asking me when will I go back and visit them. Now, I am glad I can tell them I am finished with my Ph.D. study. I hope in the sooner future I will be able to visit them. But, I want to tell them, no matter where I am, I am always with you.

Curriculum Vitæ
Fengqiao Sang

Education

2022	Ph.D. in Electrical and Computer Engineering, University of California, Santa Barbara.
2017	M.S. in Electrical and Computer Engineering, University of California, Santa Barbara.
2015	B.S. in Electrical Engineering, Drexel University.

Publications

1. **F, Sang**, J. Fridlander, V. Rosborough, S. T. Š. Brunelli, L. Coldren, J. Klamkin, J. Chen, K. Numata, R. Kawa, and M. Stephen, *Integrated photonics technology for earth science remote-sensing lidar*, in *2021 IEEE International Geoscience and Remote Sensing Symposium IGARSS*, pp. 7708–7711, IEEE, 2021
2. **Sang, F**, J. Fridlander, V. Rosborough, H. Zhao, S. T. Š. Brunelli, M. Stephen, R. Kawa, F. Chen, K. Numata, and J. Klamkin, *Monolithic integrated micro-photonics for earth science carbon dioxide remote sensing lidar*, in *In International Conference on Space Optical Systems and Applications (ICSOS)*, IEEE, 2019
3. J. Fridlander*, **F, Sang***, V. Rosborough*, F. Gambini, S. T. S. Brunelli, J. R. Chen, K. Numata, M. Stephen, L. A. Coldren, and J. Klamkin, *Dual laser indium phosphide photonic integrated circuit for integrated path differential absorption lidar*, *IEEE Journal of Selected Topics in Quantum Electronics* (2021)
4. J. Klamkin, **F, Sang**, J. Fridlander, V. Rosborough, F. Gambini, S. T. Š. Brunelli, L. Coldren, J. R. Chen, S. Kawa, K. Numata, *et. al.*, *Integrated phase-locked lasers and photonic integrated circuits for remote gas sensing*, in *2021 27th International Semiconductor Laser Conference (ISLC)*, pp. 1–2, IEEE, 2021
5. J. Fridlander, **F, Sang**, V. Rosborough, S. T. Š. Brunelli, J. Chen, K. Numata, S. Kawa, M. Stephen, L. Coldren, and J. Klamkin, *Monolithic indium phosphide dual laser photonic integrated circuit for remote sensing lidar*, in *2021 Conference on Lasers and Electro-Optics (CLEO)*, pp. 1–2, IEEE, 2021
6. V. Rosborough, **F, Sang**, J. Fridlander, H. Zhao, B. Song, S. T. Š. Brunelli, J. R. Chen, M. A. Stephen, L. Coldren, and J. Klamkin, *Monolithic integration of widely-tunable dbr and dfb lasers with one-step grating formation*, in *Integrated Photonics Research, Silicon and Nanophotonics*, pp. IM2A–5, Optical Society of America, 2019
7. Y. Liu, **F, Sang**, B. Isaac, J. Kalkavage, E. Adles, T. Clark, and J. Klamkin, *Integrated silicon nitride optical beamforming networks for wideband communications*, in *Integrated Photonics Research, Silicon and Nanophotonics*, pp. ITh3B–4, Optical Society of America, 2018

8. Y. Liu, **F, Sang**, A. Wichman, B. Isaac, J. Kalkavage, E. Adles, T. Clark, and J. Klamkin, *Ring resonator true time delay arrays with sharing optimization for wideband applications*, in *Integrated Photonics Research, Silicon and Nanophotonics*, pp. IW2A–2, Optical Society of America, 2017
9. Y. Liu, **F, Sang**, S. Pinna, B. Isaac, J. Kalkavage, E. Adles, T. Clark, and J. Klamkin, *Integrated optical beamforming network for millimeter wave communications*, in *2017 International Topical Meeting on Microwave Photonics (MWP)*, pp. 1–4, IEEE, 2017
10. V. Rosborough, J. Fridlander, **F, Sang**, F. Gambini, S. T. Š. Brunelli, J. R. Chen, S. Kawa, K. Numata, M. Stephen, L. Coldren, *et. al.*, *Photonic integration for low size, weight, and power (swap) remote gas spectroscopy*, in *Optics and Photonics for Sensing the Environment*, pp. ETu6D–2, Optical Society of America, 2021
11. V. Rosborough, J. Fridlander, **F, Sang**, F. Gambini, S. T. Š. Brunelli, J. R. Chen, S. Kawa, K. Numata, M. Stephen, L. Coldren, *et. al.*, *Residual amplitude modulation reduction in integrated indium phosphide phase modulators*, in *CLEO: Science and Innovations*, pp. STh4B–3, Optical Society of America, 2021
12. P. Verrinder, L. Wang, **F, Sang**, J. Fridlander, V. Rosborough, M. Nickerson, G. Yang, M. Stephen, L. Coldren, and J. Klamkin, *Sgdbr tunable laser on gallium arsenide for 1030 nm lidar applications*, in *2021 27th International Semiconductor Laser Conference (ISLC)*, pp. 1–2, IEEE, 2021
13. J. Fridlander, V. Rosborough, **F, Sang**, M. Nickerson, J. Chen, K. Numata, P. Verrinder, F. Gambini, S. Pinna, S. Kawa, *et. al.*, *Photonic integrated circuits for precision spectroscopy*, in *CLEO: Science and Innovations*, pp. SF3O–3, Optical Society of America, 2020
14. J. Fridlander, V. Rosborough, **F, Sang**, S. Pinna, S. Estrella, L. Johansson, and J. Klamkin, *Photonic integrated transmitter for space optical communications*, in *Free-Space Laser Communications XXXI*, vol. 10910, p. 1091026, International Society for Optics and Photonics, 2019
15. J. Fridlander, V. Rosborough, **F, Sang**, S. Pinna, S. Estrella, L. Johansson, and J. Klamkin, *High-speed rz-dpsk photonic integrated transmitter for space optical communications*, in *Laser Communication and Propagation through the Atmosphere and Oceans VIII*, vol. 11133, p. 1113309, International Society for Optics and Photonics, 2019
16. H. Zhao, S. Pinna, **F, Sang**, B. Song, S. T. Š. Brunelli, L. A. Coldren, and J. Klamkin, *High-power indium phosphide photonic integrated circuits*, *IEEE Journal of Selected Topics in Quantum Electronics* **25** (2019), no. 6 1–10
17. H. Zhao, S. Pinna, **F, Sang**, S. T. Š. Brunelli, L. A. Coldren, and J. Klamkin, *High power indium phosphide photonic integrated circuit for pulse position modulation free space optical communications*, in *2019 IEEE International Conference on Space Optical Systems and Applications (ICSOS)*, pp. 1–3, IEEE, 2019

18. H. Zhao, S. Pinna, **F, Sang**, S. T. Š. Brunelli, L. A. Coldren, and J. Klamkin, *High power indium phosphide photonic integrated circuit platform*, in *2019 Device Research Conference (DRC)*, pp. 71–72, IEEE, 2019
19. P. Verrinder, L. Wang, J. Fridlander, **F, Sang**, V. Rosborough, M. Nickerson, G. Yang, M. Stephen, L. A. Coldren, and J. Klamkin, *Gallium arsenide photonic integrated circuit platform for tunable laser applications*, *IEEE Journal of Selected Topics in Quantum Electronics* (2021)
20. J. Klamkin, Y. Liu, B. Song, **F, Sang**, and B. Isaac, *Integrated microwave photonic component technologies*, in *CLEO: Science and Innovations*, pp. JTh3D–5, Optical Society of America, 2018
21. S. Pinna, H. Zhao, S. Š. Brunelli, B. Song, **F, Sang**, and J. Klamkin, *High-power integrated indium phosphide transmitter for free-space optical communications*, in *Asia Communications and Photonics Conference*, pp. S3E–5, Optical Society of America, 2019
22. L. Wang, H. Zhao, B. Shi, S. Pinna, S. S. Brunelli, **F, Sang**, B. Song, and J. Klamkin, *High performance 1.3 μm aluminum-free quantum dot lasers grown by mocvd*, in *Optical Fiber Communication Conference*, pp. T4H–2, Optical Society of America, 2020
23. M. Stephen, J. Klamkin, L. Coldren, J. Fridlander, V. Rosborough, **F, Sang**, J. Chen, K. Numata, and R. Kawa, *Integrated micro-photonics for remote earth science sensing (impress) lidar*, in *IGARSS 2019-2019 IEEE International Geoscience and Remote Sensing Symposium*, pp. 4853–4856, IEEE, 2019
24. F. Gambini, Y. Liu, B. Song, H. Zhao, V. Rosborough, **F, Sang**, P. Velha, S. Faralli, and J. Klamkin, *Ultra-compact bragg-assisted silicon photonics orbital angular momentum emitter*, in *Integrated Photonics Research, Silicon and Nanophotonics*, pp. ITh3C–4, Optical Society of America, 2019
25. H. Zhao, S. Pinna, B. Song, S. T. Š. Brunelli, B. Isaac, **F, Sang**, L. Coldren, and J. Klamkin, *Widely tunable integrated laser transmitter for free space optical communications*, in *2018 IEEE International Semiconductor Laser Conference (ISLC)*, pp. 1–2, IEEE, 2018
26. J. Klamkin, H. Zhao, B. Song, Y. Liu, B. Isaac, S. Pinna, **F, Sang**, and L. Coldren, *Indium phosphide photonic integrated circuits: Technology and applications*, in *2018 IEEE BiCMOS and Compound Semiconductor Integrated Circuits and Technology Symposium (BCICTS)*, pp. 8–13, IEEE, 2018
27. K. Kojima, M. H. Tahersima, T. Koike-Akino, D. Jha, Y. Tang, Y. Wang, K. Parsons, **F, Sang**, and J. Klamkin, *Deep neural networks for designing integrated photonics*, in *Optical Fiber Communication Conference*, pp. Th1A–6, Optical Society of America, 2020
28. K. Kojima, Y. Tang, T. Koike-Akino, Y. Wang, D. Jha, K. Parsons, M. H. Tahersima, **F, Sang**, J. Klamkin, and M. Qi, *Inverse design of nanophotonic devices*

using deep neural networks, in *2020 Asia Communications and Photonics Conference (ACP) and International Conference on Information Photonics and Optical Communications (IPOC)*, pp. 1–3, IEEE, 2020

29. Y. Tang, K. Kojima, M. Gotoda, S. Nishikawa, S. Hayashi, T. Koike-Akino, K. Parsons, T. Meissner, B. Song, **F, Sang**, *et. al.*, *Inp grating coupler design for vertical coupling of inp and silicon chips*, in *Integrated Optics: Devices, Materials, and Technologies XXIV*, vol. 11283, p. 112830H, International Society for Optics and Photonics, 2020

30. Y. Tang, K. Kojima, M. Gotoda, S. Nishikawa, S. Hayashi, T. Koike-Akino, K. Parsons, T. Meissner, B. Song, **F, Sang**, *et. al.*, *Design and optimization of shallow-angle grating coupler for vertical emission from indium phosphide devices*,

* Authors contributed equally to this work.

Abstract

Indium Phosphide Photonic Integrated Circuits for Remote Sensing

by

Fengqiao Sang

With the acceleration of global climate change caused by accumulation of greenhouse gases in the atmosphere, many adverse effects on the environment have been observed, including shrinking glaciers, early breaking up of ice in rivers and lakes, premature flowering of trees, and shifting plant and animal habitats. In recent years, more focus has been placed on accurate monitoring of atmospheric greenhouse gasses for informing climate modelling and policy. In 2009, NASA launched the Orbiting Carbon Observatory (OCO) satellite mission to remotely measure carbon dioxide (CO_2) levels from low earth orbit using passive sensing technology. Around the same time, development of an active remote sensing system began under the Active Sensing of CO_2 Emissions over Nights, Days, & Seasons (ASCENDS) mission. A complex instrument built from individually packaged components, the active sensing system is large, heavy and power hungry. To reduce the size, weight, and power (SWaP) of the sensor, an equivalent system using photonic integrated circuit (PIC) technology is a promising solution for the future of remote sensing. Indium phosphide (InP) PIC technology is especially interesting because it offers the capability to monolithically integrate high quality lasers along with modulators and passive waveguides.

In this work, InP PICs employing an integrated path differential absorption (IPDA) lidar topology were designed for CO_2 active remote sensing. The fabricated PIC is about 1×10 mm in size and integrates two lasers, a phase modulator, a pulse generator, a photodiode, and several splitters and optical amplifiers. The overall sensing system consists

of two parts: stabilization of a leader laser at a reference wavelength and offset locking of a follower laser to the leader laser. The leader laser stabilization is achieved using a frequency modulation technique, where the leader laser is locked to a CO_2 reference cell by modulating the phase of the laser output signal at 125 MHz. The follower laser offset locking is accomplished using an optical phase lock loop, where an integrated photodiode detects the beat note between the leader and follower lasers. Compared to unlocked measurements, the leader laser stability improved by more than 20 dB for a two hour time period. The locked follower laser saw a stability improvement of more than 45 dB compared to unlocked. In addition, CO_2 active sensing was successfully demonstrated in the lab using a continuous wave signal and a pulsed signal. For the continuous wave sampling, an 8.92 dBm fiber-coupled output power was measured. For the case of pulsed sampling, the output pulses had an extinction ratio greater than 45 dB. For both sampling conditions, the PIC successfully scanned over a 20 GHz range centered at 1572.335 nm and recovered the CO_2 absorption spectrum.

In sum, we have demonstrated the feasibility of using InP PIC technology for CO_2 active remote sensing. In future, efforts will be made towards the PIC packaging and photonic-electronic integration to further reduce the SWaP of the overall system.

Contents

List of Figures

Chapter 1

Introduction

In the past few decades, significant progress has been made in photonic integrated circuit (PIC) technology. With the advantages of integration and scalability for mass production, this technology can significantly reduce the cost, size, weight and power (CSWaP) of photonic systems. Currently, there are three major material systems that are used widely in integrated photonics. These include indium phosphide (InP) and gallium arsenide (GaAs) platforms, which are compound semiconductor platforms. Another is silicon photonics (SiPh), which leverage silicon on insulator (SOI) waveguides. And yet another is silicon nitride (SiN), which typically leverages stoichiometric SiN as the waveguide core and SiO_2 for the claddings.

The InP and GaAs platforms have excellent electrical and optical properties and can be used to fabricate ultra-high speed modulators, high-performance laser sources, and highly sensitive photodiodes [1–5]. These technologies are mature and are widely used in telecommunications, data communications, and free space communications [6–10]. However, there are some limitations for the InP and GaAs platforms. Since some of the elements are rare, the cost of the substrates and epitaxy materials is high. InP substrates are also fragile and wafer size is limited, which further increases the cost. The largest commercialized wafer size for InP is 4 inches. In order to reduce the cost for PIC platforms and enable mass production, SiPh has gained significant interest. The SOI and SiN platforms have the advantage of using the mature complementary metal-oxide-semiconductor (CMOS) fabrication processes to further reduce cost and enable larger volume production. In addition, they also enable the possibilities to integrate the CMOS electronic integrated circuits (EICs) with PICs to further improve the bandwidth and efficiency of the overall system [11–13]. Silicon, however, is an indirect bandgap material, and due to this physical property, it is difficult to realize lasers sources that are critical for data communications and active sensing. In recent years, much progress has been made towards making lasers integrated with silicon photonics a reality [14–18]. As of today, the InP and GaAs material platforms are still better options for laser device integration.

To date, integrated photonics technology has rarely been used for remote sensing applications. Currently, most remote sensing space-based instruments use individually packaged components. These instruments are usually large in size and power hungry. In this thesis, a PIC-based system for remote sensing applications is introduced. With this new PIC technology, the CSWaP of the remote sensing instrument is significantly reduced.

This thesis is structured as follows. First, the basics of remote gas sensing are introduced to provide some background and insight about the application. Then, the motivation for applying PIC technology to remote sensing is discussed. Next, details of the InP PIC device design and fabrication are presented. Lastly, data from the implementation of CO_2 gas sensing with the fabricated PIC is shown and analyzed.

1.1 Remote Sensing

Remote sensing is an important method for monitoring the Earth or other planetary bodies from a distance. The sensing can be done from different orbits. For Earth science remote sensing, most applications use low-Earth orbit. Low-Earth orbits is approximately 160 to 2,000 km above Earth and satellites in this orbit can make 12-16 Earth turns per Earth day depending on the altitude, enabling them to rapidly acquire a global perspective of the data. [19].

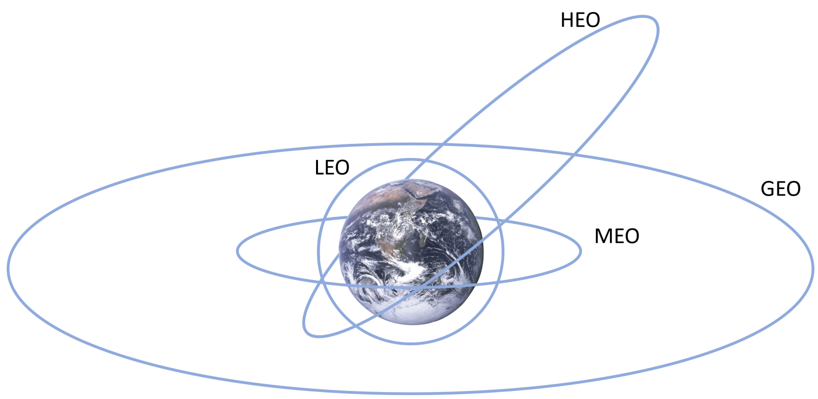

Figure 1.1: Illustration of different satellite orbits. LEO : Low-Earth orbit, approximately 160 to 2,000 km above Earth; MEO : medium-Earth orbit, approximately 2,000 to 35,500 km above Earth; HEO : high-Earth orbit, more than 35,500 km above Earth; GEO : Geostationary orbit, 35,786 km above Earth.

From a methodology perspective, remote sensing technologies can be divided into two categories: active remote sensing and passive remote sensing. Active remote sensing uses its own energy source to illuminate the target object and the reflected or backscattered energy is detected using a detection system. Passive remote sensing works by acquiring emitted or reflected natural energy. For Earth science applications, the most commonly used natural energy is sunlight. The advantage of active remote sensing is that it does not depend on an external energy source, which may change over time. Active sensing also provides more accurate measurements since the active source is more stable compared to a natural energy source. For Earth science applications, this means accurate measurements can be taken day and night, over ocean and land surfaces since there is no reliance on sunlight, the intensity and reflectivity of which varies between day and night and ocean and land surfaces. However, compared with passive remote sensing, active sensing also requires a more complicated system design, larger equipment size, and, consequently, higher power consumption.

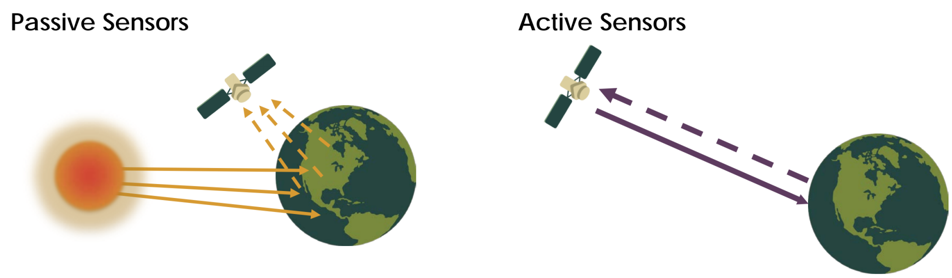

Figure 1.2: Illustration of a active and passive remote sensing (© NASA.)

Many agencies have been working on monitoring Earth for many years, such as the National Aeronautics and Space Administration (NASA) and National Oceanic and Atmospheric Administration (NOAA) in north America, the European Space Agency (ESA) and European Organisation for the Exploitation of Meteorological Satellites (EUMETSAT) in Europe, and the Japan Aerospace Exploration Agency (JAXA) and China National Space Administration (CNSA) in Asia. Many remote sensors have been built by these agencies for various monitoring purposes and some of them are introduced here. The Joint Altimetry Satellite Oceanography Network (Jason) which was built by NASA, it was a satellite series including many satellites. The Jason-1 was deployed in 2001, and its successors Jason-2 and Jason-3 were launched in 2008 and 2016, respectively. The Jason series is used to make highly detailed measurements of sea-levels on Earth to gain more insight into ocean currents and climate change [20]. The Joint Polar Satellite

System (JPSS) mission from NASA and NOAA was launched in 2011, which focused on weather forecasts and climate change monitoring. JPSS-1 was launched in 2017, and JPSS-2, JPSS-3 and JPSS-4 are targeted to be launched in 2022, 2027 and 2031 [21]. Similar to the JPSS mission, ESA has launched the Sentinel program which consists of many missions. It is posited to replace old Earth observation missions and provide a continuous data set of many Earth science areas including atmospheric, oceanic, and land monitoring [22].

1.2 Carbon Dioxide Remote Sensing

Carbon dioxide (CO_2) is one of the most common greenhouse gases today. The steady increase of its concentration has caused problems not only to the terrestrial ecosystem but also the aquatic. In order to fully understand the change of CO_2 level in the atmosphere, a lot of effort has been made in CO_2 remote sensing in recent years. NASA launched the Orbiting Carbon Observatory (OCO) series for CO_2 observation starting in 2009 and the latest instrument, OCO-3, was launched in 2019 [23]. JAXA has deployed the Greenhouse Gases Observing Satellite (GOSAT) series which observes both CO_2 and CH_4 (methane). GOSAT-1 was launched in 2009 and GOSAT-2 was launched in 2018 [24]. ESA launched its Copernicus Anthropogenic Carbon Dioxide Monitoring (CO2M) mission on Sentinel-7 as a part of the Sentinel program mentioned above. CO2M will launch two more satellites using both active and passive remote sensing technologies. The satellites will carry a near-infrared and shortwave-infrared spectrometer to monitor the CO_2 and nitrogen dioxide (NO_2) levels on Earth.

Both the OCO series and GOSAT series only used passive sensing technology, where accurate measurement requires sunlit scenes, cloud-free conditions, and accurate estimates of surface elevation [25]. The Earth's atmosphere is complex and the sunlight is scattered by the clouds and aerosols, which causes variability in the optical path length and affects the measurement. The Earth's topography also varies, so elevation variations cause changes to the measurement path and further degrade the measurement accuracy. In order to overcome these limitations, NASA has been working on the Active Sensing of CO_2 Emissions over Nights, Days, & Seasons (ASCENDS) mission from 2008 to 2018, focusing on active sensing technology for CO_2 remote sensing.

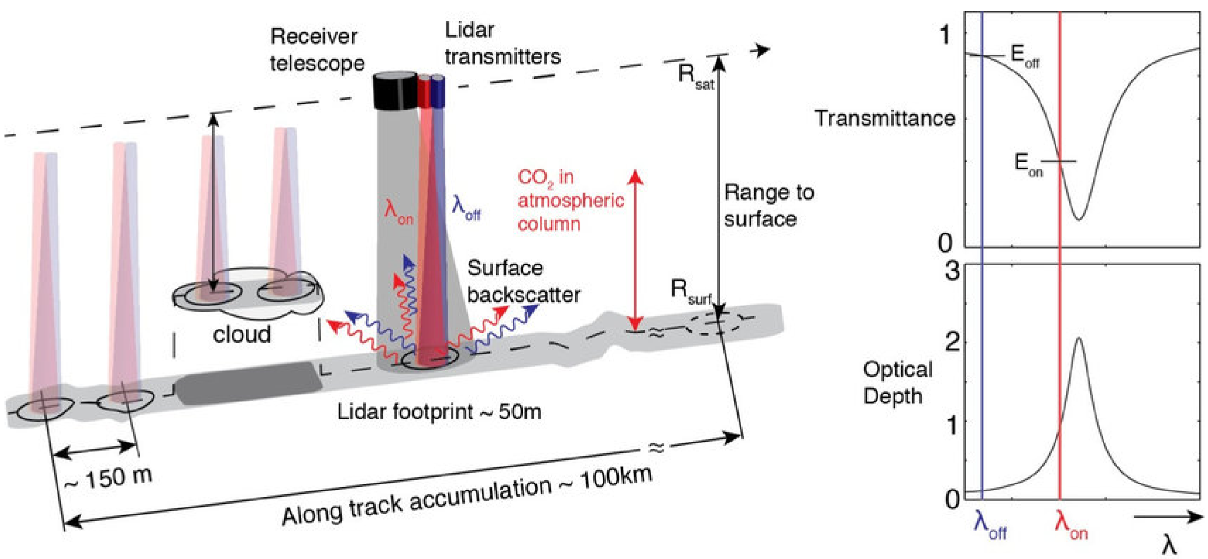

Figure 1.3: Illustration of active remote sensing using IPDA measurement from space to scattering surfaces on or near the Earths surface for ASCENDS mission. (© NASA, [25])

The ASCENDS mission uses active remote sensing with an integrated path differential absorption (IPDA) approach, as illustrated in Fig. 1.3. The IPDA approach measures the optical absorption of the target species at multiple wavelengths using a laser source [26–28]. By probing with multiple wavelengths on and off the absorption line of interest, the shape of the line is mapped. The Goddard Space Flight Center (GSFC) lidar system developed for ASCENDS probes the 1572.335 nm absorption line of CO_2. This relatively weak absorption line enables sufficient return signal and can leverage mature L-band optical components developed for the telecommunications industry. The system has successfully undergone airborne testing, logging ∼ 50 hours of flight time over Alaska, Yukon Territories and the Beaufort sea with a measurement precision within 1 ppm [29]. The success of this mission has enabled the future of CO_2 active remote sensing and has also paved the way for a PIC-based sensor to be developed.

1.3 InP PIC for CO_2 Active Remote Sensing

In recent years, the maturity of PIC technology has enabled forays into remote sensing motivated by the potential for significant reduction of instrument CSWaP. Many PIC platforms can be used for remote sensing applications, including InP, GaAs, SOI, and SiN. Each of them carries its own optical and electrical advantages and different transparency window (wavelength region), which can be used for different sensing applications. InP-based material systems are usually used for the wavelength range from 1300 nm to 1550

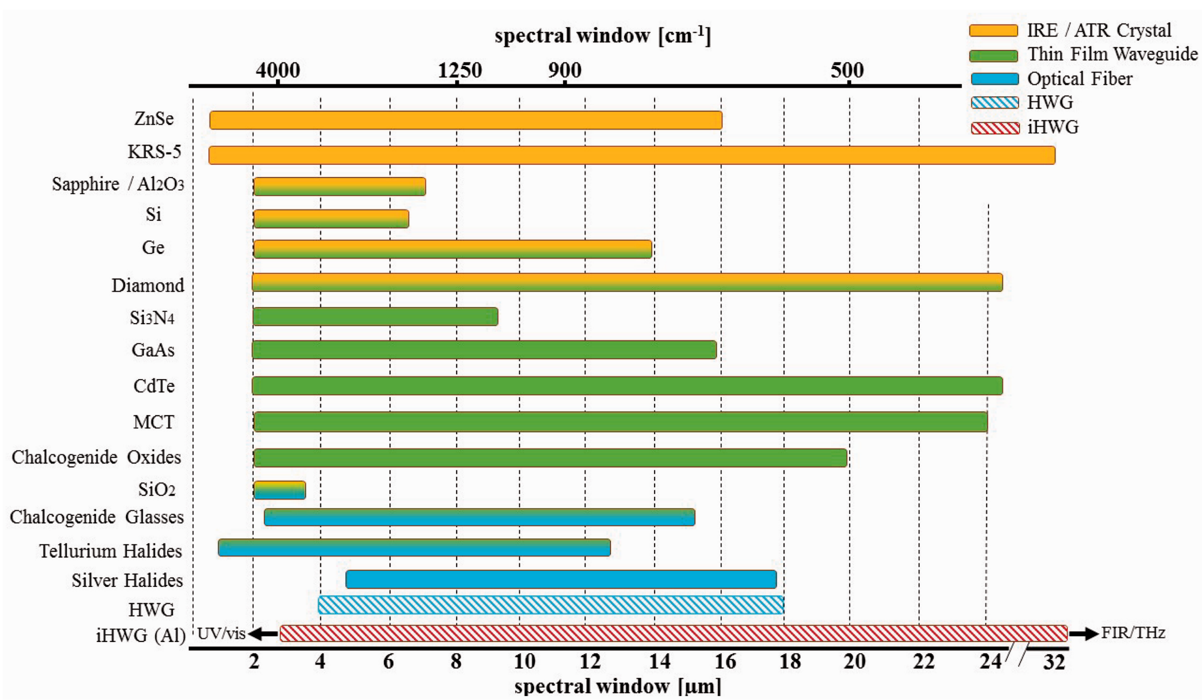

Figure 1.4: Overview of the most prevalent MIR transmitting waveguide materials (© SAGE Publications, [30])

nm, which covers the C band and O band for fiber optics and free space communication. The wavelength range can be extended to L band (1565 nm to 1625 nm) with specific epitaxial material design [31, 32]. GaAs is widely used for 1.3 μm applications [33], and it can also be designed to work at 1030 nm region for lidar applications [34, 35]. SOI covers the range from 1.2 μm - 3.7 μm and 100 μm - 200 μm, except for the 2.6 μm - 2.9 μm region, where SiO_2 has strong absorption [36]. SiN has an extremely broad transparency region from visible light to the infrared region which is from $\sim$ 400 nm up to 7 μm [37, 38]. As a reference, an overview of most prevalent MIR transmitting waveguide materials is shown in Fig. 1.4 [30].

For CO_2 active remote sensing at 1572.335 nm [27, 28], the InP PIC technology is an ideal choice. With this technology, a high performance InP laser can be fabricated with a lasing wavelength covering the target wavelength range centered at 1572.335 nm. Other

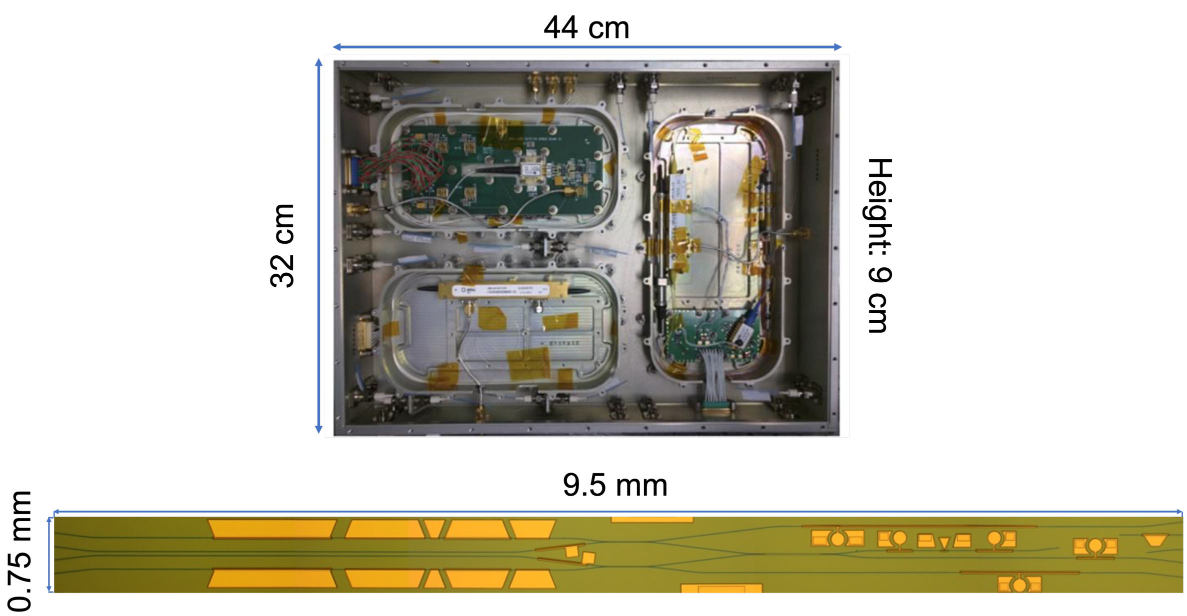

Figure 1.5: Images of NASA's current seed laser module based on discrete components and new seed laser module based on InP PIC technology. (top) NASA's current seed laser module for active remote sensing(© NASA); (bottom) InP PIC designed and fabricated for the active remote sensing.

photonic components such as modulators, photodiodes, semiconductor optical amplifiers (SOA) and splitters, can also be monolithically integrated on the same PIC using this material system. This results in a significant CSWaP reduction of the optical system.

The seed laser module in NASA's current system was built using discrete photonic components and has a size of 44 cm $\times$ 32 cm $\times$ 9 cm. With InP PIC technology, the size of the PIC module shrinks to 8.3 mm $\times$ 0.7 mm cm $\times$ 0.16 mm. Both modules are shown in Fig. 1.5. In addition, the PIC can be packaged into a butterfly package, which provides isolation from outside environment, further performance improvement, and ease of electrical connection. The required electronic circuits can be implemented in a PCB to achieve close electronic-photonic integration, which will dramatically reduce the power consumption of the seed laser module. Since the InP platform can cover a lasing range from 1300 to 1600 nm, this sensing technology is not limited to CO_2 sensing at 1572.335 nm, but can be extended to other wavelengths with minor adjustments. Other potential applications include CH_4 sensing at 1653 nm and 1331 nm [39–41].

1.4 Preview of Dissertation

Motivated by the continuous climate changes caused by greenhouse gases and the resulting increasing demands on the monitoring of greenhouse gases, we have leveraged NASA's current CO_2 active remote sensing system architecture for implementation of an InP PIC-based system with significantly reduced CSWaP. CO_2 sensing was successfully demonstrated in the lab environment, which fundamentally and experimentally proves the possibility of InP PIC-based CO_2 active remote sensing.

In this dissertation, an overview of the InP PIC platform is firstly introduced in Chapter 2, where different components and integration platforms are discussed. Then, the epitaxial material design and PIC fabrication details are covered in Chapter 3. The design details of components used in the PICs are covered in Chapter 4, including lasers, phase modulators (PMs), SOAs, photodiodes (PDs), and couplers. A pulse generator is introduced in Chapter 5, which is designed for pulsing an SOA to achieve pulse exinction ratios greater than 35 dB. A higher extinction ratio (ER) can be achieved by driving it from reverse voltage bias to forward current injection. The overall PIC system architecture and controls are introduced in Chapter 6 and Chapter 7, where the detailed methodology and performance of the sensing system are discussed. At the end, a summary and future work are discussed in Chapter 8.

Bibliography

[1] L. A. Coldren, S. C. Nicholes, L. Johansson, S. Ristic, R. S. Guzzon, E. J. Norberg, and U. Krishnamachari, *High performance inp-based photonic icsa tutorial*, *Journal of Lightwave Technology* **29** (2011), no. 4 554–570.

[2] L. A. Coldren, S. W. Corzine, and M. L. Mashanovitch, *Diode lasers and photonic integrated circuits*, vol. 218. John Wiley & Sons, 2012.

[3] K. Williams, E. Bente, D. Heiss, Y. Jiao, K. Ławniczuk, X. Leijtens, J. Van der Tol, and M. Smit, *Inp photonic circuits using generic integration*, *Photonics Research* **3** (2015), no. 5 B60–B68.

[4] F. M. Soares, M. Baier, T. Gaertner, M. Feyer, M. Möhrle, N. Grote, and M. Schell, *High-performance inp pic technology development based on a generic photonic integration foundry*, in *Optical Fiber Communication Conference*, pp. M3F–3, Optical Society of America, 2018.

[5] M. Smit, K. Williams, and J. van der Tol, *Past, present, and future of inp-based photonic integration*, *APL Photonics* **4** (2019), no. 5 050901.

[6] S. Arafin and L. A. Coldren, *Advanced inp photonic integrated circuits for communication and sensing*, *IEEE Journal of Selected Topics in Quantum Electronics* **24** (2017), no. 1 1–12.

[7] J. Klamkin, H. Zhao, B. Song, Y. Liu, B. Isaac, S. Pinna, F. Sang, and L. Coldren, *Indium phosphide photonic integrated circuits: Technology and applications*, in *2018 IEEE BiCMOS and Compound Semiconductor Integrated Circuits and Technology Symposium (BCICTS)*, pp. 8–13, IEEE, 2018.

[8] R. W. Going, M. Lauermann, R. Maher, H.-S. Tsai, A. Hosseini, M. Lu, N. Kim, P. Studenkov, S. W. Corzine, J. Summers, *et. al.*, *1.00 (0.88) tb/s per wave capable coherent multi-channel transmitter (receiver) inp-based pics with hybrid integrated sige electronics*, *IEEE Journal of Quantum Electronics* **54** (2018), no. 4 1–10.

[9] H. Zhao, S. Pinna, B. Song, L. Megalini, S. T. Š. Brunelli, L. A. Coldren, and J. Klamkin, *Indium phosphide photonic integrated circuits for free space optical links*, *IEEE Journal of Selected Topics in Quantum Electronics* **24** (2018), no. 6 1–6.

[10] H. Zhao, S. Pinna, F. Sang, B. Song, S. T. Š. Brunelli, L. A. Coldren, and J. Klamkin, *High-power indium phosphide photonic integrated circuits*, *IEEE Journal of Selected Topics in Quantum Electronics* **25** (2019), no. 6 1–10.

[11] R. Soref, *The past, present, and future of silicon photonics*, *IEEE Journal of selected topics in quantum electronics* **12** (2006), no. 6 1678–1687.

[12] B. Jalali and S. Fathpour, *Silicon photonics*, *Journal of lightwave technology* **24** (2006), no. 12 4600–4615.

[13] D. Thomson, A. Zilkie, J. E. Bowers, T. Komljenovic, G. T. Reed, L. Vivien, D. Marris-Morini, E. Cassan, L. Virot, J.-M. Fédéli, *et. al.*, *Roadmap on silicon photonics*, *Journal of Optics* **18** (2016), no. 7 073003.

[14] A. W. Fang, H. Park, O. Cohen, R. Jones, M. J. Paniccia, and J. E. Bowers,

Electrically pumped hybrid algainas-silicon evanescent laser, *Optics express* **14** (2006), no. 20 9203–9210.

[15] D. Liang and J. E. Bowers, *Recent progress in lasers on silicon*, *Nature photonics* **4** (2010), no. 8 511–517.

[16] D. Liang and J. E. Bowers, *Recent progress in heterogeneous iii-v-on-silicon photonic integration*, *Light: Advanced Manufacturing* **2** (2021), no. 1 1–25.

[17] C. Xiang, J. Guo, W. Jin, L. Wu, J. Peters, W. Xie, L. Chang, B. Shen, H. Wang, Q.-F. Yang, *et. al.*, *High-performance lasers for fully integrated silicon nitride photonics*, *Nature communications* **12** (2021), no. 1 1–8.

[18] C. Xiang, J. Liu, J. Guo, L. Chang, R. N. Wang, W. Weng, J. Peters, W. Xie, Z. Zhang, J. Riemensberger, *et. al.*, *Laser soliton microcombs heterogeneously integrated on silicon*, *Science* **373** (2021), no. 6550 99–103.

[19] M. Craglia, M. F. Goodchild, A. Annoni, G. Camara, M. F. Gould, W. Kuhn, D. Mark, I. Masser, D. Maguire, S. Liang, *et. al.*, *Next-generation digital earth*, .

[20] F. Maiwald, O. Montes, S. Padmanabhan, D. Michaels, A. Kitiyakara, R. Jarnot, S. T. Brown, D. Dawson, A. Wu, W. Hatch, *et. al.*, *Reliable and stable radiometers for jason-3*, *IEEE Journal of Selected Topics in Applied Earth Observations and Remote Sensing* **9** (2016), no. 6 2754–2762.

[21] M. D. Goldberg, H. Kilcoyne, H. Cikanek, and A. Mehta, *Joint polar satellite system: The united states next generation civilian polar-orbiting environmental satellite system*, *Journal of Geophysical Research: Atmospheres* **118** (2013), no. 24 13–463.

[22] M. Berger, J. Moreno, J. A. Johannessen, P. F. Levelt, and R. F. Hanssen, *Esa's sentinel missions in support of earth system science*, *Remote Sensing of Environment* **120** (2012) 84–90.

[23] P. Srivastava, M. W. Bennett, G. Bedrosian, R. Rosenberg, B. Solish, and R. R. Basilio, *Establishing launch readiness of nasa iss instrument oco-3*, in *IGARSS 2020-2020 IEEE International Geoscience and Remote Sensing Symposium*, pp. 6101–6104, IEEE, 2020.

[24] R. Glumb, G. Davis, and C. Lietzke, *The tanso-fts-2 instrument for the gosat-2 greenhouse gas monitoring mission*, in *2014 IEEE Geoscience and Remote Sensing Symposium*, pp. 1238–1240, IEEE, 2014.

[25] S. R. Kawa, J. B. Abshire, D. F. Baker, E. V. Browell, D. Crisp, S. M. Crowell, J. J. Hyon, J. C. Jacob, K. W. Jucks, B. Lin, *et. al.*, *Active sensing of co2 emissions over nights, days, and seasons (ascends): Final report of the ascends ad hoc science definition team*, .

[26] G. C. Bjorklund, *Frequency-modulation spectroscopy: a new method for measuring weak absorptions and dispersions*, *Optics letters* **5** (1980), no. 1 15–17.

[27] K. Numata, J. R. Chen, and S. T. Wu, *Precision and fast wavelength tuning of a dynamically phase-locked widely-tunable laser*, *Optics express* **20** (2012), no. 13 14234–14243.

[28] K. Numata, J. R. Chen, S. T. Wu, J. B. Abshire, and M. A. Krainak, *Frequency stabilization of distributed-feedback laser diodes at 1572 nm for lidar measurements of atmospheric carbon dioxide*, *Applied optics* **50** (2011), no. 7 1047–1056.

[29] G. R. Allan, J. B. Abshire, H. Riris, J. Mao, W. E. Hasselbrack, K. Numata,

J. Chen, R. Kawa, M. Rodriguez, and M. Stephen, *Lidar measurements of co2 column concentrations in the arctic region of north america from the ascends 2017 airborne campaign*, in *Lidar Remote Sensing for Environmental Monitoring XVI*, vol. 10779, p. 1077906, International Society for Optics and Photonics, 2018.

[30] T. Schädle and B. Mizaikoff, *Mid-infrared waveguides: a perspective*, *Applied spectroscopy* **70** (2016), no. 10 1625–1638.

[31] F. Sang, J. Fridlander, V. Rosborough, S. T. Š. Brunelli, L. Coldren, J. Klamkin, J. Chen, K. Numata, R. Kawa, and M. Stephen, *Integrated photonics technology for earth science remote-sensing lidar*, in *2021 IEEE International Geoscience and Remote Sensing Symposium IGARSS*, pp. 7708–7711, IEEE, 2021.

[32] J. Fridlander, F. Sang, V. Rosborough, F. Gambini, S. T. S. Brunelli, J. R. Chen, K. Numata, M. Stephen, L. A. Coldren, and J. Klamkin, *Dual laser indium phosphide photonic integrated circuit for integrated path differential absorption lidar*, *IEEE Journal of Selected Topics in Quantum Electronics* (2021).

[33] V. Ustinov and A. Zhukov, *Gaas-based long-wavelength lasers*, *Semiconductor science and technology* **15** (2000), no. 8 R41.

[34] P. Verrinder, L. Wang, F. Sang, J. Fridlander, V. Rosborough, M. Nickerson, G. Yang, M. Stephen, L. Coldren, and J. Klamkin, *Sgdbr tunable laser on gallium arsenide for 1030 nm lidar applications*, in *2021 27th International Semiconductor Laser Conference (ISLC)*, pp. 1–2, IEEE, 2021.

[35] P. Verrinder, L. Wang, J. Fridlander, F. Sang, V. Rosborough, M. Nickerson, G. Yang, M. Stephen, L. A. Coldren, and J. Klamkin, *Gallium arsenide photonic integrated circuit platform for tunable laser applications*, *IEEE Journal of Selected Topics in Quantum Electronics* (2021).

[36] R. A. Soref, S. J. Emelett, and W. R. Buchwald, *Silicon waveguided components for the long-wave infrared region*, *Journal of Optics A: Pure and Applied Optics* **8** (2006), no. 10 840.

[37] J.-M. Fedeli and S. Nicoletti, *Mid-infrared (mid-ir) silicon-based photonics*, *Proceedings of the IEEE* **106** (2018), no. 12 2302–2312.

[38] J. Klamkin and M. Stephen, *Integrated photonics technology for space-based remote-sensing*, in *IGARSS 2020-2020 IEEE International Geoscience and Remote Sensing Symposium*, pp. 3471–3474, IEEE, 2020.

[39] B. Niu, H. Yu, L. Yu, D. Zhou, L. Zhao, J. Pan, and W. Wang, *1.65 um three-section distributed bragg reflective (dbr) laser for ch4 gas sensor*, in *Optoelectronic Devices and Integration IV*, vol. 8555, p. 85550Z, International Society for Optics and Photonics, 2012.

[40] G. Plant, M. Nikodem, D. Sonnenfroh, and G. Wysocki, *Chirped laser dispersion spectroscopy for remote sensing of methane at 1.65 μm–analysis of system performance*, in *CLEO: Science and Innovations*, pp. JW2A–79, Optical Society of America, 2013.

[41] V. Weldon, J. O'Gorman, J. Pérez-Camacho, D. Mcdonald, J. Hegarty, and B. Corbett, *Methane sensing with a novel micromachined single-frequency fabry-perot laser diode emitting at 1331 nm*, *IEEE Photonics Technology Letters* **9** (1997), no. 3 357–359.

Chapter 2

Indium Phosphide PIC Platforms

Over the past decades, many indium phosphide platforms have been investigated. The most common ones include butt-joint growth, selective area growth, quantum well intermixing, and offset quantum well. Each platform has its own advantages, and can be used to design and fabricate different types of integrated optical components. This chapter will give a brief introduction to the different types of integrated optical components and different kinds of platforms.

2.1 1. Integrated Optical Components

The photonic components can be mainly divided into two types: active components and passive components. The main difference between them is whether they generate or detect an optical signal. Common active components include lasers, optical amplifiers, and photodiodes. Some common passive components are splitters and combiners, also known as couplers. Some devices can belong to either of those catagories depending on how you would like to define them. These include different kinds of phase modulators and amplitude modulators, which do not generate any optical power, but modulate the optical signal. For the discussion below, I will refer to them as active components.

2.1.1 Active Components

In this section, different kinds of active components will be introduced, including lasers, semiconductor optical amplifiers (SOAs), photodiodes (PDs) and modulators. The laser is one of the most important active components. Two types of commonly used single frequency semiconductor lasers are introduced here. They are distributed feedback (DFB) lasers and distributed Bragg reflector (DBR) lasers [1, 2]. The main difference between the DFB lasers and DBR lasers is the grating and gain placement. DFB lasers use a continuous Bragg grating in the same region as the gain section. Commonly a quarter wave shift is added to the center of the grating to achieve single mode lasing [1, 3]. Since the length of the gain region needs to be long enough to provide enough optical power, DFB laser gratings usually use a low refractive index contract grating and a long length design to achieve the targeted reflectivity. DFB lasers are usually thermally tuned, but the tuning range is very limited. Due to its simplified structure and long mirror design, the output of DFB lasers is very stable and can achieve a kHz range linewidth. Today, DFB lasers are widely used in data communication and telecommunication industries as optical sources.

DBR lasers use distributed Bragg reflector gratings, where the gratings are separated into two main parts: front mirror and back mirror. Since both mirrors are located at two ends of the gain region, DBR lasers usually use highly reflective gratings with shorter lengths. The grating of the front mirror has a relatively low reflectivity compared with the grating of the back mirror [2, 3]. Typically, the reflectivity of the front mirror is around 30 %, and the reflectivity of the back mirror can be as high as 90 %. Traditional DBR lasers have a moderate tuning range of 5 nm - 7 nm, but some specially design

DBR lasers can achieve a larger tuning wavelength range. For example, sampled grating DBR (SGDBR) lasers can achieve up to a 40 nm tuning range. DBR lasers are also used in the communications industry. Due to their wider tuning ability, DBR lasers are also used widely in other industries where wide tunability is required, such as in active sensing and Lidar sensing.

Many factors need to be carefully considered in order to achieve the desired performance of either a DFB or DBR laser, including epitaxial material development, grating and device design, and fabrication process optimization. Furthermore, for different applications, lasers need to be designed differently to satisfy the given requirements.

An SOA usually contains a gain section, which can be used as an amplifier or an absorber depending on the biasing condition. An SOA is usually placed in front of the laser's front mirror to control the output power by forward biasing it at different current levels. It can also be used as an absorber to absorb the unwanted light at the back side of a laser by reverse biasing it using a voltage source. Depending on the application, SOAs can also be designed for other purposes. For example, it can also be designed to be a pulse carver by applying a pulsed current signal.

Unlike lasers and SOAs which take an electrical signal as their input and generate an optical signal as their output, PDs are used to convert an optical signal into electrical signal. They are widely used in all kinds of receivers where an optical signal is required to be converted into an electrical signal for processing. Depending on the needs of the application, there are many types of PDs available, such as p-i-n photodiodes, avalanche photodiodes (APD), Schottky photodiodes and uni-traveling-carrier photodiodes (UTC-PD) [4–7].

Modulators are usually used to modify the optical signal based on the characteristics of an applied electrical field. Commonly used modulators include electroabsorption modulators (EAMs) and Mach-Zehnder interferometer modulators (MZMs). EAMs can be further divided into bulk EAMs and quantum well based EAMs. A bulk EAM does not have quantum wells. Its waveguide works as the modulation medium. In reverse bias, the Franz-Keldysh effect in a bulk waveguide changes the effective index of the optical mode as a function of the applied electrical field. A quantum well based EAM uses the quantum-confined Stark effect (QCSE) to change the effective band shift of the quantum well through application of an electrical field [3, 8, 9]. Since the quantum well absorption edge is much sharper, it is more sensitive to the electric field and thermal changes. QW-based EAMs are more efficient than bulk EAMs using the Franz-Keldysh effect.

An MZM uses an interferometric structure, where the input light is separated into two arms for phase modulation, then combined together at the output. The two arms usually use a material with a strong electro-optic effect. Applying electric fields to the two arms changes the refractive index of the material and further results in phase changes in the arms. Intensity modulation is achieved by modulating a single arm or by modulating the two arms with different signals, such as in a push-pull configuration.

2.1.2 Passive Components

In this section, different kinds of passive components will be introduced, including multimode interference (MMI) couplers, directional couplers, star couplers, arrayed waveguide gratings (AWGs), and Echelle gratings. The MMI couplers, directional couplers, and star couplers are mainly used for power splitting and combining. The AWGs and Echelle gratings are mainly used for signal separating and combining at different wavelengths.

An MMI coupler uses the principle of self-imaging in multimode waveguides. The input field profile is periodically reproduced as a single or multiple images while propagating through the multimode waveguide [3]. Figure 2.1 shows the mirrored single image,

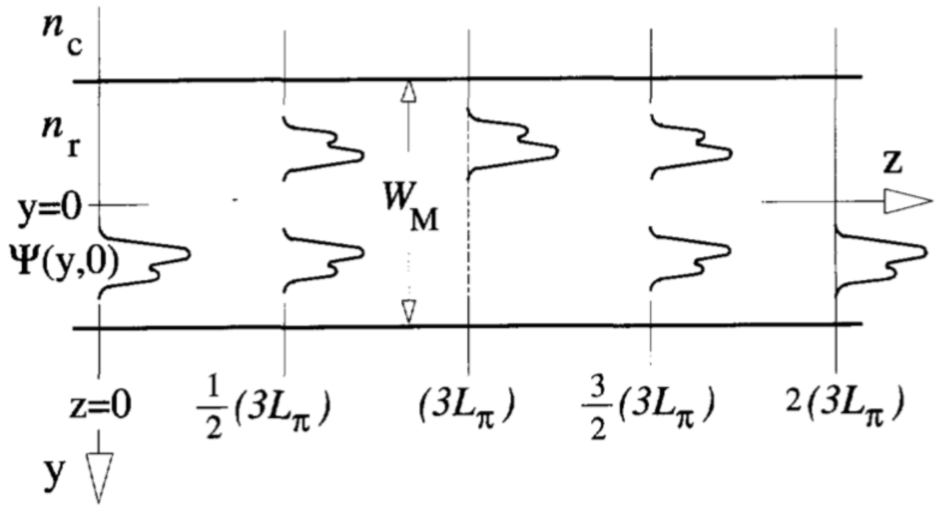

Figure 2.1: Mulitmode waveguide showing the input field $\Phi(y, 0)$, a mirrored single image at $(3L_\pi)$, a direct single image at $2(3L_\pi)$, and two-fold images at $\frac{1}{2}(3L_\pi)$ and $\frac{3}{2}(3L_\pi)$. (© IEEE 1995, [10].)

direct single image, and two fold image at different locations of the original electric field profile $\Phi(y, 0)$. By choosing different lengths and widths of MMI couplers, we can design them to have a specific self-image profile at the output end.

A directional coupler uses co-directional coupling from coupled mode theory. It is a two-waveguide system as shown in Fig. 2.2. Two waveguides are placed close enough that

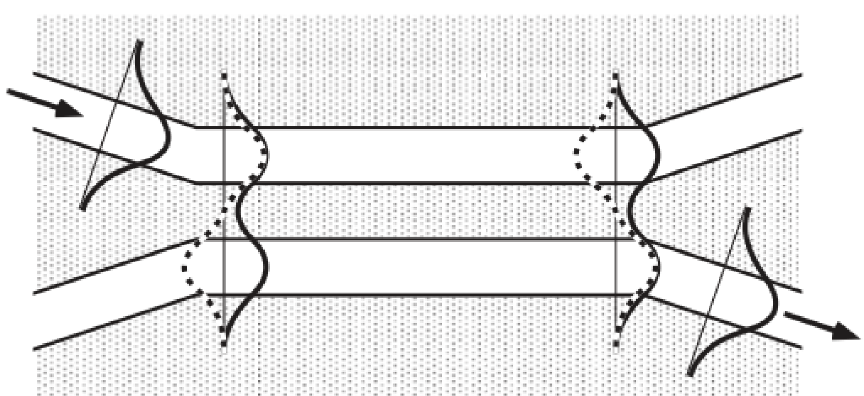

Figure 2.2: Illustration of a directional coupler with even (solid) and odd (dotted) eigenmodes. (© John Wiley & Sons 2012, [3].)

the modes can perturb each other to form new eigenmodes [3, 11]. The superposition of the first even and odd eigenmodes of the directional coupler have different phase velocities. By controlling the length of the coupling region we can achieve our target coupling ratio by controlling the phase difference between those two eigenmodes.

A star coupler uses the diffraction of light propagation to direct the light from N input waveguides into M output waveguides. Fig. 2.3 shows an illustration of a star coupler. The input waveguides and output waveguides are separated by different angles and spacing. A slab waveguide is placed in between the input and output wavegudes for free propagation of the light. By designing the positions and angles of the inputs and outputs, all the input signals can be coupled to each output waveguide. Because the coupling efficiency is limited at the output end, it is very important to optimize the

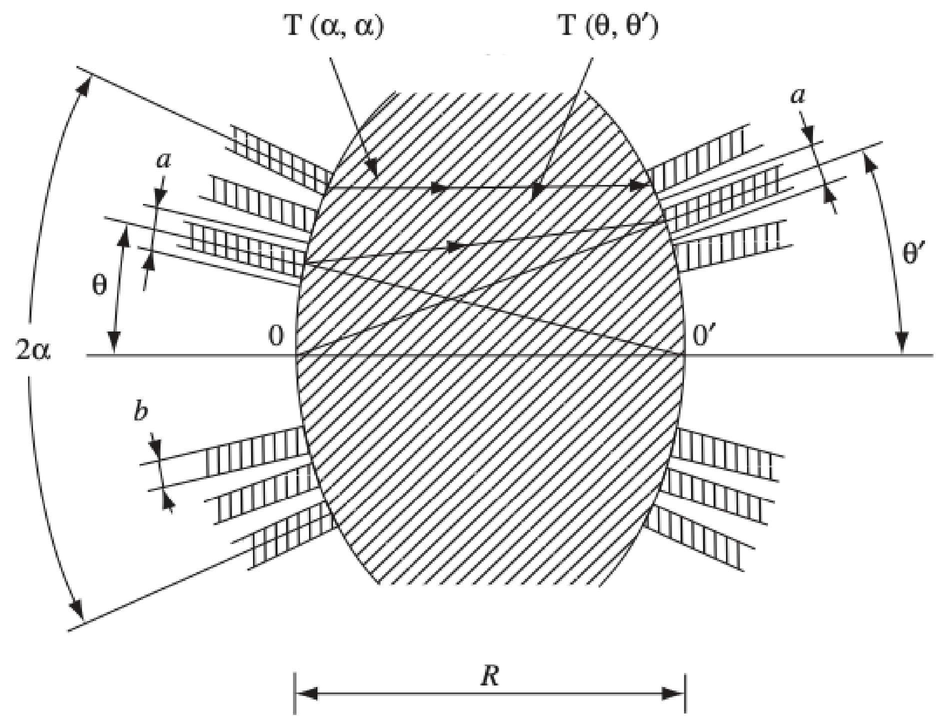

Figure 2.3: Illustration of a star coupler. (© IET 1988, [12].)

coupling efficiency for the output waveguides to minimize the insertion loss. [3].

An AWG works like a prism. It separates the different wavelength signals into different output ports. There are two free propagation regions (FPRs) in the design. The beam from the input goes into the first FPR and propagates freely, becoming divergent. Then the beam is separated into multiple paths, each with a path delay that is an integer multiple of the central wavelength as shown in Eq. 2.1.

$$\Delta L = m \frac{\lambda_c}{N_g} \tag{2.1}$$

On the receiver side, all those signal paths go into the second FPR. By designing the geometry at the receiver side, the divergent beams at different wavelengths can be transformed into a convergent one with the same amplitude and phase profile as the input one at each output ports.

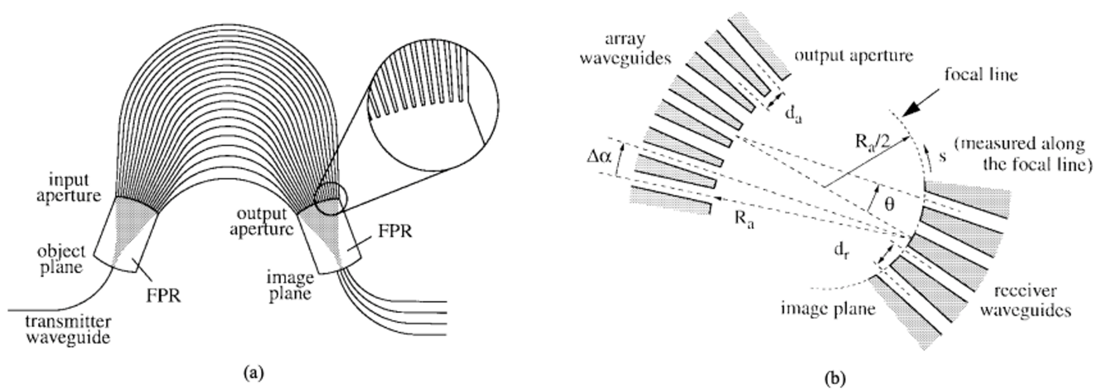

Figure 2.4: Illustration of an arrayed waveguide grating. (© IEEE 1996, [13].)

2.2 Integration Platforms

Many types of mature integration platforms have been developed for the indium phosphide material system. The most popular ones include vertical twin-guide, butt-joint regrowth, selective area growth, offset quantum well (OQW), dual quantum well and quantum well intermixing (QWI).Each platform is shown in Fig. 2.5, and will be briefly discussed in this section.

2.2.1 Vertical Twin-Guide

The vertical twin-guide platform has the advantage of allowing independent properties in the upper and lower waveguides. On the other hand, since the separation between the two waveguides is relatively large, a long coupling length is needed to achieve vertical light coupling [14] [15] between the two waveguides. With this platform, the epitaxial material design can be optimized for active and passive components individually, and both active and passive components can accomplish their best performance without limiting each other.

2.2.2 Butt-Joint Regrowth

The butt-joint regrowth platform also has the advantage of allowing independent design of properties for the active and passive sections. The downside is that a critical alignment regrowth is required [14]. The regrowth material properties will determine the performance of the actual devices. Depending on the size or shape of the regrowth area, it is important to optimize the etch and regrowth process in order to get a good material regrowth in both the lateral and vertical directions [16].

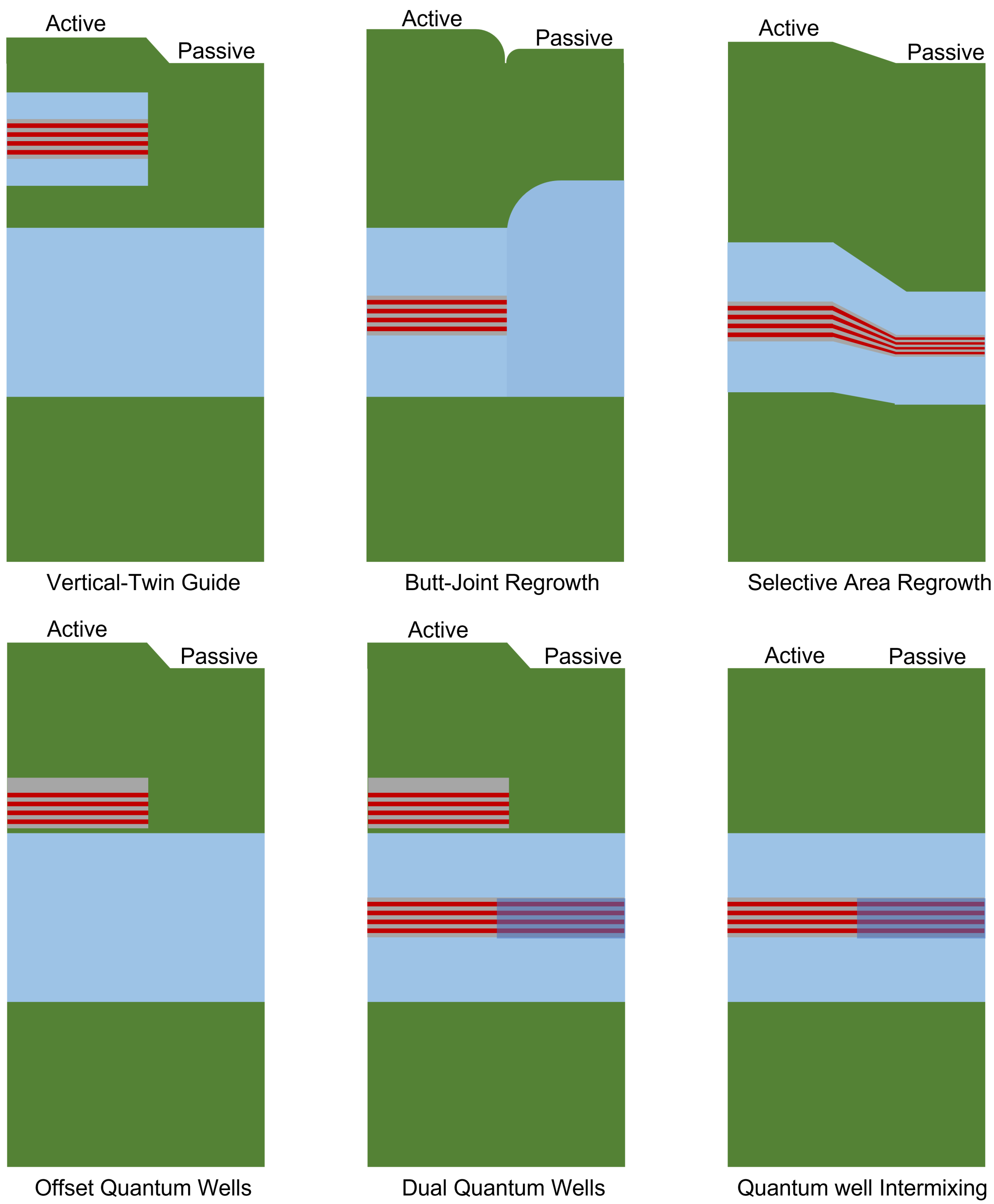

Figure 2.5: Illustration of different integration platforms

2.2.3 Selective Area Growth

The selective area growth technique allows growth of multiple absorption edges across the sample in a single growth step [14]. It also enables the possibility to directly grow different types of materials together. Much research has been done in trying to grow nano-wires or nano-patterns on different materials, especially to grow III - V materials on silicon-based materials such as Si, SiN, and SiO_2 [17] [18].

2.2.4 Offset Quantum Wells (OQW)

The offset quantum well platform is fabrication and regrowth friendly. It only requires a single regrowth and it can integrate most of the photonic components together. However, because the quantum wells are above the waveguide instead of centered in the waveguide, the net modal gain is reduced. In addition, since the quantum wells are etched away in the passive region, there is a thin step between the active and passive components. The waveguide mode has a slight distortion between the active and passive components, which may cause reflections and degrade the device performance if not handled carefully [14].

2.2.5 Dual Quantum Wells (DQWs)

The dual quantum well platform is similar to the OQW platform but includes a second stack of quantum wells to remove the tradeoff between laser and modulator performance by allowing customization of the band edge for each [14]. During the process, the lower bandgap quantum wells used for light generation are etched away in passive region and the higher bandgap quantum wells are kept everywhere. Then, a regrowth is followed to form the overall structure. The higher bandgap quantum wells are designed to have a band edge suitable for the passive and modulator regions. Due to QCSE, the efficiency of the phase modulators is higher than that of phase modulators in the OQW platform, which use the Franz-Keldysh effect.

2.2.6 Quantum Well Intermixing (QWI)

The quantum well intermixing platform combines the advantages of the OQW and DQW platforms. It only has one quantum well stack and only requires one regrowth. It also has a high modulation efficiency for modulators. The QWI platform uses controlled intermixing of atoms between the barriers and wells to create multiple quantum well band edges across the sample. This can allow efficient modulators and low loss passive regions by blue-shifting the bandgap of the quantum wells in the passive regions more than in the modulator regions [14] [19]. Compared with the OQW platform, the QWI platform does not have a discontinuity at the active/passive interface and it provides greater modal gain since the quantum wells can be in the centered in the waveguide layer. In addition, the modulators have a higher modulation efficiency from QCSE compared to the OQW platform, which uses the Franz-Keldysh effect only. One of the drawbacks is that the diffusion process in the intermixing technique can vary across and within samples, so the intermixing process needs to be carefully controlled for each sample.

2.3 Conclusion

For the active remote sensing application discussed, we are mainly focused on OQW platform and QWI platforms. Both platforms can be used to integrate both active and passive devices together. The QWI platform has the advantage of easily integrating high performance DFB lasers and high efficiency modulators, which are useful to the PIC performance for sensing applications. The OQW platform has the advantage of easy and quick fabrication and so it was included for demonstration of cost friendly PICs with moderate performance. The work presented in this thesis uses the OQW platform.

Bibliography

[1] K. Utaka, S. Akiba, K. Sakai, and Y. Matsushima, *$\lambda/4$-shifted ingaasp/inp dfb lasers*, *IEEE journal of quantum electronics* **22** (1986), no. 7 1042–1051.

[2] L. A. Coldren, S. C. Nicholes, L. Johansson, S. Ristic, R. S. Guzzon, E. J. Norberg, and U. Krishnamachari, *High performance inp-based photonic icsa tutorial*, *Journal of Lightwave Technology* **29** (2011), no. 4 554–570.

[3] L. A. Coldren, S. W. Corzine, and M. L. Mashanovitch, *Diode lasers and photonic integrated circuits*, vol. 218. John Wiley & Sons, 2012.

[4] T.-P. Lee, C. Burrus, and A. Dentai, *Ingaas/inp pin photodiodes for lightwave communications at the 0.95-1.65 μm wavelength*, *IEEE Journal of Quantum Electronics* **17** (1981), no. 2 232–238.

[5] J. C. Campbell, S. Demiguel, F. Ma, A. Beck, X. Guo, S. Wang, X. Zheng, X. Li, J. D. Beck, M. A. Kinch, *et. al.*, *Recent advances in avalanche photodiodes*, *IEEE Journal of selected topics in quantum electronics* **10** (2004), no. 4 777–787.

[6] A. Chizh, S. Malyshev, and K. Mikitchuk, *High-speed high-power inalas/ingaas/inp schottky photodiode*, in *2015 International Topical Meeting on Microwave Photonics (MWP)*, pp. 1–4, IEEE, 2015.

[7] T. Ishibashi, N. Shimizu, S. Kodama, H. Ito, T. Nagatsuma, and T. Furuta, *Uni-traveling-carrier photodiodes*, in *Ultrafast Electronics and Optoelectronics*, p. UC3, Optical Society of America, 1997.

[8] M. N. Sysak, L. A. Johansson, J. W. Raring, M. Rodwell, L. A. Coldren, and J. Bowers, *A high efficiency, current injection based quantum-well phase modulator monolithically integrated with a tunable laser for coherent systems*, in *Coherent Optical Technologies and Applications*, p. CFC6, Optical Society of America, 2006.

[9] J.-I. Shim, M. Yamaguchi, P. Delansay, and M. Kitamura, *Refractive index and loss changes produced by current injection in ingaas (p)-ingaasp multiple quantum-well (mqw) waveguides*, *IEEE Journal of Selected Topics in Quantum Electronics* **1** (1995), no. 2 408–415.

[10] L. B. Soldano and E. C. Pennings, *Optical multi-mode interference devices based on self-imaging: principles and applications*, *Journal of lightwave technology* **13** (1995), no. 4 615–627.

[11] E. A. Marcatili, *Dielectric rectangular waveguide and directional coupler for integrated optics*, *Bell System Technical Journal* **48** (1969), no. 7 2071–2102.

[12] C. Dragone, *Efficient n× n star coupler based on fourier optics*, *Electronics Letters* **24** (1988), no. 15 942–944.

[13] M. K. Smit and C. Van Dam, *Phasar-based wdm-devices: Principles, design and applications*, *IEEE Journal of selected topics in quantum electronics* **2** (1996), no. 2 236–250.

[14] L. A. Coldren, *Inp-based photonic integrated circuits*, in *2008 Conference on Lasers*

and Electro-Optics and 2008 Conference on Quantum Electronics and Laser Science, pp. 1–2, 2008.

[15] V. M. Menon, F. Xia, and S. R. Forrest, *Photonic integration using asymmetric twin-waveguide (atg) technology: part ii-devices*, *IEEE Journal of Selected Topics in Quantum Electronics* **11** (2005) 30–42.

[16] J. Wallin, G. Landgren, K. Streubel, S. Nilsson, and M. Öberg, *Selective area regrowth of butt-joint coupled waveguides in multi-section dbr lasers*, *Journal of crystal growth* **124** (1992), no. 1-4 741–746.

[17] L. Megalini, B. Bonef, B. C. Cabinian, H. Zhao, A. Taylor, J. S. Speck, J. E. Bowers, and J. Klamkin, *1550-nm ingaasp multi-quantum-well structures selectively grown on v-groove-patterned soi substrates*, *Applied Physics Letters* **111** (2017), no. 3 032105.

[18] K. Tomioka, T. Tanaka, S. Hara, K. Hiruma, and T. Fukui, *Iiiv nanowires on si substrate: Selective-area growth and device applications*, *IEEE Journal of Selected Topics in Quantum Electronics* **17** (2011), no. 4 1112–1129.

[19] E. Skogen, J. Raring, G. Morrison, C. Wang, V. Lal, M. Masanovic, and L. Coldren, *Monolithically integrated active components: a quantum-well intermixing approach*, *IEEE Journal of Selected Topics in Quantum Electronics* **11** (2005), no. 2 343–355.

Chapter 3

Epitaxial Material Design and PIC Fabrication

This chapter presents the epitaxial structure and fabrication process for the CO_2 remote sensing PICs. The whole process is based on an InP OQW platform. The OQW platform has the advantage of integrating active and passive components with a moderate fabrication process complexity. InP is a direct band-gap III-V compound semiconductor, and its related compound can be grown on InP substrates with great lattice matching. Here, lattice matched $In_xGa_{1-x}As_yP_{1-y}$ is used as quantum well material to achieve the target photoluminescence (PL) spectrum. The OQW epitaxial structure was designed based on the requirements for this sensing application, namely a center wavelength of 1572.335 nm, low passive losses, and efficient phase modulation.

3.1 Epitaxial Material Design

The overall epitaxial structure is based on an InP substrate grown by metal organic chemical vapor deposition (MOCVD) [1, 2]. All the device fabrication was based on an OQW platform. Besides the initial base epitaxial material growth, an additional MOCVD p-side regrowth was required to achieve the overall functionality of the device. The initial base epitaxy growth was on an n-type InP substrate. The waveguide and quantum wells were grown together in this growth to form the base structure of the photonic components. A second growth, also called a regrowth, grows the p-type InP cladding above the fabricated base epitaxy to form the p-i-n junction over the whole structure.

3.1.1 Detailed Base Layer Structure

The overall structure of the base epitaxy is shown in Fig. 3.1. The top layer is a 200 nm InP cap layer. Beneath that, a 25 nm $In_xGa_{1-x}As_yP_{1-y}$ separate confinement heterostructure (SCH) layer is used as a stop layer for the InP wet etch. Under the top SCH, the active region consists of seven compressively strained $In_xGa_{1-x}As_yP_{1-y}$ quantum wells (QWs) and eight tensile-strained barriers to form a multiple quantum

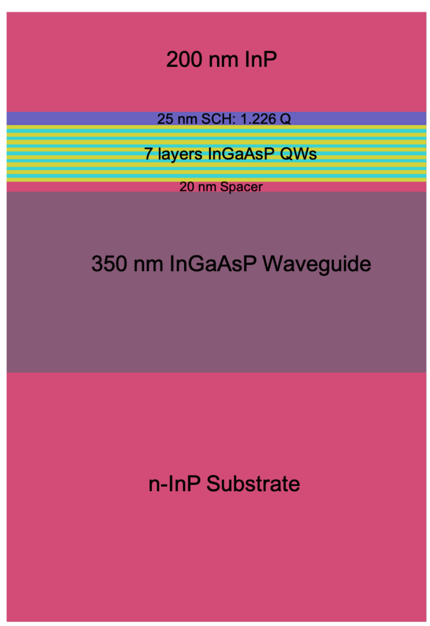

Figure 3.1: Structure of Base Epitaxy

well (MQW) stack with PL emission at 1560 - 1565 nm. The PL emission wavelength was chosen below 1572 nm to account for wavelength red-shift with heating under normal device operation. The quantum wells were 6.5 nm thick and the barriers were 8 nm thick. Below the MQW stack is a 350 nm thick 1.3Q $In_xGa_{1-x}As_yP_{1-y}$ waveguide layer. A 20 nm InP spacer was used between the MQW stack and the waveguide layer as stop etch layer for $In_xGa_{1-x}As_yP_{1-y}$ MQW wet etch during the active region definition. Finally, an n-type InP buffer layer is above the n-type substrate which is used to set back the n-doping from the MQW stack and the center of the optical mode.

Name	Layer	Thickness (nm)	Composition		Doping			Bandgap		Perpendicular Strain (%)	Notes
			x	y	Type	Dopant	Concentration (cm^{-3})	Energy (eV)	Wavelength (nm)		
Substr.	InP	~350,000	-		N	S	~3-5e+18	-	-	-	2'' substrate
Buffer	InP	800	-		N	Si	1.00E+18	-	-	-	
Buffer	InP	100	-		N	Si	8.00E+17	-	-	-	
Buffer	InP	100	-		N	Si	6.00E+17	-	-	-	
WG	In(x)GaAs(y)P	350	0.72	0.605	N	Si	1.00E+17	0.954	1300	0	Lattice matched
Spacer	InP	20	-		N	Si	5.00E+16	-	-	-	
Barrier	In(x)GaAs(y)P	8	0.732	0.52	UID		-	1.008	1230	-0.204	
QW	In(x)GaAs(y)P	6.5	0.732	0.852	UID		-	0.727	1706	0.912	
Barrier	In(x)GaAs(y)P	8	0.732	0.52	UID		-	1.008	1230	-0.204	
QW	In(x)GaAs(y)P	6.5	0.732	0.852	UID		-	0.727	1706	0.912	
Barrier	In(x)GaAs(y)P	8	0.732	0.52	UID		-	1.008	1230	-0.204	
QW	In(x)GaAs(y)P	6.5	0.732	0.852	UID		-	0.727	1706	0.912	
Barrier	In(x)GaAs(y)P	8	0.732	0.52	UID		-	1.008	1230	-0.204	
QW	In(x)GaAs(y)P	6.5	0.732	0.852	UID		-	0.727	1706	0.912	7x QWs and 8x Barriers (PL emission wavelength = 1565 nm)
Barrier	In(x)GaAs(y)P	8	0.732	0.52	UID		-	1.008	1230	-0.204	
QW	In(x)GaAs(y)P	6.5	0.732	0.852	UID		-	0.727	1706	0.912	
Barrier	In(x)GaAs(y)P	8	0.732	0.52	UID		-	1.008	1230	-0.204	
QW	In(x)GaAs(y)P	6.5	0.732	0.852	UID		-	0.727	1706	0.912	
Barrier	In(x)GaAs(y)P	8	0.732	0.52	UID		-	1.008	1230	-0.204	
QW	In(x)GaAs(y)P	6.5	0.732	0.852	UID		-	0.727	1706	0.912	
Barrier	In(x)GaAs(y)P	8	0.732	0.52	UID		-	1.008	1230	-0.204	
SCH	In(x)GaAs(y)P	25	0.7676	0.504	UID		-	1.011	1226	0	Lattice matched
Cap	InP	30	-		UID		-	-	-	-	
Cap	InP	170	-		P	Zn	5.00E+17	-	-	-	

UID = Un Intentional Doped

Table 3.1: Compositions of Base Epitaxy Layer Structure A

Based on the OQW structure, two base epitaxial structures A and B were designed. In order to achieve the target PL spectrum, the MQW layers' $In_xGa_{1-x}As_yP_{1-y}$ composition in A and B has a small difference. The details of those two base epitaxy layer structures are shown in Table 3.1 and Table 3.2 above. For both structures, the 350 nm waveguide layer was lattice matched n^+ $In_xGa_{1-x}As_yP_{1-y}$ with a band gap wavelength of 1.3 μm. The same MQW layer structure is used in each of the two structures where the QWs are compressively strained and the barriers are tensilely strained. For structure A, the

Name	Layer	Thickness (nm)	Composition		Doping			Bandgap		Perpendicular Strain (%)	Notes
			x	y	Type	Dopant	Concentration (cm^{-3})	Energy (eV)	Wavelength (nm)		
Substr.	InP	625 ± 25 µm	-		N	S	2-8e+18	-	-	-	3" substrate
Buffer	InP	800	-		N	Si	1.00E+18	-	-	-	
Buffer	InP	100	-		N	Si	8.00E+17	-	-	-	
Buffer	InP	100	-		N	Si	6.00E+17	-	-	-	
WG	In(x)GaAs(y)P	350	0.72	0.605	N	Si	1.00E+17	0.954	1300	0	Lattice matched
Spacer	InP	20	-		N	Si	5.00E+16	-	-	-	
Barrier	In(x)GaAs(y)P	8	0.732	0.52	UID		-	1.008	1230	-0.204	
QW	In(x)GaAs(y)P	6.5	0.732	0.849	UID		-	0.729	1700	0.902	
Barrier	In(x)GaAs(y)P	8	0.732	0.52	UID		-	1.008	1230	-0.204	
QW	In(x)GaAs(y)P	6.5	0.732	0.849	UID		-	0.729	1700	0.902	
Barrier	In(x)GaAs(y)P	8	0.732	0.52	UID		-	1.008	1230	-0.204	
QW	In(x)GaAs(y)P	6.5	0.732	0.849	UID		-	0.729	1700	0.902	
Barrier	In(x)GaAs(y)P	8	0.732	0.52	UID		-	1.008	1230	-0.204	
QW	In(x)GaAs(y)P	6.5	0.732	0.849	UID		-	0.729	1700	0.902	7x QWs and 8x Barriers (PL emission wavelength = 1560 nm)
Barrier	In(x)GaAs(y)P	8	0.732	0.52	UID		-	1.008	1230	-0.204	
QW	In(x)GaAs(y)P	6.5	0.732	0.849	UID		-	0.729	1700	0.902	
Barrier	In(x)GaAs(y)P	8	0.732	0.52	UID		-	1.008	1230	-0.204	
QW	In(x)GaAs(y)P	6.5	0.732	0.849	UID		-	0.729	1700	0.902	
Barrier	In(x)GaAs(y)P	8	0.732	0.52	UID		-	1.008	1230	-0.204	
QW	In(x)GaAs(y)P	6.5	0.732	0.849	UID		-	0.729	1700	0.902	
Barrier	In(x)GaAs(y)P	8	0.732	0.52	UID		-	1.008	1230	-0.204	
SCH	In(x)GaAs(y)P	25	0.7676	0.504	UID		-	1.011	1226	0	Lattice matched
Cap	InP	30	-		UID		-	-	-	-	
Cap	InP	170	-		P	Zn	5.00E+17	-	-	-	

Table 3.2: Compositions of Base Epitaxy Layer Structure B

targeted center PL emission is at 1565 nm. The QW layers used a composition of 73.2% indium and 85.2% of arsenide and the barrier layers used a composition of 73.2% indium and 52% arsenide, which resulted in a perpendicular strain of 0.912% and -0.204% for the QW and barrier layers, respectively. For structure B, the targeted center PL emission is at 1560 nm. It used the same composition as A for the barrier layers, but the QW layers used a composition of 73.2% indium and 84.9% of arsenide, where it had a perpendicular strain of 0.902%. For Both MQW designs, the center PL emission wavelength is designed to be lower than the target laser emission wavelength which is $\sim$ 1572 nm on purpose. This is because of the PL emission will shift to longer wavelength due to thermal effects after the device is fabricated.

The PL spectrum of the grown material for each of the two structures was measured and is shown below in Fig.3.2 and Fig. 3.3. Two PL peaks can be observed. The peak around 1302 nm is the peak from the waveguide layer, and the peak around 1560 nm is the peak from the MQWs. The measured grown epitaxy PL spectrum of structure A is very close to our designed emission spectrum, where the MQWs has a peak at

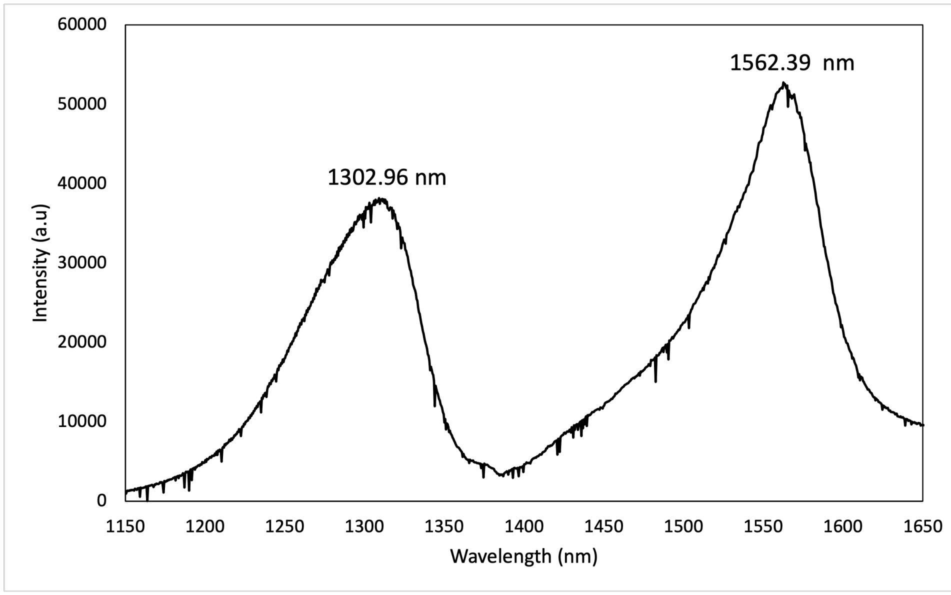

Figure 3.2: Measured PL Spectrum of Structure A

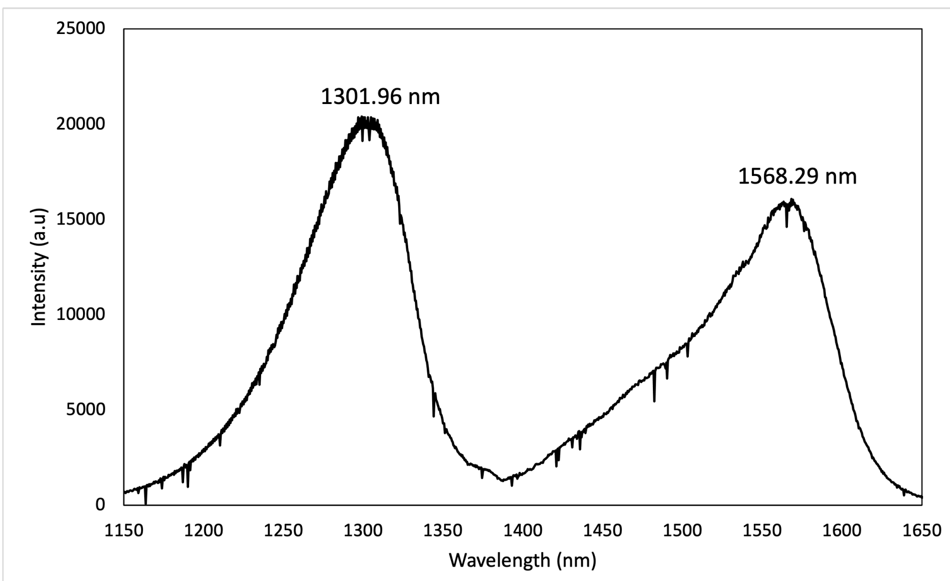

Figure 3.3: Measured PL Spectrum of Structure B

1562.39 nm with designed peak at 1565 nm. Unfortunately, the measured grown epitaxy PL spectrum for structure B is a little bit far away compared to our designed emission spectrum, where the MQWs has a peak at 1568.29 nm with designed peak at 1560 nm.

Many reasons could have lead to this, especially when those two structures were grown at different vendors with different substrate sizes. Since the PL peak is still within the tuning range of our SGDBR laser design, the device level performance should not be affected significantly from this difference.

3.1.2 Details of Regrowth

A regrowth is required for the OQW platform in order to form the overall p-i-n structure. The regrowth deposited the p^+ InP cladding and p^+ $In_{0.528}Ga_{0.468}As$ contact layer using MOCVD. The detailed structure is shown in Table 3.4, where a 1850 nm p^+ InP layer and a 100 nm p^+ $In_{0.532}Ga_{0.468}As$ layer and a 500 nm p^+ InP layer are grown from bottom to top. The 1850 nm p^+ InP is used to form ridge that confines and guides the optical mode. The 100 nm p^+ $In_{0.528}Ga_{0.468}As$ is the p contact layer for the device. The final 500 nm p^+ InP layer is the cap layer to protect the other layers during the fabrication.

Layer	Thickness (nm)	Type	Dopant	Doping concentration (cm^{-3})
InP	500	P	Zn	1.00E+18
$In_{0.532}Ga_{0.468}As$	100	P	Zn	2.50E+19
InP	820	P	Zn	1.00E+18
InP	510	P	Zn	7.00E+17
InP	440	P	Zn	5.00E+17
InP	30	P	Zn	1.50E+18
InP	10	P	Zn	5.00E+17
InP	40	P	Zn	UID
Starting on base epitaxy	N/A	N/A	N/A	N/A

Figure 3.4: Structure of Regrowth Epitaxy

3.2 OQW Fabrication Process

The main goal of this fabrication is to realize the monolithic integration of the following functions: light generation and amplification, phase and amplitude modulation, light combining and splitting and beat note detection. The OQW platform has the advantages of simplicity and robustness, and is also capable of integrating all the devices required to accomplish those functions. For the PICs fabricated based on the OQW platform, two lasers, splitters, amplitude and phase modulators, and photodiodes are integrated.

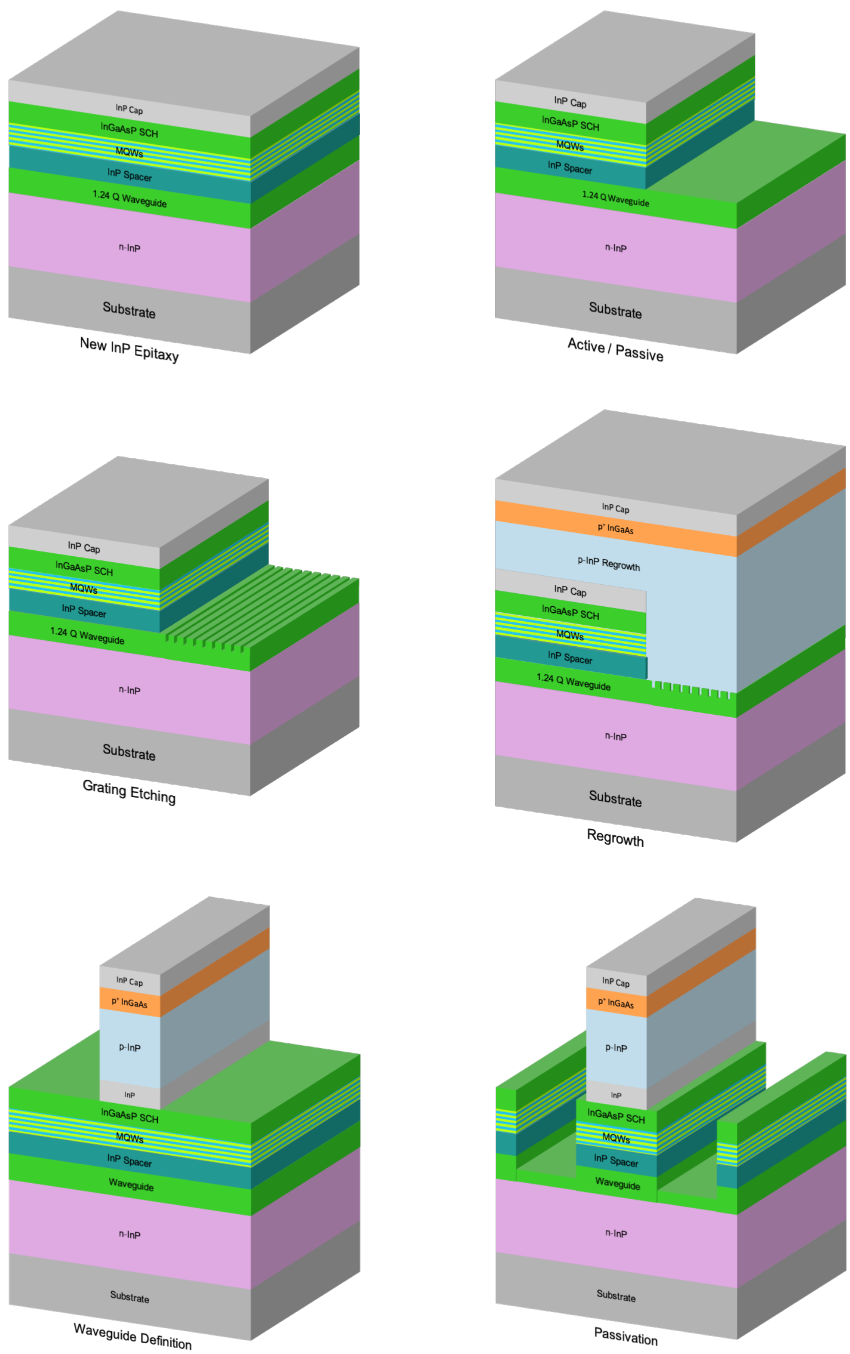

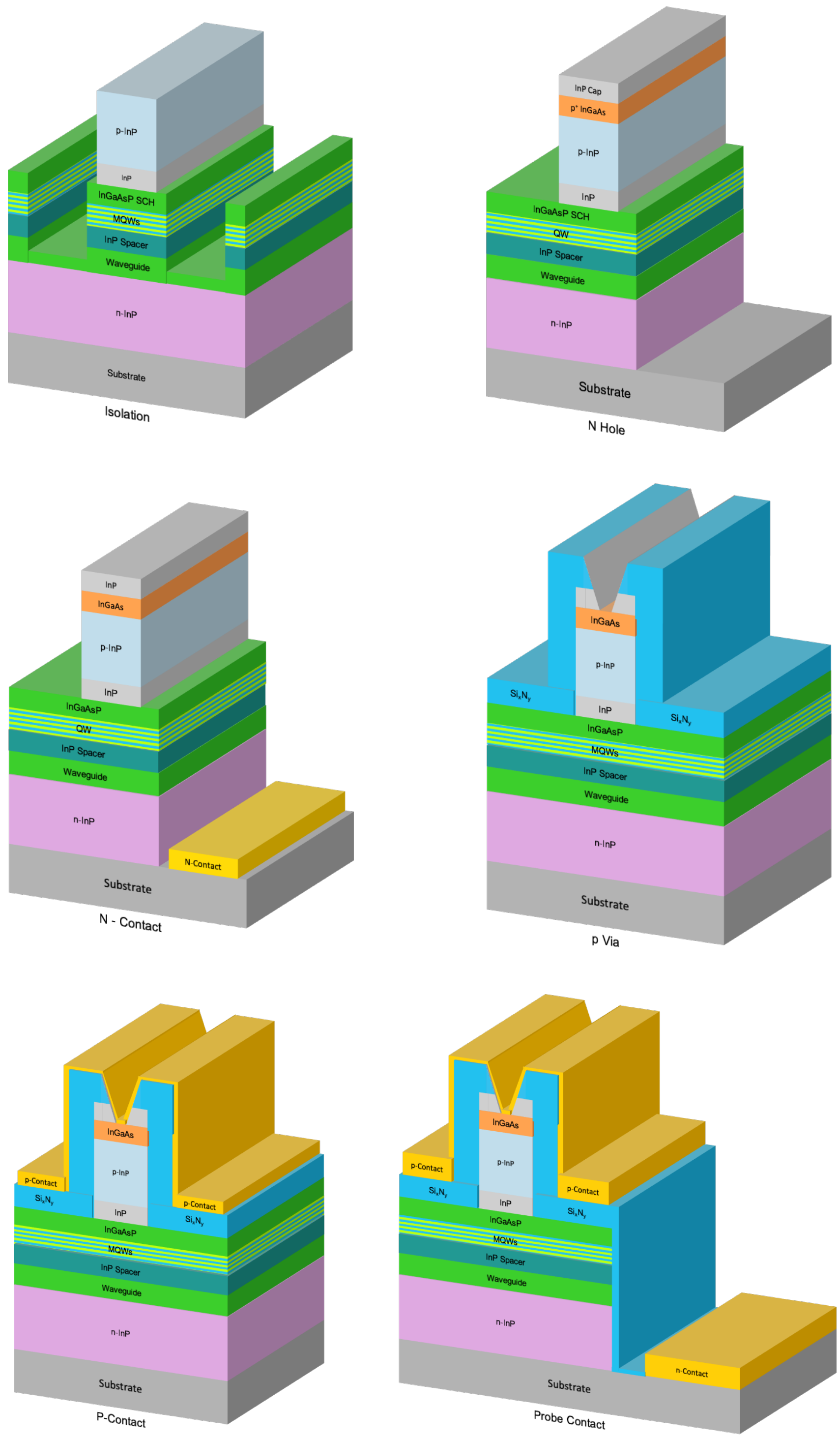

Figure 3.5: OQW Fabrication Process Flow

The OQW fabrication consists of eleven main steps. The first step is the active/passive definition, where the MQW stack is removed everywhere except for the regions of active devices. The second step is the grating formation, where the laser gratings are defined and etched. Then the next step is the regrowth, where p InP and p^+ $In_xGa_{1-x}As$ layers are grown to form the p-i-n/p-n junction. After that, the ridge is defined through dry and wet etch processes. A "passivation" etch is performed to improve high-speed device performance. The electrical isolation between devices is formed and n-contacts are made. A layer of BCB is added to the high-speed devices to decrease the parasitic capacitance of the devices if needed. At the end, vias are opened above ridge and the p contacts and probe metal are deposited. The overall process flow is shown in Fig. 3.5 below and the details of each step are described and introduced in the following section.

3.2.1 Active/Passive Definition

For the OQW platform fabrication, the first step is the active/passive definition. In this step, the active region and passive region are formed by selectively removing the 200 nm InP cap layer and the MQW layer in the passive regions. To achieve this, a dielectric Si_xN_y mask is first deposited using plasma enhanced chemical vapor deposition (PECVD) and then patterned using an i-line wafer stepper projection lithography system. Next, an $CF_4/CHF_3/O_2$ inductively coupled plasma (ICP) dry etch is used to pattern the dielectric hard mask. Two selective wet etches are performed to form the passive region by etching away the InP cap and MQW layers [3]. The first wet etch is an InP etch using $HCL : H_3PO_4$ (1:3). It etches the 200 nm InP cap layer and stops at the 25 nm $In_xGa_{1-x}As_yP_{1-y}$ SCH layer. The second wet etch is an $In_xGa_{1-x}As_yP_{1-y}$ etch using $H_2O_2 : H2SO_4 : DI$ (1:1:10). It etches the the SCH layer and MQW layers and stops at the 20 nm InP spacer layer. After the wet etch, the dielectric Si_xN_y mask is removed using a buffered HF (BHF) wet etch [4]. Microscope images of the sample after corresponding etching processes are shown in Fig. 3.6, where Fig. 3.6(a) shows the dry etched dielectric patterns after the PR is stripped, and Fig. 3.6(b) shows the wet etched patterns after the dielectric mask is removed.

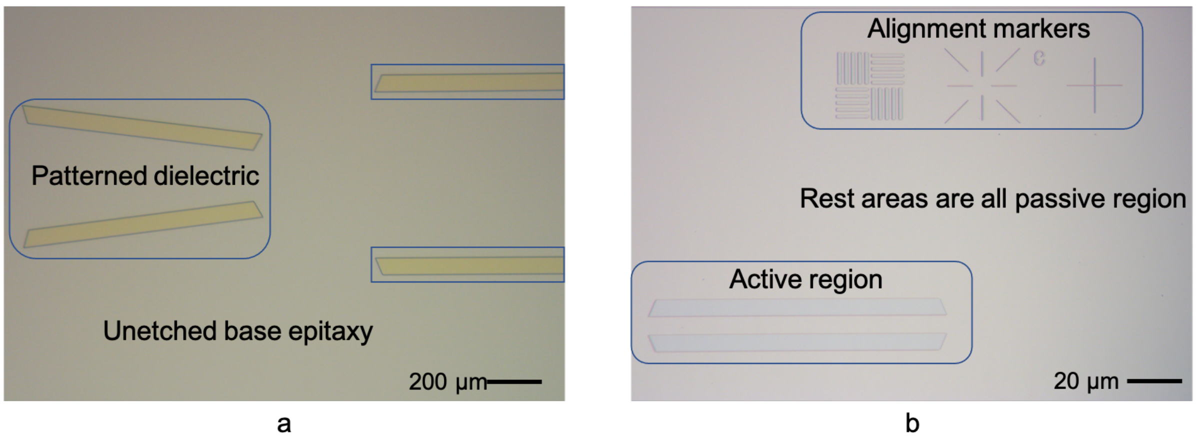

Figure 3.6: Microscope image of active/passive processes. (a) Dry etched dielectric patterns before wet etch; (b) Wet etched active/passive region after stripping the dielectric mask.

3.2.2 Grating Formation

Following the active/passive definition, the front and back laser mirror Bragg gratings are defined. Since the size of the gratings is in the range of hundreds of nanometers, the gratings are patterned using electron-beam lithography (EBL) system which can achieve a sub 10 nm resolution [5]. The resist patterns are first patterned using EBL on a 30 nm Si_xN_y layer deposited using PECVD. Then, the patterns are transferred to the Si_xN_y layer using a $CF_4/CHF_3/O_2$ ICP dry etch. The final grating patterns are dry etched using $CH_4/H_2/Ar$ reactive-ion etching (RIE) with the patterned Si_xN_y layer as a hard mask. At the end, the Si_xN_y dielectric hard mask is removed using a BHF wet etch.

For the grating etch step, the EBL process needs to be carefully calibrated, where

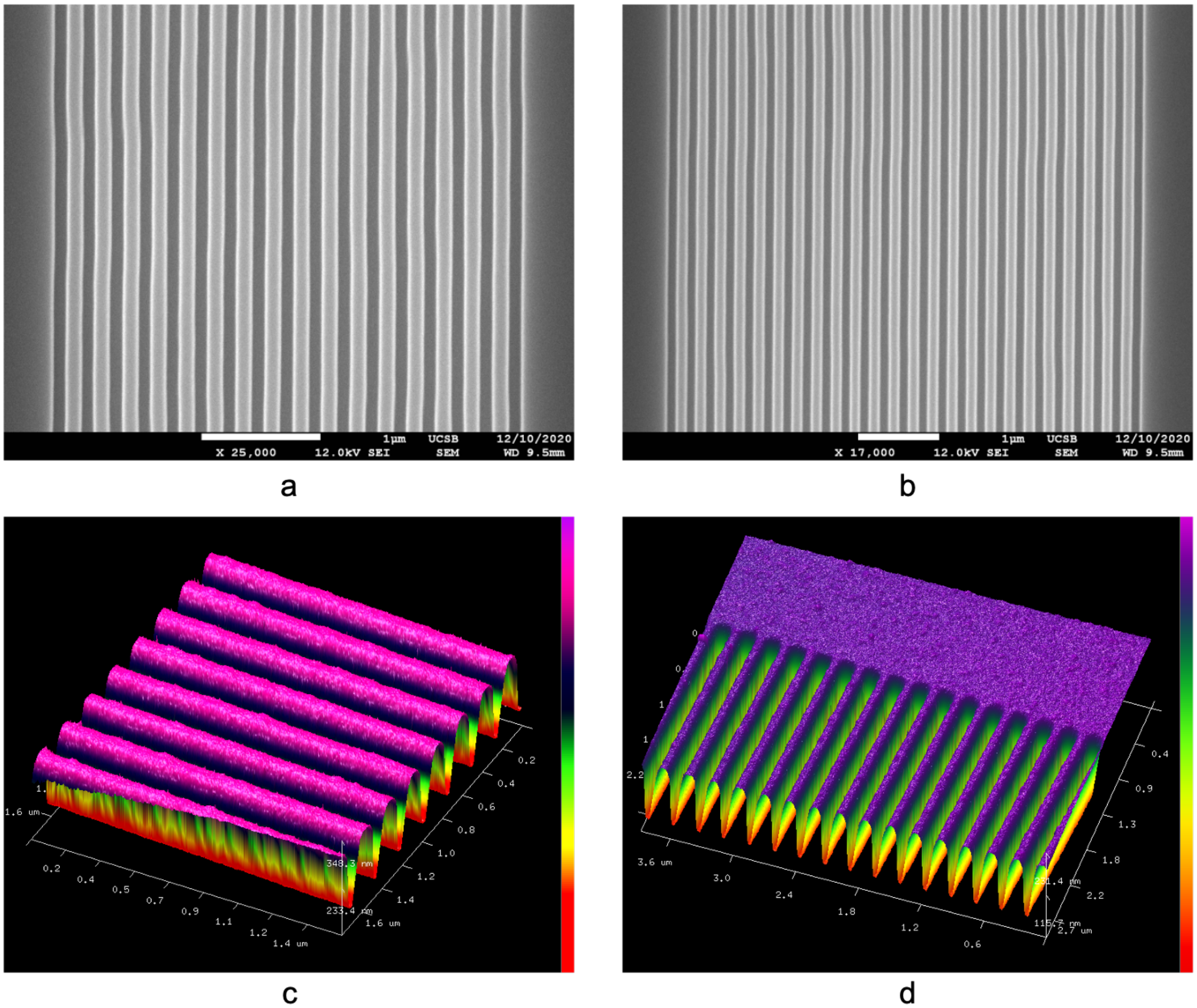

Figure 3.7: Images of grating measurement. (a) SEM image of front mirror grating ; (b) SEM image of back mirror grating; (c-d) Images of grating's AFM measurement

the dose, pattern size and proximity correction need to be calibrated together in order to achieve an uniform and accurate EBL resist pattern. In addition, due to the imperfection of the dry etch process in the direction perpendicular to the sample surface, roughness on the sidewall, and rounding in the corner can be observed. Those defects vary depending on the etching tool, etching condition, etching depth, etching rate, and etching material. Those effects need to be considered into the calibration process in order to get an accurate etched grating pattern with targeted depth on the sample.

The dry etched grating is shown in Fig. 3.7, where Fig. 3.7 (a,b) are the SEM top view image of a sampled grating in the front and back mirror, respectively. Fig. 3.7 (c,d) are the grating measurements from atomic force microscope (AFM). From those images, the defects from the etching process are observed, which makes the etched grating more similar to a trapezoid with rounded corners instead of a perfectly rectangular shape with rounded corners [6].

3.2.3 Regrowth

Then, the regrowth is performed. Since the details of the regrowth structures were discussed above in section 3.1.2, this part will focus on the sample surface preparations before the regrowth. There are three main steps for the sample surface preparations. The first one is the pure sulphuric acid (H_2SO_4) dip. This step is used to clean up the left-over organic residue from the grating etch step. Then, in order to minimize concentration of Si incorporated at the regrowth interface, a UV ozone photoreactor and a BHF etch are used. The UV ozone photoreactor generates O_3 from O_2 using a photochemical reaction under 185 nm UV light. Then the ozone is dissociated into molecular oxygen O_2 and singlet atomic oxygen $O(^1D)$ under 253 nm UV light. The $O(^1D)$ has a strong oxidizing agent, which can react with inorganic and organic materials. Here it is used to remove the organic residue on the sample surface, but it also oxidizes the surface material. Then, the BHF is used to remove the oxidized surface material and Si atom from fabrication process.

The sample is first dipped into pure H_2SO_4 for 40s. Then, the sample is exposed to BHF for 60s followed by a DI water rinse and N_2 blow dry. Then, the UV ozone is warmed up for 20 minutes or longer, and the sample after BHF treatment is placed in the UV ozone photoreactor for 1 hour. After the UV ozone, 60s BHF is used again to remove the surface oxide and Si atom. After the second BHF dip, the sample is immediately put into the load lock chamber of the MOCVD system. The structure in Table 3.4 was grown and, shown in Fig. 3.8, are microscope images of the surface after the regrowth. The left image shows a high quality regrowth and the image on the right shows a relatively low quality regrowth.

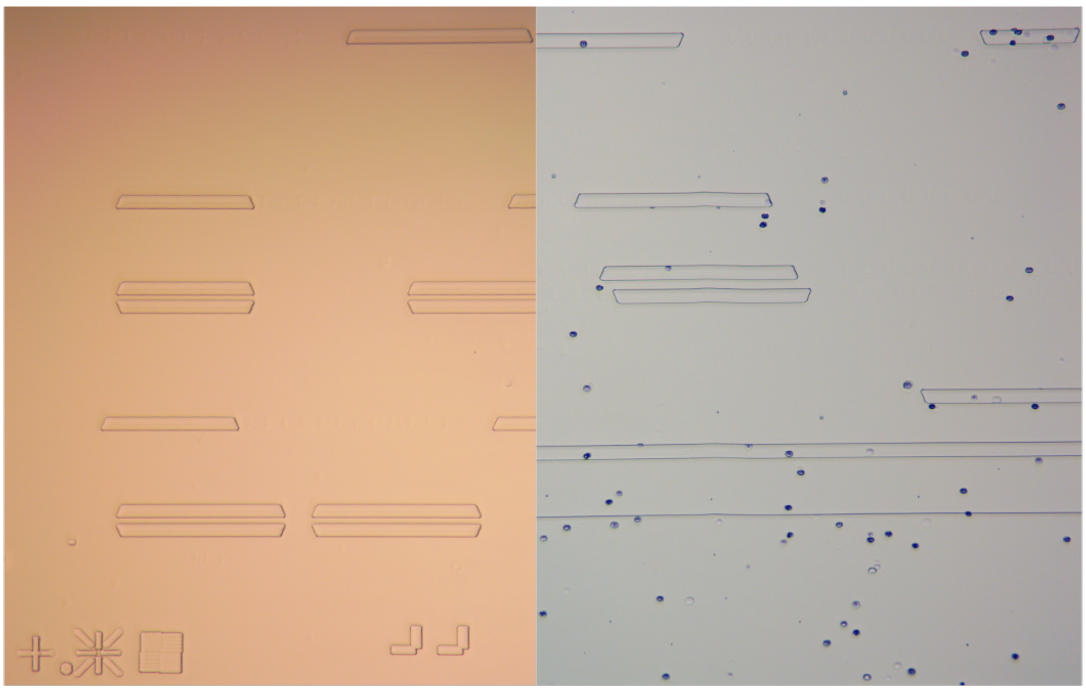

Figure 3.8: Microscope images of samples after regrowth. (left) A high quality regrowth ; (right) A relatively low quality regrowth.

3.2.4 Ridge Formation

Following the regrowth of the p InP cladding and p^+ $In_{0.528}Ga_{0.468}As$ contact layer, a ridge is formed to guide the optical mode. There are two types of ridge etch widely used in the OQW platform: a surface ridge etch and a deep ridge etch. The surface ridge etch only removes the regrowth layers and stops above the waveguide layer. For a deep ridge structure, the etch goes through the waveguide layer and into the n-side to form a more highly confined optical mode.

For the PICs and devices designed for this application, only a surface ridge was used. The ICP dry etch and $HCL\ InP$ selective wet etch were used in the surface ridge formation process. The ICP dry etch etches through the $p^+\ In_{0.528}Ga_{0.468}As$ contact layer and stops in the $p\ InP$ cladding. The $HCL\ InP$ selective wet etch continues the etch and stops above the QWs or waveguide layer. Since the $HCL\ InP$ selective wet etch is crystal plane dependent the ridge needs to be patterned in the [110] plane so that the wet etch etches the [011] and [01$\bar{1}$] plane and results in a very smooth sidewall [7].

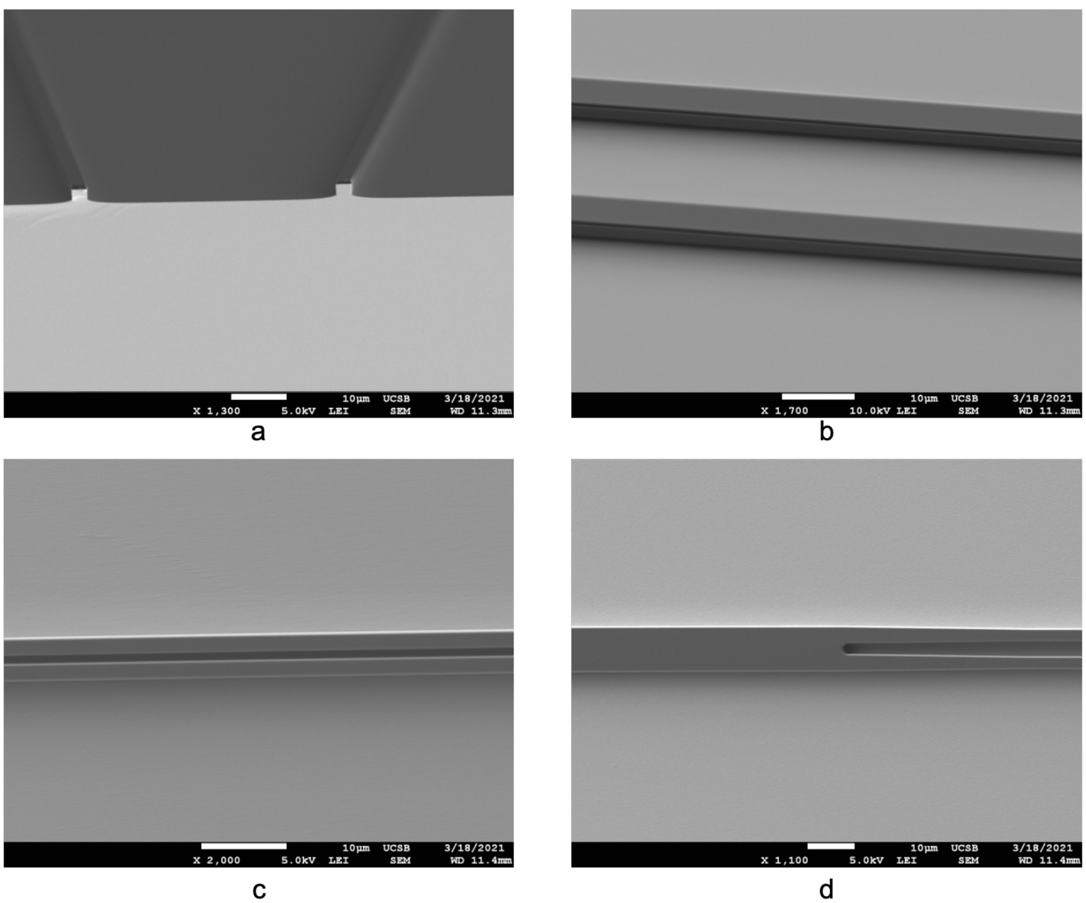

Figure 3.9: SEM images of surface ridges. (a) A cross view of formed surface ridges; (b) A side view of formed surface ridges; (c) A top view of the coupling section of the directional coupler; (d) A top view of the right half of the 2×2 MMI.

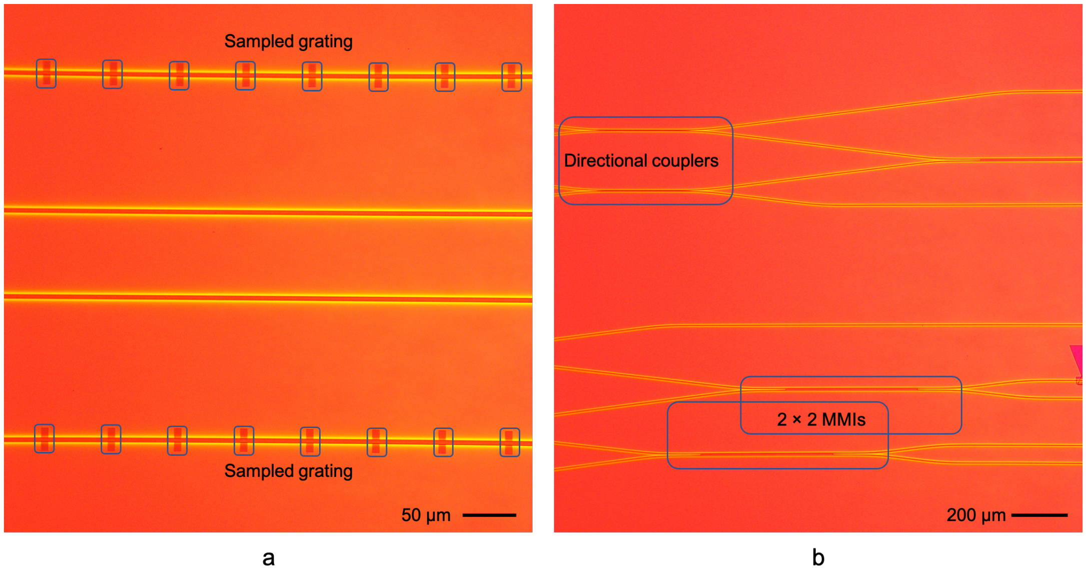

Figure 3.10: Microscope images of surface ridges. (a) A top view of sampled grating of back mirrors; (b) A top view of directional couplers and 2 × 2 MMIs.

The process details of the ridge etch step are listed below. First, 200 nm of Si_xN_y and 500 nm of SiO_2 are deposited using PECVD as the hard mask. The hard mask is patterned with an i-line stepper in the [110] plane and is etched using the CF_4/CHF_3 ICP etch. Then, the photoresist is stripped and a $Cl_2/H_2/Ar$ ICP etch is used to etch the InP and $In_xGa_{1-x}As$ material to form the initial ridge. For this ICP etch, the ideal stop depth is ~ 1 μm below the p^+ $In_{0.528}Ga_{0.468}As$ contact layer for a ~ 3 μm height ridge. Then, a 20s $NH_4OH : DI$ (1:3) dip is recommended to clean up the organics on the sidewall from the ICP etch. Finally, an InP selective wet etch using $HCL : H_3PO_4$ (1:3) is performed to further etch the ridge and stop on the $In_xGa_{1-x}As_yP_{1-y}$ layer. After the ridge formation, the waveguides for the devices are formed and showed in Fig. 3.9 and Fig. 3.10. The Fig.3.9 (a-b) shows the cross view and side view of the formed surface ridges. Figure 3.9 (c-d) show the top view of the coupling section of the directional coupler and right half of the 2×2 MMI. The Fig. 3.10(a) shows top view of the sampled gratings of laser's back mirrors. The Fig. 3.10(b) shows the top view of the directional couplers and 2×2 MMIs.

3.2.5 Passivation

During the regrowth, the p InP and p^+ $In_xGa_{1-x}As$ layers are grown with Zn doping. This causes the regrowth surface to be also unintentionally Zn doped, especially when the surface is $In_xGa_{1-x}As_yP_{1-y}$, which is easier to be doped than InP. This forms a thin highly conductive Zn doped $In_xGa_{1-x}As_yP_{1-y}$ layer on the regrowth surface. This thin layer works as a conductive plane of a capacitor and introduces a parasitic capacitance to the devices, which degrades the performance of high-speed devices. So, the thin Zn doped $In_xGa_{1-x}As_yP_{1-y}$ layer needs to be etched away to improve the high-speed device performance [8]. In our case, they are photodiodes and high-speed phase modulators.

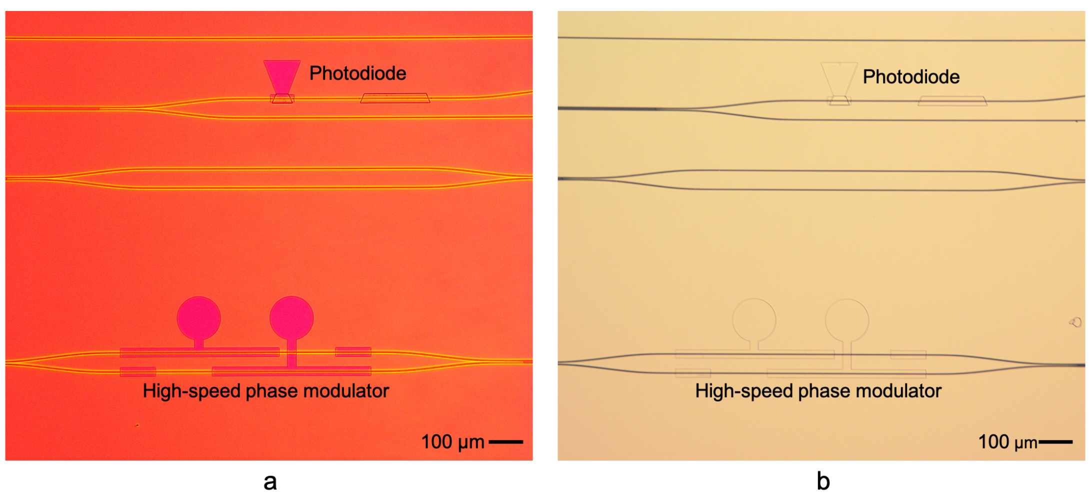

Figure 3.11: Microscope images of passivation. (a) Passivation on photodiode and phase modulator with dielectric hard mask above for better contrast; (b) Passivation on photodiode and phase modulator without dielectric hard mask.

The detailed processes are shown here. First, the photoresist is spun above the sample, and patterned using i-line stepper lithography system to only expose the high speed devices to outside environment. Then a thin layer $(80 \sim 100nm) of In_xGa_{1-x}As_yP_{1-y}$ material is etched away in the exposed area using the $CH_4 : H_2 : Ar$ RIE dry etch. The

RIE dry etch is set at a very low etch rate in order to control the etch depth accurately. The etched patterns are shown in Fig. 3.11.

3.2.6 Electrical Isolation

The electrical isolation is achieved by removing the p^+ $In_{0.528}Ga_{0.468}As$ contact layer on the ridge using wet etch between the electrical connections. The semi-self align technique is used for this step in order to reduce the alignment requirement for the lithography system. First, a layer of dielectric hard mask is deposited using PECVD. Then, a layer of photoresist thicker than the ridge is applied on the sample.

Since the p^+ $In_{0.528}Ga_{0.468}As$ contact layer is only on the ridge, which is $\sim$ 3 μm higher than the sample surface, a wider pattern can be used to reduce the lithography system requirement. The pattern is partially exposed and developed to remove some photoresist above the ridge. Then, an O_2 plasma is used to remove the extra photoresist above the ridge. Since the ridge is $\sim$ 3 μm above sample surface, doing so will only expose the top of the ridge to the outside environment. Then the dielectric hard mask is etched using $CF_4/CHF_3/O_2$ ICP etch. The HCL : H_3PO_4 (1:3) InP selective wet

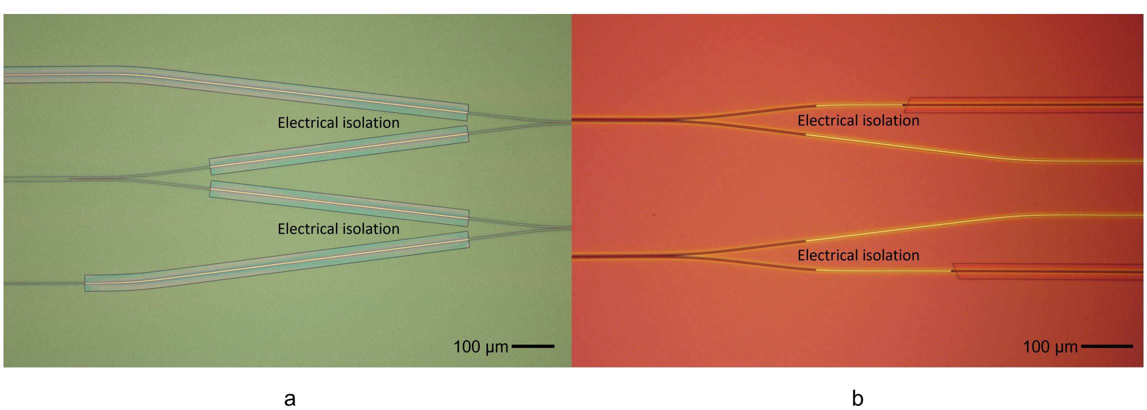

Figure 3.12: Microscope images of electrical isolation. (a) Electrical isolation after ICP dielectric hard mask etch; (b) Electrical isolation after InP and $In_xGa_{1-x}As$ wet etch.

etch is used to remove the 500 nm InP cap layer, and the $H_2O_2 : H2SO_4 : DI$ (1:1:10) solution is used to etch the $In_{0.528}Ga_{0.468}As$ contact layer selectively. The electrically isolated waveguide is shown in Fig. 3.12. Fig. 3.12 (a) shows the isolation after dielectric hard mask ICP etch and Fig. 3.12 (b) shows the isolation after the $In_{0.528}Ga_{0.468}As$ layer is removed.

3.2.7 N Metal Hole & N Metal Contact

After the electrical isolation step, the n-metal holes and n-metal contacts are formed. The n-metal hole is formed by etching a hole into the n-substrate [9]. First, a 300 nm dielectric hard mask is deposited using PECVD. The n-hole pattern is transferred to the dielectric hard mask using a $CF_4/CHF_3/O_2$ ICP etch. Then, the n-metal hole is formed using $CH_4/H_2/Ar$ RIE etching into the substrate, followed by a 5 s $HCL : H_3PO_4$ (1:3) InP wet clean. Fig. 3.13 shows the etched holes around a photodiode and phase modulator to form the ground for the ground-signal-ground (GSG) and ground-signal-ground-signal-ground (GSGSG) high speed pads.

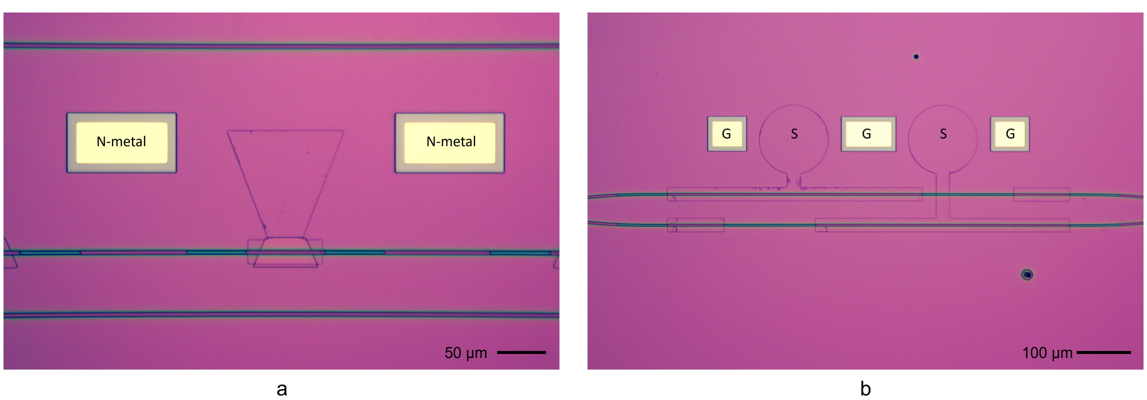

Figure 3.13: Microscope images of N metal holes. (a) N metal holes around photodiode for GSG pad; (b) N metal holes around the phase modulator fro GSGSG pad.

3.2.8 BCB Definition

The divinylsiloxane-bis-benzocyclobutene (BCB) is a low dielectric constant material. It is photopatternable and widely used in semiconductor fabrication to reduce the parasitic capacitance of high speed devices [10]. For our application, the requirement for the device speed performance is not very high, so the BCB was not used for most rounds device fabrication.

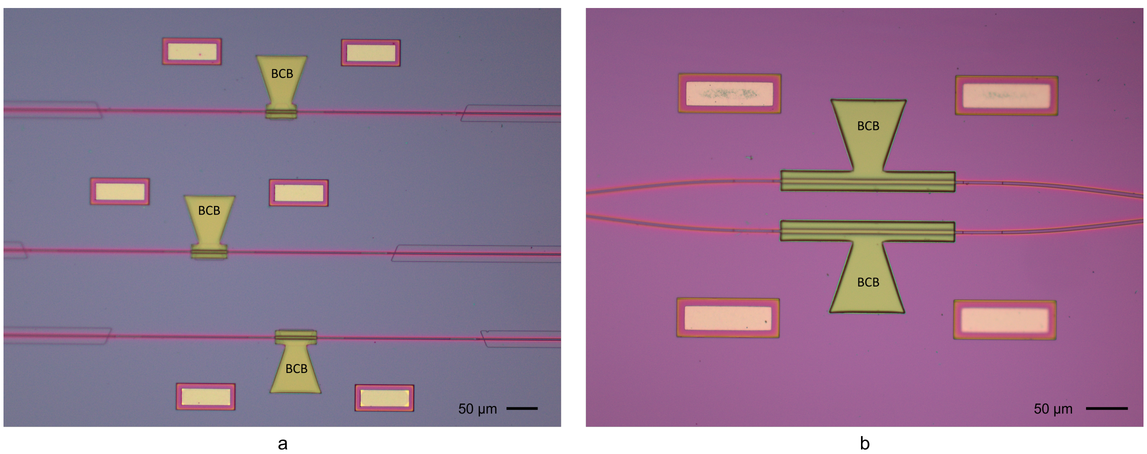

Figure 3.14: Microscope images of patterned BCB. (a) BCB patterns on the photodiode; (b) BCB patterns on the phase modulator.

For the BCB definition, first, a thin layer of Si_xN_y is deposited on the sample to improve the BCB adhesion. Then, the BCB is applied and spun uniformly over the sample, and exposed using an i-line stepper lithography system. The unexposed BCB is removed by a BCB developer. The BCB is cured in an oven with N_2 for 4 hours at 250 °C. Once the BCB is exposed and cured, it becomes insoluble in most commonly used solvents and it becomes hard to strip, especially after the curing. In Fig. 3.14, the cured BCB patterns for high-speed photodiodes and phase modulators are shown.

Following BCB patterning, BCB vias are opened on the top of n-via and n-metal. A layer of dielectric hard mask is deposited above the BCB and BCB vias are patterned and transferred to the dielectric hard mask using a CF_4/CHF_3 ICP etch. Then, the

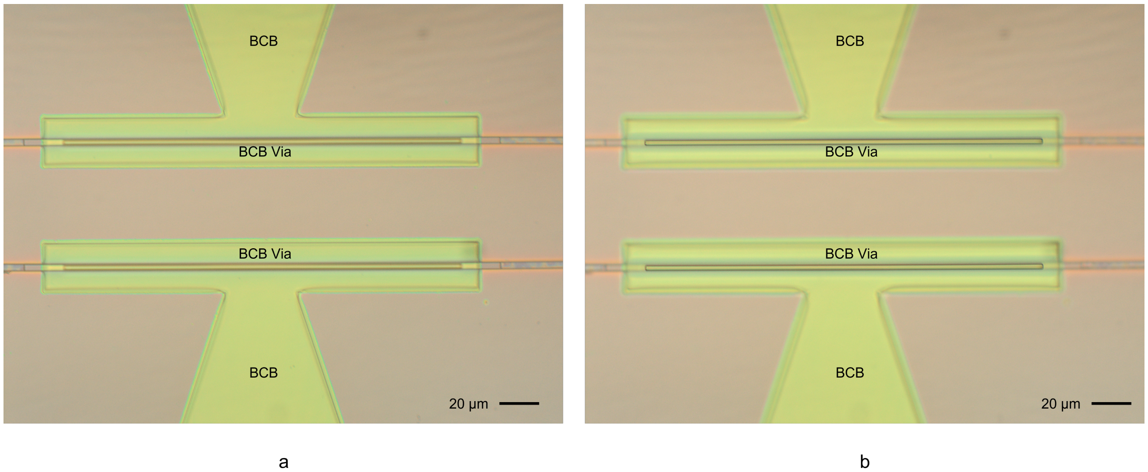

Figure 3.15: Microscope images of opened BCB Vias on phase modulator. (a) Opened BCB vias with microscope focus on the BCB; (b) Opened BCB vias with microscope focus on the vias.

BCB is etched away using a $CF_4 : O_2$ ICP etch. Then, a new layer of dielectric hard mask is deposited again using PECVD. The same BCB vias are patterned again. The dielectric hard mask is etched away using a CF_4/CHF_3 ICP etch to open the BCB vias on the ridge and expose the n-contact layer. Fig. 3.15 shows the opened BCB vias on the ridge with the microscope focused on the BCB and focused on the vias. The BCB via etching is performed in two steps because the via in the BCB widens significantly during the etch.

3.2.9 N & P Via Definition

The n & p via step opens vias in the n-holes and in the InP cap layer above the InGaAs p-contact on to of the ridges so that the final probe metal may be deposited. For our fabrication process, the two types of vias are opened together in single lithography and etch process. The vias are patterned on a layer of dielectric hard mask. The dielectric hard mask is etched away using a dry RIE etch. At this point, the n-vias are now open. Then, the p-vias are opened by further etching away the InP cap layer on top of the ridge using the $HCL : H_3PO_4$ (1:3) selective InP wet etch. Fig. 3.16 shows the opened vias on the laser mirror, SOA, photodiode and phase modulator.

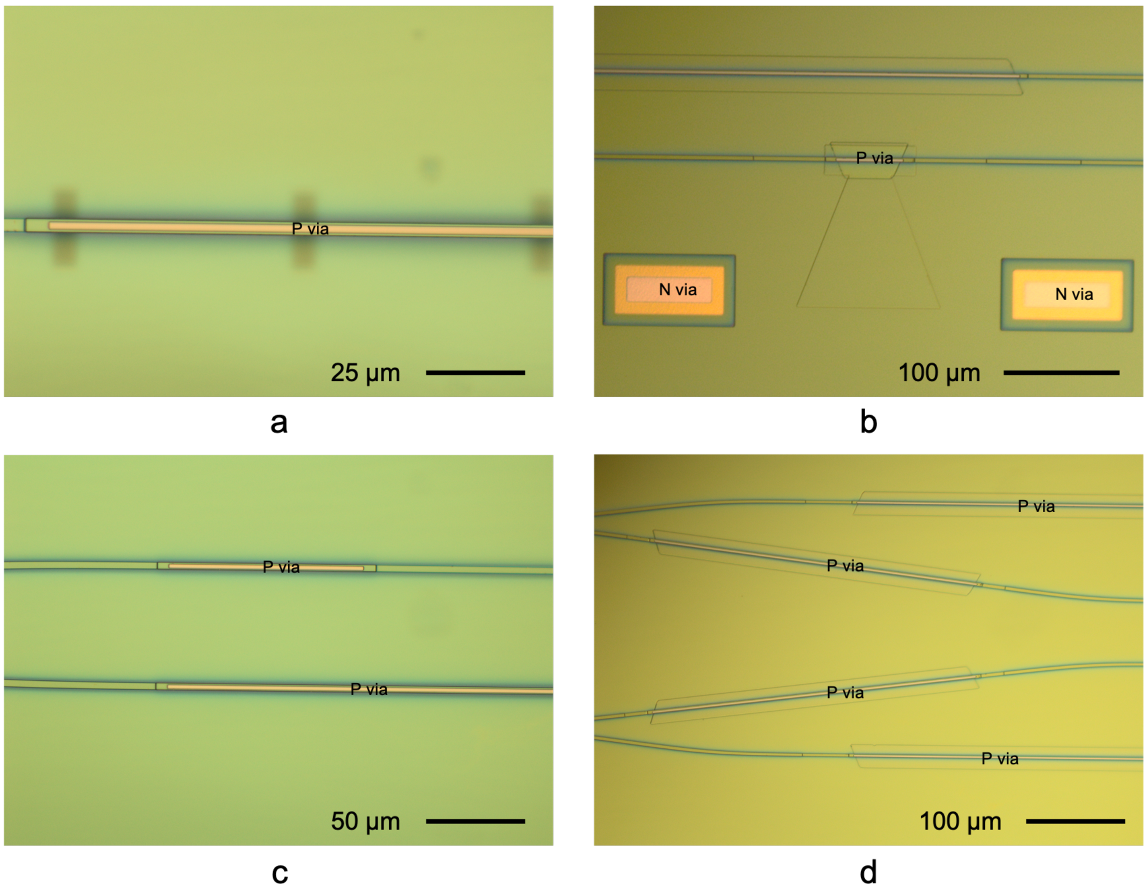

Figure 3.16: Microscope images of opened n & p vias. (a) P vias on laser mirror; (b) N & P vias around photodiode; (c) P vias on phase modulators; (d) P vias on SOAs.

3.2.10 Probe Metal Deposition

At last, the p-contacts are formed and the probe metal is deposited using electron-beam deposition with a standard lift-off process. Two depositions are performed. First, the p-contact is formed by depositing Ti/Pt/Au, then the final probe metal is deposited using Ti/Au [9]. After lift-off, the contacts need to go through rapid thermal anneal (RTA) to improve their electrical performance. The fabricated die is shown in Fig. 3.17.

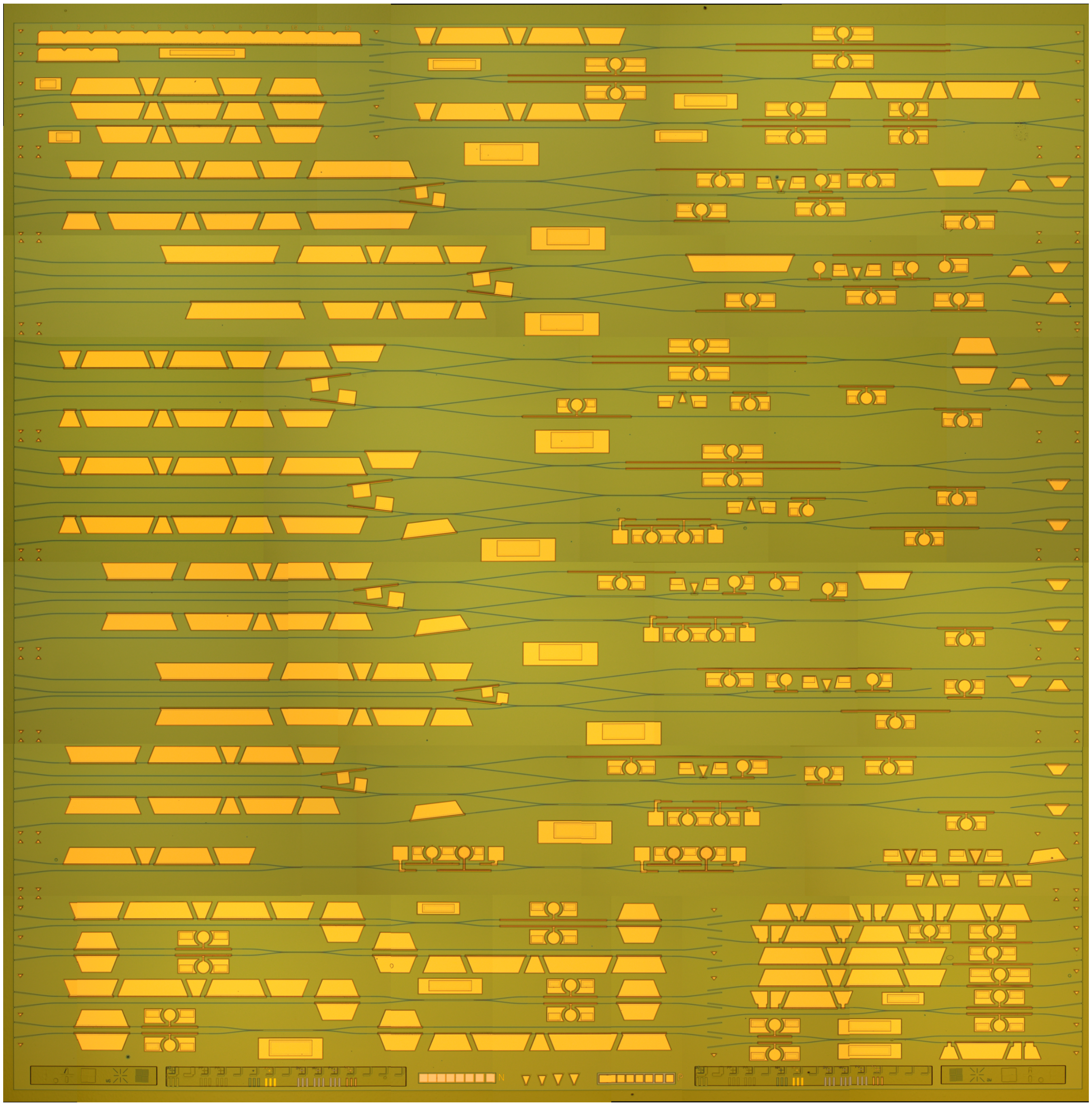

Figure 3.17: Microscope image of a fabricated die.

3.2.11 Post Processing

After finishing the fabrication of the samples, several steps need to be performed before they are ready for test. These steps are lapping for substrate thinning, back-side metal deposition, cleaving and antireflective (AR) coating of the facets. In order to achieve good thermal performance and good cleaving quality of the InP sample, it needs to be thinned down to between 120 $\mu m \sim 180$ μm. Then, the backside is cleaned, and Ti/Au is deposited on the backside of the substrate to form the backside n-pad [9]. After cleaving into bars, an anti-reflective (AR) is deposited on the facets to improve the device performance. Then, the sample is separated into single PICs for testing.

3.3 Conclusion

In sum, three generations of OQW fabrication were completed. Clear improvements were seen between each generation. In the first generation, we demonstrated the fundamental functionality of some key devices, but the PIC was not fully functional. In the second generation, a PIC was found that was functioning properly except for the photodiode, but the overall PIC yield was low. In the third generation, a fully functional was characterized with many others expected to be functional as well.

Bibliography

[1] M. Gibbon, J. Stagg, C. Cureton, E. Thrush, C. Jones, R. Mallard, R. Pritchard, N. Collis, and A. Chew, *Selective-area low-pressure mocvd of gainasp and related materials on planar inp substrates*, *Semiconductor science and technology* **8** (1993), no. 6 998.

[2] P. Wolfram, E. Steimetz, W. Ebert, B. Henninger, and J.-T. Zettler, *Growth of ingaasp/inp-laser structures monitored by using ras techniques*, *Journal of Crystal growth* **248** (2003) 240–243.

[3] A. Clawson, *Guide to references on iii–v semiconductor chemical etching*, *Materials Science and Engineering: R: Reports* **31** (2001), no. 1-6 1–438.

[4] Y. Kunii, S. Nakayama, and M. Maeda, *Wet etching of doped and nondoped silicon oxide films using buffered hydrogen fluoride solution*, *Journal of the Electrochemical Society* **142** (1995), no. 10 3510.

[5] C. Vieu, F. Carcenac, A. Ppin, Y. Chen, M. Mejias, A. Lebib, L. Manin-Ferlazzo, L. Couraud, and H. Launois, *Electron beam lithography: resolution limits and applications*, *Applied Surface Science* **164** (2000), no. 1 111–117. Surface Science in Micro Nanotechnology.

[6] H. Zhao, *Integrated Photonics Technologies for Free Space Optical*

Communications. PhD thesis, 2019. Copyright - Database copyright ProQuest LLC; ProQuest does not claim copyright in the individual underlying works; Last updated - 2021-05-14.

[7] L. Stulz and L. Coldren, *Orientation of (100) ingaasp/inp wafers by hci chemical etching*, *J. Electrochem. Soc.* **130** (1983), no. 7 1628–1630.

[8] J. S. Barton, *The integration of Mach-Zehnder modulators with sampled grating DBR lasers*. University of California, Santa Barbara, 2004.

[9] A. Baca, F. Ren, J. Zolper, R. Briggs, and S. Pearton, *A survey of ohmic contacts to iii-v compound semiconductors*, *Thin Solid Films* **308** (1997) 599–606.

[10] C. O'Connor, R. Barr, J. Calvert, A. Choubey, M. Gallagher, E. Iagodkine, J.-S. Oh, A. Politis, and K. Wang, *Photopatternable laminate bcb dielectric*, in *International Symposium on Microelectronics*, vol. 2014, pp. 000580–000584, International Microelectronics Assembly and Packaging Society, 2014.

Chapter 4

Components Design

In this chapter, the design of the PIC components is introduced. The components were designed based on the epitaxial material design and OQW fabrication process discussed in chapter 3. They mainly include SGDBR and DBR lasers for light generation, straight and Mach-Zehnder modulators for phase and amplitude modulation, semiconductor optical amplifiers for power amplification and pulse generation, photodiodes for beat note detection, and couplers for power splitting.

4.1 Lasers

Unlike passive sensing, which relies on the reflection of solar light, active sensing uses a laser light source, which makes the laser one of the most important system components. Commonly used InP-based lasers include distributed feedback (DFB) lasers, distributed Bragg reflector (DBR) lasers, and sampled grating distributed Bragg reflector (SGDBR) lasers [1–4]. Due to limitations of the epitaxial material and fabrication, it is difficult to create a DFB laser structure in the OQW platform. The DBR and SGDBR lasers were the main choices for the laser source for this application.

A DBR laser uses continuous single burst DBR gratings for the front and back mirrors and has a moderate wavelength tuning range, typically 5 - 7 nm [3]. An SGDBR laser uses sampled DBR gratings in the front and back mirrors and can easily achieve a 30 - 40 nm tuning range [3, 4]. Since the CO_2 remote sensing requires a lasing wavelength centered at 1572.335 nm with 40 GHz tuning range[5–7], both the epitaxial material and the lasers need to be carefully designed to hit the target wavelength. The details of the epitaxial material design and optimization were already discussed in Chapter 3. This section focuses on the design and characterization of the DBR and SGDBR lasers.

4.1.1 DBR lasers

DBR lasers are constructed with four sections: front mirror, gain, phase and back mirror. The detailed structure of the DBR laser based on OQW platform is shown in Fig. 4.1. The gain section is defined through the active & passive step described in 3.2.1. The gain section is an active region where the quantum wells remain, whereas the phase, and front and back mirror sections are passive sections where the quantum wells are etched away. The phase section can be tuned by current injection which is mainly the result of band-filling in the material to provide a negative change in the refractive index [8].

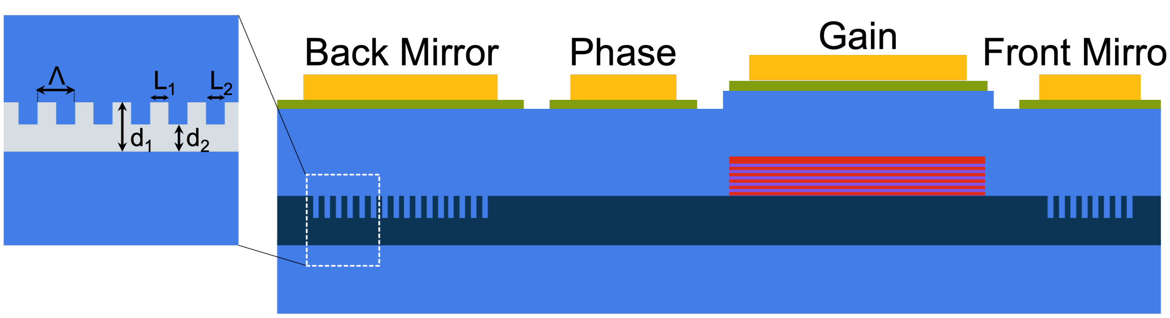

Figure 4.1: Structure of a DBR laser.

The Bragg gratings used in the DBR mirrors are formed by periodically etching away part of the waveguide material as demonstrated in the left side of Fig. 4.1. This periodic structure is called a Bragg grating and it introduces a small periodical change in the effective index of the optical mode. For these etched gratings, the relation between the effective index (n_1 in the unetched area and n_2 for etched area in the grating), grating period (Λ) and Bragg wavelength (λ_0) is given by Eq. 4.1 [3]:

$$\Lambda = \frac{\lambda_0}{4}(\frac{1}{n_1} + \frac{1}{n_2}) \tag{4.1}$$

The width of the mirror spectrum at half maximum ($\Delta\lambda_{FWHM}$), the coupling constant (κ), and the reflectivity of the grating mirror (r_g) can be determined using Eq. 4.2 - 4.4 [3]; where L_g is the length of the grating, r is the reflectivity of single grating per period, and m is number of gratings. Thus, $2mr$ is the net reflection from m grating periods. By making the following definition $\Delta\bar{n} \equiv \mid \bar{n}_1 - \bar{n}_2 \mid$, $\bar{n} \equiv (\bar{n}_2 + \bar{n}_1)/2$, we get the follow relationship:

$$\Delta\lambda_{FWHM} = \frac{\lambda^2}{2 \cdot \bar{n}_g L_g}\frac{3.76}{\pi} \tag{4.2}$$

$$\kappa L_g \equiv 2mr = \frac{m\Delta\bar{n}}{\bar{n}} = \frac{L_g}{\Lambda}(\frac{\Delta\bar{n}}{\bar{n}}) \tag{4.3}$$

$$r_g = tanh\,[\,m\,ln(\frac{1+r}{1-r})\,] \tag{4.4}$$

For a small index difference, which is the situation for a DBR mirror in the OQW platform, the coupling constant (κ) and reflectivity of the grating mirror (r_g) can be further simplified to Eq. 4.5 - 4.6 using Eq.4.1.

$$\kappa = \frac{2\Delta\bar{n}}{\lambda_0} = \frac{2 \mid n_2 - n_1 \mid}{\lambda_0} \tag{4.5}$$

$$r_g \approx tanh(\kappa L_g) \tag{4.6}$$

Based on the models discussed above, the DBR lasers are designed and their detailed parameters are shown in Table. 4.1. In order to achieve an emission wavelength around 1572 nm for this application, both mirrors use a 244 nm grating period with etched section L_2 and unetched section L_1 length of 124 nm and 120 nm. For a grating etch depth of 100 nm, the calculated coupling constant κ of the grating is 368.2 cm^{-1}. The corresponding Bragg wavelength for the grating is 1573.6 nm. The simulated reflectivity of the mirrors is shown in Fig. 4.2 & 4.3. The front mirror consists of 100 grating periods with a total length of 24.4 μm and a reflectivity of 48.0% at the Bragg wavelength. The back mirror consists of 350 grating periods with a total length of 85.4 μm and a reflectivity of 96.5% at the Bragg wavelength. The total reflectivity of both mirrors is 46.4% at the Bragg wavelength.

Front Mirror					
Period (nm) Λ	Grating (nm) L1/L2	Burst Length (μm)	Number of Period	Etch Depth (nm) $d_1 - d_2$	Bragg Wavelength (nm)
244	124/120	24.4	100	100	1573.6
Back Mirror					
Period (nm) Λ	Grating (nm) L1/L2	Burst Length (μm)	Number of Period	Etch Depth (nm) $d_1 - d_2$	Bragg Wavelength (nm)
244	124/120	85.4	350	100	1573.6

Table 4.1: DBR Mirror Parameters

Figure 4.4 shows a microscope image of a fabricated DBR device. The DBR laser has a 500 μm gain section and a 75 μm phase section. It uses the front and back mirror

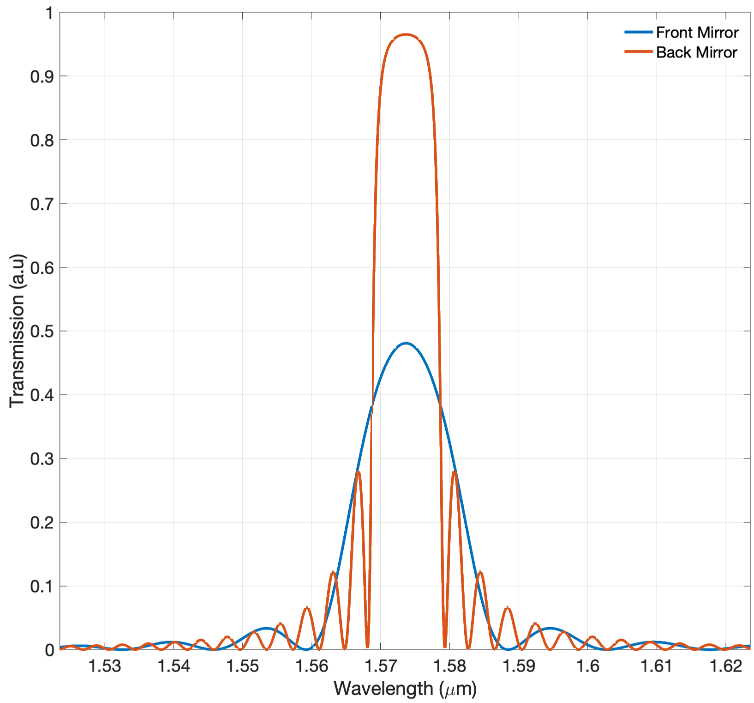

Figure 4.2: Simulated reflectivity of front and back DBR mirrors.

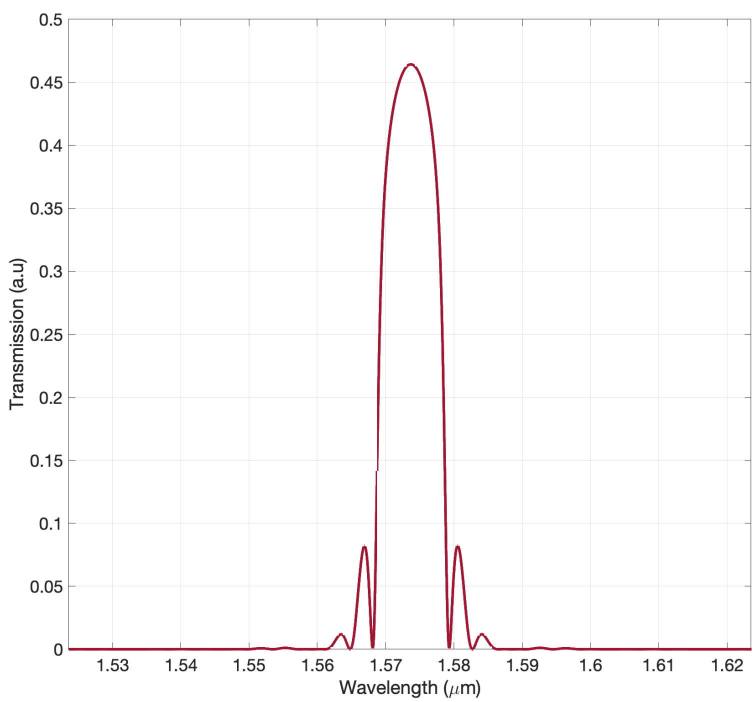

Figure 4.3: Simulated reflectivity of overall DBR mirrors.

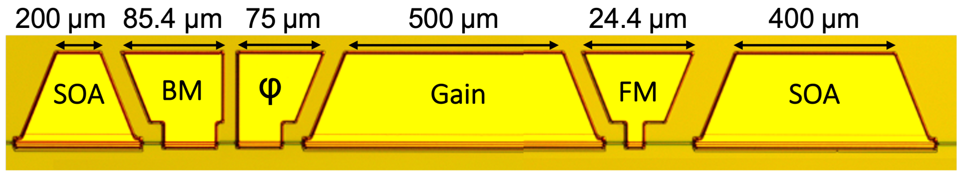

Figure 4.4: Microscope image of a fabricated DBR laser.

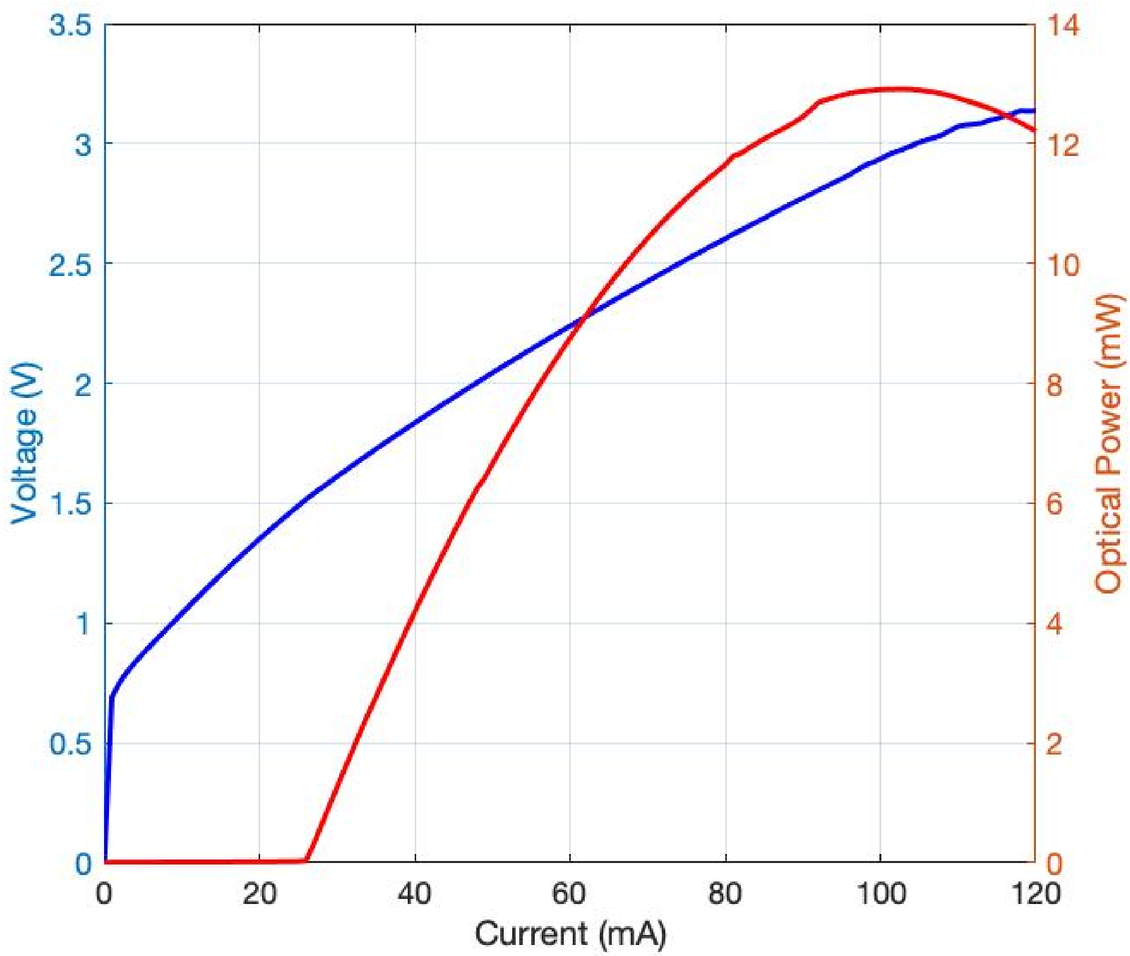

Figure 4.5: Light-current-voltage characterization of the DBR laser.

design shown in Table 4.1. An SOA is added before the back mirror to absorb the light emitted from the backside, which improves the stability of the laser by preventing any reflection off the back facet from returning to the laser cavity. The light-current-voltage

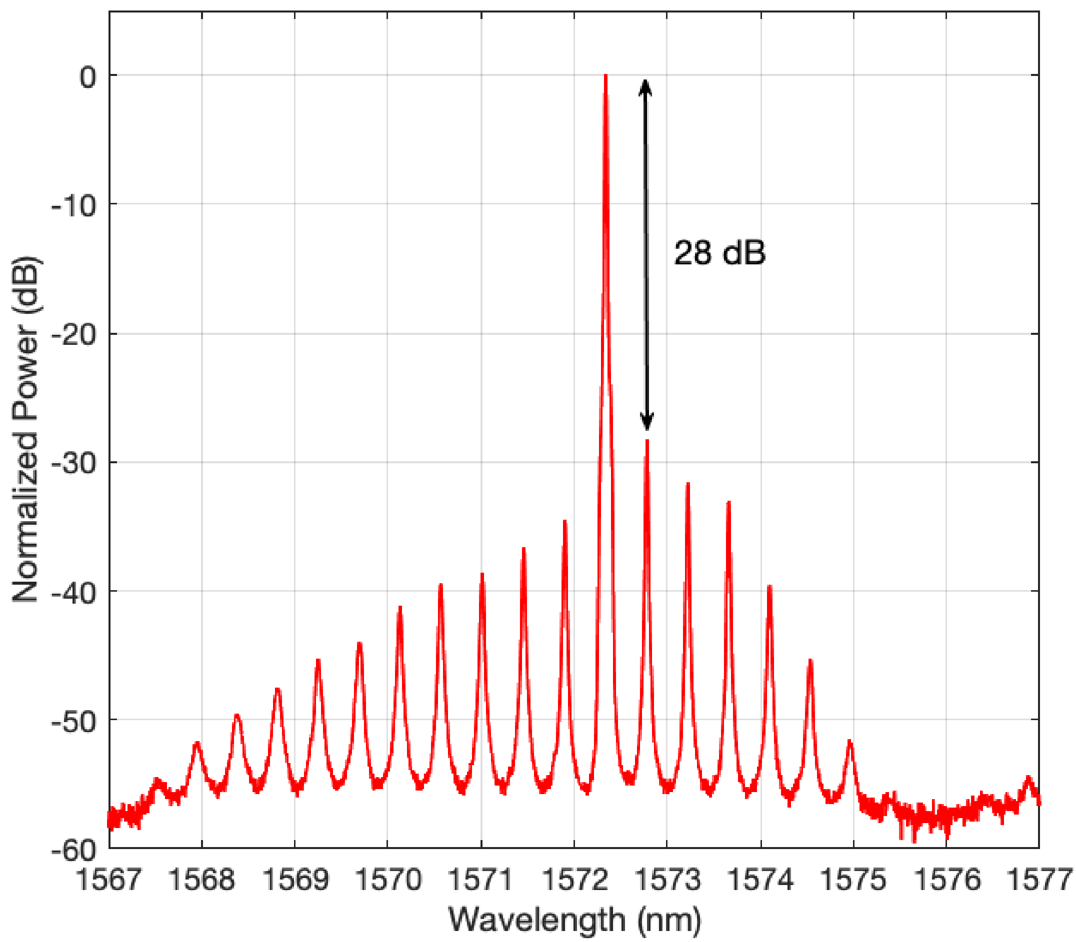

Figure 4.6: Optical spectrum of DBR laser at 1572.338 nm.

(LIV) characteristics of the DBR laser were measured on-chip by reverse biasing the integrated SOA following the front mirror so it could be used as a photodetector. From Fig. 4.5, the characterized DBR laser has a turn-on voltage at 0.69 V and a low lasing threshold current of 26 mA. The laser achieves a maximum output power of 12.9 mW for 100 mA of injected current. The optical spectrum around the target wavelength was also characterized and shown in Fig. 4.6. The side mode suppression ratio (SMSR) of 28 dB is relatively low for a DBR laser, which typically exhibit SMSR's around 40 dB.

Analysis shows that this was mainly caused by the reflectivity of the back mirror being too high, which caused the reflectivity for the first side mode to approach that of the center mode, degrading the SMSR and also yielding a low lasing threshold current.

4.1.2 SGDBR lasers

The SGDBR laser shares the same base structure as DBR laser, in that is also consists of a front mirror, gain section, phase section, and back mirror. Unlike the DBR laser, which uses a continuous Bragg grating for the mirrors, the SGDBR laser contains sampled Bragg gratings. The detailed structure of an SGDBR laser is illustrated in Fig. 4.7.

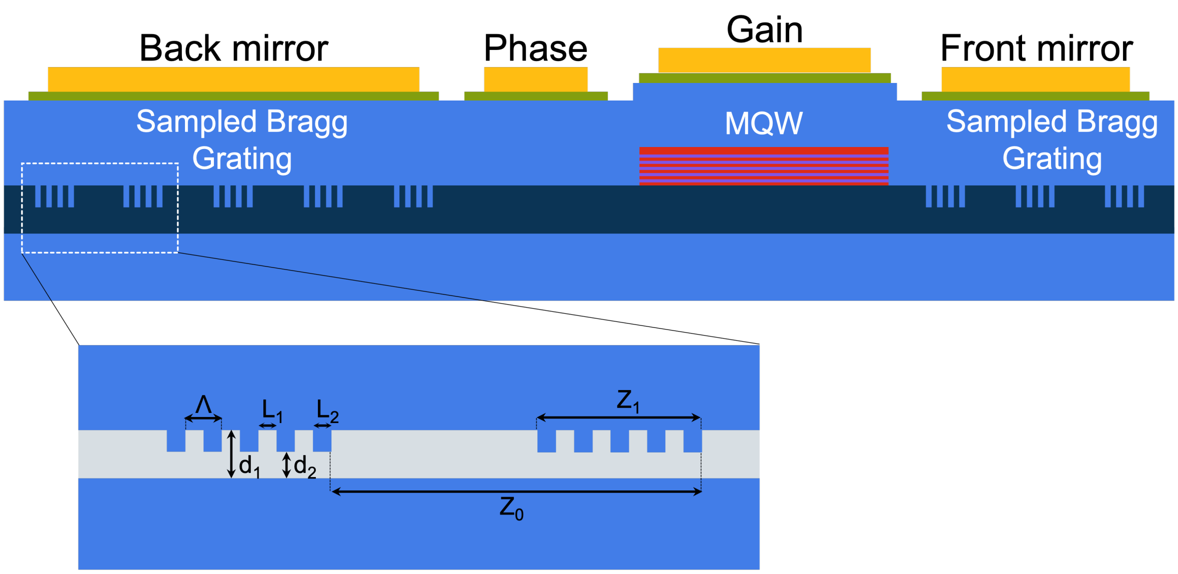

Figure 4.7: Structure of an SGDBR laser.

The coupling constant κ_p of the sampled Bragg grating is defined based on its structure with the following equation [3]:

$$\kappa_p = \kappa_g \frac{Z_1}{Z_0} \frac{sin(\pi p Z_1/Z_0)}{(\pi p Z_1/Z_0)} e^{-j\pi p Z_1/Z_0} \tag{4.7}$$

where p is the order number, Z_0 is the sampling period, Z_1 is the length of the grating burst, and κ_g is the coupling constant for the continuous, unsampled grating, which can be calculated using the same method for calculating the DBR mirror coupling constant in Eq. 4.5. Then, the spatially averaged coupling constant $\bar{\kappa}$ can be calculated by [3]:

$$\bar{\kappa} = \frac{N_{Burst} \cdot L_{burst} \cdot \kappa}{L_{mirror}} \tag{4.8}$$

where the N_{Burst} is the number of bursts and L_{burst} is the length of the burst which is Z_1 in Fig. 4.7. The L_{mirror} is the length of the mirrors which equals [3]:

$$L_{mirror} = (N_{burst} - 1) \cdot Z_0 + L_{burst} \tag{4.9}$$

Based on these equations, the effective length L_{eff} and power reflectivity R'_B of each mirror can be calculated by [3]:

$$L_{eff} = \frac{1}{2\bar{\kappa}} \, tanh(\bar{\kappa}) \, L_{mirror} \tag{4.10}$$

$$R'_B = \mid r'_B \mid^2 = tanh^2(\kappa N_{burst} L_{burst}) \tag{4.11}$$

Then, the full-width-half-maximum (FWHM) of the reflectance peaks ($\Delta\lambda_{FWHM}$), wavelength spacing between the peaks ($\Delta\lambda_{peak}$), and the bandwidth of the envelope ($\Delta\lambda_{env}$) can be calculated using the equations below [3]:

$$\Delta\lambda_{FWHM} = \frac{\lambda^2}{2 \cdot \bar{n_g} L_{eff}} \frac{3.76}{\pi} \tag{4.12}$$

$$\Delta\lambda_{peak} = \frac{\lambda^2}{2 \cdot \bar{n_g} Z_1} \tag{4.13}$$

$$\Delta\lambda_{env} = \frac{\lambda^2}{2 \cdot \bar{n_g} Z_0} \tag{4.14}$$

The SGDBR laser mirrors are designed based on the relationships above and the design details are shown in Table 4.2. Similar to the DBR mirrors, the SGDBR mirrors also used a 244 nm period, 100 nm deep grating etch, and a 124 nm unetched and 120 nm etched duty cycle, which yield a Bragg wavelength at 1573.6 nm and an unsampled coupling constant (κ_g) of 368.2 cm^{-1}. The front mirror comprises 5 bursts, with each burst having a period of 68.712 μm and a burst length of 4.148 μm (17 periods), resulting in a 4.91 nm wavelength spacing between peaks ($\Delta\lambda_{peak}$). The back mirror consists of 12 bursts. Each burst has a period of 61.34 μm and a burst length of 6.1 μm (25 periods), which results in a $\Delta\lambda_{peak}$ of 5.52 nm.

Front Mirror								
Period (nm) Λ	Grating (nm) L1/L2	Etch Depth (nm) $d_1 - d_2$	Burst Length (μm) Z_1	Gratings in Each Burst	Number of Bursts	Burst Spacing (μm) Z_0	$\Delta\lambda_{peak}$ (nm)	Bragg Wavelength (nm)
244	124/120	100	4.148	17	5	68.712	4.91	1573.6
Back Mirror								
Period (nm) Λ	Grating (nm) L1/L2	Etch Depth (nm) $d_1 - d_2$	Burst Length (μm) Z_1	Gratings in Each Burst	Number of Bursts	Burst Spacing (μm) Z_0	$\Delta\lambda_{peak}$ (nm)	Bragg Wavelength (nm)
244	124/120	100	6.1	25	12	61.34	5.52	1573.6

Table 4.2: SGDBR Mirror Parameters.

Figure 4.8 & 4.9 shows the corresponding simulated reflectivity of the mirrors. From the simulation, the front mirror has a 31.8 % reflectivity at the Bragg wavelength, and the back mirror has a 79.1 % reflectivity at the Bragg wavelength. Overall, both mirrors achieve a total reflectivity of 25.2 % at 1574.14 nm with the nearest side peaks at 1568.94 nm and 1579.38 nm (5.2 nm and 5.24 nm away from center).

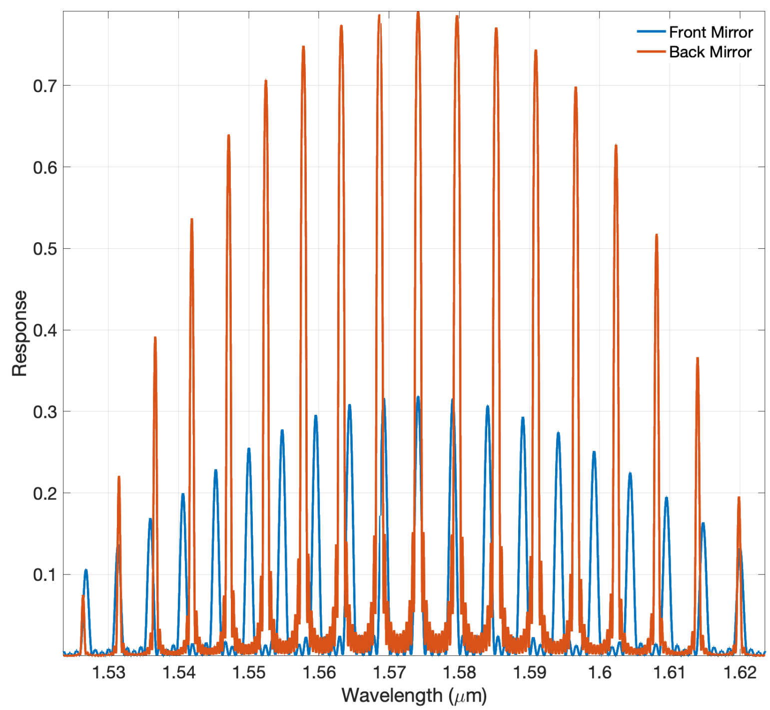

Figure 4.8: Simulated reflectivity of front and back SGDBR mirrors.

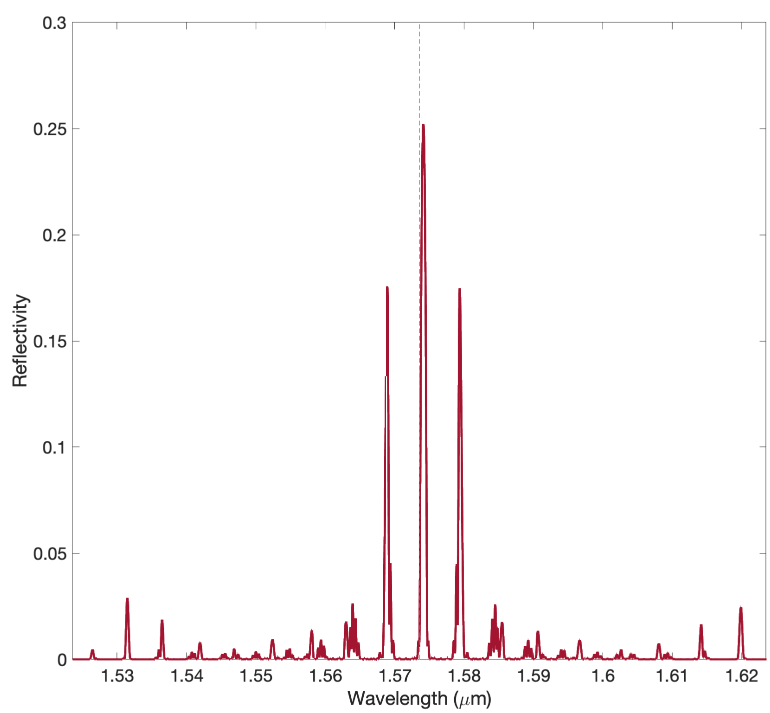

Figure 4.9: Simulated reflectivity of overall SGDBR mirrors.

After fabrication, the SGDBR laser was characterized. The LIV characteristics at different temperatures were first measured and are shown in Fig. 4.10. The temperature was controlled through an external TEC under the laser. At room temperature (20 $^\circ C$), the laser has a turn-on voltage of 0.67 V and a lasing threshold current (I_{th}) of 40 mA. As the temperature was increased from 15 $^\circ C$ to 30 $^\circ C$, an increase in I_{th} from 36.7 mA at 15 $^\circ C$ to 42.4 mA at 30 $^\circ C$ was observed. The change in I_{th} is mainly caused by its relation with temperature: $I_{th} = I_0 e^{T/T_0}$. The decrease of I_{th} results in an increase of the maximum output power, since more current is used for stimulated emission. The output power can be calculated by the following equation while above

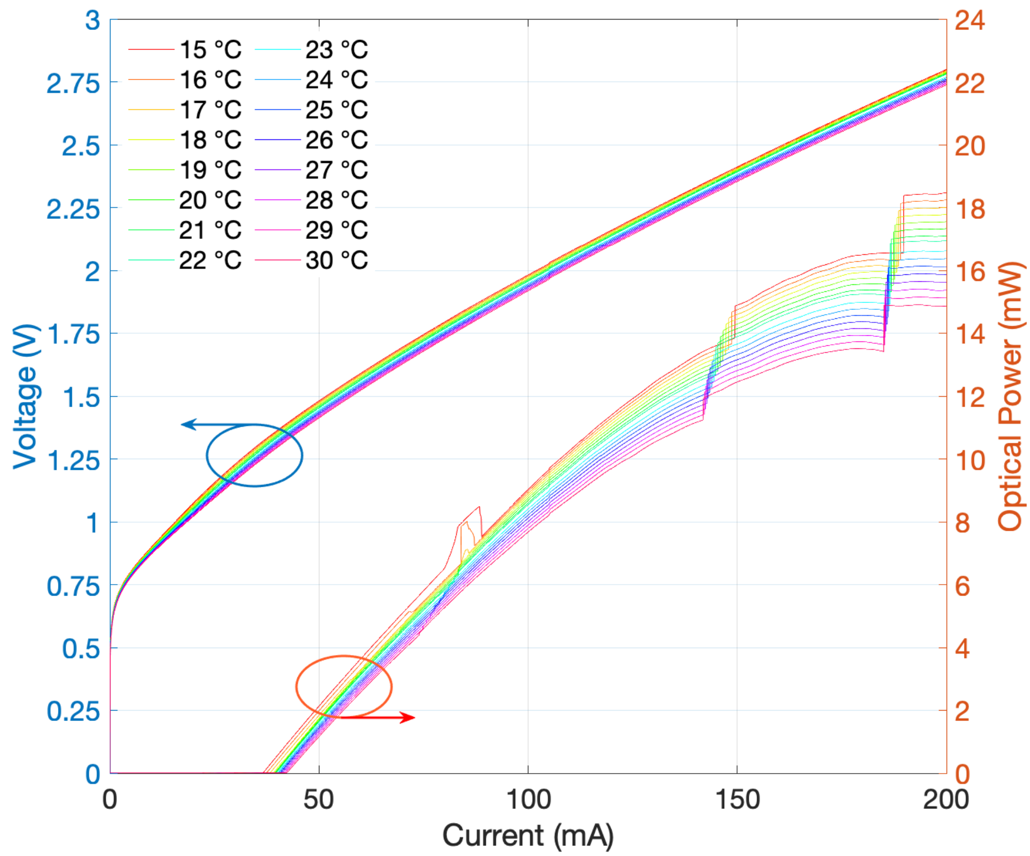

Figure 4.10: Light-current-voltage characterization of the SGDBR laser at different temperature.

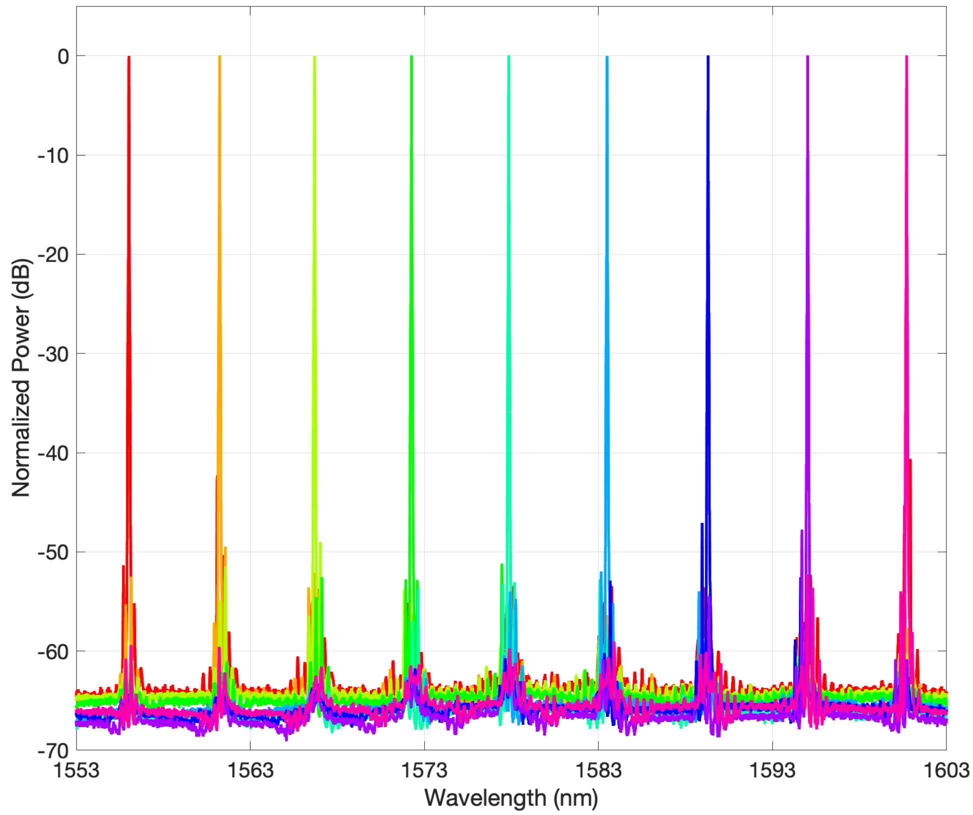

Figure 4.11: Overlaid SGDBR laser spectra showing a 40 nm tuning range.

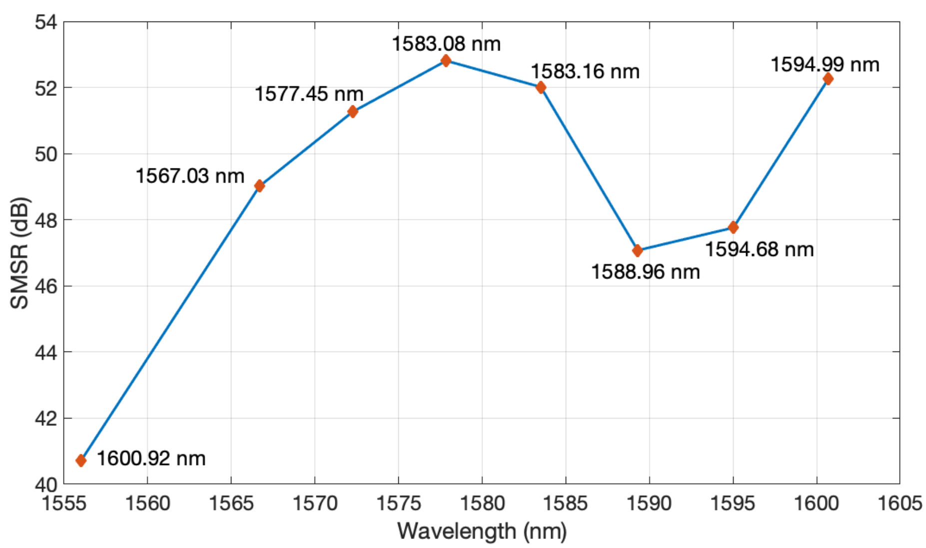

Figure 4.12: SMSR of SGDBR laser at different emission wavelengths with the lowest SMSR side mode wavelength labeled aside.

threshold: $P_0 = \eta_d \frac{h\nu}{q}(I - I_{th})$, where η_d is the differential quantum efficiency, $h\nu$ is the energy of the photon at frequency 'ν', and q is the charge of electron which is $1.60217662 \times 10^{-19}$ coulombs.

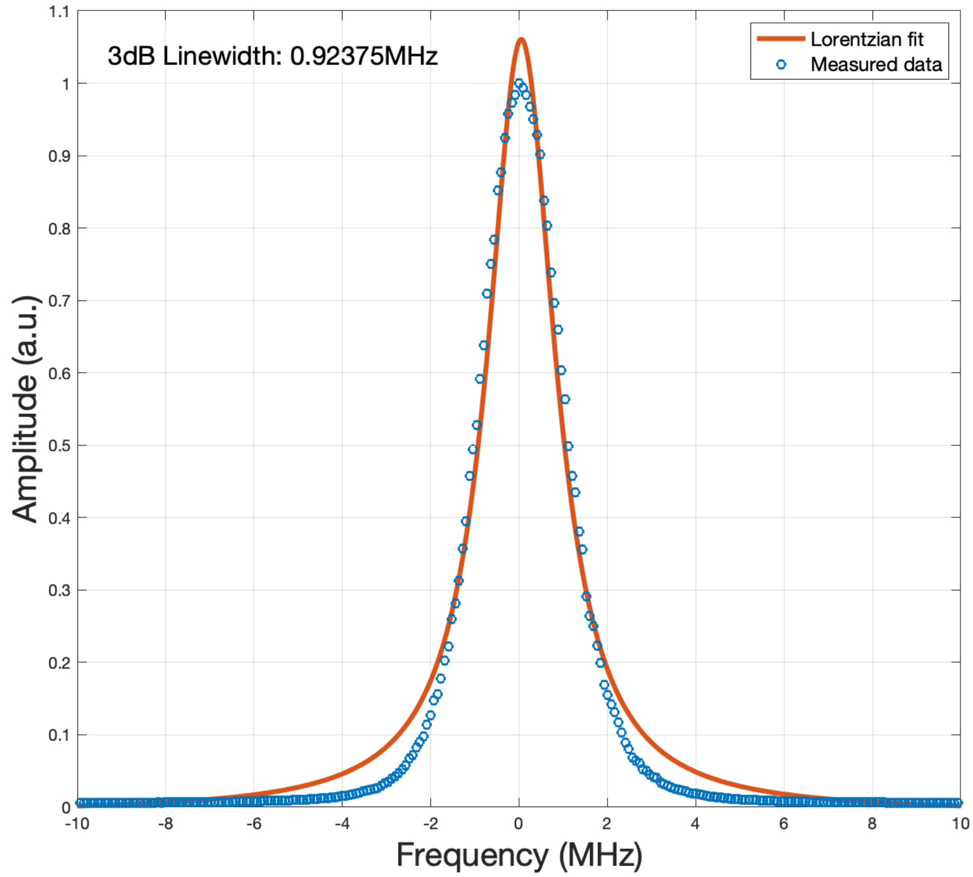

Figure 4.13: Measured delayed self-heterodyne SGDBR laser linewidth spectrum demonstrating a 3-dB linewidth of 0.92 MHz.

The tuning characteristics of the SGDBR laser were measured and are shown in Fig. 4.11 & 4.12, where overlaid optical spectra and their corresponding SMSR at different emission wavelengths are presented. The characterization demonstrated a 44 nm tuning range from 1556 nm to 1600 nm with 40 dB minimum SMSR. Finally, a linewidth measurement of the SGDBR laser was taken using a delayed self-heterodyne technique. As can be seen from the Lorentzian fit to the data in Fig. 4.13, the laser demonstrated a 3-dB linewidth of 0.92 MHz for electrical spectrum analyzer (ESA) settings of 5 μs sweep time, 2 MHz resolution bandwidth, and 20 KHz video bandwidth.

4.2 Phase Modulators

A phase modulator is used to modulate the phase of the optical signal through application of an external electric field. Based on the application and material platform, phase modulators have different modulation efficiency, bandwidth, residual amplitude modulation (RAM), size, and power consumption. In this work, there are three phase modulators that are designed and integrated on the OQW-based InP PIC. They are a traditional straight phase modulator, regular Mach-Zehnder-based phase modulator, and a novel low-RAM Mach-Zehnder-based phase modulator, dubbed the shift-and-dump

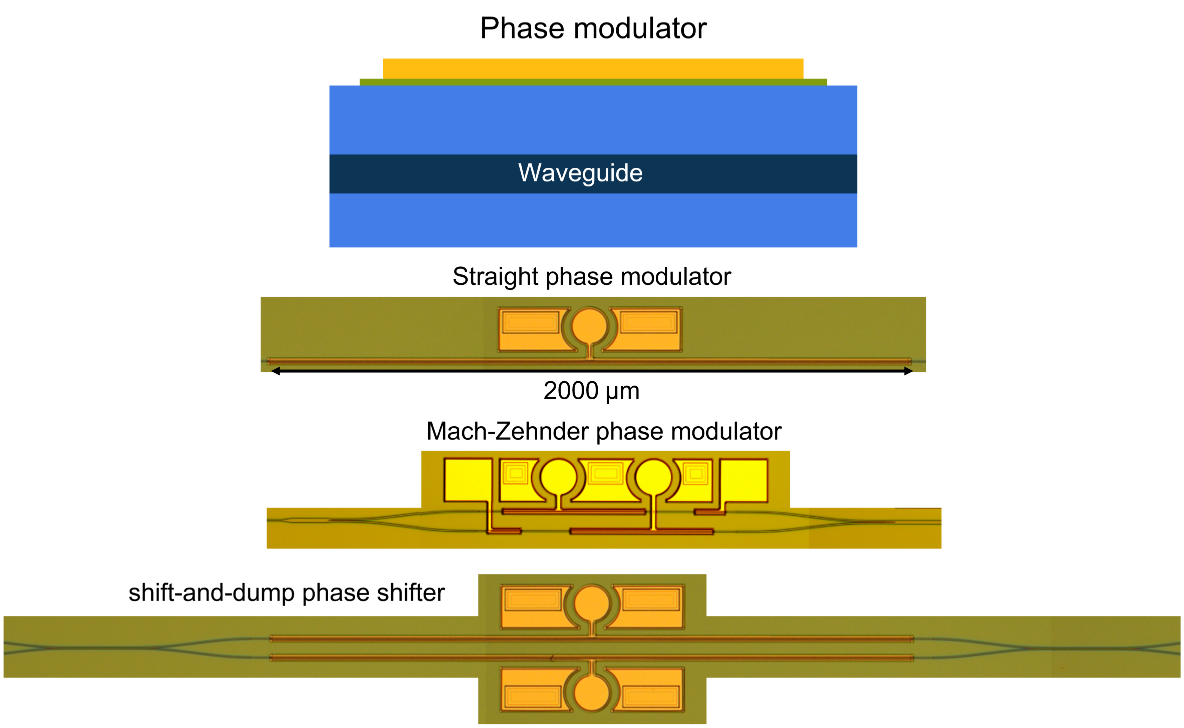

Figure 4.14: (top) Structure of phase modulator based on OQW platform; (middle) Microscope image of a fabricated 2000 μm straight phase modulator;(bottom) Microscope image of a fabricated SDPS low-RAM phase modulator.

phase shifter (SDPS). The structure of each phase modulator type and microscope images of each are shown in Fig. 4.14.

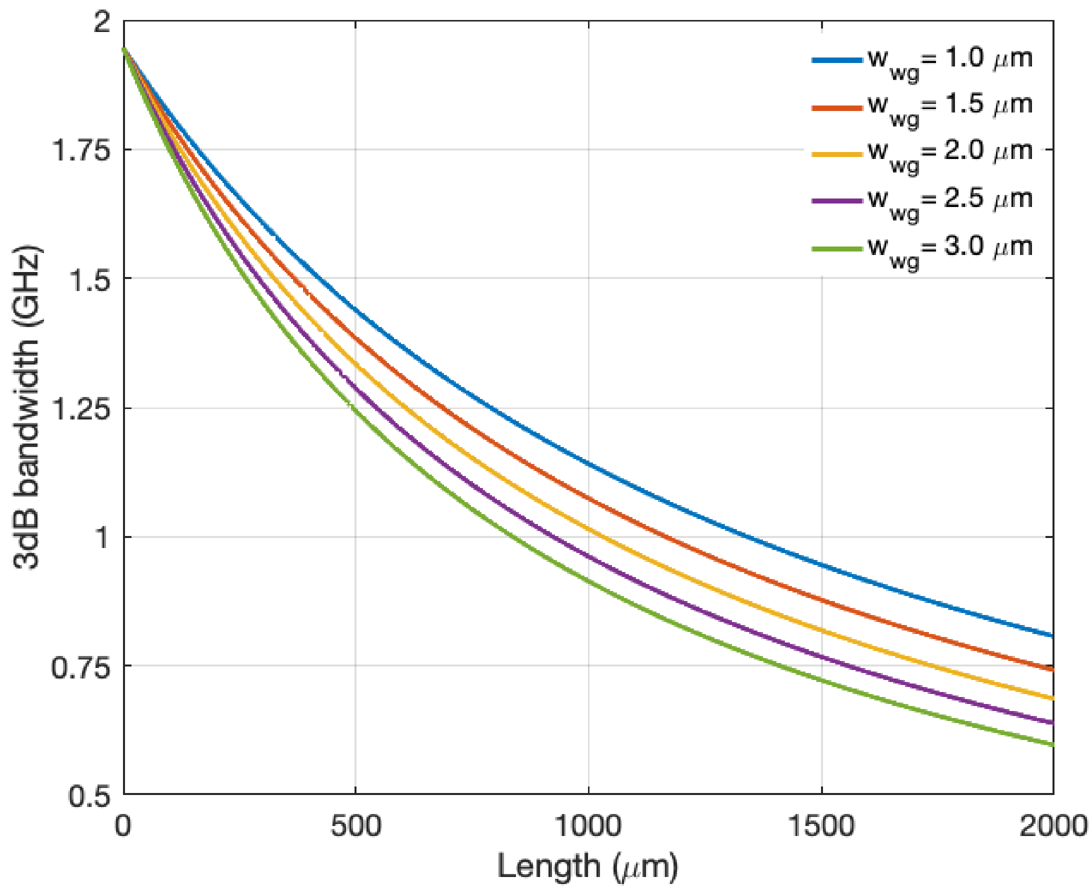

Figure 4.15: Bandwidth performance simulation for phase modulator with different waveguide length and width.

The straight phase modulator is a bulk EAM phase modulator, which uses the free carrier plasma effect, or Franz-Keldysh effect to change the effective index of the waveguide by injecting electrons or applying an electric field [3, 9, 10]. The Mach-Zehnder phase modulator is based on a Mach-Zehnder interferometer structure. The regular Mach-Zehnder phase modulator has a balanced coupler at the input and output, and both arms are modulated for phase modulation. The novel low-RAM Mach-Zehnder-based phase modulator has unbalanced couplers at the input and output, it can be used for phase modulation while one arm is modulated and a constant bias is applied to the second arm.

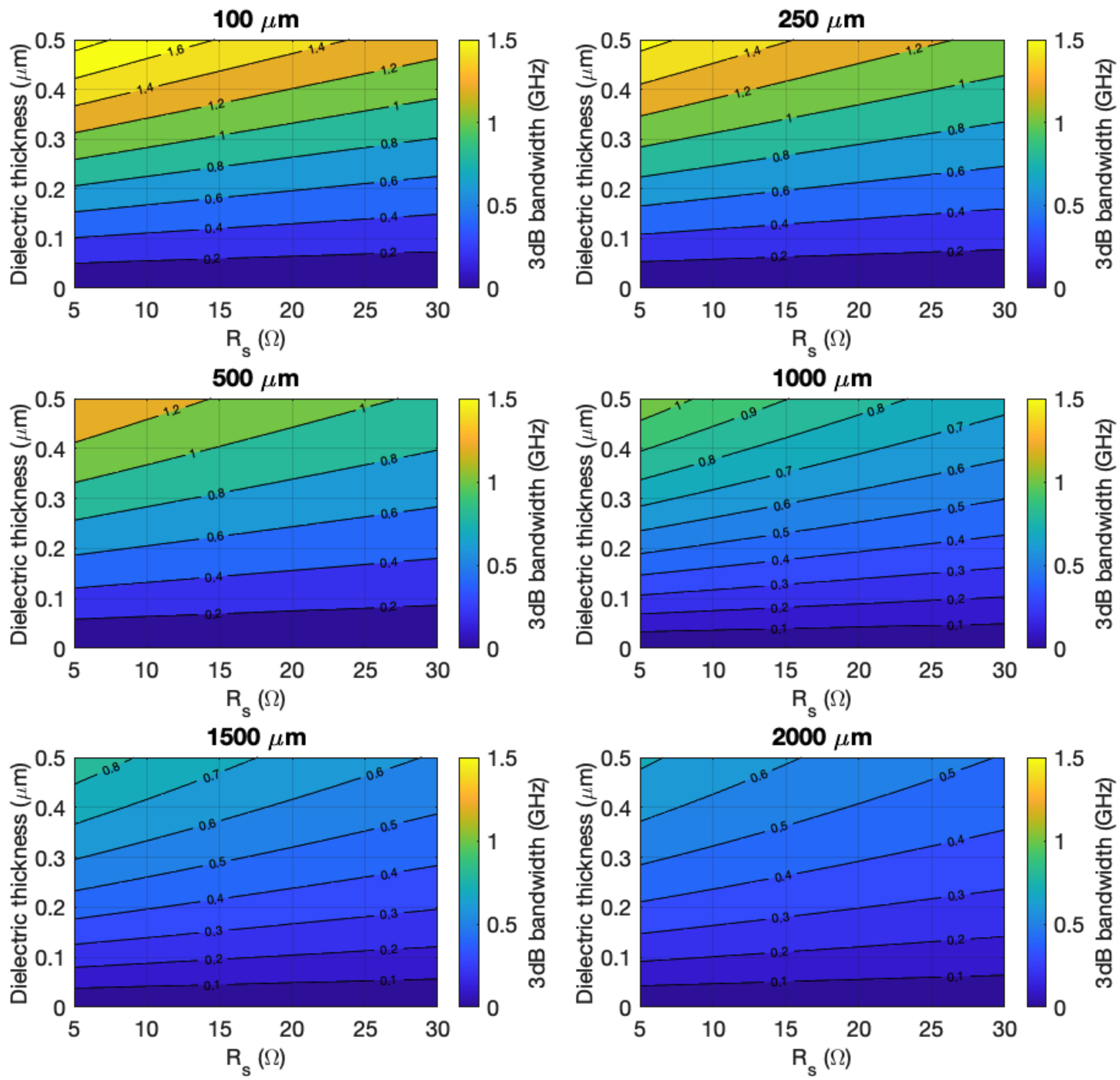

Figure 4.16: Bandwidth performance simulation for phase modulator with different dielectric thickness and R_s.

The bandwidth of phase modulators based on an equivalent RC circuit model of the structure was simulated and is shown in Fig. 4.15 & 4.16. For this application, the phase modulator only needs to operate at 125 MHz, so based on the simulation, even a modulator with a length of 2500 μm can still easily satisfy this requirement.

In addition, the RAM and the modulation efficiency for the straight phase modulator and Mach-Zehnder phase modulator are characterized in Fig. 4.17 & 4.18. From the characterization, the Mach-Zehnder phase modulator has a smaller RAM compared to the straight phase modulator. But, since the length of the Mach-Zehnder phase modulator is shorter than the straight phase modulator, the overall modulation efficiency of the Mach-Zehnder phase modulator is a little lower than that of the straight phase modulator.

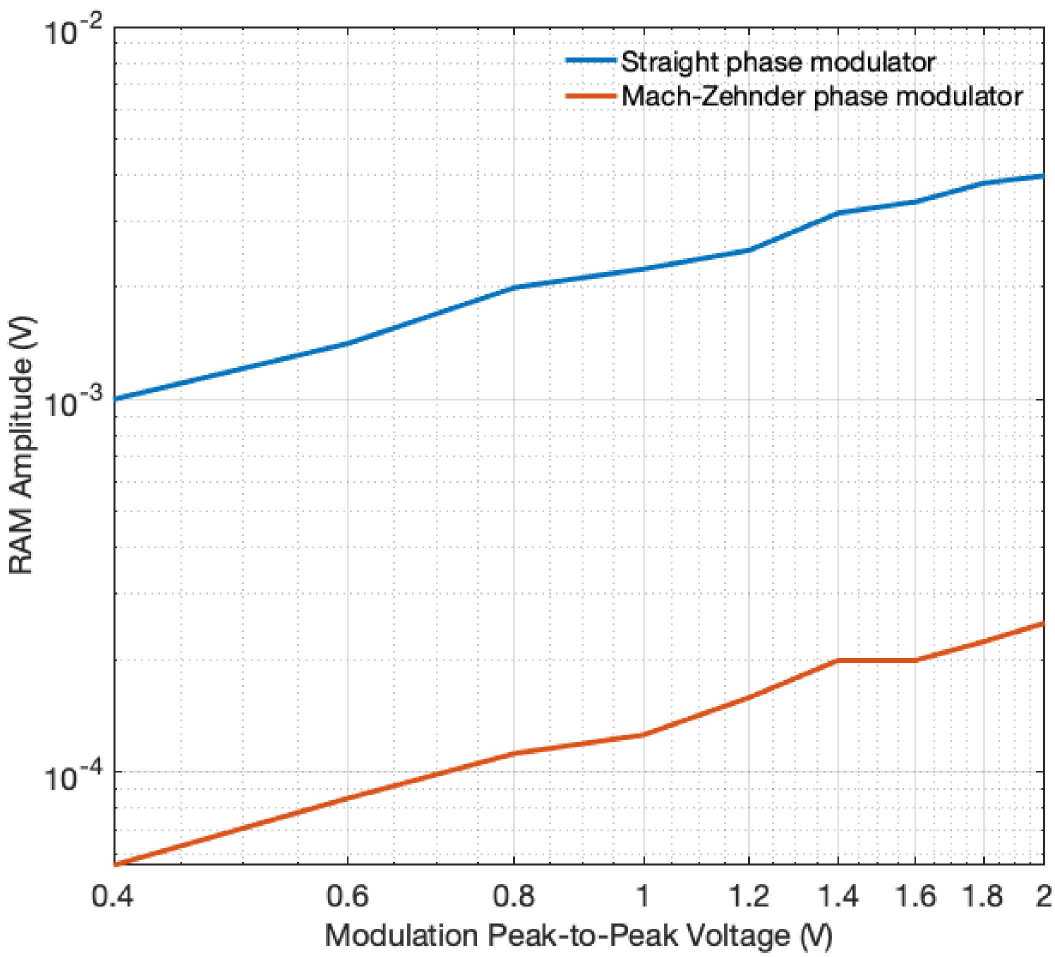

Figure 4.17: RAM of the straight phase modulator and Mach-Zehnder phase modulator.

A more detailed RAM and efficiency analysis of the fabricated phase modulators can be found in [11], where the bias conditions, experimental setup and testing conditions are included. In summary, under 25 mA forward bias with a ± 2.5 mA current swing, the straight phase modulator has a RAM of approximate 8 %. Under -3 V reversed bias with a ± 0.5 V voltage swing, it has a RAM of approximate 27.8 % [11].

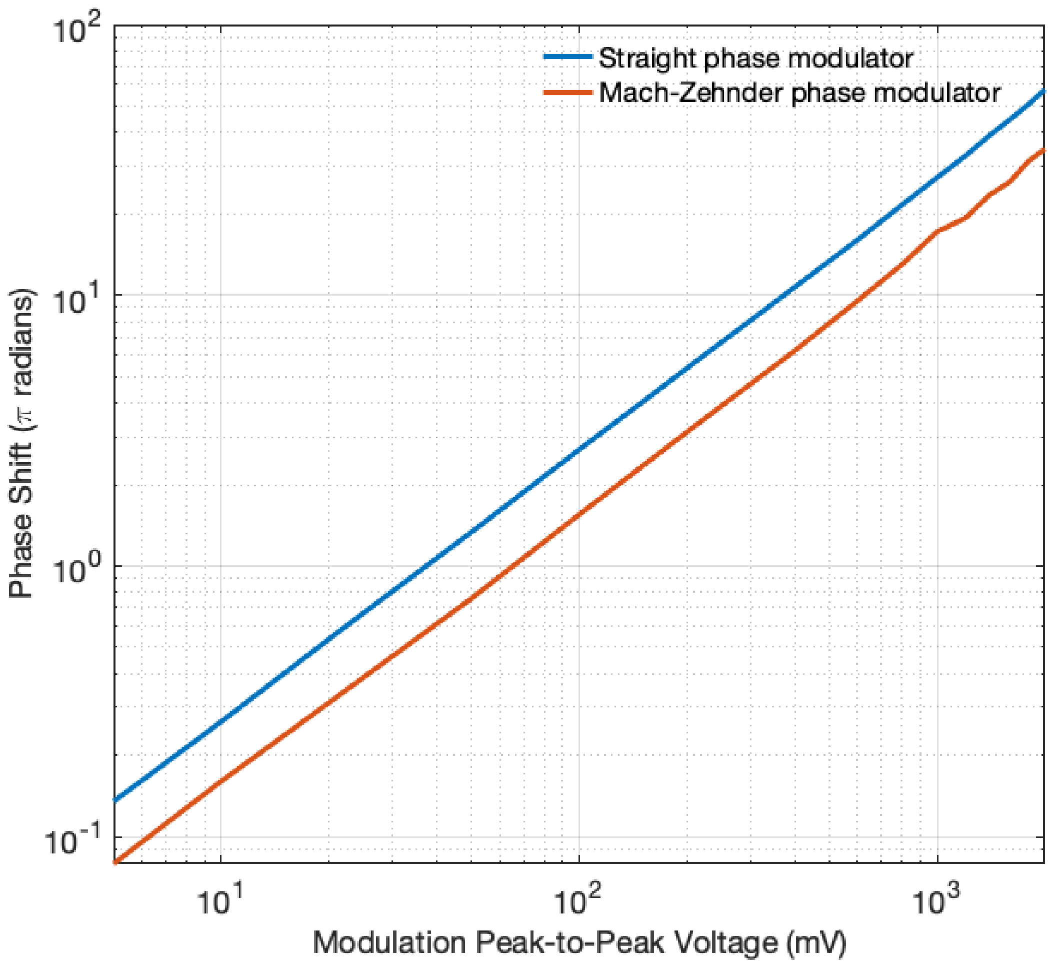

Figure 4.18: Modulation efficiency of the straight phase modulator and Mach-Zehnder phase modulator at a bias of 25 mA.

The SDPS low-RAM phase modulator is a new type of phase modulator that was designed in order to achieve low RAM. It is based on a Mach-Zehnder interferometer structure with a specific power splitting ratio for the input and output power splitting.

The unequal splitting ratio at the input and output is used to compensate the amplitude change caused by the phase modulation. By carefully designing the splitting ratio and length of the phase modulator, the SDPS low-RAM phase modulator can achieve an almost constant total loss despite varying loss in the modulated arm as the phase changes [12, 13]. From measurements, the SDPS low-RAM phase modulator achieved a 50 % decrease in RAM compared with the 2500 μm straight phase modulator tested above. More details of the SDPS low-RAM phase modulator can be found in [11, 12].

4.3 Semiconductor optical amplifiers

A semiconductor optical amplifier (SOA) is one of the most common devices used to boost optical power. It is an optical active section that is used without any optical feedback [3].The structure of the SOA in the OQW platform is shown in Fig. 4.19. The gain of the SOA depends on its length and pumping level, which is given by $G_0 = e^{\Gamma g(N)L}$, where L is the length of SOA, Γ is the confinement factor, and g is the material gain at the given pumping level [3].

Figure 4.19: (left) Microscope image of a fabricated SOA; (right) Structure of SOA based on OQW platform.

SOAs were used to compensate for waveguide losses and further amplify the optical power at different places in the PIC. In addition, they were also used as pulse carvers

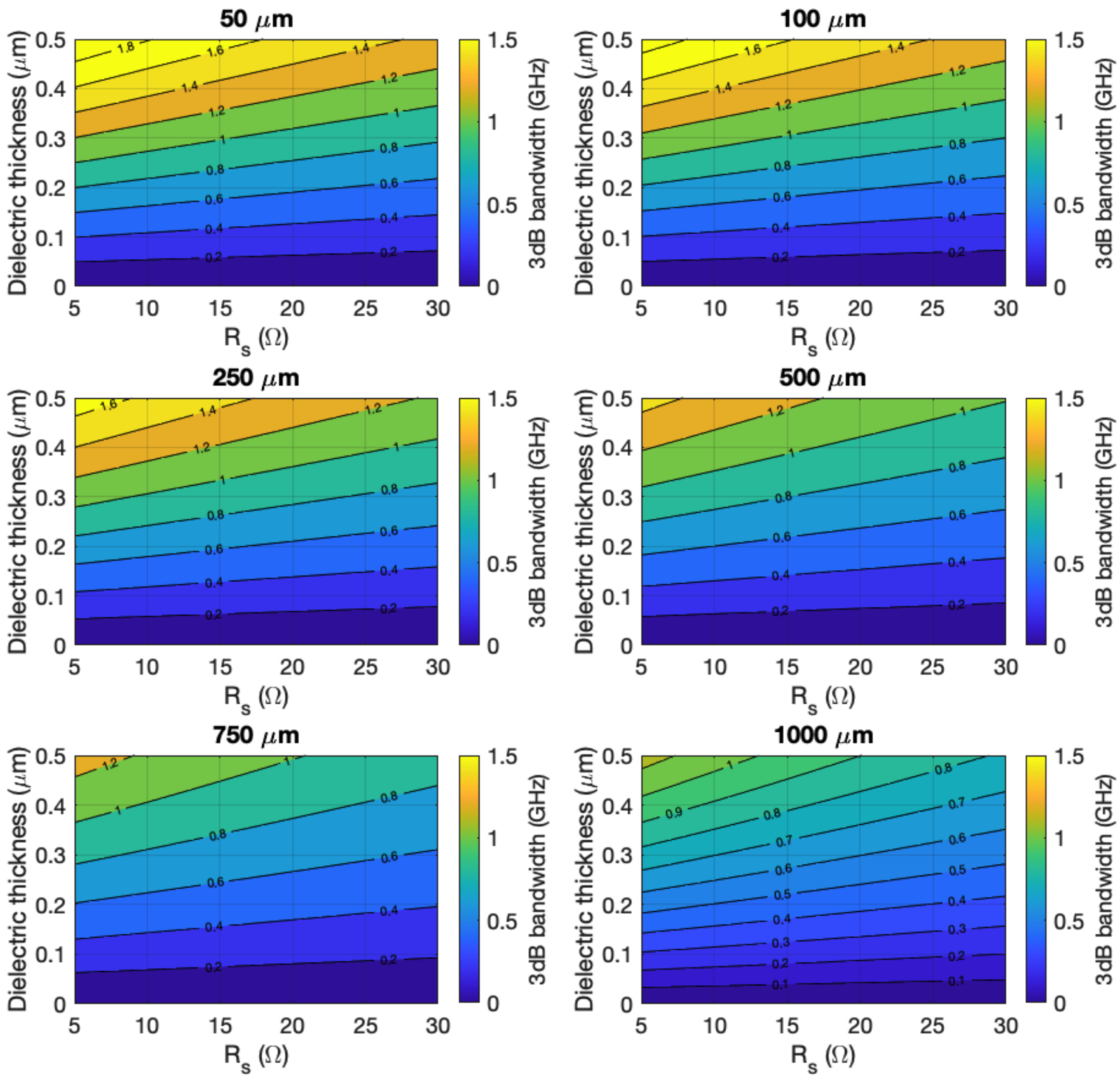

Figure 4.20: Bandwidth performance simulation for SOA with different dielectric thickness and R_s.

to generate the target 1 μs pulse signal at the output. For the SOA pulse carver, a proper length needs to be chosen in order to generate the 1 μs pulse signal. A simulation was done based on an equivalent RC model of the device, and the results are shown in Fig. 4.20. Our SOA device uses a 0.3 μm thick dielectric for sidewall passivation and isolation, and the resulting series resistance (R_s) is usually around 7 Ω. From the simulation, for 1 μs pulse signal generation, the length of the SOA is not a limiting factor based on the device parameters. From the power aspect, we are trying to achieve as high as possible optical power, while also trying to keep the size of the PIC as small as possible. Eventually, considering the trade-off between the two factors, a 500 μm SOA was used in most of PICs.

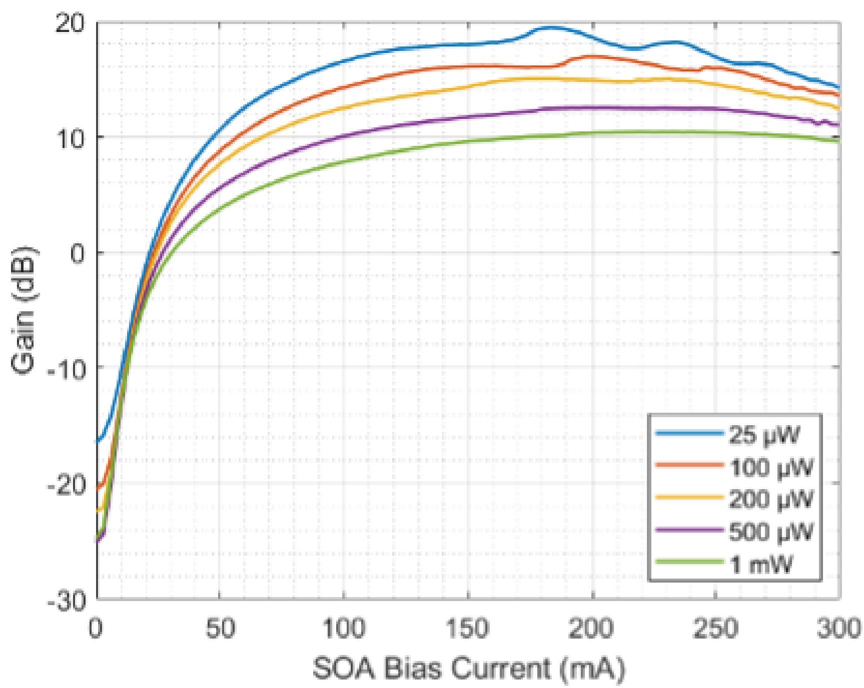

Figure 4.21: SOA gain characterization at different input power levels.(© UCSB 2021, [11].)

One of the fabricated 500 μm SOAs was characterized at different power input and bias levels and the results are shown in Fig. 4.21. The SOA provided most of the gain from transparency to 150 mA, where it achieves 18 dB gain for a 25 μW input level and 9.6 dB gain for a 1 mW input level. In addition, the SOAs on the PIC were also characterized with all of the other PIC devices biased and the corresponding data is shown in Fig. 7.44. But, there's one thing that we need to be careful about: the broadband spontaneous emission from SOA can degrade the signal noise ratio, especially if the input power level to the SOA is too low at the desired output wavelength. Careful consideration needs to go into SOA placement in the PIC for power boosting in order to achieve the best performance.

4.4 Photodiodes

The role of a photodiode (PD) is to convert an optical signal into an electrical signal. There are many types of photodiodes available, and they mainly include PIN-PD, uni-traveling carrier photodiode (UTC-PD) and avalanche photodiode (APD) [14–16]. The PIN-PD is the most common PD, and it is widely used due to its simple structure and moderate performance. The UTC-PD uses a specially designed epitaxial material structure to achieve high power and high bandwidth photon detection. UTC-PD's can achieve more than 60 GHz bandwidth[17]. They can be used for millimeter communication (30 GHz $\sim$ 300 GHz) and other high bandwidth applications. APDs are highly sensitive photodiodes. They use the avalanche effect to achieve a large internal gain [15]. They are usually operated under hundreds volts of reverse bias voltage and are mainly

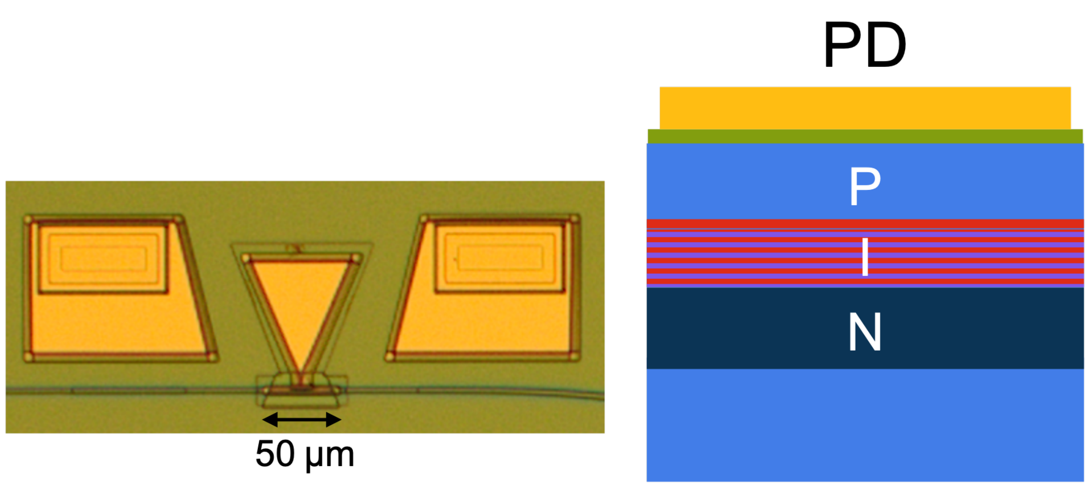

Figure 4.22: (left) Microscope image of a fabricated PD; (right) Structure of PD based on OQW platform.

used for sensitive photon detection such as single-photon detection and laser microscopy.

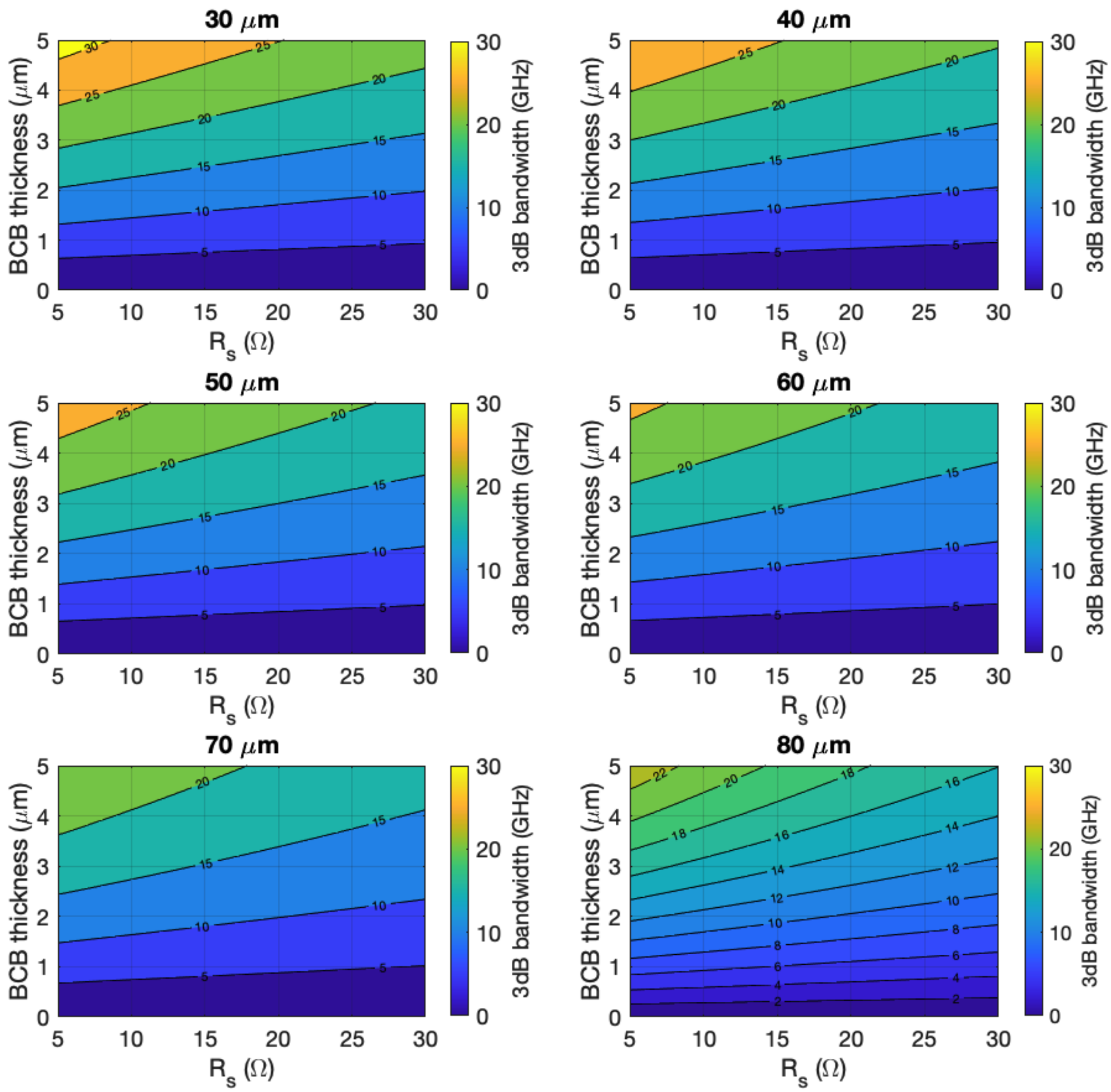

Figure 4.23: Bandwidth performance simulation for PD with different BCB thickness and R_s.

The PD used here is a PIN-PD since this type can be easily integrated into the OQW process without major changes to the epitaxial material and fabrication process. The epitaxial material structure of the PIN-PD is the same as that of the SOA and is shown in Fig. 4.22, where a PIN junction is formed vertically. For operation, usually a −3 V to −5 V bias voltage is applied to the PIN-PD to help it absorb more photons from the waveguide.

The simulated bandwidth performance for different BCB thicknesses and series resistance values (R_s) is shown in Fig. 4.23. The BCB thickness used in the fabrication process was around 3 μm with a corresponding R_s of around 10 Ω for the PD. In order to achieve the 15 GHz 3 dB bandwidth, four different sizes of PDs were designed and fabricated in the first generation. The lengths used were 30 μm, 40 μm, 50 μm and 60 μm. However, in the later generations, in order to reduce the complexity of fabrication process, the BCB layer was removed. So, the PDs in the later rounds do not have the BCB layer.

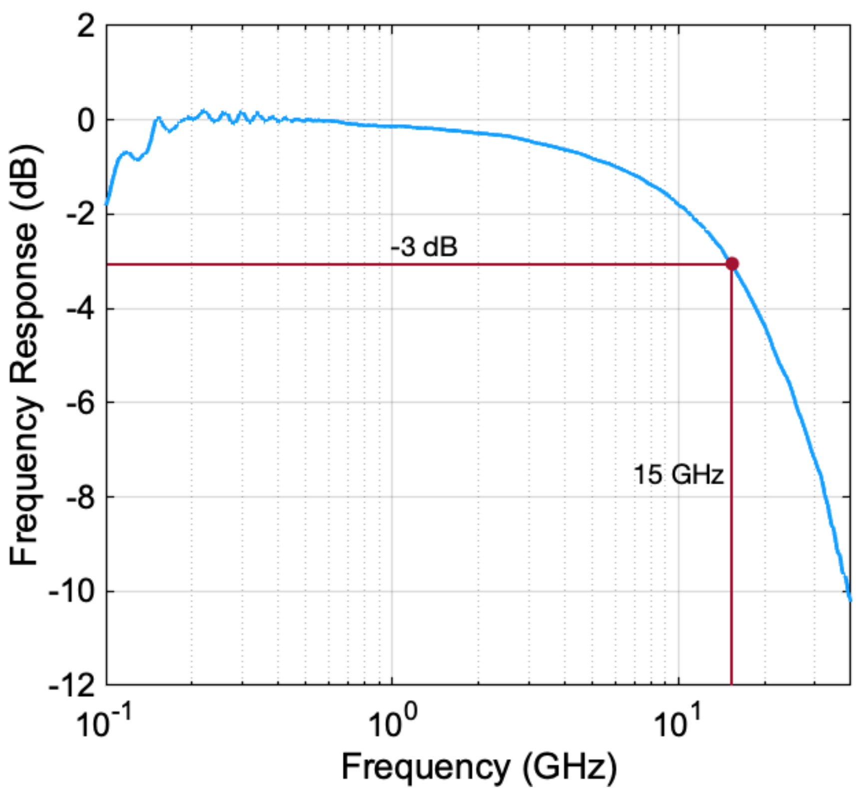

Figure 4.24: Integrated photodiode with BCB normalized frequency response measurement demonstrating 15 GHz 3-dB bandwidth.

The fabricated PDs with BCB were tested, and a $\sim$ 15 GHz 3-dB bandwidth was achieved across all the PD designs, as shown in Fig. 4.24. This is mainly because parasitic capacitance from the contact is dominating compared with other equivalent capacitance and all the PDs used a similar contact pad size due to limitations of the wire bonding machine in the lab. The PDs without BCB are expected to have a 3-dB bandwidth around 2 GHz from measurement, which is parasitic capacitance limited. Fortunately, the PDs without BCB are still able to detect the beat note signal up to 10 GHz as shown in Fig. 7.41. Without the BCB layer, the 3-dB bandwidth of the PD was around 5 GHz, which is limited by the parasitic capacitance over the junction.

4.5 Couplers

Couplers are used widely in photonic integrated circuits to split, combine and mix signals. The most common ones are the multimode interference coupler and directional coupler. The multimode interference coupler uses self-imaging theory and directional couplers use coupled mode theory. In this section, the designed and fabricated multimode interference couplers and directional couplers will be discussed.

4.5.1 Multimode Interference Coupler

1×2 and 2×2 multimode interference (MMI) couplers were designed and fabricated. The main advantages of the MMI couplers are their design simplicity and high tolerance to fabrication inaccuracies [3, 18]. They also have a broader optical bandwidth than directional couplers, and the same design can work over a broad range of optical wavelengths. But, MMI couplers can only be used for equal power splitting or mixing, and cannot achieve unequal power splitting and mixing. Unless carefully designed, they are also prone to generating back reflections.

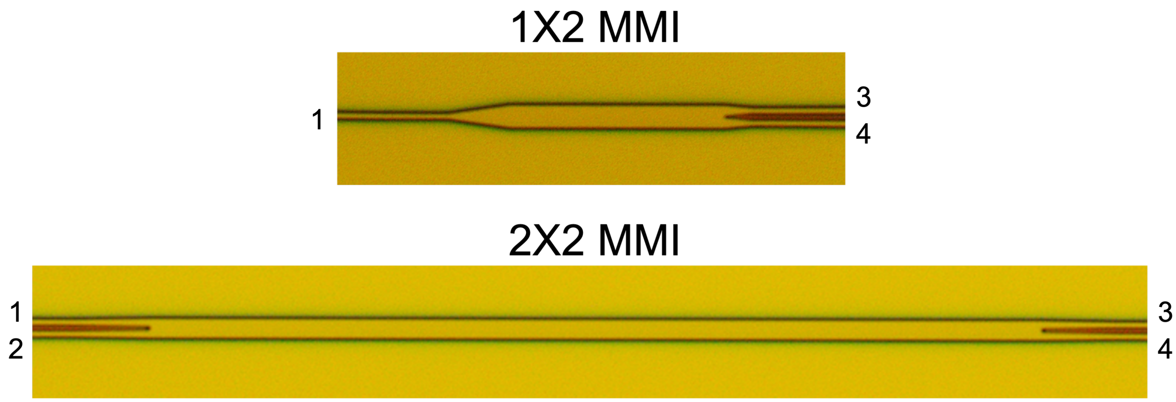

Figure 4.25: Microscope images of the fabricated 1×2 and 2×2 MMIs.

	Left Waveguide		Left Taper		Mid Coupler		Right Taper		Right Waveguide		S Parameter in Power			
	um		um		um		um		um		%			
	L	W	L	W	L	W	L	W	L	W	S31	S41	S32	S42
1x2MMI OQW	10	2.89	33	12	113	12	15	5.5	10	2.89	49.8	49.8	NA	NA
2x2MMI OQW	10	2.89	40	4	460	10	40	4	10	2.89	49.5	49.7	49.6	49.5

Table 4.3: Design specifications of the 1×2 and 2×2 MMIs with simulated power splitting ratio.

The fabricated MMI couplers and their corresponding design specifications are shown in Fig. 4.25, and Table 4.3, where the 1×2 MMI coupler uses a width of 12 μm, and the 2×2 MMI coupler uses a width of 10 μm in order to keep a compact size. The power splitting ratio was simulated in Lumerical's MODE software using an eigenmode expansion (EME) solver and the corresponding simulated XY plane (same viewing angle as the microscope image above) power profiles are shown in Fig. 4.26 for 1×2 MMI, and in Fig. 4.27 for 2×2 MMI.

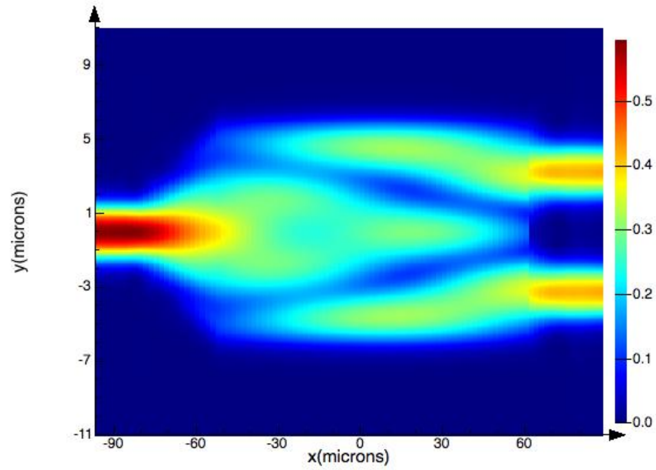

Figure 4.26: Simulated XY plane power profile of the 1×2 MMI.

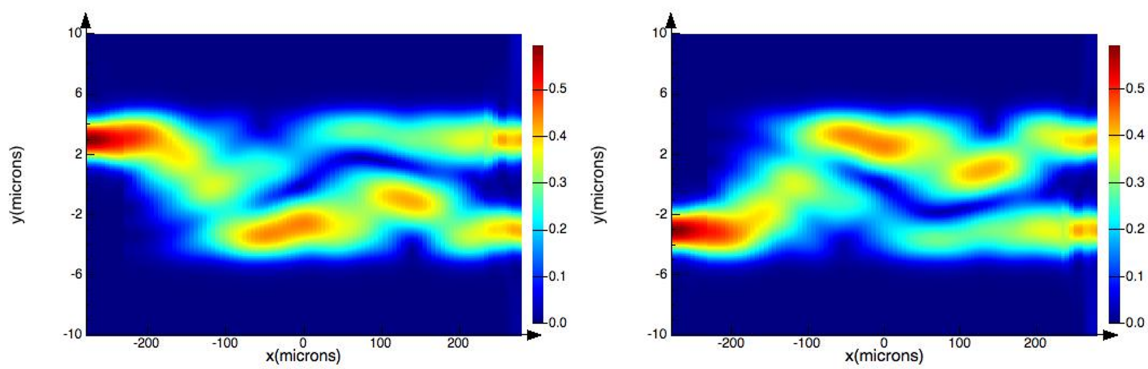

Figure 4.27: Simulated XY plane power profile of the 2×2 MMI.

4.5.2 Directional Couplers

Directional couplers (DCs) are usually used for unequal signal splitting and mixing. By controlling the length of the coupling region in the directional coupler, a splitting ratio at any percentage can be achieved [3, 19]. But, since directional couplers consist of two parallel waveguides that need to be put closely next to each other in order to form the cross coupling, they requires a higher fabrication accuracy compared to MMI couplers. In addition, the splitting ratio is highly frequency dependent, so DCs need to be redesigned for different wavelengths.

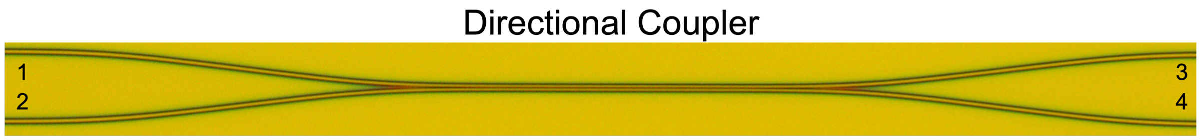

Figure 4.28: Microscope image of the fabricated directional coupler.

Left Waveguide	Tapered Left Waveguide	Coupler Region		Coupling Gap	Tapered Right Waveguide	Right Waveguide	S Parameter in Power			
um	um	um		um	um	um	%			
W	W	L	W	W	W	W	S31	S41	S32	S42
2.89	2	180	2	1	2	2.89	73.7	21.7	21.7	73.7

Table 4.4: Design specifications of the directional coupler.

Figure 4.28 shows a fabricated directional coupler. A taper is added to the adiabatic bend to taper the 2.89 μm waveguide down to 2 μm for reducing the length of the directional coupler. Table. 4.4 shows the corresponding design specifications of the directional coupler, which has a coupling region length of 180 μm and coupling gap of 1 μm.

Since directional couplers are very sensitive to the coupling length and coupling gap, and are also highly frequency dependent, directional couplers simulations were done in Lumerical's MODE software using the EME engine. The simulation results are shown in Fig. 4.29 $\sim$ 4.31. From these simulations, it can be seen that the directional coupler reaches a total 100 % cross coupling for a coupling length of 761 μm and a coupling gap of 1 μm at a wavelength of 1572.335 nm. For a 180 μm long directional coupler with a 1 μm gap, the coupling ratios for wavelengths from 1550 nm to 1700 nm have a

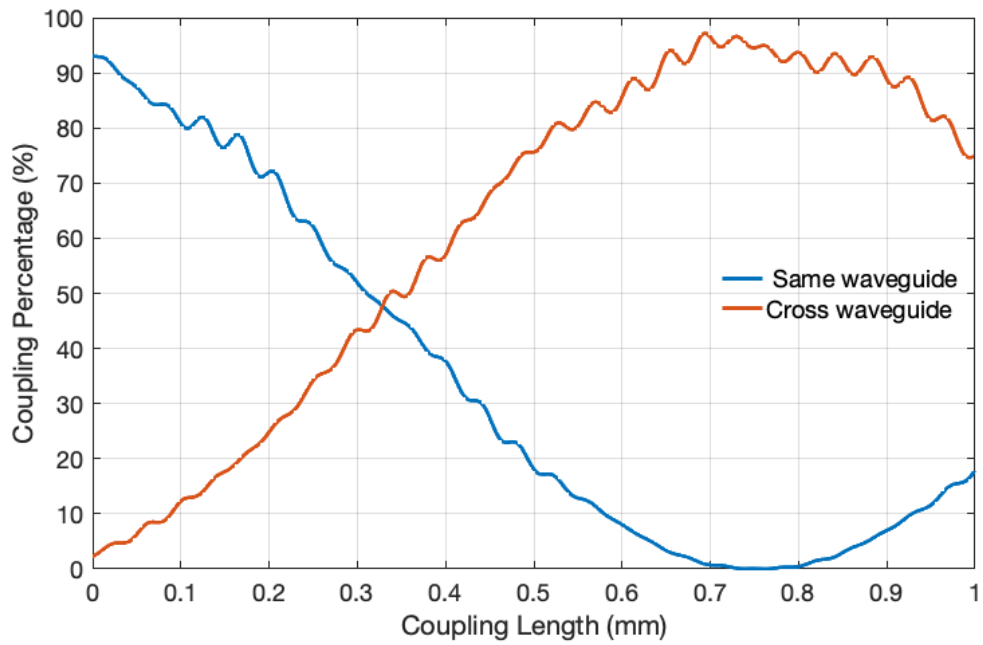

Figure 4.29: Simulation of directional coupler coupling ratio at different coupling length at 1572.335 nm optical wavelength.

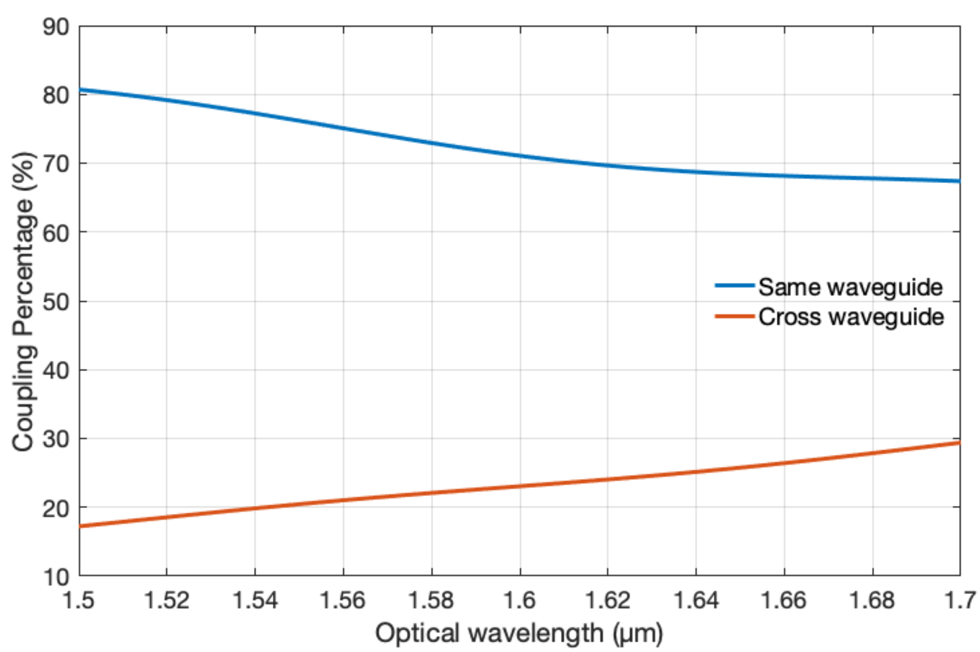

Figure 4.30: Simulation of directional coupler coupling ratio at different optical wavelengths with 180 μm coupling length.

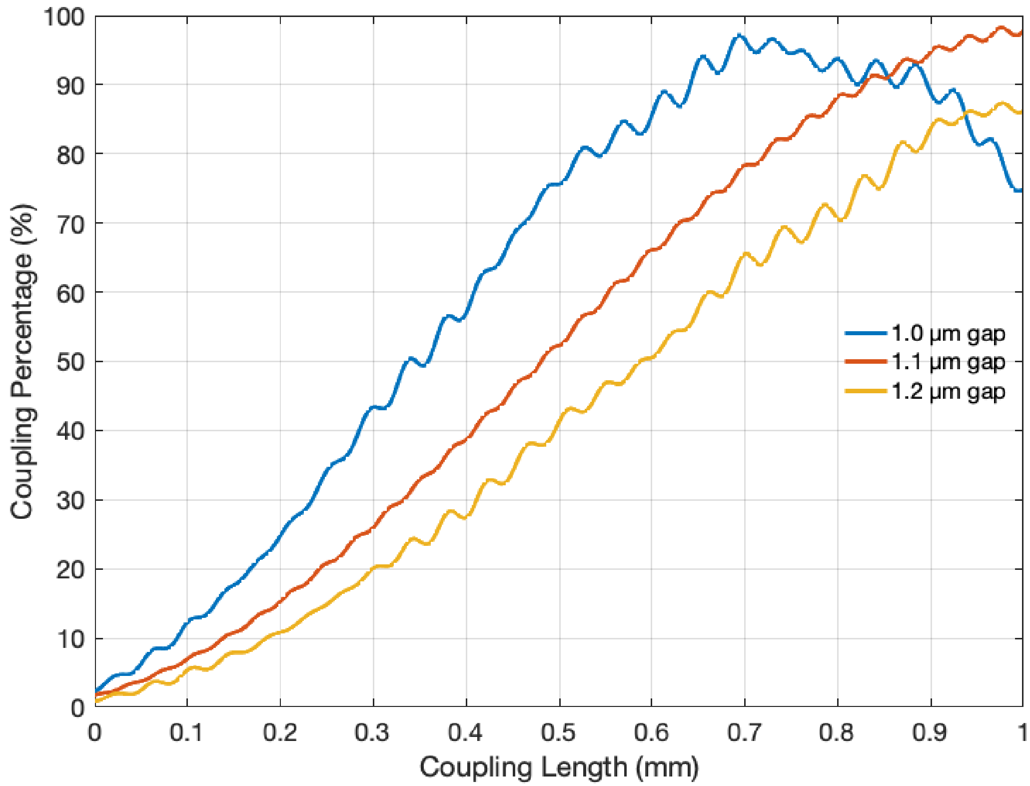

Figure 4.31: Simulation of directional couplers with different coupling gaps with 180 μm coupling length at 1572.335 nm optical wavelength.

difference of around 13 %. At last, the coupling ratios for different coupling gaps and different coupling lengths at 1572.335 nm were calculated. For a 20 % coupling ratio, the 1 μm, 1.1 μm and 1.2 μm gaps need coupling lengths of 168 μm, 242 μm, and 300 μm, respectively. Therefore, a 1 μm gap was chosen to keep the total length of the PIC manageable, considering the expected passive losses and fabrication complexity.

4.6 Conclusion

Different kind of devices used in the PIC were introduced in this section. Not all of these devices were used in the final PIC. A down selection of components was made based on the first round of results to help reduce the PIC complexity and improve the fabrication yield. During the down selection, a big decision we made was that only SGDBR lasers and photodiodes without a BCB layer were to be used in the second round. Although the DBR and SGDBR lasers were both working well, we chose to use an SGDBR laser instead of a DBR laser because the SGDBR lasera have a much wider tunability for reaching the target wavelength. We used epitaxial wafers grown both in our group at UCSB by and outside vendor. Although the same epitaxial material design was used for both growths, the quality of the epitaxial wafers differed slightly. By using an SGBDR laser which can tune over 40 nm, we minimized the risk associated with differences between the material indices used in the design and the actual refractive indices of layers grown in different reactors. Even if the center wavelength of the SGDBR laser turned out slightly different for each sample, the laser could be tuned back to 1572.335 nm. For the photodiode, since adding the BCB layer complicates the fabrication process and the photodiode is the only place the BCB layer is used, the BCB layer was removed to accelerate the fabrication process. After all the fabrication runs and testing, if more time was allowed, I would strongly suggest adding the BCB layer to the photodiodes to improve the their bandwidth since this was the main performance limitation of our latest generation PIC. More details of the PIC structure, design, and testing are discussed in Chapters 6 and 7.

Bibliography

[1] K. Utaka, S. Akiba, K. Sakai, and Y. Matsushima, *$\lambda/4$-shifted ingaasp/inp dfb lasers*, *IEEE journal of quantum electronics* **22** (1986), no. 7 1042–1051.

[2] L. A. Coldren, S. C. Nicholes, L. Johansson, S. Ristic, R. S. Guzzon, E. J. Norberg, and U. Krishnamachari, *High performance inp-based photonic icsa tutorial*, *Journal of Lightwave Technology* **29** (2011), no. 4 554–570.

[3] L. A. Coldren, S. W. Corzine, and M. L. Mashanovitch, *Diode lasers and photonic integrated circuits*, vol. 218. John Wiley & Sons, 2012.

[4] Y. Akulova, G. Fish, P.-C. Koh, C. Schow, P. Kozodoy, A. Dahl, S. Nakagawa, M. Larson, M. Mack, T. Strand, C. Coldren, E. Hegblom, S. Penniman, T. Wipiejewski, and L. Coldren, *Widely tunable electroabsorption-modulated sampled-grating dbr laser transmitter*, *IEEE Journal of Selected Topics in Quantum Electronics* **8** (2002), no. 6 1349–1357.

[5] K. Numata, J. R. Chen, S. T. Wu, J. B. Abshire, and M. A. Krainak, *Frequency stabilization of distributed-feedback laser diodes at 1572 nm for lidar measurements of atmospheric carbon dioxide*, *Applied optics* **50** (2011), no. 7 1047–1056.

[6] F. Sang, J. Fridlander, V. Rosborough, S. T. Š. Brunelli, L. Coldren, J. Klamkin, J. Chen, K. Numata, R. Kawa, and M. Stephen, *Integrated photonics technology*

for earth science remote-sensing lidar, in *2021 IEEE International Geoscience and Remote Sensing Symposium IGARSS*, pp. 7708–7711, IEEE, 2021.

[7] J. Fridlander, F. Sang, V. Rosborough, F. Gambini, S. T. S. Brunelli, J. R. Chen, K. Numata, M. Stephen, L. A. Coldren, and J. Klamkin, *Dual laser indium phosphide photonic integrated circuit for integrated path differential absorption lidar*, *IEEE Journal of Selected Topics in Quantum Electronics* (2021).

[8] B. R. Bennett, R. A. Soref, and J. A. Del Alamo, *Carrier-induced change in refractive index of inp, gaas and ingaasp*, *IEEE Journal of Quantum Electronics* **26** (1990), no. 1 113–122.

[9] M. N. Sysak, L. A. Johansson, J. W. Raring, M. Rodwell, L. A. Coldren, and J. Bowers, *A high efficiency, current injection based quantum-well phase modulator monolithically integrated with a tunable laser for coherent systems*, in *Coherent Optical Technologies and Applications*, p. CFC6, Optical Society of America, 2006.

[10] J.-I. Shim, M. Yamaguchi, P. Delansay, and M. Kitamura, *Refractive index and loss changes produced by current injection in ingaas (p)-ingaasp multiple quantum-well (mqw) waveguides*, *IEEE Journal of Selected Topics in Quantum Electronics* **1** (1995), no. 2 408–415.

[11] J. M. Fridlander, *Photonic Integrated Circuits for Remote Sensing Lidar.* PhD thesis, University of California, Santa Barbara, 2021.

[12] V. Rosborough, J. Fridlander, F. Sang, F. Gambini, S. T. Š. Brunelli, J. R. Chen, S. Kawa, K. Numata, M. Stephen, L. Coldren, *et. al.*, *Residual amplitude modulation reduction in integrated indium phosphide phase modulators*, in *CLEO: Science and Innovations*, pp. STh4B–3, Optical Society of America, 2021.

[13] N. Dupuis, J. E. Proesel, H. Ainspan, C. W. Baks, M. Meghelli, and B. G. Lee, *Nanosecond-scale shift-and-dump mach–zehnder switch*, *Optics letters* **44** (2019), no. 18 4614–4616.

[14] T.-P. Lee, C. Burrus, and A. Dentai, *Ingaas/inp pin photodiodes for lightwave communications at the 0.95-1.65 μm wavelength*, *IEEE Journal of Quantum Electronics* **17** (1981), no. 2 232–238.

[15] J. C. Campbell, S. Demiguel, F. Ma, A. Beck, X. Guo, S. Wang, X. Zheng, X. Li, J. D. Beck, M. A. Kinch, *et. al.*, *Recent advances in avalanche photodiodes*, *IEEE Journal of selected topics in quantum electronics* **10** (2004), no. 4 777–787.

[16] T. Ishibashi, N. Shimizu, S. Kodama, H. Ito, T. Nagatsuma, and T. Furuta, *Uni-traveling-carrier photodiodes*, in *Ultrafast Electronics and Optoelectronics*, p. UC3, Optical Society of America, 1997.

[17] B. Isaac, S. Pinna, Y. Liu, and J. Klamkin, *Efficiency of waveguide uni-traveling-carrier photodiodes for microwave signal generation*, in *Optical Fiber Communication Conference (OFC) 2019*, p. Th3B.6, Optical Society of America, 2019.

[18] L. B. Soldano and E. C. Pennings, *Optical multi-mode interference devices based on self-imaging: principles and applications*, *Journal of lightwave technology* **13** (1995), no. 4 615–627.

[19] E. A. Marcatili, *Dielectric rectangular waveguide and directional coupler for integrated optics*, *Bell System Technical Journal* **48** (1969), no. 7 2071–2102.

Chapter 5

Pulse Generator Design and Characterization

A pulsed current source is a common piece electronic equipment that is used to generate pulsed current signals with various pulse widths and periods. Such an instrument usually only supports positive current output. In this chapter, a custom designed pulse generator that can support both positive current output and negative voltage output is introduced.

The pulse generator was designed to drive an SOA as an optical pulse carver, where the SOA is used as an optical power amplifier under positive current injection and an optical power absorber under negative voltage bias. Compared to driving the SOA with a forward bias only, driving the SOA from a reverse bias voltage to a forward bias current provides an improved extinction ratio by reducing the off state power. The details of the pulse generator are discussed in this chapter. It was successfully used to generate a pulsed signal from -2 V to 200 mA, which are the voltage and current values typically used for an SOA in reverse and forward bias, respectively.

5.1 Pulse Generator Circuit Design

The pulse generator design is shown in Fig. 5.1. It is based on a switching circuit to switch the output between the negative voltage source (V5) and positive current source (I1). The switching is achieved using a pair of bipolar junction transistors (Q1 & Q2) [1, 2]. When the input signal (V1) is high, Q2 turns off, and the negative voltage from V5 is applied to the device under test (DUT) through the operation amplifier (U1). When the input (V1) is low, Q2 turns on, and I1 is injected into the DUT. In addition, Q1 works as a current dump. When Q2 is turned off, the current from I1 passes through Q1 and the dumping resistor R5 into ground.

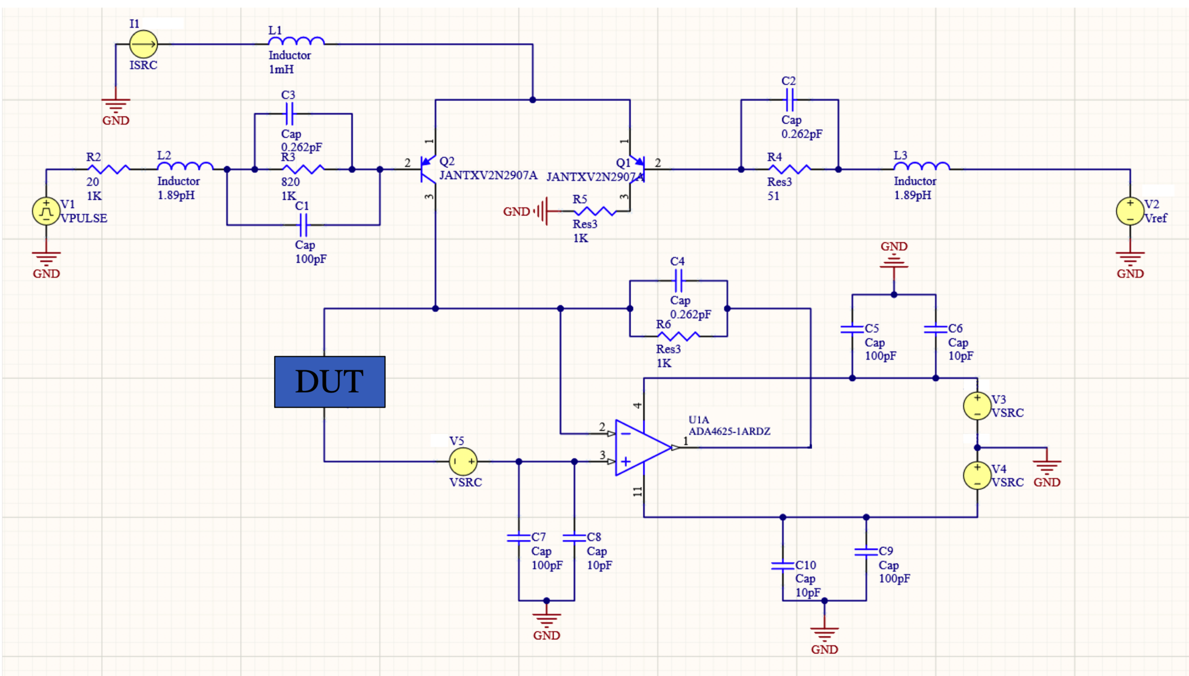

Figure 5.1: Schematic of the pulse generator.

A simulation of the circuit was created by setting up Spice models of the components in Altium Designer. The simulation results are shown in Fig. 5.2 - 5.4. In the simulation, −10 V is set for V5, the supply voltages of U1 (V3 & V4) are set to ± 15 V, Q1's bias voltage V2 is set to 3.3 V, and the I1 current is set to 200 mA. The RF input V1 is set to

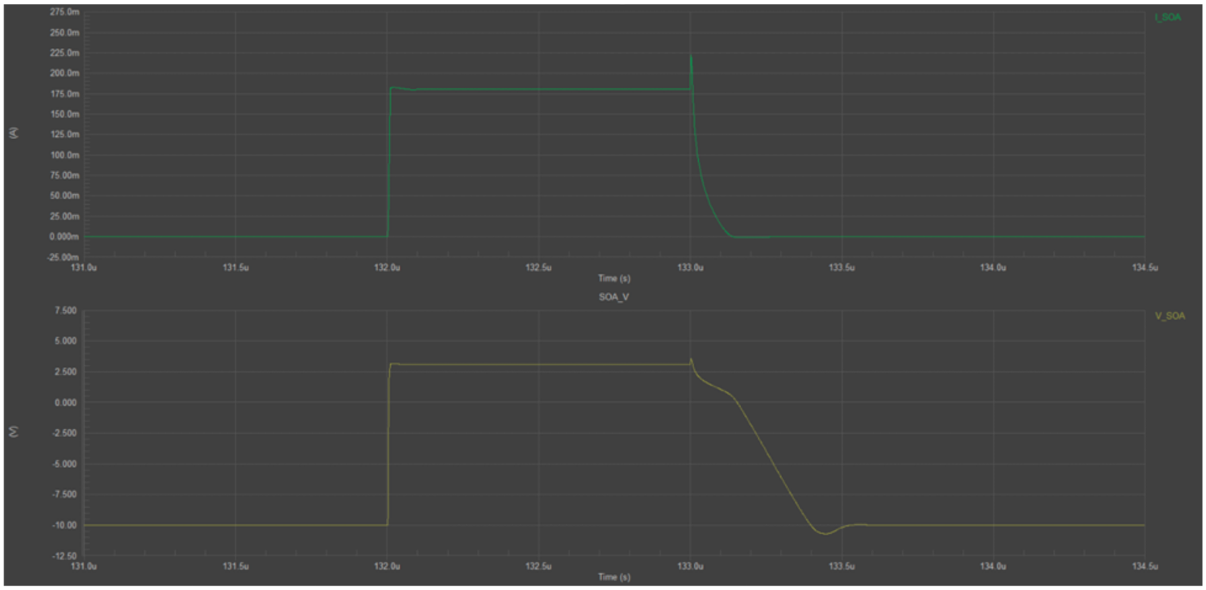

Figure 5.2: Altium Designer simulation of the pulse generator circuit output, which has 1 μs pulse width with 133 μs pulse period from -10 V to 180 mA.

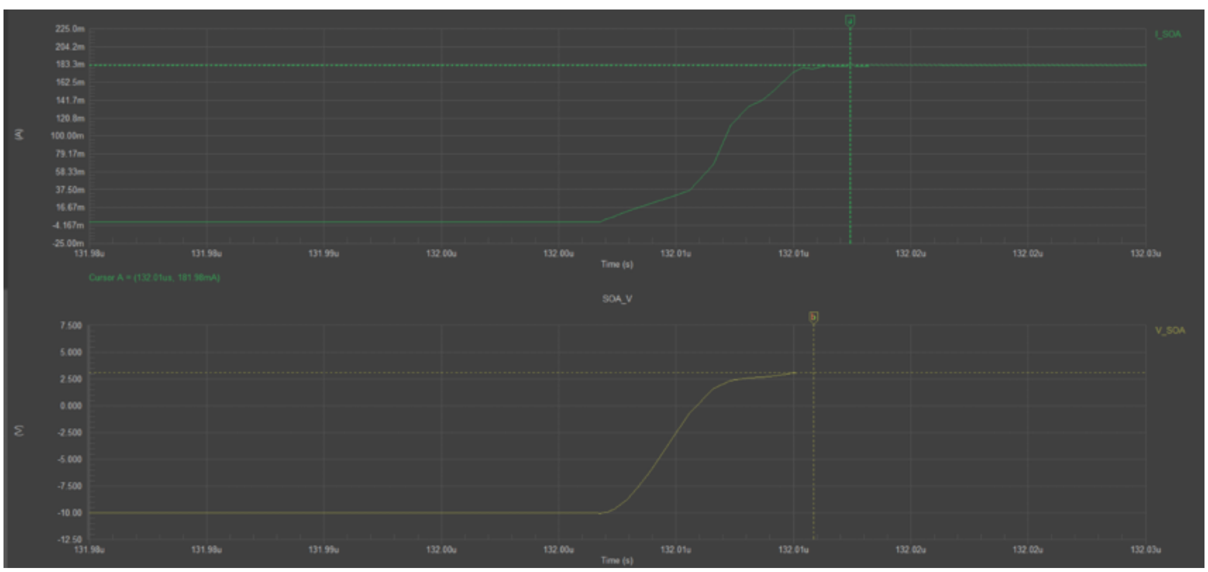

Figure 5.3: Altium Designer simulation of the pulse generator circuit, zoomed in rising edge signal of the 1 μs pulse width with 133 μs pulse period from -10 V to 180 mA.

5 V with 1 μs pulse. As can be seen from the simulation results, the rising edge is much sharper than the falling edge, where the rising time is around 10 ns, but the falling time is around 400 ns. From Fig. 5.4, we can observe that from 180 mA to 0 mA, the falling

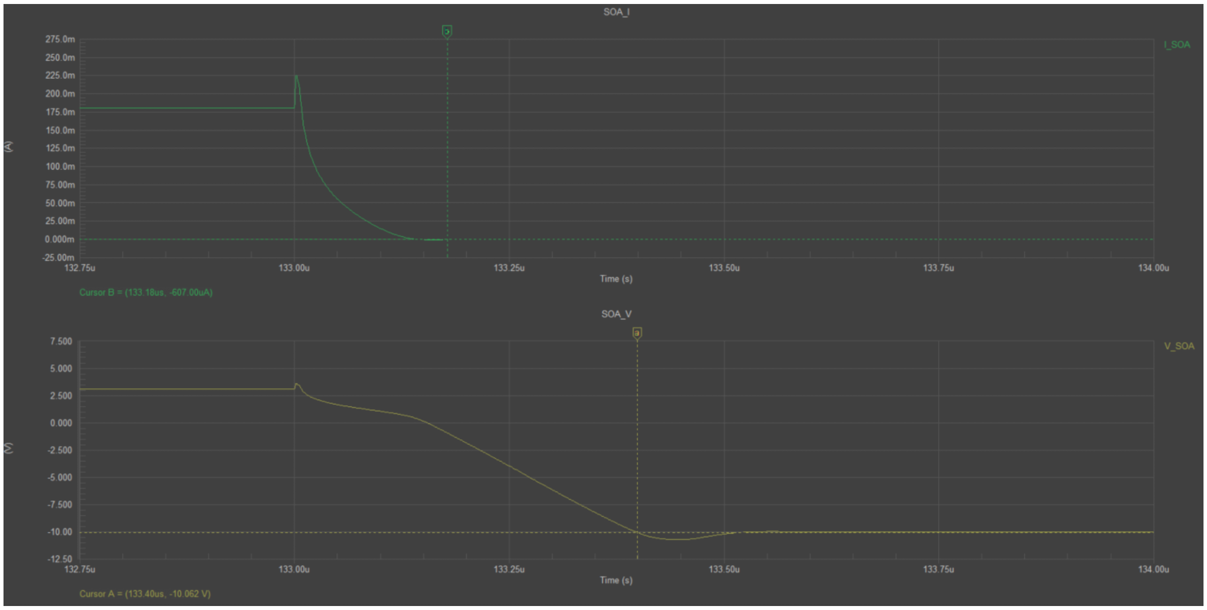

Figure 5.4: Altium Designer simulation of the pulse generator circuit, zoomed in falling edge signal of the 1 μs pulse width with 133 μs pulse period from -10 V to 180 mA.

time is around 180 ns, but to further achieve -10 V, 220 ns was needed. This indicates that the charging and discharging time for C4 capacitor is the main limitation of the falling time.

5.2 Pulse Generator PCB Layout

A PCB board was designed for the pulse generator based on the schematic shown in Fig. 5.1. The PCB board layout is shown in Fig. 5.5 & 5.6. The PCB board has dimensions of 500 mil (12.7 mm) by 3575 mil (90.805 mm) and a thickness of 32.6 mil (0.828 mm). The detailed PCB stack and via combinations are shown in Fig. 5.7. In order to improve the performance and reduce the cross talk between different types of signals, a four-layer PCB stack was used. The top layer is the RF signal layer, the second layer is the digital power supply, the third layer is the analog power supply, and the fourth layer is the ground layer. The PCB uses an SMA connector for the input

RF signal connection. The output uses the soft bondable gold GSG..GSG pads for wire bonding with an extra SMA connector soldering pad available for external connection. In addition, the all digital and analog supplies are combined into one socket for easy installation. The fabricated PCB is shown in Fig. 5.8.

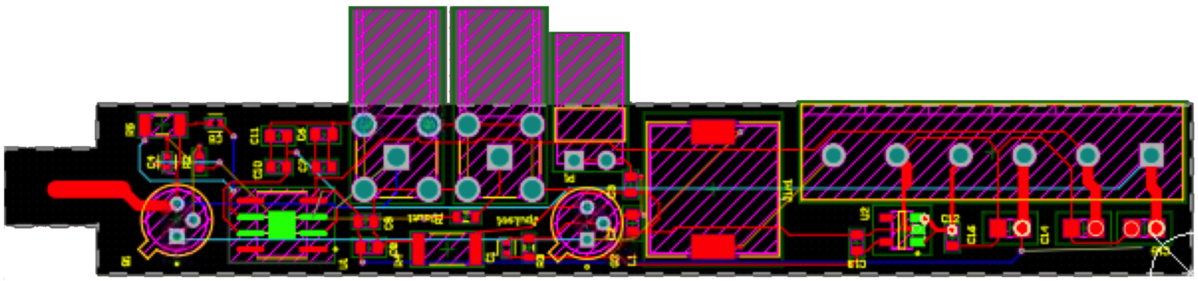

Figure 5.5: 2D routing view of the PCB layout.

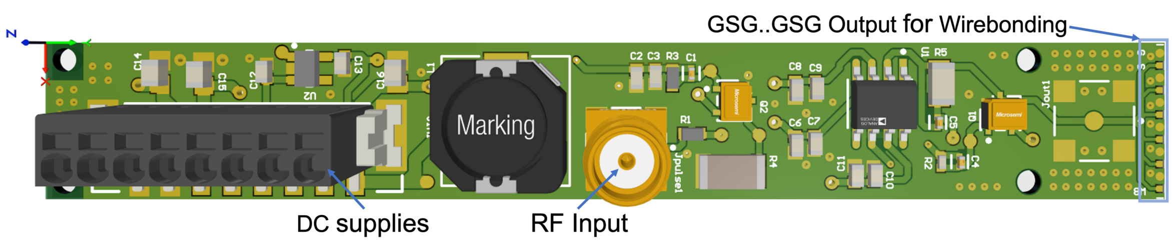

Figure 5.6: 3D view of the PCB layout.

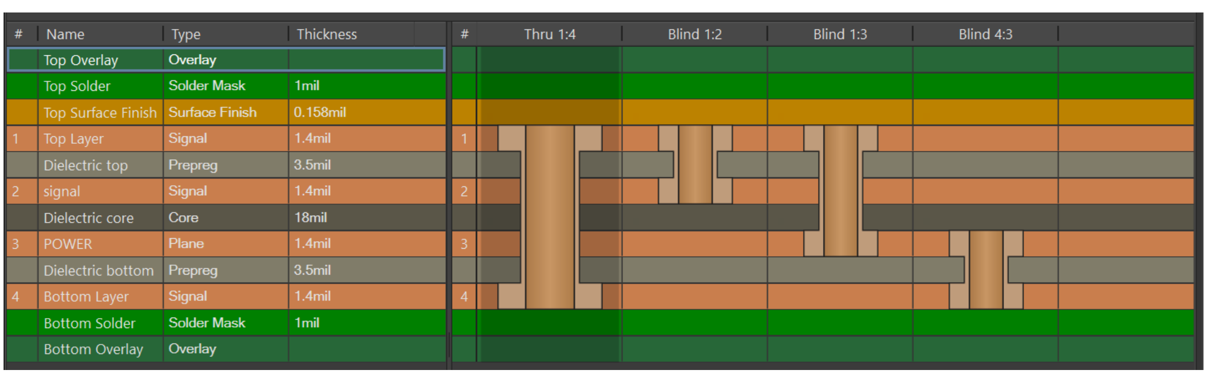

#	Name	Type	Thickness
	Top Overlay	Overlay	
	Top Solder	Solder Mask	1mil
	Top Surface Finish	Surface Finish	0.158mil
1	Top Layer	Signal	1.4mil
	Dielectric top	Prepreg	3.5mil
2	signal	Signal	1.4mil
	Dielectric core	Core	18mil
3	POWER	Plane	1.4mil
	Dielectric bottom	Prepreg	3.5mil
4	Bottom Layer	Signal	1.4mil
	Bottom Solder	Solder Mask	1mil
	Bottom Overlay	Overlay	

Figure 5.7: Details of PCB stacks and Vias.

Figure 5.8: Image of received manufactured PCB under test.

5.3 Pulse Generation

The fabricated pulse generator PCB was tested in the lab for its functionality performance. For the test, V2 was biased at 2 V. V1 has a pulsed or rectangular signal with a peak-to-peak amplitude of 2.5 V and a 500 mV offset. The signal at different pulse widths was tested for the 133 μs pulse period and is shown in Fig. 5.9. A pulsed signal was successfully generated from a reverse bias of - 2 V to a forward bias of 200 mA. Unfortunately, the rising time of the pulse signal was long compared to the simulation. There was a 0.6 μs turn-on delay between the input and the output signal and a 1.1 μs turn-off delay between the input and the output signal. The main reason for this is that the Q2 turn-on and turn-off was delayed due to an improper capacitor and resistor combination. The rising and falling time of the pulse signal was 2.5 μs and 1 μs, respectively. The rectangular pulse generation was also tested and is shown in Fig. 5.10. From the rectangular pulse test, it can be seen that the rising delay is insignificant, but

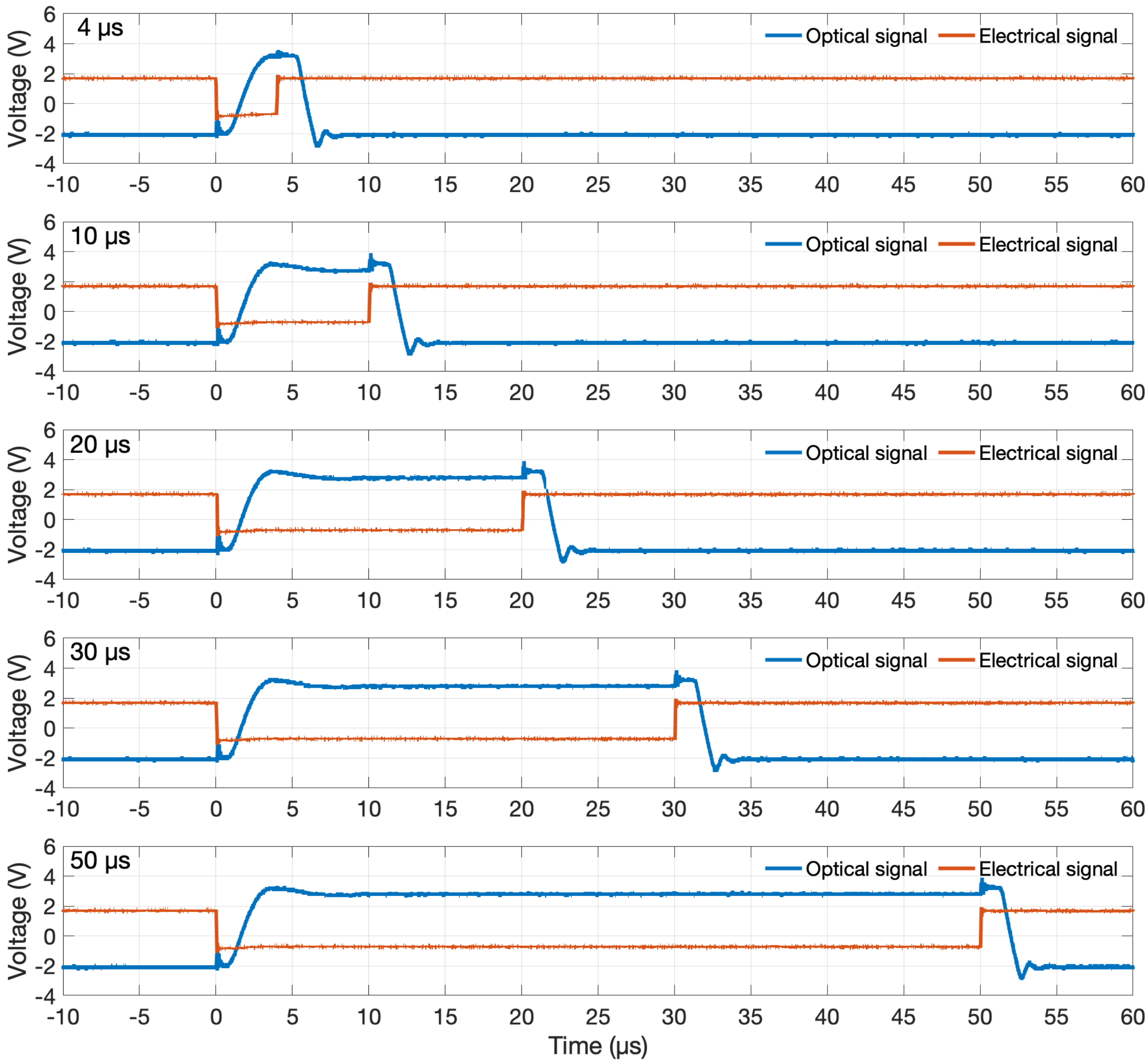

Figure 5.9: Tested data of the manufactured pulse generator at different pulse widths with 113 μs pulse period from -2 V to 200 mA.

the turn-off delay is still around 1.1 μs. The rising and falling time were 3 μs and 1 μs, respectively.

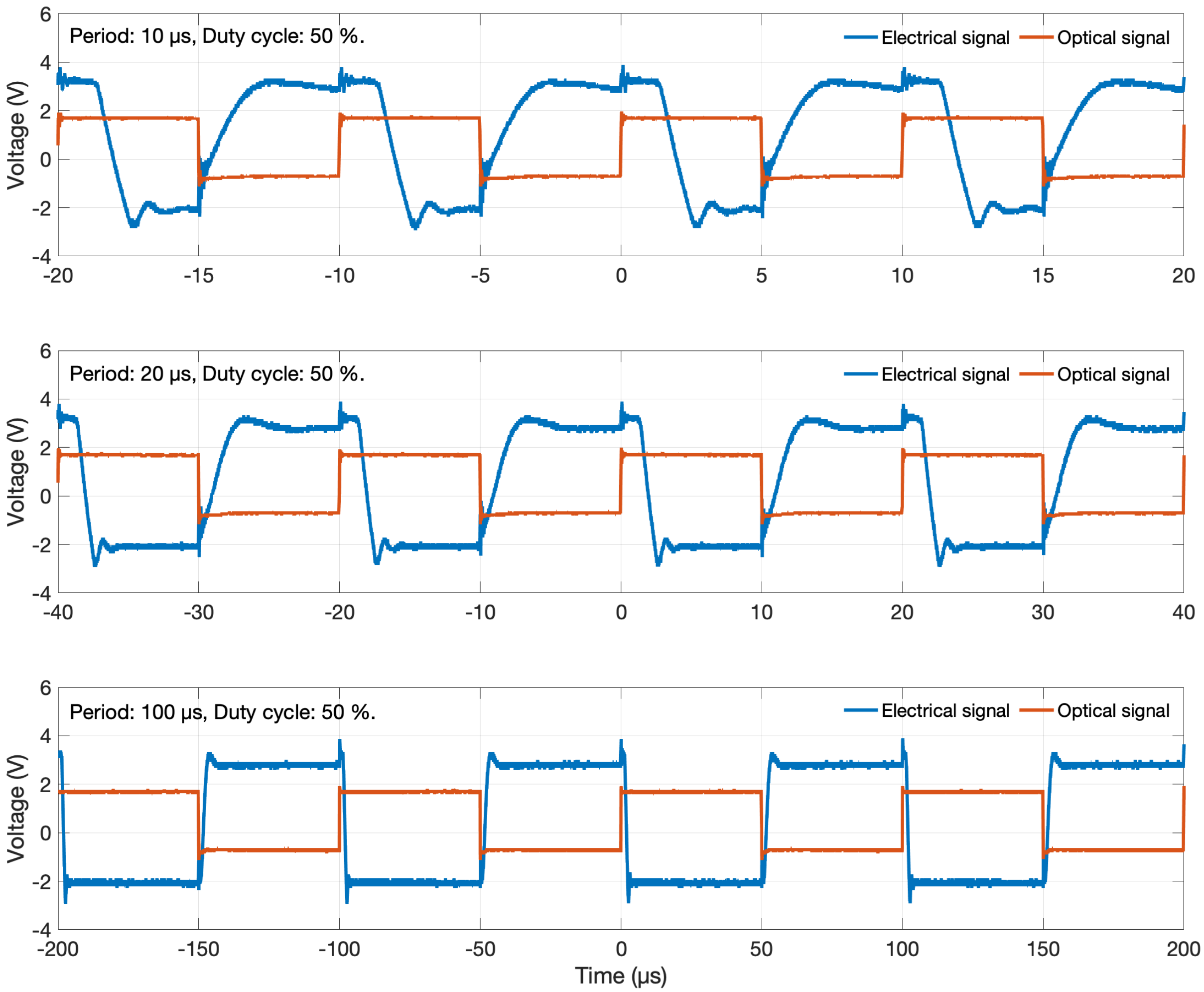

Figure 5.10: Tested data of the manufactured pulse generator at different pulse widths with 113 μs pulse period from -2 V to 200 mA.

5.4 Conclusion

A pulse generator was designed, laid out, manufactured, and tested. The functionality of the pulse generator was tested and reported above. Overall, The pulse generator was functional, albeit with relatively long rising and falling times compared when with the simulation. This was mainly caused by an improper implementation of the capacitor and resistor in the charging and discharging loop. In order to improve the performance of this pulse driver, optimization of the capacitor and resistor is needed.

Bibliography

[1] G. Gonzalez, *Microwave transistor amplifiers analysis and design*. Prentice-Hall, Inc., 1996.

[2] M. Campola, B. Freeman, and K. Yau, *Total ionizing dose test of microsemis silicon switching transistors jantxv2n2222aub and 2n2907aub*, .

Chapter 6

Photonic Integrated Circuit Architecture and Design

This chapter introduces both the NASA architecture and the PIC-based architecture. For the NASA architecture, the discussion mainly focuses on the methodology used for achieving CO_2 remote sensing. The comparison between the NASA architecture and the PIC-based architecture is analyzed, and the arrangement and layout of the PICs are also discussed and investigated.

6.1 Architecture

In this section, two versions of the sensing system architecture are introduced. One is the current NASA architecture which is mainly based on commercial off-the-shelf (COTS) products. Another is the PIC-based architecture, which is designed and optimized for the PIC enabled sensing system.

6.1.1 NASA Architecture

The NASA system design is based on an integrated path differential absorption (IPDA) lidar architecture [1, 2] and is shown in Fig. 6.1. A DFB laser is used as the master laser, where it works as an absolute reference for the slave DS-DBR laser [3, 4]. The slave DS-DBR laser is controlled using the dynamic OPLL system to sweep over the target frequency ($\sim$ 40 GHz) [4]. An MZM is used to convert the CW signal

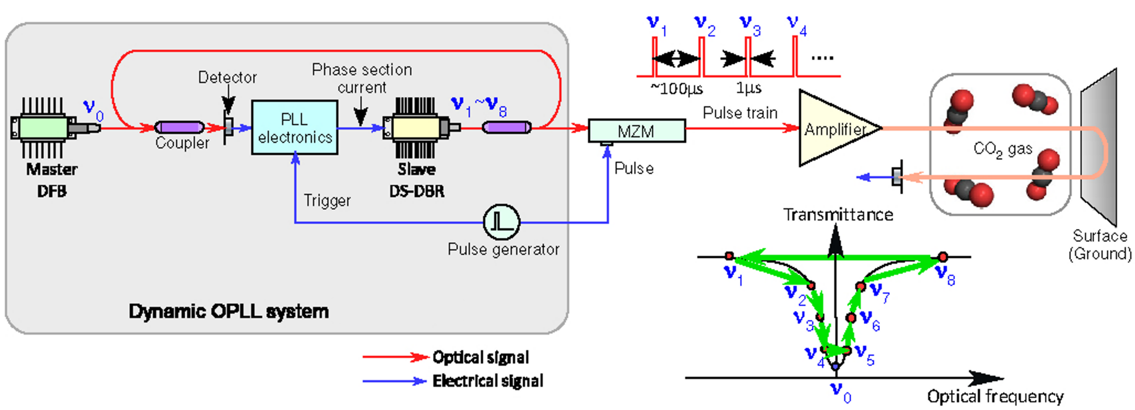

Figure 6.1: NASA's Architecture of the precision fast laser tuning technique and its application for CO2 remote sensing. (© OSA 2012, [1].)

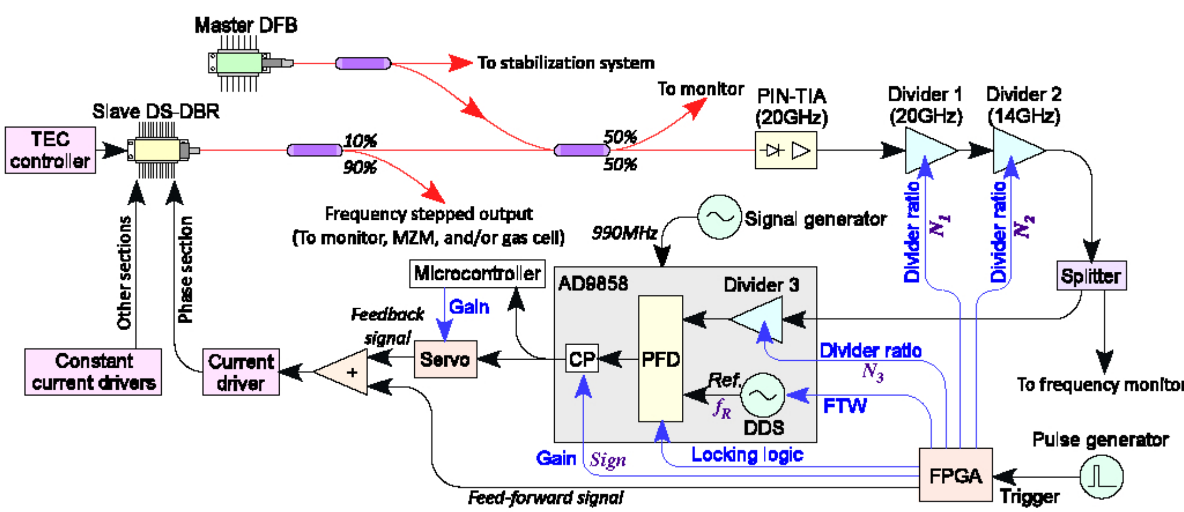

Figure 6.2: Details of OPLL system. (© OSA 2012, [1].)

into a pulse train, and an optical amplifier is used to amplify the output power for the CO_2 transmission through the atmosphere. On the receiver side, the reflected power at different wavelengths is detected to recover the transmittance spectrum of the CO_2 absorption line. The concentration of CO_2 is derived from the absorption line shape and knowledge of the corresponding sensing conditions.

The details of the OPLL system are shown in Fig. 6.2. The master DFB laser is maintained at 1572.335 nm using a stabilization system based on a frequency modulation technique. The slave DS-DBR laser is tuned to the target frequency by choice of bias current and temperature. Only the phase section of the DS-DBR laser is used for the feedback signal and frequency switching. All other sections of the slave laser are biased with a constant current. The beat note signal is generated using a 20 GHz PIN-TIA photodetector before it is divided down and sent into an AD9858 IC from Analog Devices. The AD9858 IC integrates the function of a divider, a phase frequency detector (PFD), a current pump (CP), and a direct digital synthesizer (DDS) [5]. The frequency of the

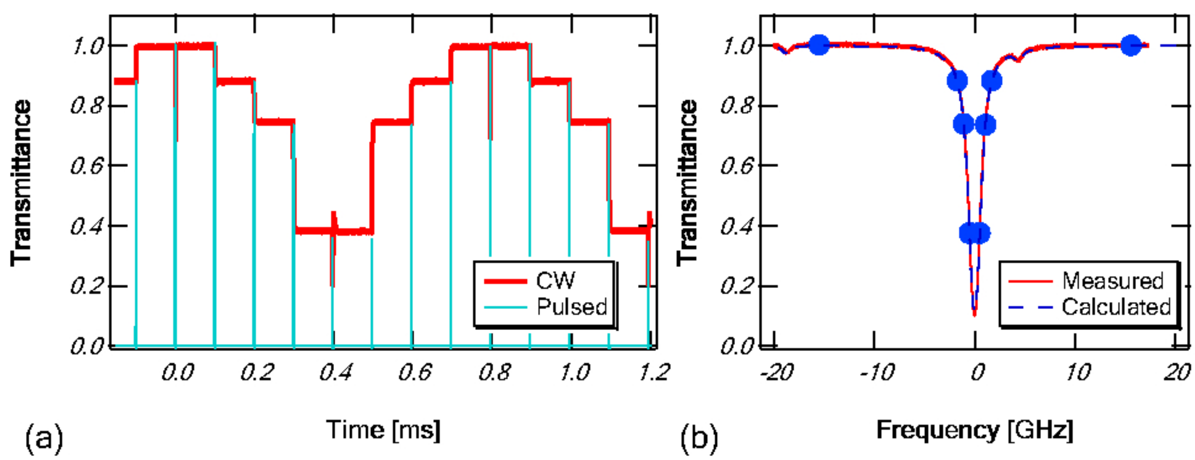

Figure 6.3: Measured transmittance of CO_2 in a gas cell using the NASA system. (a) Transmittance vs. time measured in frequency-stepped mode with and without the pulse modulation. (b) Transmittance spectra measured by continuously scanning the same laser (solid line) and by stepping the frequency (solid circle). The calculated transmittance (dashed blue) is also plotted for comparison. (© OSA 2012, [1].)

beat note signal is divided with three frequency dividers. Divider 1 uses UXD20PE from Centellax, Inc., divider 2 uses UXN14M9PE also from Centellax, Inc., and divider 3 is integrated in AD9858. After the three dividers, the frequency of the beat note signal is lower than the maximum frequency of the PFD which is 150 MHz. Then, the frequency difference between the divided beat note signal and the target signal is detected from the PFD. A field programmable gate array (FPGA) is used to control all the parameters including the loop filter gain, CP and DDS, and to send the feedback signal to the phase section of the DS-DBR. The FPGA also automatically switches to each frequency using a external pulse signal as a trigger. One of the results measured under this system is shown in Fig. 6.3, and more results are shown in their corresponding publications and information on the NASA ASCENDS mission [1, 6–8].

6.1.2 PIC-based Architecture

The PIC-based architecture was designed and developed based on the NASA architecture described above. Building on the system developed at NASA ensures the functionality and performance of the new system. In addition, it also enables NASA to reuse their current reliable control system without a major update for qualifying the PIC-based system. However, this is not the only way to achieve accurate absolute optical frequency measurements. An optical frequency synthesizer (OFS) can also be used to achieve similar results and research has shown that an OFS can achieve the required sub hundred hertz accuracy [9].

The detailed PIC-based architecture, shown in Fig. 6.4, also uses the IPDA lidar topology with two lasers. The components within the light blue area are integrated into an InP PIC, which includes two SGDBR (leader and follower) lasers, a phase modulator, a photodiode, a pulse carver, splitters and couplers. The leader laser is the equivalent of the master laser in the NASA system. It is locked to the CO_2 reference cell using a frequency modulation technique. The leader laser output is phase modulated at 125 MHz using either a straight phase modulator or an MZM phase modulator and then sent into the CO_2 reference cell. The modulated signal is detected after the CO_2 reference cell by an external photodiode with a TIA integrated. A Moku:Lab instrument is used to extract the error signal by mixing the detected signal and the delayed 125 MHz modulation signal together. The signal filtering and PID control is also performed in the Moku:Lab. Next, the processed signal is sent into the phase section of the leader laser to achieve the stabilization. The follower laser is the equivalent of the slave laser in the NASA system.

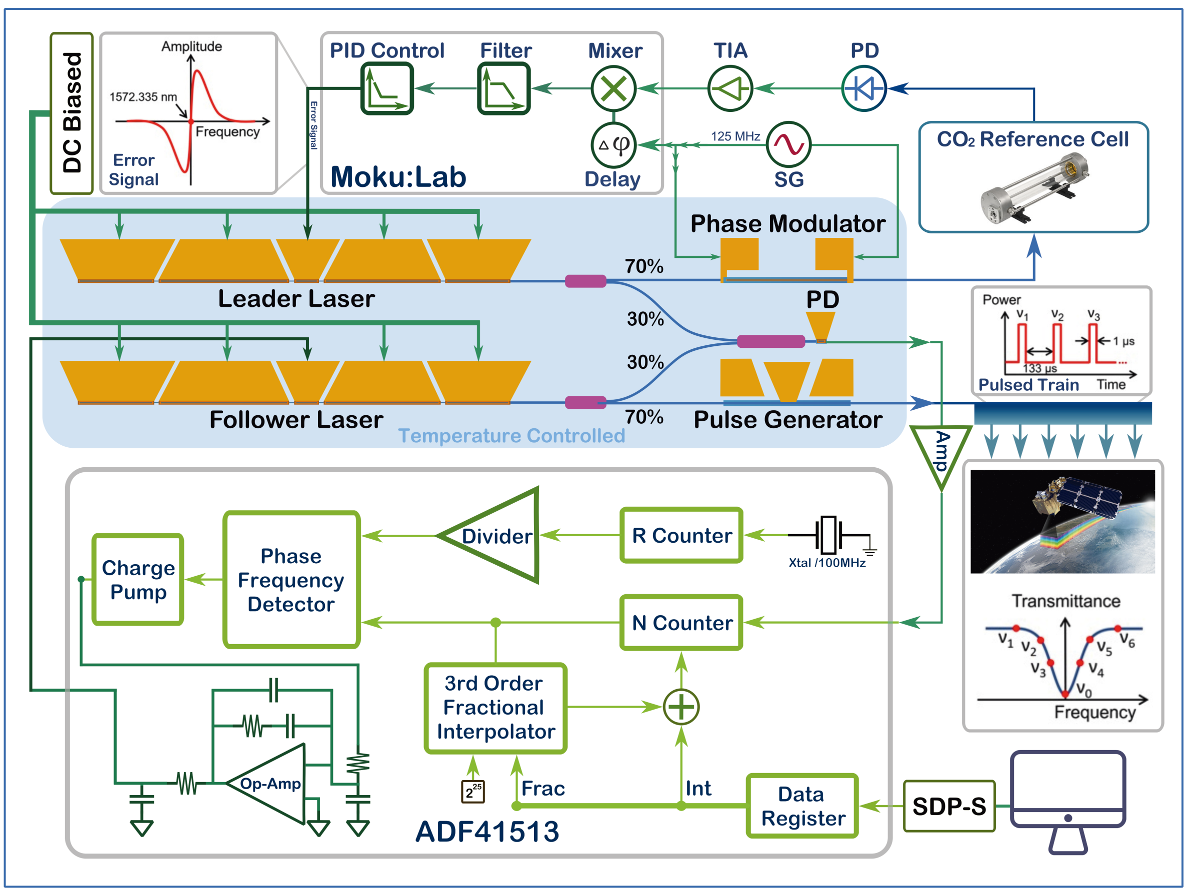

Figure 6.4: PIC-based Architecture.

It is controlled using an OPLL system to step over the target frequencies. The OPLL is achieved using the integrated photodiode and the ADF41513 evaluation board from Analog Devices. The integrated photodiode detects the beat note signal between the leader and follower lasers. The beat note signal is amplified and sent into the ADF41513 evaluation board for frequency difference detection. A feedback signal is generated based on the frequency difference between the input signal and target frequency. The details of this generation process are discussed in chapter 7.2.2. Then, the generated feedback signal is sent back into the phase section of the follower laser to accomplish the wavelength sweep. Lastly, an MZM or an SOA is used to convert the CW signal from the follower laser into a pulse train as the final output for performing sensing in the lab, which is discussed later in chapter 7.3.2.

6.2 PIC Design and Combinations

Many generations of PICs were designed and laid out for the PIC-based architecture. In this section, the details of the PIC design and layout optimization are discussed. The PIC design section mainly covers how the PICs were implemented, which includes selection of device types and the PIC level arrangement and optimization. The layout optimization focuses on the arrangement of components at the mask level, specifically, different PICs were arranged in the lithography field to achieve the best yield of the fabricated devices.

The PICs are designed to be incorporated into the PIC-based architecture. Many PIC designs with different components were fabricated in order to achieve the best performance. Overall, two types of lasers and phase modulators and three types of power splitters and pulse generators were considered and designed.

The two types of lasers considered are SGDBR lasers and DBR lasers. The SGDBR lasers provide a wider tuning range (30 nm - 40 nm) and a better SMSR, but they have a larger device size. The DBR lasers provide a smaller tuning range (5 nm - 7 nm) and a smaller device size, but they have a moderate SMSR. For both laser designs, an SOA following the laser's front mirror can be added to further amplify the optical output power of the laser. The SGDBR and DBR lasers are both fabricated and tested in the first generation (PIC No. $1 \sim 4$). From the test results, the SGDBR achieved better performance in terms of SMSR, tuning range and accuracy in tuning to 1572.335 nm. Consequently, the PICs designed for the following generations only contained SGDBR lasers.

Two types of phase modulators, straight phase modulators and low RAM MZM phase modulators, were used. The straight phase modulators use the Franz-Keldysh effect in which the refractive index of the material is changed by application of an electric field. The RAM of the straight phase modulator depends on modulation depth and the efficiency of the Franz-Keldysh effect. For the OQW platform, the modulation efficiency of the bulk waveguide material depends on the offset between the operating wavelength and waveguide bandgap. The offset needs to be choose carefully. A smaller offset yields more efficient phase modulation but also higher absorption loss, so the corresponding RAM performance is not exceptional [10]. In order to further reduce the RAM, a low RAM MZM phase modulator was designed [11]. The low RAM MZM phase modulator also uses the Franz-Keldysh effect for phase modulation, but by properly designing the MZM structure, the RAM can be compensated for. The structure of the low RAM MZM phase modulator needs to be designed and fabricated carefully to achieve the best RAM performance. Most of the PICs still utilized the straight phase modulator and, even though the RAM is not ideal, it was low enough to establish the locking for the PIC to perform the overall sensing [12–15]. To help keep the RAM low, the straight phase modulators were operated in forward bias, where the plasma carrier effect, rather than the Franz-Keldysh effect, dominates.

Three types of pulse carvers were used: an SOA based pulse generator, an MZM based pulse generator, and a combination of both. The SOA works as both a pulse generator and an optical amplifier. It provides more than 40 dB extinction ratio with amplified output power, but the modulation bandwidth of the SOA is limited. The MZM modulator usually provides 20 - 40 dB extinction ratio with higher frequency response [16, 17]. But the output power is low since no amplification is applied. The hybrid combination was designed and used in order to achieve a superior extinction ratio and a high output power.

Based on the components described above, many combinations of PICs were designed and fabricated through several fabrication rounds. The details of PIC combinations used are shown in Table. 6.1. PICs 1 $\sim$ 4 are the first generation design, where main focus was to find the best components for the PIC architecture. For this reason, many different kinds of components were used, including both DBR and SGDBR lasers. From test results, the DBR laser did not provide a huge performance improvement compared with the SGDBR lasers. Therefore, the SGDBR laser was chosen for further PIC designs due to its wide tunability and good SMSR. The use of widely tunable lasers also enables the possibility of implementing sensing over a wider range of wavelengths when compared to PICs with DBR lasers. The MMIs, phase modulators, MZMs and SOAs were shown to be working properly in the first generation PICs. But, the directional couplers had a very low yield due to limitations of the fabrication process.

Based on the experimental data from the first generation, PICs 5 - 9 were designed and fabricated for the second generation. The second generation PICs were more focused on narrowing down the component selection range and improving their designs. The combination of SGDBR leader and follower lasers with a straight phase modulator and SOA pulse generator was prioritized. The SGDBR laser designs were improved and the im-

PIC No.	Leader Laser	Follower Laser	Laser SOA	Power Splitter	Phase Modulator	Pulse Generator
1	SGDBR	SGDBR	Yes	DC & MMI	Straight	SOA
2	SGDBR	SGDBR	Yes	MMI	Straight	SOA
3	DBR	DBR	Yes	DC & MMI	Straight	MZM & SOA
4	DBR	SGDBR	Yes	DC & MMI	Straight	MZM & SOA
5	SGDBR	SGDBR	Yes	DC & MMI	Straight	SOA
6	SGDBR	SGDBR	Yes	DC & MMI	Straight	SOA
7	SGDBR	SGDBR	Yes	MMI	Straight	MZM
8	SGDBR	SGDBR	Yes	DC & MMI	Low RAM	MZM
9	SGDBR	SGDBR	No	DC	Straight	SOA
10	SGDBR	SGDBR	Yes	MMI	Straight	SOA
11	SGDBR	SGDBR	No	DC	Straight	SOA
12	SGDBR	SGDBR	Yes	DC	Low RAM	SOA
13	SGDBR	SGDBR	Yes	DC	Low RAM	MZM & SOA
14	SGDBR	SGDBR	No	DC & MMI	Straight	MZM & SOA
15	SGDBR	SGDBR	No	DC & MMI	Straight	SOA
16	SGDBR	SGDBR	No	MMI	Straight	MZM & SOA

Table 6.1: Detail structures of the PIC designed and fabricated from all rounds. PICs No. $1 \sim 4$ are from the first generation, PICs No. $5 \sim 9$ are from the second generation, and PICs No. $10 \sim 16$ are from the third generation.

proved designs are shown in Chapter 4.1.2. The directional couplers were redesigned and are discussed in Chapter 4.5. In addition, a novel low RAM phase modulator was designed and included in the PIC to further reduce the RAM of the phase modulator. The MZM & SOA combination pulse generator was replaced with an MZM only to reduce the length of the PIC. The second generation test results showed that the updated SGDBR lasers had very good performance. The redesigned directional coupler helped solve the low yield problem. But, the MZM pulse generator had a lower extinction ratio than the pulsed SOA and did not satisfy the 40 dB extinction ratio requirement. We successfully performed the locking experiment using an external photodiode for a PIC design comprising SGDBR lasers, a straight phase modulator and an SOA pulse generator. Unfortunately, the overall PIC yield was relatively low, especially the photodiode used to detect the beat note, which did not generate sufficient photocurrent.

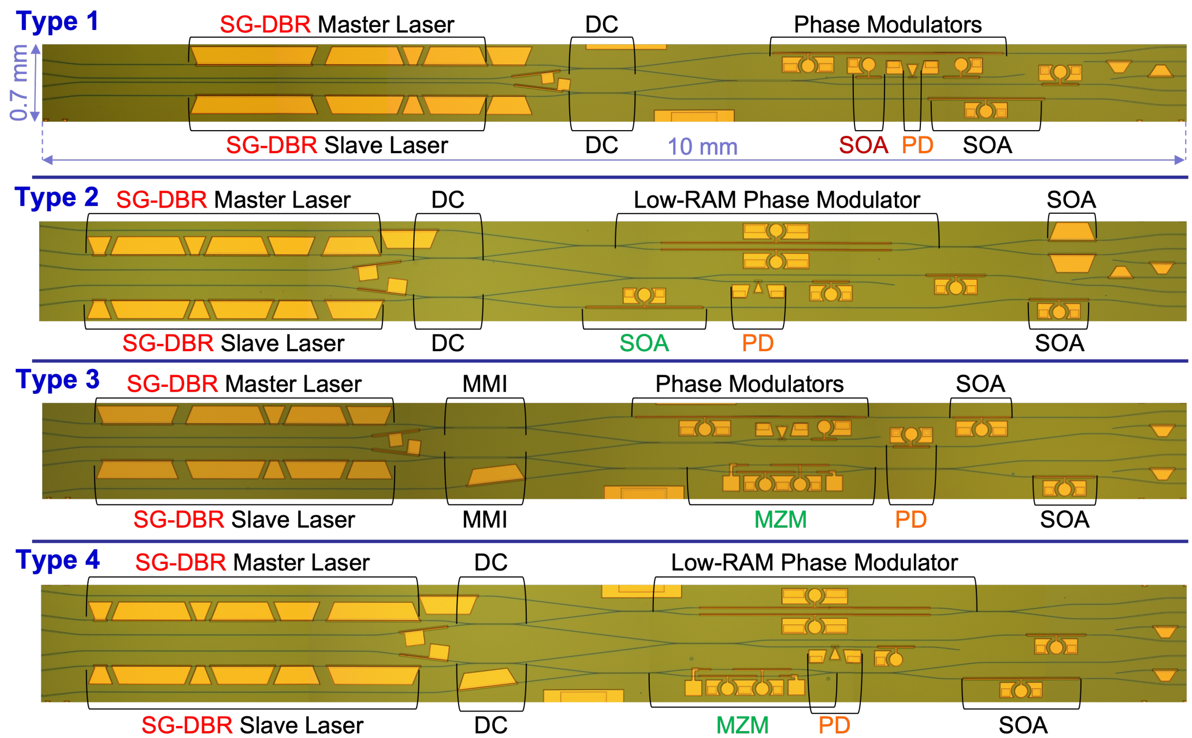

Figure 6.5: Details of different types of fabricated PICs.

Finally, for the third generation, PICs 10 - 16 were designed with the PIC fabrication yield and future PIC packaging in mind. In the third generation, the number of PICs on the mask was increased by 40 % compared with the second generation. The designs can be divided into four types, which are shown in Fig. 6.5. Half of the PICs used the SGDBR laser, straight phase modulator, and SOA pulse generator combination (type 1 design shown above). In addition, a specially designed waveguide taper array was included at the output side of all the PICs. The output waveguides were designed so that they could be cleaved to have either the angled outputs ideal for lab testing or regularly spaced straight outputs for packaging with a fiber array. In the third generation, the PIC fabrication yield improved significantly and the overall sensing experiment was successfully performed using the type 1 PIC. A fully functional PIC enabled a gas sensing experiment in the lab, which is discussed in detail in Chapter 7.

6.3 Conclusion

The new PIC-based architecture was designed based on an existing NASA architecture. Three generations of PICs were designed and fabricated for the new PIC-based architecture. Each generation focused on different aspects of the PIC optimization. The first generation mainly focused on finding the best performing devices for the PIC architecture, so many different types of components were included. In the second generation, PIC components were down selected and optimized based on characterization of the first generation devices. Additionally, more investment was placed in a few PIC architectures that were identified as promising. The third generation focused on PIC architecture optimization, improving the PIC yield, and designing for future PIC packaging. After three generations' iteration of the PIC design and fabrication process, we successfully demonstrated CO_2 active sensing using a fully integrated PIC in a lab environment [12, 13].

Bibliography

[1] K. Numata, J. R. Chen, and S. T. Wu, *Precision and fast wavelength tuning of a dynamically phase-locked widely-tunable laser*, *Optics express* **20** (2012), no. 13 14234–14243.

[2] G. C. Bjorklund, *Frequency-modulation spectroscopy: a new method for measuring weak absorptions and dispersions*, *Optics letters* **5** (1980), no. 1 15–17.

[3] A. Ward, D. Robbins, G. Busico, E. Barton, L. Ponnampalam, J. Duck, N. Whitbread, P. Williams, D. Reid, A. Carter, and M. Wale, *Widely tunable ds-dbr laser with monolithically integrated soa: design and performance*, *IEEE Journal of Selected Topics in Quantum Electronics* **11** (2005), no. 1 149–156.

[4] K. Utaka, S. Akiba, K. Sakai, and Y. Matsushima, *$\lambda/4$-shifted ingaasp/inp dfb lasers*, *IEEE journal of quantum electronics* **22** (1986), no. 7 1042–1051.

[5] A. D. Inc., *Datasheet of ad9858: 1 gsps direct digital synthesizer (rev. c)*, *Analog Devices Inc.*

[6] K. Numata, J. R. Chen, S. T. Wu, J. B. Abshire, and M. A. Krainak, *Frequency stabilization of distributed-feedback laser diodes at 1572 nm for lidar measurements of atmospheric carbon dioxide*, *Applied optics* **50** (2011), no. 7 1047–1056.

[7] J. B. Abshire, H. Riris, G. R. Allan, C. J. Weaver, J. Mao, X. Sun, W. E. Hasselbrack, A. Yu, A. Amediek, Y. Choi, *et. al.*, *A lidar approach to measure co2 concentrations from space for the ascends mission*, in *Lidar Technologies, Techniques, and Measurements for Atmospheric Remote Sensing VI*, vol. 7832, p. 78320D, International Society for Optics and Photonics, 2010.

[8] J. B. Abshire, H. Riris, G. R. Allan, C. J. Weaver, J. Mao, X. Sun, W. E. Hasselbrack, S. R. Kawa, and S. Biraud, *Pulsed airborne lidar measurements of atmospheric co2 column absorption*, *Tellus B: Chemical and Physical Meteorology* **62** (2010), no. 5 770–783.

[9] S. Arafin, A. Simsek, S.-K. Kim, S. Dwivedi, W. Liang, D. Eliyahu, J. Klamkin, A. Matsko, L. Johansson, L. Maleki, *et. al.*, *Towards chip-scale optical frequency synthesis based on optical heterodyne phase-locked loop*, *Optics express* **25** (2017), no. 2 681–695.

[10] M. Chin, *Comparative analysis of the performance limits of franz-keldysh effect and quantum-confined stark effect electroabsorption waveguide modulators*, *IEE Proceedings-Optoelectronics* **142** (1995), no. 2 109–114.

[11] V. Rosborough, J. Fridlander, F. Sang, F. Gambini, S. T. Š. Brunelli, J. R. Chen, S. Kawa, K. Numata, M. Stephen, L. Coldren, *et. al.*, *Residual amplitude modulation reduction in integrated indium phosphide phase modulators*, in *CLEO: Science and Innovations*, pp. STh4B–3, Optical Society of America, 2021.

[12] F. Sang, J. Fridlander, V. Rosborough, S. T. Š. Brunelli, L. Coldren, J. Klamkin, J. Chen, K. Numata, R. Kawa, and M. Stephen, *Integrated photonics technology for earth science remote-sensing lidar*, in *2021 IEEE International Geoscience and Remote Sensing Symposium IGARSS*, pp. 7708–7711, IEEE, 2021.

[13] J. Fridlander, F. Sang, V. Rosborough, F. Gambini, S. T. S. Brunelli, J. R. Chen, K. Numata, M. Stephen, L. A. Coldren, and J. Klamkin, *Dual laser indium phosphide photonic integrated circuit for integrated path differential absorption lidar*, *IEEE Journal of Selected Topics in Quantum Electronics* (2021).

[14] V. Rosborough, J. Fridlander, F. Sang, F. Gambini, S. T. Š. Brunelli, J. R. Chen, S. Kawa, K. Numata, M. Stephen, L. Coldren, *et. al.*, *Photonic integration for low size, weight, and power (swap) remote gas spectroscopy*, in *Optics and Photonics for Sensing the Environment*, pp. ETu6D–2, Optical Society of America, 2021.

[15] J. Fridlander, F. Sang, V. Rosborough, S. T. Š. Brunelli, J. Chen, K. Numata, S. Kawa, M. Stephen, L. Coldren, and J. Klamkin, *Monolithic indium phosphide dual laser photonic integrated circuit for remote sensing lidar*, in *CLEO: Science and Innovations*, pp. JTu3A–89, Optical Society of America, 2021.

[16] K. Prosyk, T. Brast, M. Gruner, M. Hamacher, D. Hoffmann, R. Millett, and K.-O. Velthaus, *Tunable inp-based optical iq modulator for 160 gb/s*, in *European Conference and Exposition on Optical Communications*, pp. Th–13, Optical Society of America, 2011.

[17] Y. Ogiso, J. Ozaki, Y. Ueda, N. Kashio, N. Kikuchi, E. Yamada, H. Tanobe, S. Kanazawa, H. Yamazaki, Y. Ohiso, *et. al.*, *Over 67 ghz bandwidth and 1.5 v $v\pi$ inp-based optical iq modulator with nipn heterostructure*, *Journal of lightwave technology* **35** (2016), no. 8 1450–1455.

Chapter 7

Device and Photonic Integrated Circuit Control

This chapter introduces the device, subsystem and system level control for CO_2 remote sensing. The PIC used for the measurement in this section is shown in Fig. 7.1. It has a dimension of 9500 μm by 750 μm. The PIC uses a straight phase modulator for the leader laser phase modulation, and an SOA for the 1 μs pulse signal generation. First, the PIC's laser tuning, phase modulation, and pulse generation are discussed at the device level. Then, the two subsystem measurements, the leader laser frequency modulation stabilization and follower laser offset phase locking, are introduced and the characterization results are discussed. Finally, the overall CO_2 remote sensing using an external CO_2 test cell for both CW and pulsed sensing conditions in a lab environment is introduced and demonstrated.

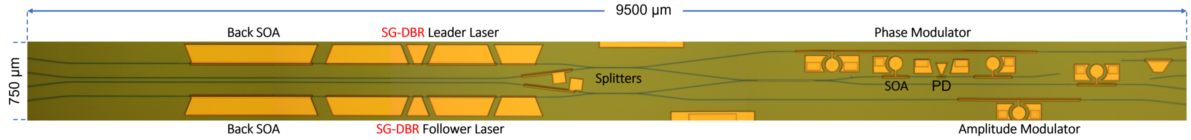

Figure 7.1: Microscope image of fabricated PIC.

7.1 Device Control

This section introduces the device level control of the PIC. The performance of PIC devices key to the sensing operation are presented and these pave the way for the subsystem and overall system level measurements.

7.1.1 SGDBR Laser Control

This section focuses on the tuning and control of the SGBDR laser at the CO_2 absorption peak centered at 1572.335 nm. The PIC used for the CO_2 sensing experiment has the same SGDBR laser design that is discussed in Chapter 4 for both the follower and leader lasers. The tuning and control of the laser is achieved through current injection in the mirrors and phase section, and thermal tuning. Details of each tuning and control mechanism are discussed in this section.

7.1.1.1 Mirror Control

In order to target a lasing wavelength of 1572.335 nm, the mirrors are designed to have a Bragg wavelength at 1574.14 nm, as shown in Fig. 4.8. By controlling the mirrors,

Leader SGDBR Laser					
	backSOA	Back Mirror	Phase	Gain	Front Mirror
Current	120.00 mA	4.32 mA	5.95 mA	120.00 mA	27.00 mA
Voltage	1.940 V	0.914 V	1.406 V	2.139 V	1.549 V
Follower SGDBR Laser					
	backSOA	Back Mirror	Phase	Gain	Front Mirror
Current	OFF	3 mA	4.5 mA	120.00 mA	26.80 mA
Voltage	OFF	0.887 V	1.276 V	2.135 V	1.542 V
Other Compoents on PIC					Temperature settings
	Phase Modulator	SOA before Photodiode	Photodiode	Amplitude Modulator	TEC with 10 KΩ Thermistor
Current	25.00 mA	50.00 mA	-2.99 mA	120.00 mA	11.66 KΩ
Voltage	1.040 V	1.910 V	-3.0 V	1.688 V	21.6 °C *
* Temperature settings in °C is converted from resistance with following formula and comsunptions: Rset=R0*exp-B*((1/273+Tref)-(1/273+Tset)), with B=4000, Tref=25 °C with R0=10 KΩ					

Table 7.1: PIC settings to tune the leader and follower laser to 1572.335 nm together.

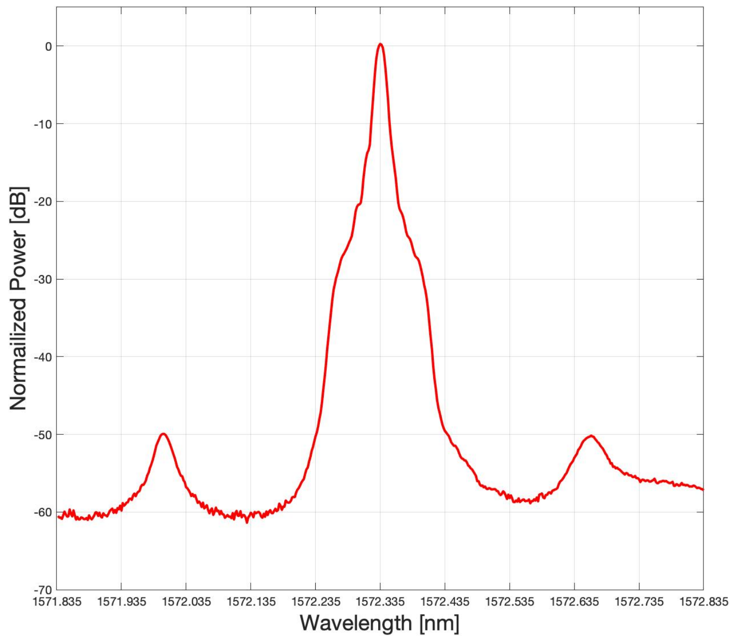

Figure 7.2: Spectrum of leader laser tuned to 1572.335 nm.

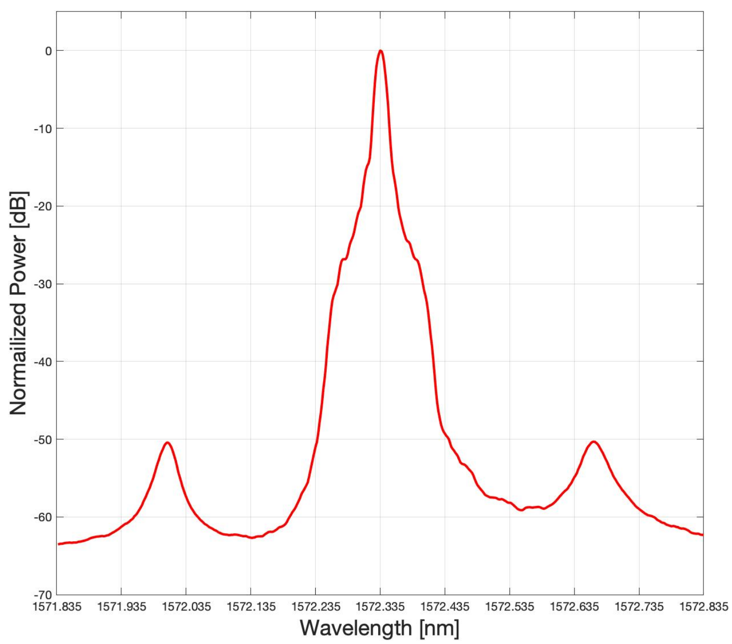

Figure 7.3: Spectrum of follower laser tuned to 1572.335 nm.

phase section and stage temperature, the leader and follower lasers are successfully tuned to 1572.335 nm at the same time. The detailed parameter settings are shown in Table

7.1 and the optical spectra for leader laser and follower laser are shown in Fig. 7.2 and Fig. 7.3.

7.1.1.2 Phase Control

In order to show that the SGDBR lasers can achieve up to a 20 GHz tuning range centered at 1572.335 nm through phase tuning alone, the phase tuning of both leader and follower lasers was characterized. By tuning the phase section of each laser, the leader and follower lasers successfully achieved a 20 GHz or greater tuning range around 1572.335 nm. In Fig. 7.4, the leader laser is tuned over a full phase tuning cycle by injecting current from 0 to 10 mA. The laser provides a tuning range of 37.6 GHz with corresponding wavelengths from 1572.225 nm to 1572.535 nm and a minimum SMSR of 31 dB. In Fig.7.5, the follower laser is tuned over a full phase tuning cycle by injecting current from 0 to 11 mA. The follower laser tuning range was 38.2 GHz from 1572.171 nm to 1572.487 nm with a 37 dB minimum SMSR.

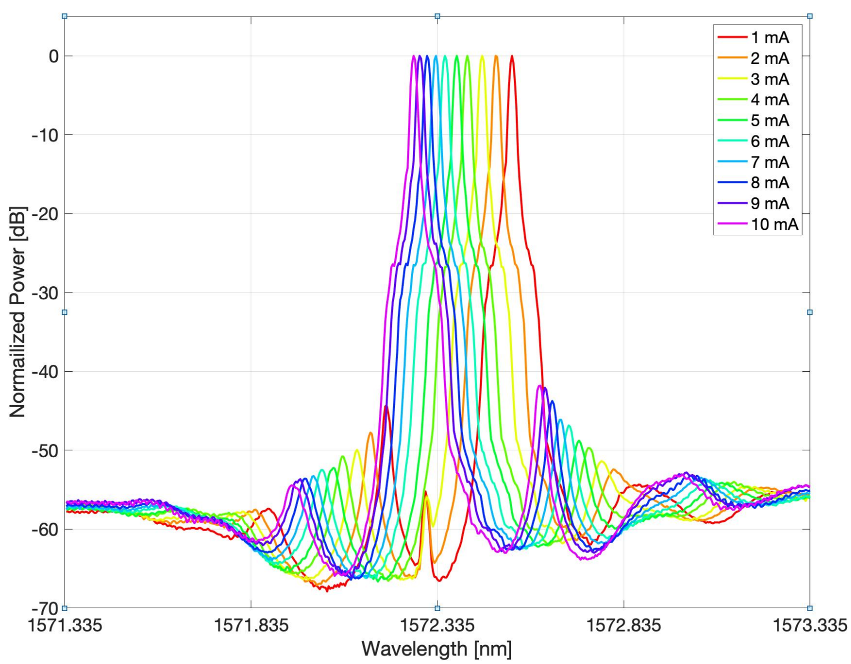

Figure 7.4: Phase tuning spectra of leader laser.

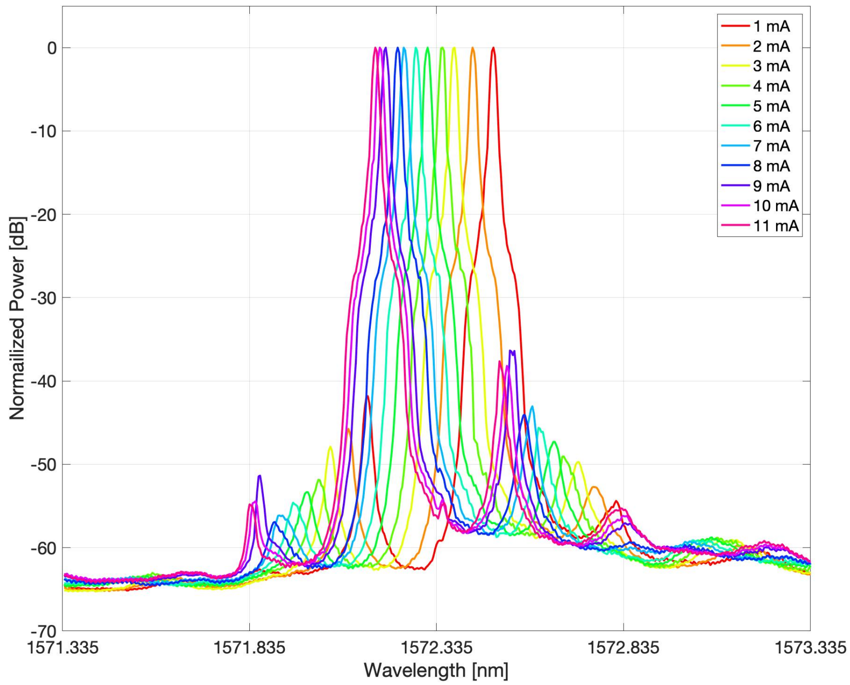

Figure 7.5: Phase tuning spectra of follower laser.

7.1.1.3 Thermal Control

The InP material is very sensitive to thermal effects [1]. The thermal characteristics of the leader laser were measured. The spectrum was recorded from 10 °C (283.15 K) to 40 °C (313.15 K). The leader laser is thermally tuned from 1571.044 nm to 1574.38 nm with a 45 dB minimum SMSR. The spectra are shown in Fig. 7.6.

Thermal tuning under the same conditions was also characterized for the follower laser. In Fig. 7.7, the spectrum of follower laser with stage temperature is shown. The wavelength is tuned from 1571.032 nm to 1574.372 nm with a minimum SMSR of 42 dB.

Degradation in the laser power with an increase in temperature is observed for both lasers. This is because as the temperature increases the threshold current I_{th} also increases, and the differential quantum efficiency η_d decreases [2].

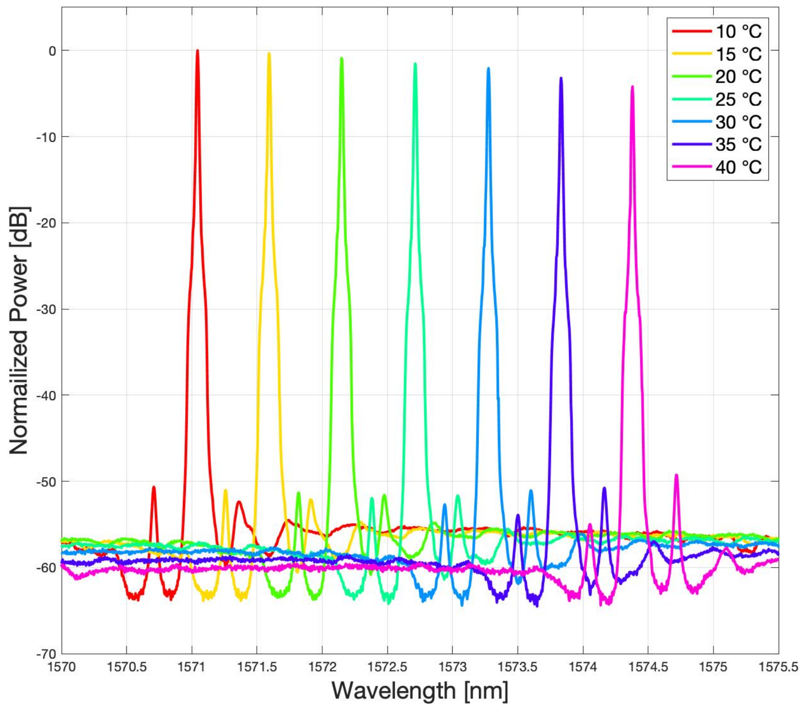

Figure 7.6: Thermal tuning spectra of leader laser.

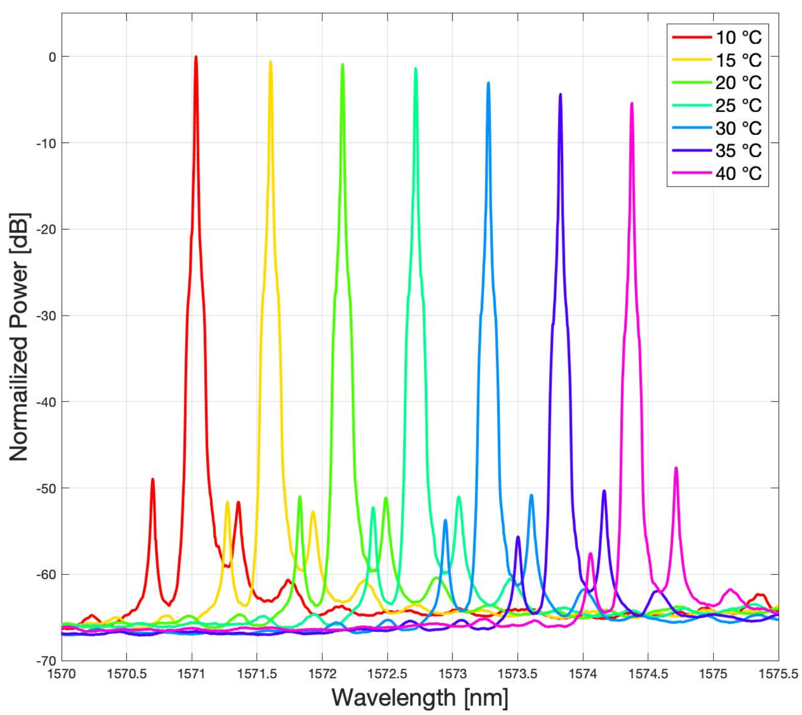

Figure 7.7: Thermal tuning spectra of follower laser.

7.1.2 Phase Modulation

A 2 mm-long straight phase modulator was used in the PIC. The phase modulator modulates the phase of the leader laser output at a frequency of 125 MHz. The modulated output signal is used for locking the leader laser to the CO_2 reference cell for stabilization at 1572.335 nm. The phase modulator in the PIC under test was characterized at different biases and modulation frequencies.

First, the loss of the 2 mm straight phase modulator on the PIC was characterized under forward and reverse bias conditions. Under forward bias, the loss characteristic is shown in Fig. 7.8, which shows a 10 dB loss at 98 mA injection current. Under reverse bias, the loss characteristic is shown in Fig. 7.9, which shows a 9.5 dB loss at -8 V reverse bias voltage.

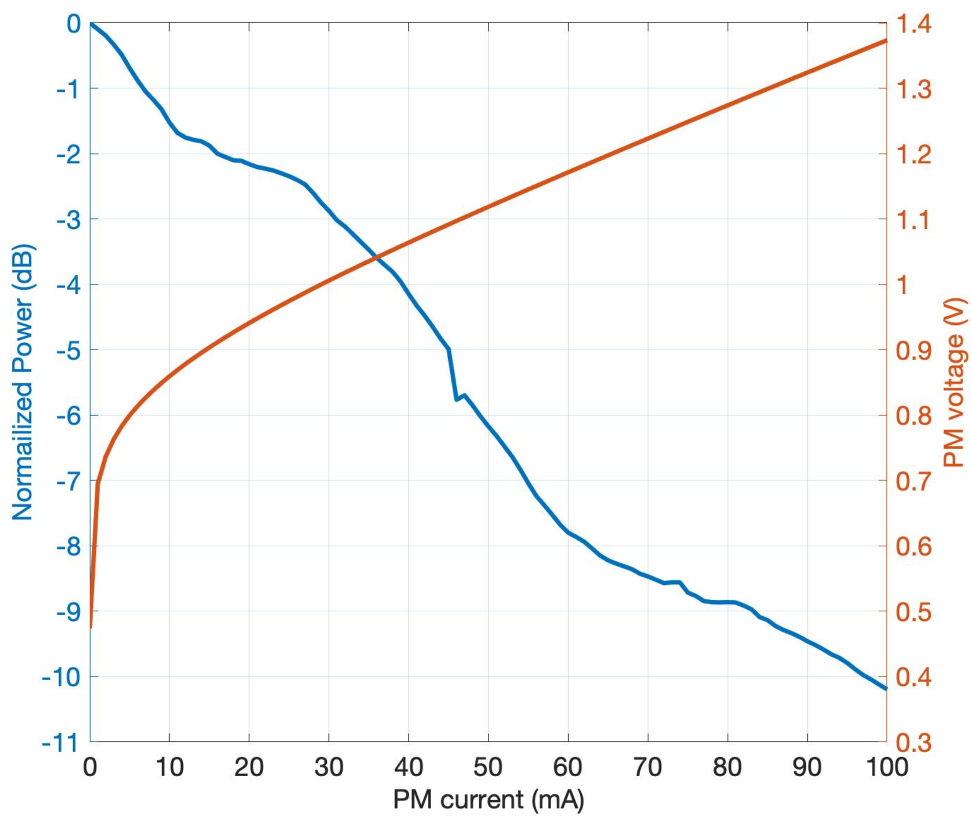

Figure 7.8: Power-current-voltage characterization of forward biased PM.

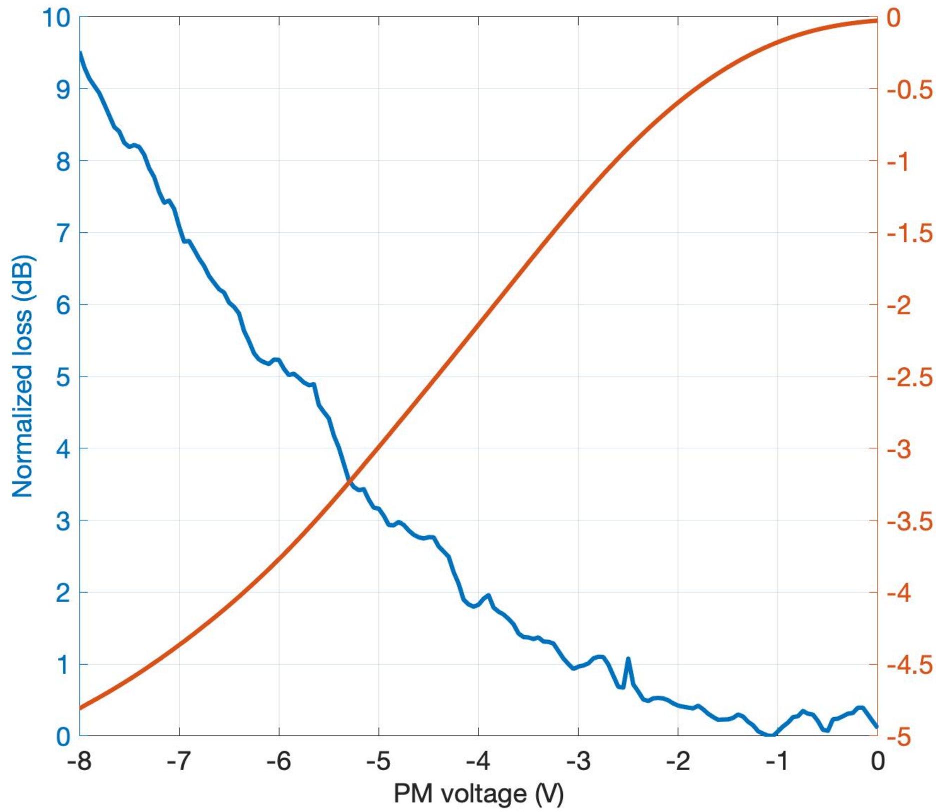

Figure 7.9: Loss-current-voltage characterization of reverse biased PM.

Based on the phase modulator efficiency characteristics obtained in the lab, forward bias modulation has a better efficiency and lower residual amplitude modulation (RAM) compared to reverse bias modulation. Although a higher loss was measured in forward bias, the phase modulation is also more efficient in forward bias, so the loss incurred for a pi phase shift is less in forward bias than in reverse bias. In order to achieve the best efficiency and RAM using the straight phase modulator, a 25 mA forward bias current with -7 dBm modulation power is used for the PIC's phase modulation in the following subsystem and system level measurement.

The modulated signal after the CO_2 cell is shown below in Fig. 7.10 for different phase modulation frequencies. From the measurement, the phase modulator works from 50 MHz to 200 MHz. However, the signal is distorted severely at 50 MHz and also slightly at 200

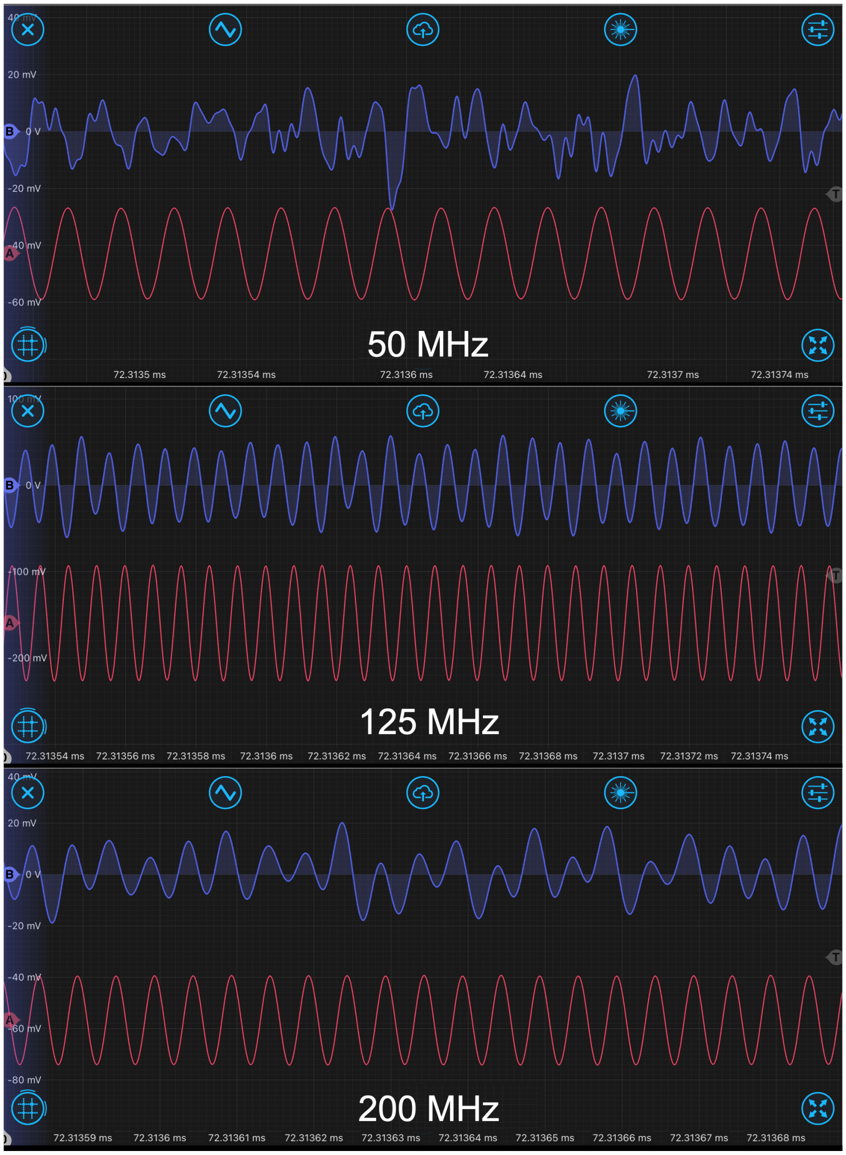

Figure 7.10: Modulated phase signal after CO_2 cell at different frequencies with 25 mA forward bias and -7 dBm modulation signal; red lines are modulation signals from signal generator, and blue lines are modulated signals received after CO_2 cell.

MHz. At lower modulation frequencies, the modulated phase signal does not dominate the phase change at that modulation frequency. Instead, noise from other components are mixed with the modulated phase signal, which makes the modulated signal distorted. After the signal passes through the CO_2 cell, which works as a frequency discriminator, it is hard to extract the error signal from the distorted signal. At a frequency higher than

200 MHz, the modulation efficiency decreases due to the speed of the phase modulation mechanisms in forward bias. A stronger modulation signal could be used, but it would increase the RAM of the phase modulator. In order to optimize the overall system performance, 125 MHz modulation frequency was chosen for the subsequent subsystem and system level measurements.

7.1.3 Pulse Generation

The remote sensing requires a pulsed output with 1 μs pulse width and 134 μs period as the final output from the PIC. Generating a high extinction ratio output pulse signal is also very important for the PIC. In Chapter 6, many kinds of topology for pulse generation were discussed in detail. In the PIC under test, as shown in Fig. 7.1, a 1 mm long SOA is used to carve the CW signal into the required pulse signal. The speed and extinction ratio of the SOA are characterized and discussed below.

In Fig. 7.11, the speed of the SOA is characterized. A pulsed signal with a width from 0.1 μs to 1 μs is injected into the SOA, and the output signal is measured using an external high-speed photodetector. From the results, the minimum achievable pulse width for the SOA is $\sim$0.2 μs. This is mainly caused by large parasitic capacitance for such a long device, which limits the high speed performance of the SOA. This can be seen in Fig. 4.20, where the bandwidth of SOA as a function of its length is simulated. For a 1000 μm long SOA, the simulated bandwidth is around 600 MHz. In addition, the extinction ratio of the SOA from 0 mA to 150 mA with 1μs pulse width is shown in Fig. 7.12. The SOA shows a 45 dB extinction ratio from 0 mA to 150 mA with 1μs pulse width. The rising time of the signal is 62.4 ns, and the falling time of the signal is 87.6 ns.

A comparison between the input electrical pulse signal and output optical pulse signal

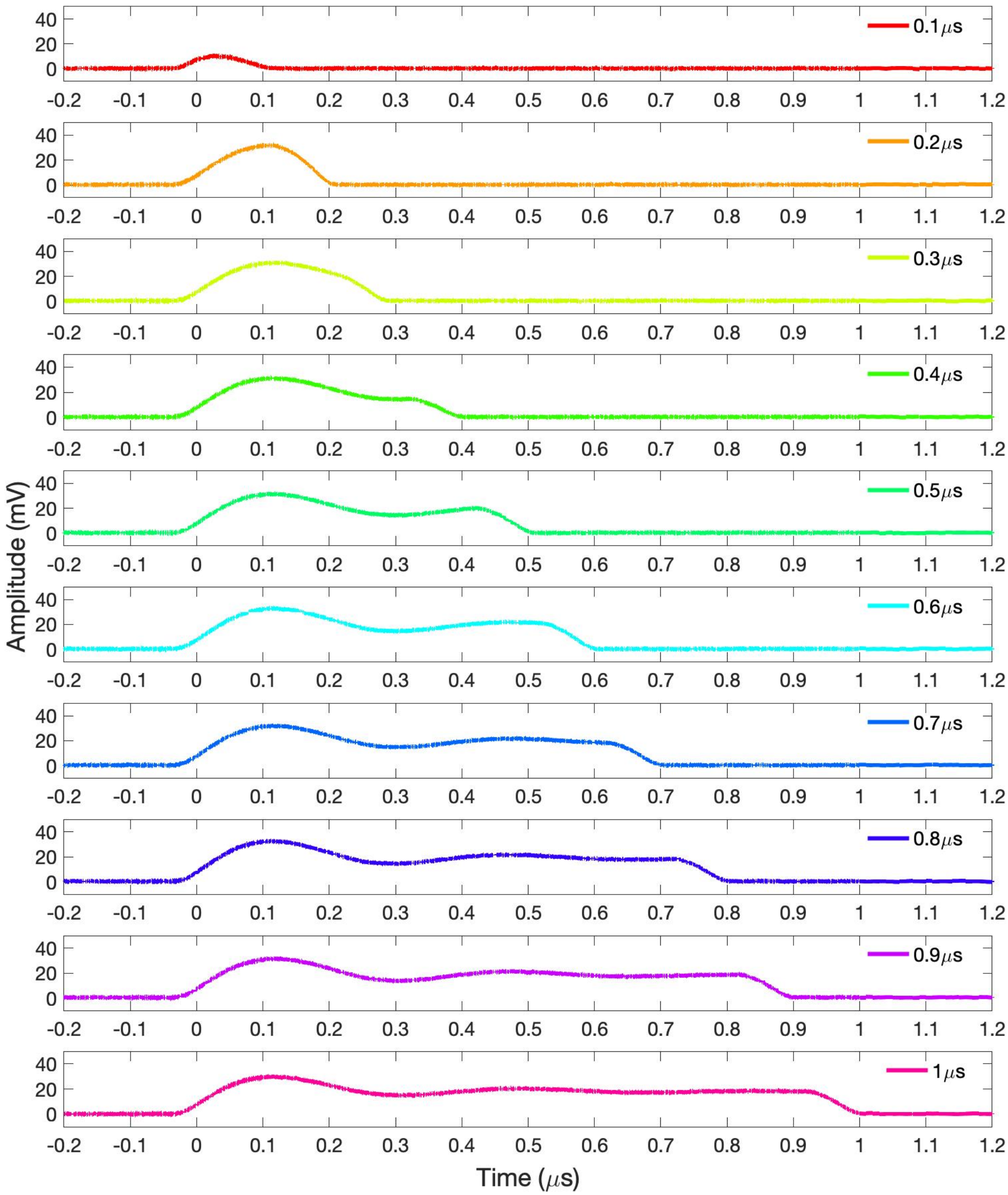

Figure 7.11: Generated pulse signal from 0.1 μs to 1 μs from 0 mA to 150 mA.

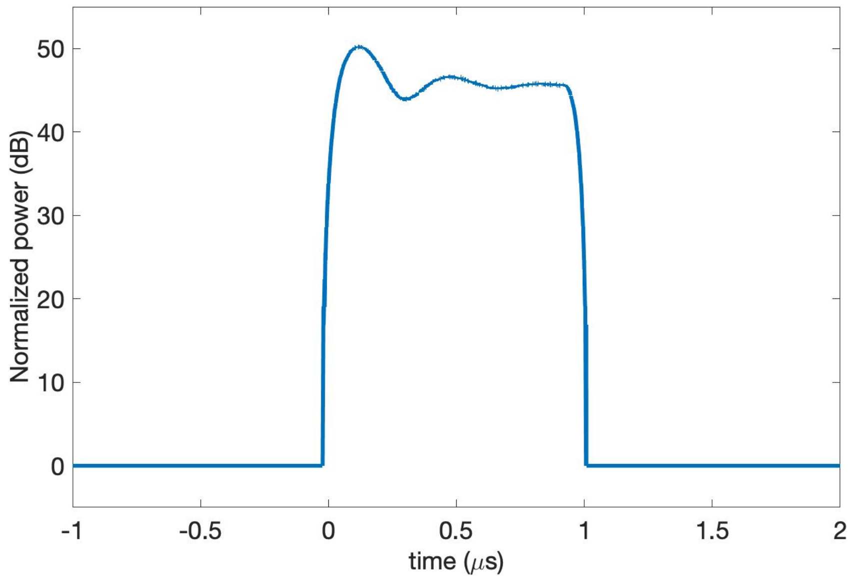

Figure 7.12: Optical output pulse signal from 0 mA to 150 mA with 1 μs pulse width in dB.

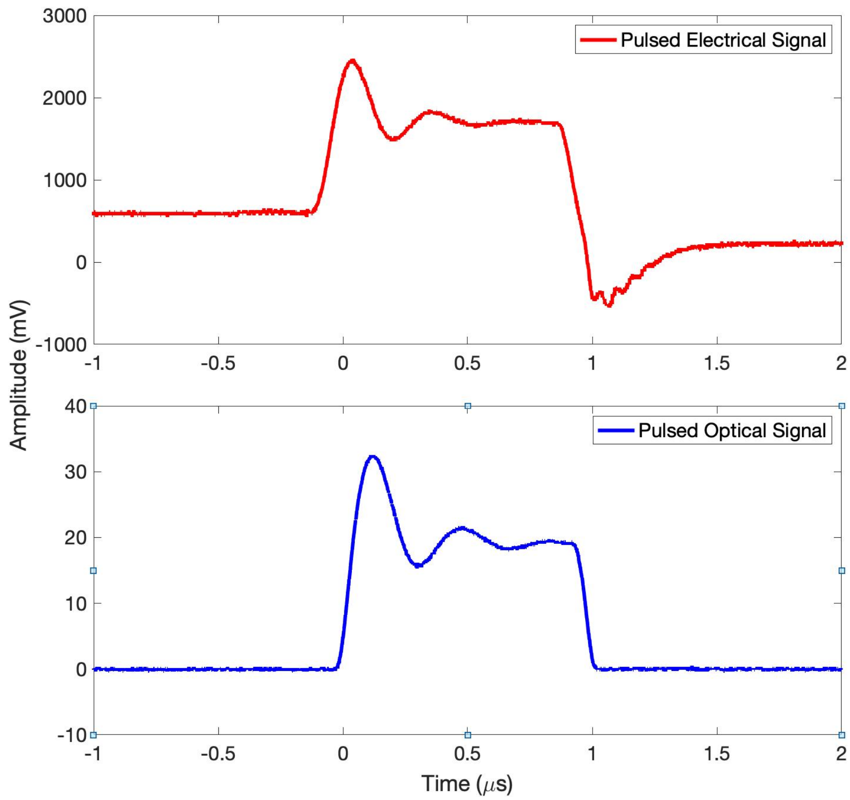

Figure 7.13: Input electrical pulse and output optical pulse signal from 0 mA to 150 mA with 1 μs pulse width.

is shown in Fig. 7.13. It shows that the overshot is mostly caused by the electrical signal instead of the SOA's over-damped response.

7.2 Subsystem PIC Control

The subsystem PIC measurements are introduced in this section. They include two main parts: the leader laser frequency stabilization and the follower laser offset phase locking. The leader laser frequency stabilization locks the leader laser to the peak of the CO_2 absorption line using an external CO_2 reference cell. The follower laser offset phase locking locks the follower laser to the leader laser using the integrated photodiode through an OPLL. Both locking systems need an error or feedback signal to establish the stabilization and offset locking. The overall settings on the PIC for the subsystem level measurements are shown in Table 7.2, where both lasers are tuned slightly off the target wavelength on purpose.

Leader SGDBR Laser					
	backSOA	Back Mirror	Phase	Gain	Front Mirror
Current	120.00 mA	3.20 mA	5.20 mA	120.00 mA	26.00 mA
Voltage	1.940 V	0.886 V	1.359 V	2.146 V	1.526 V
Follower SGDBR Laser					
	backSOA	Back Mirror	Phase	Gain	Front Mirror
Current	OFF	0.60 mA	5.60 mA	120.00 mA	26.80 mA
Voltage	OFF	0.786 V	1.358 V	2.149 V	1.542 V
Other Compoents on PIC					**Temperature settings**
	Phase Modulator	SOA before Photodiode	Photodiode	Amplitude Modulator	TEC with 10 KΩ Thermistor
Current	25.00 mA	50.00 mA	-2.739 mA	120.00 mA	11.66 KΩ
Voltage	1.035 V	1.910 V	-3.000 V	1.679 V	21.6 °C *
* Temperature settings in °C is converted from resistance with following formula and comsunptions: Rset=R0*exp-B*((1/273+Tref)-(1/273+Tset)), with B=4000, Tref=25 °C with R0=10 KΩ					

Table 7.2: PIC settings for subsystem level measurements.

7.2.1 Leader Laser Frequency Stabilization

The leader laser frequency stabilization is used to lock the frequency of the leader laser to the center of the absorption line at 1572.335 nm. A diagram of the test setup is shown in Fig. 7.14. The locking is achieved by modulating the phase of the laser output at 125 MHz using the phase modulator. Then, an error signal is generated using a mixer to extract the frequency difference between the local oscillator (LO) and the detected signal after the CO_2 reference cell. The error signal is processed using PID control, and sent back to the phase section of the leader laser to achieve frequency stabilization. Overall, we achieved a 2.75 MHz peak to peak drift over a 2 hour locking measurement and a standard deviation of 0.45 MHz, representing a stability improvement of 23 dB compared with the unlocked laser.

7.2.1.1 Frequency Stabilization Mechanism

The detailed mechanism of the leader laser frequency stabilization is shown in Fig. 7.15. Before starting the stabilization, the leader laser is tuned to $\sim$ 1572.335 nm using the settings in Table. 7.2. Then, based on the discussion in Chapter 7.1.2, the 2 mm straight phase modulator is forward biased at 25 mA and modulated with a -7 dBm signal

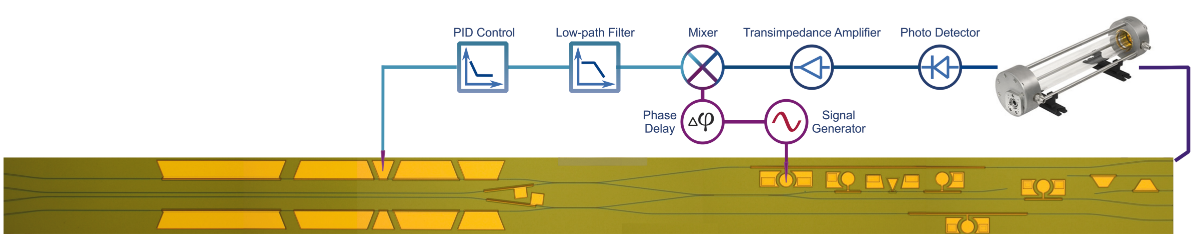

Figure 7.14: Leader laser frequency stabilization Mechanism.

at 125 MHz. The modulated signal is sent through the CO_2 Herriott reference cell where the photodetector and trans-impedance amplifier (TIA) are embedded on the output PCB. Then, a Moku:lab laser locking box (an instrument from Liquid Instruments) is used, which includes the functions of mixer, low-path filter and PID control. The output signal is processed in the laser locking box to generate an error signal. Then the error signal is sent to the modulation channel of the phase section's current supply. Finally, the error signal is converted to the voltage signal with a transfer function of 2.5 mA/V.

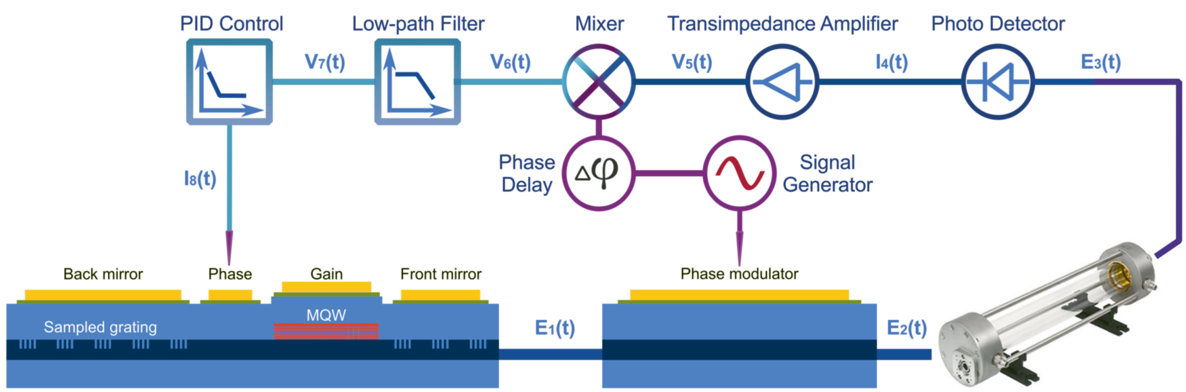

Figure 7.15: Leader laser frequency stabilization Mechanism in detail.

The detailed mathematical model of the locking control loop is described below. By assuming that the laser is a single frequency laser generating radiation at the optical carrier frequency ω_c, the $E_1(t)$ can be expressed as Eq. 7.1.

$$E_1(t) = E_0\, e^{j\omega_c t} + c.c. \tag{7.1}$$

The phase modulator is driven by a sinusoidal RF field at ω_m, which is 125 MHz for this measurement. Since the modulated signal is applied on the E_1 as a Bessel function, the phase modulated electric field E_2 can be described by Eq. 7.2, where M is the modulation index and the J_n is the n^{th} order Bessel function.

$$E_2(t) = E_1 \sum_{-\infty}^{\infty} J_n(M)\, e^{jn\omega_m t} + c.c. = E_0 \sum_{-\infty}^{\infty} J_n(M)\, e^{j(\omega_c + n\omega_m)t} + c.c. \tag{7.2}$$

Depending on the modulation depth, a different n^{th} order Bessel function will be the strongest order. Since we are modulating the phase modulator with a relatively low modulation depth, we can assume that $M << 1$, and $J_0(M) \cong 1$, $J_{\pm1}(M) = \pm M/2$. This makes the first three order terms the main terms. All other terms are small and will vanish out quickly, so they can be ignored. Then, $E_2(t)$ is simplified to Eq. 7.4.

$$E_2(t) = E_0\, [\, J_{-1}(M) e^{j(\omega_c - \omega_m)t} + J_0(M) e^{j\omega_c t} + J_{+1}(M) e^{j(\omega_c + \omega_m)t}\,] + c.c. \tag{7.3}$$

$$E_2(t) = E_0\, e^{j\omega_c t}\, [\, -\frac{M}{2} e^{-j\omega_m t} + 1 + \frac{M}{2} e^{+j\omega_m t}\,] + c.c. \tag{7.4}$$

The $E_2(t)$ is passed through the CO_2 Herriott reference cell, which works as a frequency discriminator. We assume the CO_2 cell has a path length of L, and its intensity-absorption coefficient α and index of refraction η are frequency dependent. The frequency dependent amplitude attenuation and phase shift can be expressed as Eq. 7.5, where $n = -1, 0, 1$ corresponds to the first three order of the Bessel function with a frequency at $\omega_c - \omega_m$, ω_c, and $\omega_c + \omega_m$.

$$\delta_n = \alpha_n L \qquad\qquad \varphi_n = \eta_n L(\omega_x + n\omega_m)/c \tag{7.5}$$

In order to represent the attenuation and phase change at each frequency, we can use the quantity T_n to represent the corresponding changes at each order, where T_n is defined in Eq. 7.6. The transmitted field $E_3(t)$ can be described as Eq. 7.23.

$$T_n = e^{-\delta_n - j\varphi_n} \tag{7.6}$$

$$E_3(t) = T_n E_2(t) = E_0\, e^{j\omega_c t}\,[-\frac{T_{-1}M}{2}e^{-j\omega_m t} + T_0 + \frac{T_1 M}{2}e^{+j\omega_m t}\,] + c.c. \tag{7.7}$$

The current generated from the photodetector can be calculated through its responsivity R, where $I_4(t) = R\,|E_3(t)|^2$. If we expand it by dropping all the imaginary terms and M^2 terms since $M << 1$, we can get the Eq. 7.8.

$$\begin{aligned} I_4(t) = R\,E_0^2\,e^{-2\delta_0}\,\{\,1 + [\,e^{\delta_0-\delta_1}cos(\varphi_1-\varphi_0) - e^{\delta_0-\delta_{-1}}cos(\varphi_0-\varphi_{-1})]\,M\,cos(\omega_m t) \\ +[\,e^{\delta_0-\delta_1}sin(\varphi_1-\varphi_0) - e^{\delta_0-\delta_{-1}}sin(\varphi_0-\varphi_{-1})]\,M\,sin(\omega_m t)\,\} \end{aligned} \tag{7.8}$$

We can assume $|\delta_0 - \delta_{-1}|$, $|\delta_0 - \delta_1|$, $|phi_0 - \varphi_{-1}|$, and $|phi_1 - \varphi_0|$ are much smaller than 1, which is true for weak absorption and weak dispersion. Using the small angle approximation $sin(x) \approx x$, $cos(x) \approx 1 - x^2/2 \approx 1$, and the small value linear approximation of the complicated exponential function, $e^x \approx 1 + x$, Eq. 7.8 can be further simplified. It becomes Eq. 7.10.

$$\begin{aligned} I_4(t) = R\,E_0^2\,e^{-2\delta_0}\,\{\,1 + [\,e^{\delta_0-\delta_1} - e^{\delta_0-\delta_{-1}}]\,M\,cos(\omega_m t) \\ +[\,e^{\delta_0-\delta_1}(\varphi_1-\varphi_0) - e^{\delta_0-\delta_{-1}}(\varphi_0-\varphi_{-1})]\,M\,sin(\omega_m t)\,\} \end{aligned} \tag{7.9}$$

$$\begin{aligned} I_4(t) = R\,E_0^2\,e^{-2\delta_0}\,\{\,1 + [\,(1+\delta_0-\delta_1) - (1+\delta_0-\delta_{-1})]\,M\,cos(\omega_m t) \\ +[\,(1+\delta_0-\delta_1)(\varphi_1-\varphi_0) - (1+\delta_0-\delta_{-1})(\varphi_0-\varphi_{-1})]\,M\,sin(\omega_m t)\,\} \end{aligned} \tag{7.10}$$

Since φ_n and δ_n are small values, we can further assume any $\varphi_n \delta_n$ terms are much smaller than φ_n and δ_n terms. So, we can neglect all the $\varphi_n \delta_n$ terms to further simplify the Eq. 7.10, and it becomes Eq. 7.11.

$$I_4(t) = R\,E_0^2\,e^{-2\delta_0}\,[\,(\delta_{-1} - \delta_1)\,M\,cos(\omega_m t) + (\varphi_1 + \varphi_{-1} - 2\varphi_0)\,M\,sin(\omega_m t)\,] \tag{7.11}$$

Then, a TIA is used to convert the current signal to voltage signal If we use a quantity G to represent the transfer function of the TIA, then $V_5(t) = GI_4(t)$.

$$V_5(t) = G\,R\,E_0^2\,e^{-2\delta_0}\,[\,(\delta_{-1} - \delta_1)\,M\,cos(\omega_m t) + (\varphi_1 + \varphi_{-1} - 2\varphi_0)\,M\,sin(\omega_m t)\,] \tag{7.12}$$

The $V_5(t)$ is mixed with the local oscillator signal $sin(\omega_{LO}(t) + \Delta\varphi_{LO})$ to form $V_6(t)$. Ideally, the ω_{LO} should be equal to ω_m, but the laser is not an ideal source in the real world and the lasing frequency will drift slightly as a function of time. Since an ideal source is assumed in the mathematical model, the real laser signal would be equivalent to adding an external time dependant frequency drift signal to ω_m. Here we separate it from the laser source term to avoid confusion. Since the phase delay is adjustable, we can assume the $V_5(t)$ and LO signal are in-phase with each other. The mixed signal $V_6(t)$ becomes Eq. 7.13, and it can be expanded to Eq. 7.14.

$$V_6(t) = V_5(t) * sin(\omega_{LO} t) \tag{7.13}$$

$$V_6(t) = G\,R\,E_0^2\,e^{-2\delta_0}\,[\,(\delta_{-1} - \delta_1)\,M\,cos(\omega_m t) + (\varphi_1 + \varphi_{-1} - 2\varphi_0)\,M\,sin(\omega_m t)\,] * sin(\omega_{LO} t) \tag{7.14}$$

For convenience, we define the quantities

$$A = G\,R\,M\,E_0^2\,e^{-2\delta_0} \tag{7.15}$$

$$\delta_{-1} - \delta_1 = \Delta\delta \tag{7.16}$$

$$\varphi_1 + \varphi_{-1} - 2\varphi_0 = \Delta\varphi \tag{7.17}$$

If we further expand $V_6(t)$ out using the quantities defined above, we can observe that there will be three main frequency terms at $-\omega_{LO}$, $\omega_m - \omega_{LO}$, and $\omega_m + \omega_{LO}$. The negative frequency can be neglected since it's not real. Then the $\omega_m + \omega_{LO}$ term is filtered out using a low-path filter. Finally, only the signal $V_7(t)$ containing the $\omega_m - \omega_{LO}$ term is left. By applying the above conditions, the simplified $V_6(t)$ is shown in Eq. 7.18.

$$V_6(t) = A\,[\,\Delta\delta\,cos((\omega_m - \omega_{LO})t) + \Delta\varphi\,sin((\omega_m - \omega_{LO})t)\,] \tag{7.18}$$

At last, the $V_6(t)$ signal goes into a proportional-integral-derivative (PID) controller. Then the processed signal is sent to the modulation channel of the current supply with a transfer function of H which is 2.5 mA/V. The overall control function of the PID controller is shown in Eq. 7.19, where K_p, K_i, and K_d are non-negative coefficients for the proportional, integral, and derivative terms respectively [3]. The final output signal

$I_8(t)$ is Eq. 7.20.

$$u(t) = K_p\,e(t) + K_i \int_0^t e(\tau)\,dx + K_d \frac{\partial e(t)}{\partial t} \tag{7.19}$$

$$I_8(t) = H\{\,K_p\,V_6(t) + K_i \int_0^t V_6(\tau)\,dx + K_d \frac{\partial V_6(t)}{\partial t}\,\} \tag{7.20}$$

Overall, from this mathematical model, we can observe a relation between the laser frequency and error signal as shown in Fig. 7.16. When the laser is not at the peak of the absorption line, an in-phase error signal is generated which tunes the laser toward the center. When the laser is at the peak of the absorption line, where $\omega_m = \omega_{LO}$, the in

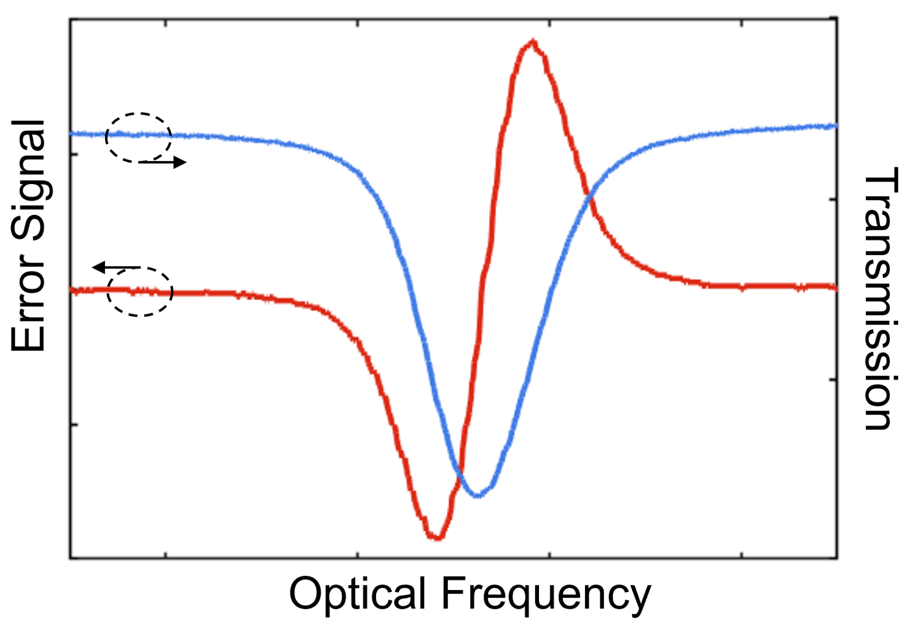

Figure 7.16: In phase error signal.

phase error signal becomes zero.

7.2.1.2 Frequency Stabilization Performance

The frequency stabilization results and performance are summarized in this section. During the frequency stabilization, the laser is successfully locked to the CO_2 absorption peak at 1572.335 nm. The leader laser fiber-coupled output power is around -5 dBm with the phase modulator forward biased at 25 mA and modulated at -7 dBm with a 125 MHz modulation frequency. The optical spectrum was recorded and is shown in Fig

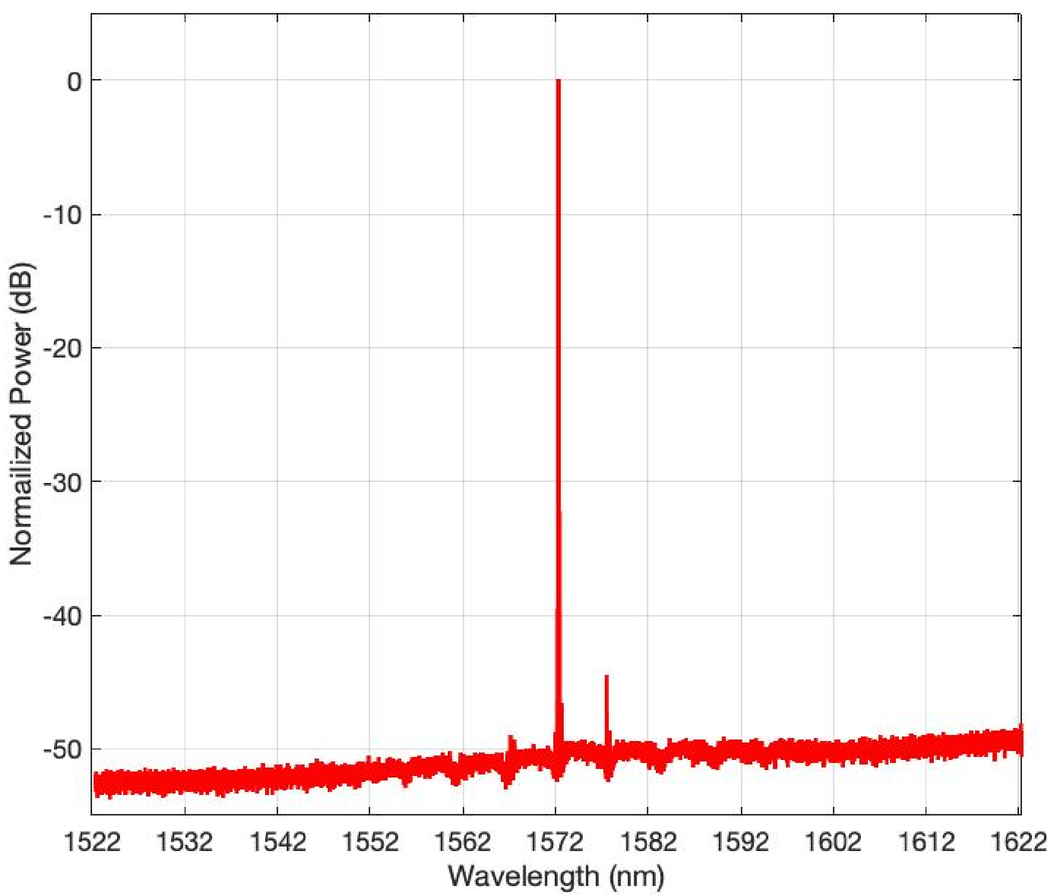

Figure 7.17: Normalized optical spectrum of leader laser locked to the CO_2 with 100 nm span absorption center at 1572.335 nm.

.7.17 and Fig .7.18, with a 100 nm and 1 nm wavelength span, respectively.

The spectrum with a 100 nm span shows that the leader laser is single frequency over the whole range with a side mode suppression ratio (SMSR) of 44.5 dB. The 1 nm span spectrum shows the lasing wavelength after the laser is locked to the CO_2 cell, with an absorption peak at exactly 1572.335 nm and a 46.5 dB SMSR.

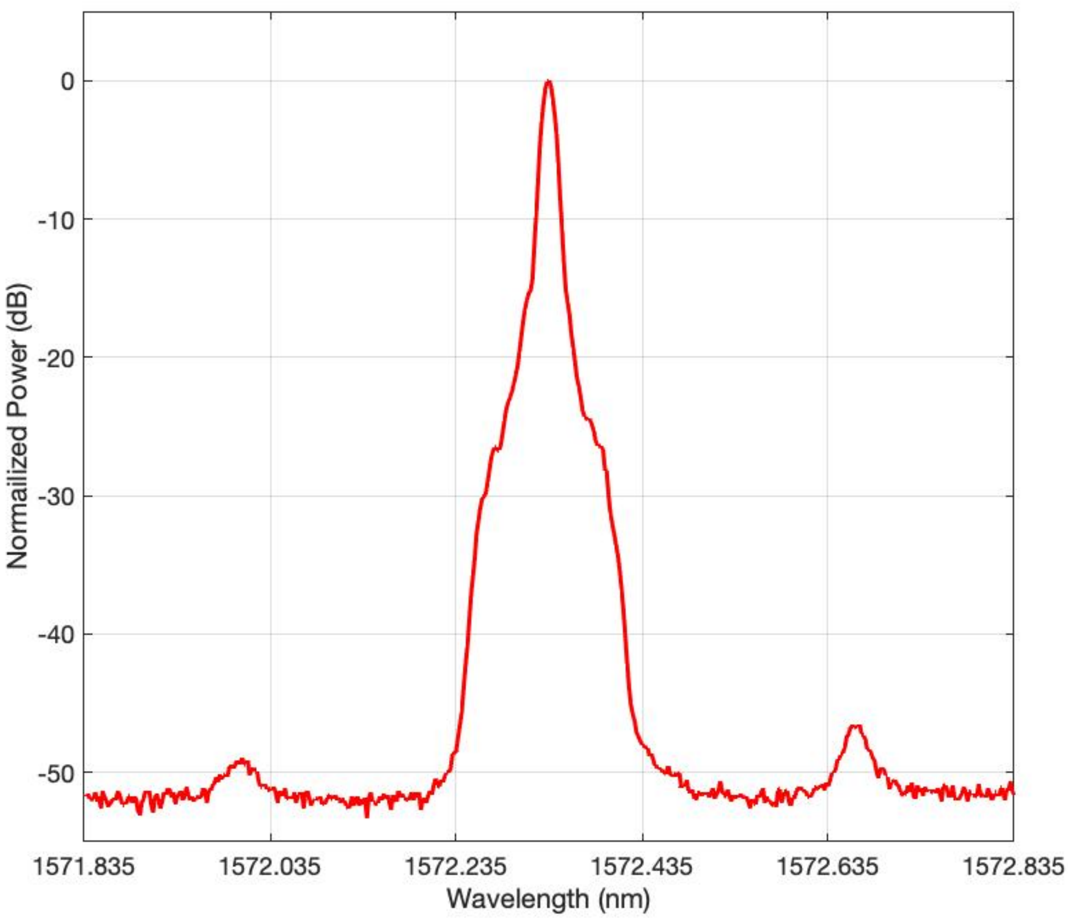

Figure 7.18: Normalized optical spectrum of leader laser locked to the CO_2 with 1 nm span absorption center at 1572.335 nm.

The linewidths of unlocked and locked leader laser output are measured using a delayed self-heterodyne technique. The linewidth of unlocked leader laser output is 0.935

MHz as shown in Fig. 7.19. The linewidth of the locked leader laser is 1.692 MHz and is shown in Fig. 7.20. Both linewidths are measured using the following conditions: 5 μs swept time, 2 MHz resolution bandwidth, and a 20 KHz video bandwidth. All the integrated components on the PIC were set using the parameters shown in Table 7.2. The linewidth is broadened by 80% when the locking system turns on, but 1.692 MHz linewidth still satisfies NASA's minimum requirement of less than 50 MHz for a 15 μs sweep time [4–7].

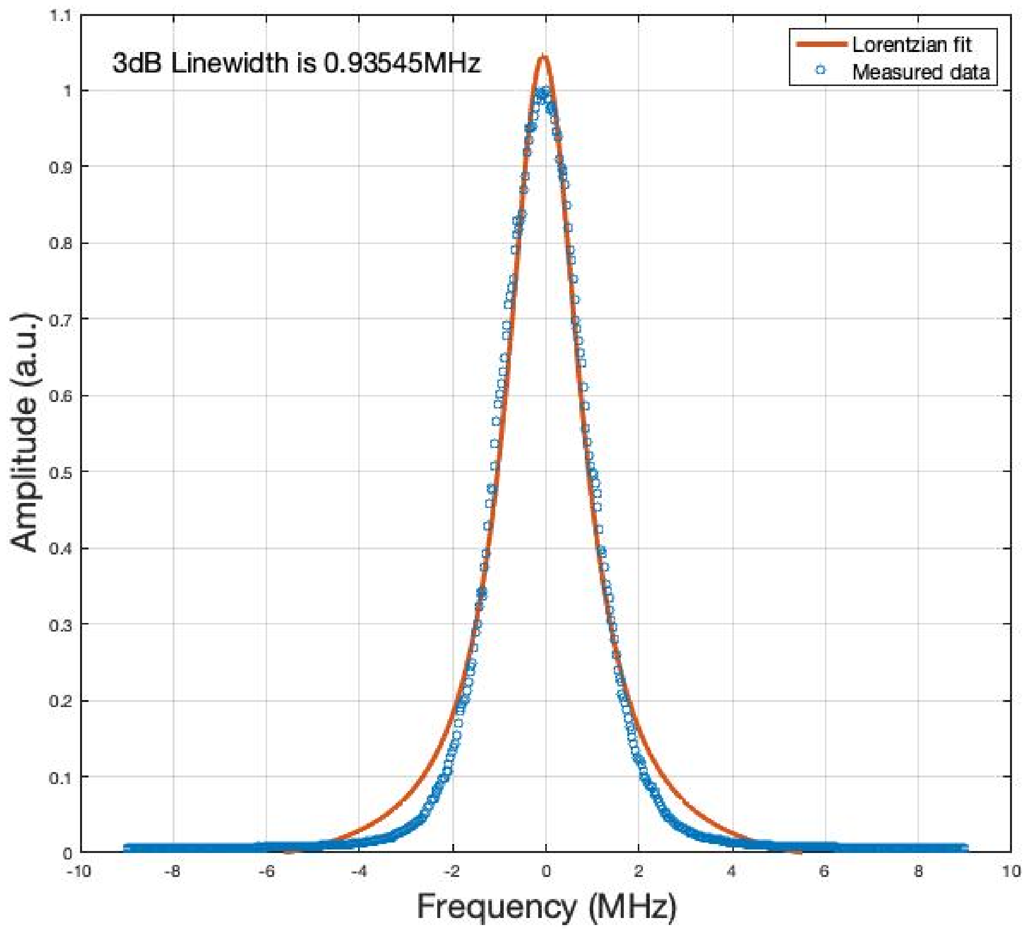

Figure 7.19: Unlocked leader side output linewidth with Lorentzian fit.

Next, the frequency stabilization performance of the leader laser output is charac-

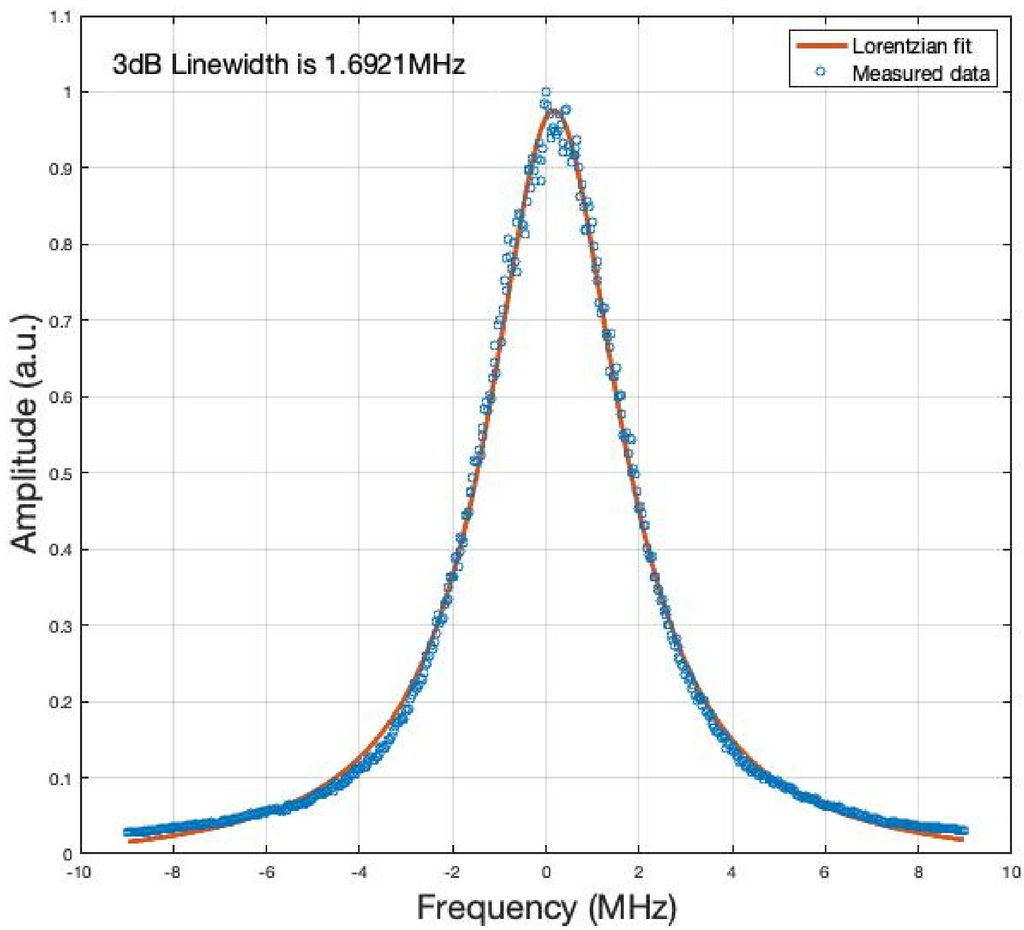

Figure 7.20: Locked leader side output linewidth with Lorentzian fit.

terized by measuring a beat note signal with a commercial external cavity laser (ECL). First, the ECL is tuned to roughly 1 GHz away from 1572.335 nm. Then, the leader laser output is mixed with the ECL output using an external 50 % - 50 % directional coupler. An external photodiode and driver amplifier are used to detect and amplify the beat note signal between the leader laser output and the ECL output. Finally, the beat note frequency drift is recorded using a frequency counter with 1 s gate time.

Data taken over two hours and eight hours was recorded to show the performance of the frequency stabilization. In the lab, the locking system is able to continuously run

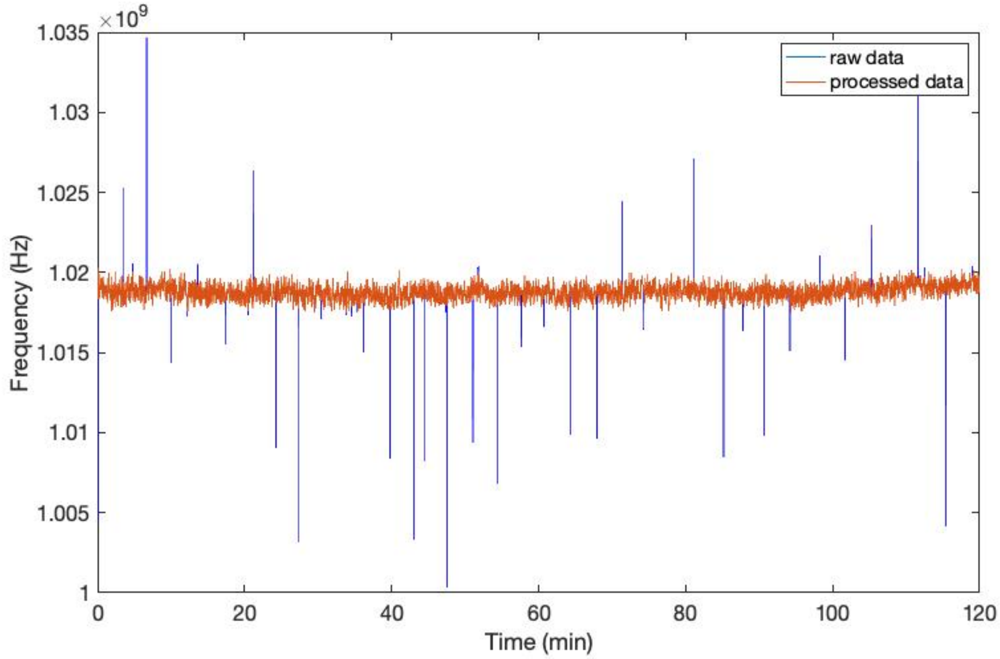

Figure 7.21: 2 hour leader side stabilization raw data vs. processed data.

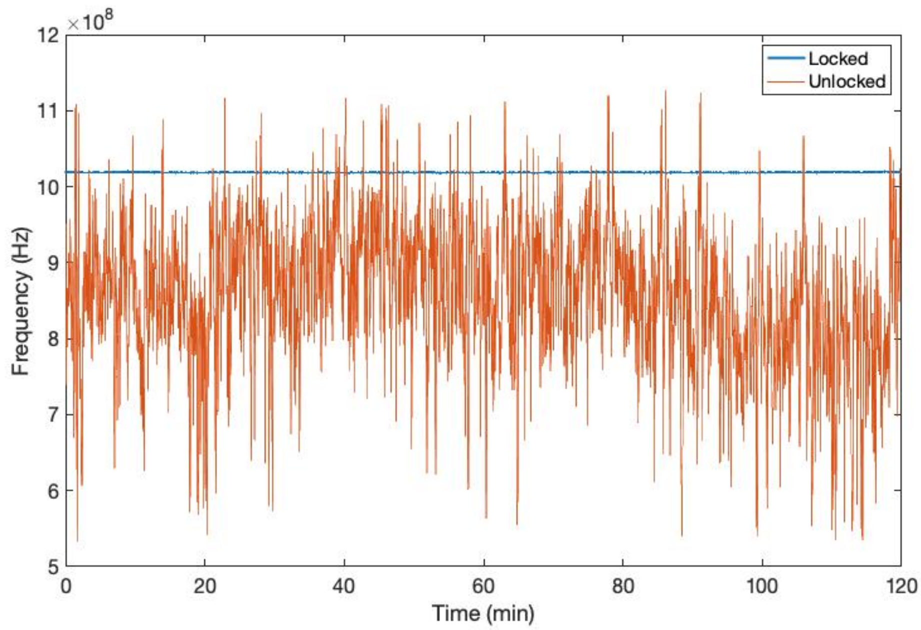

Figure 7.22: 2 hour leader side stabilization processed locked data vs. unlocked data.

without unlocking for more than 24 hours. But, the stabilization performance degrades as the fiber alignment shifts away due environmental vibrations. The two hour stabilization data is shown in Fig. 7.21, where the raw data and processed data are both presented. Spikes are observed in the raw data directly read out from the frequency counter. In order to check whether the spikes were real or not, the same signal was split into two channels, and one was connected to the ESA. From the ESA, no huge frequency changes were observed when spikes occurred on the frequency counter. The spikes may be due to noise from the frequency counter we used. Unfortunately, the frequency counter that was used for previous measurements and had a higher accuracy and less noise had to be

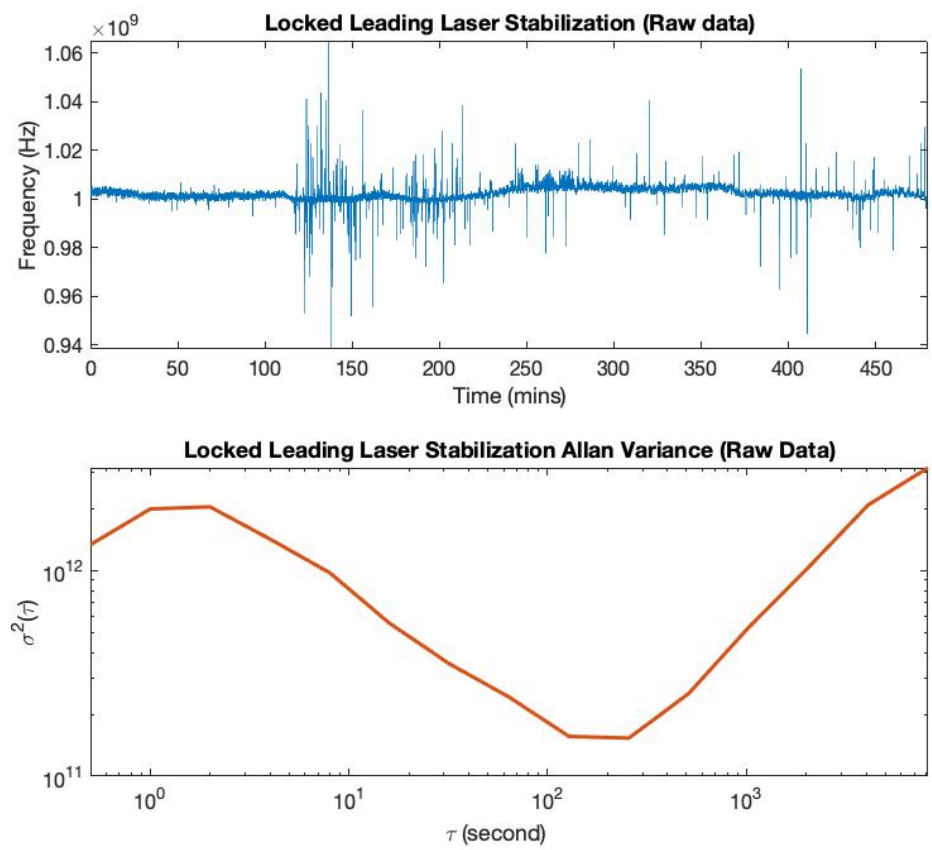

Figure 7.23: 8 hour leader side stabilization raw data with Allan variance.

returned to NASA. Therefore, all the stabilization data was taken contained spikes and those spikes were removed using a linear filter in MATLAB.

For the leader laser stabilization, the filter applied replaces any data points above 99.7% and below 0.6% of the overall data range with a linear fit of its adjacent value. The comparison of the processed locked data and the processed unlocked data with the above filter is shown in Fig. 7.22. With the locking enabled, the peak-to-peak frequency drift is reduced from 592.26 MHz to 2.75 MHz, and the standard deviation of the frequency drift is reduced from 94.33 MHz to 0.45 MHz. The peak-to-peak and standard deviation

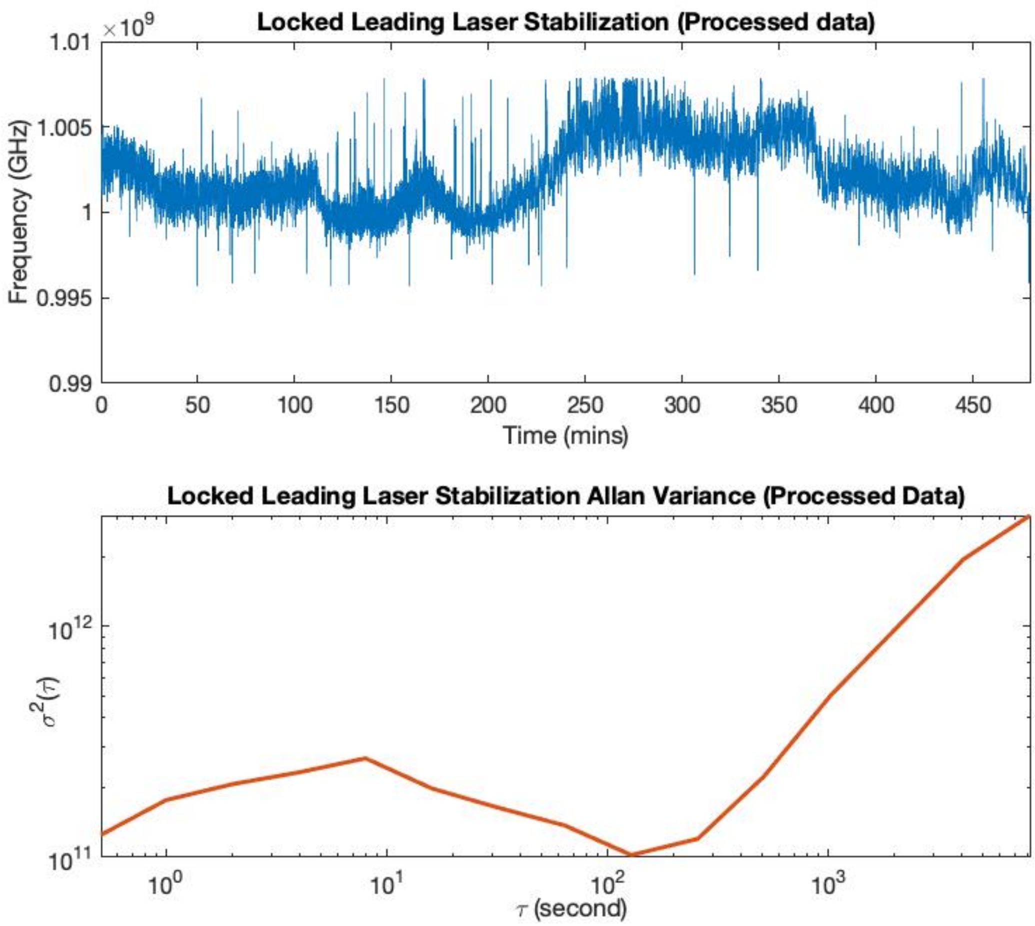

Figure 7.24: 8 hour leader side stabilization processed data with Allan variance.

stabilization performance improves by 215 times (23.33dB) and 207 times (23.18 dB), respectively.

The eight hour stabilization is shown in Fig. 7.23 and Fig. 7.24. The Allan variance is calculated for the raw and the processed data to show the corresponding long term frequency noise performance. But, since the recorded data is limited, the Allan variance only shows up to 2^{13} seconds.

7.2.2 Follower Laser Offset Phase Locking

The follower laser is offset locked to the leader laser through an optical phase lock loop (OPLL). The setup is shown in Fig. 7.25. An integrated PIN photodiode is used to generate the beat note signal between the leader and follower lasers. The beat note signal is sent into PLL electronics where the EV-ADF41513SD1Z board from Analog Devices is used. The signal is sent back into the phase section of the follower laser to achieve the offset locking.

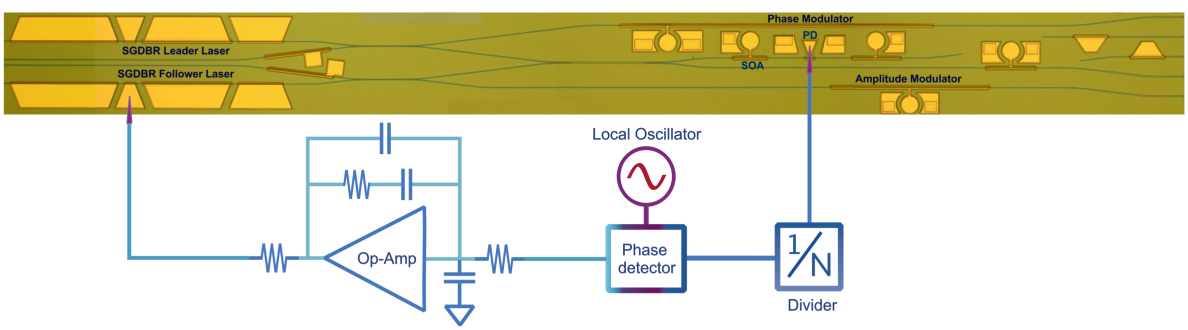

Figure 7.25: Follower laser offset phase locking mechanism.

7.2.2.1 Offset Phase Locking Mechanism

The follower laser offset phase locking mechanism is achieved using the EV-ADF4151 3SD1Z board shown in Fig. 7.27 for OPLL control and the EVAL-SDP-CS1Z board shown in Fig. 7.26 for computer communication, both of which are from Analog Devices [8, 9]. The EV-ADF41513SD1Z board is an evaluation board of the ADF41513 PLL synthesizer. It consists of two main parts. The first part is the ADF41513 PLL synthesizer, and its functional block diagram is shown in Fig. 7.28. It integrates two counters, dividers, phase detectors, and a charge pump [9]. The second part is an OPLL loop filter of the ADF41513 PLL synthesizer, where a 4-pole filter is used for the op-amp to convert the current signal into a voltage output, as shown in Fig. 7.29.

The functional block diagram of the follower laser offset phase locking mechanism is shown in Fig. 7.29, where the functional block of the OPLL is simplified. The simplified mathematical model of the OPLL is derived below. First, assuming both the leader and follower lasers are single frequency lasers that generate radiation at optical carrier frequencies at ω_l and ω_f. The corresponding electric fields E_1 and E_2 can be expressed as:

$$E_1(t) = E_0\, e^{j\omega_l t} + c.c. \tag{7.21}$$

$$E_2(t) = E_0'\, e^{j\omega_f t} + c.c. \tag{7.22}$$

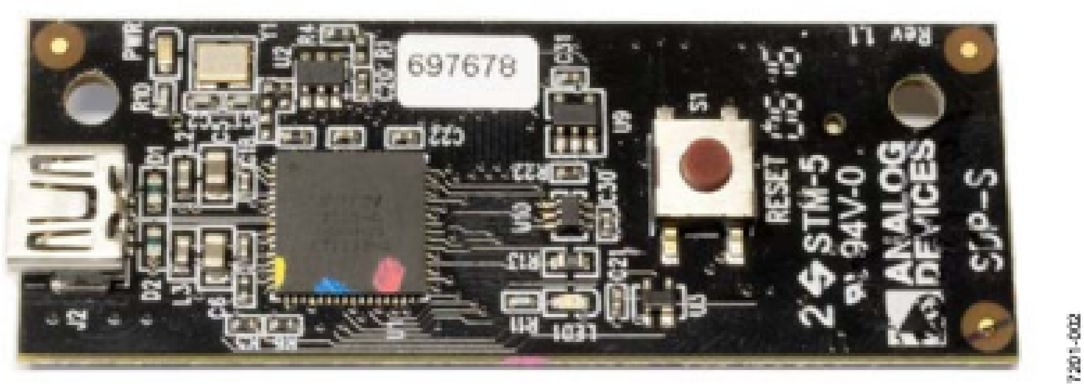

Figure 7.26: Functional block of follower laser offset phase locking mechanism.(© Analog Devices, [8].)

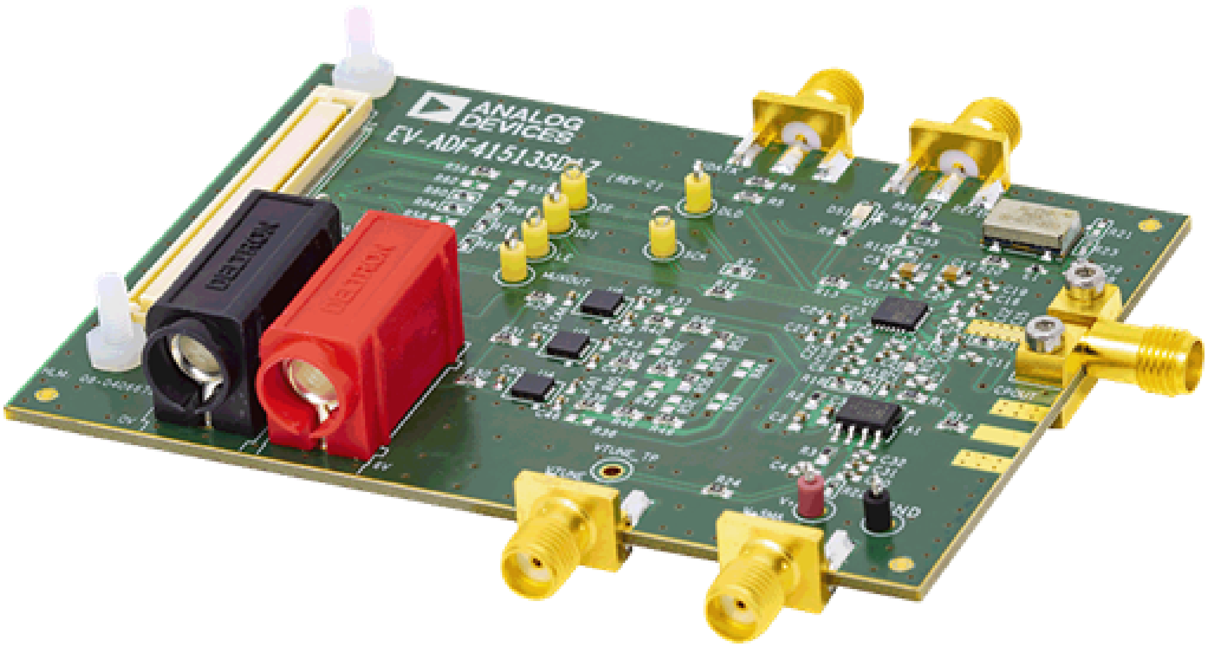

Figure 7.27: Functional block of follower laser offset phase locking mechanism.(© Analog Devices, [8].)

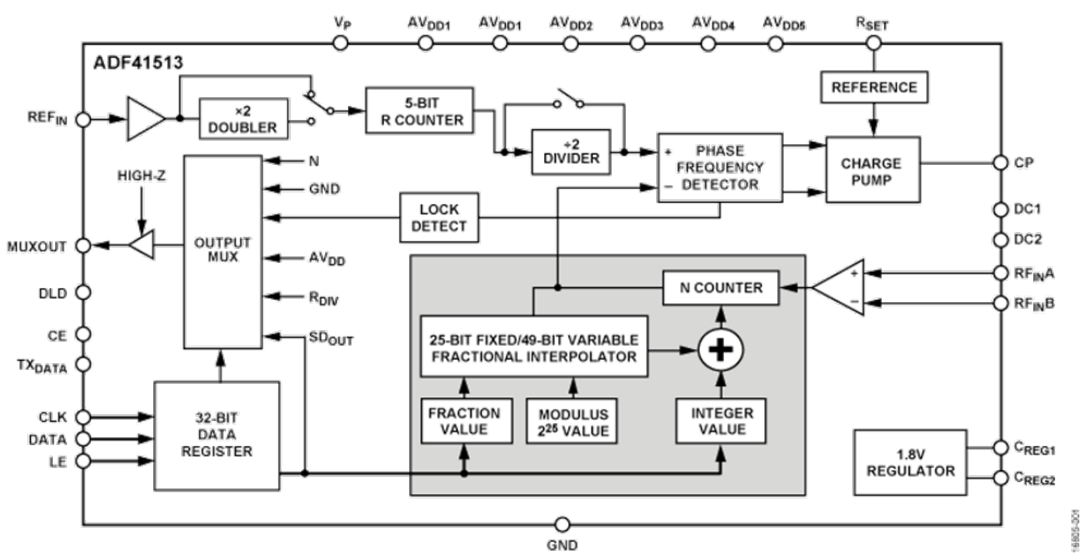

Figure 7.28: Functional block of ADF41513 IC.(© Analog Devices, [9].)

Then the combined signal E_3 can be expressed as Eq. 7.23, where φ_l and φ_f are the phase delay due to the path length difference.

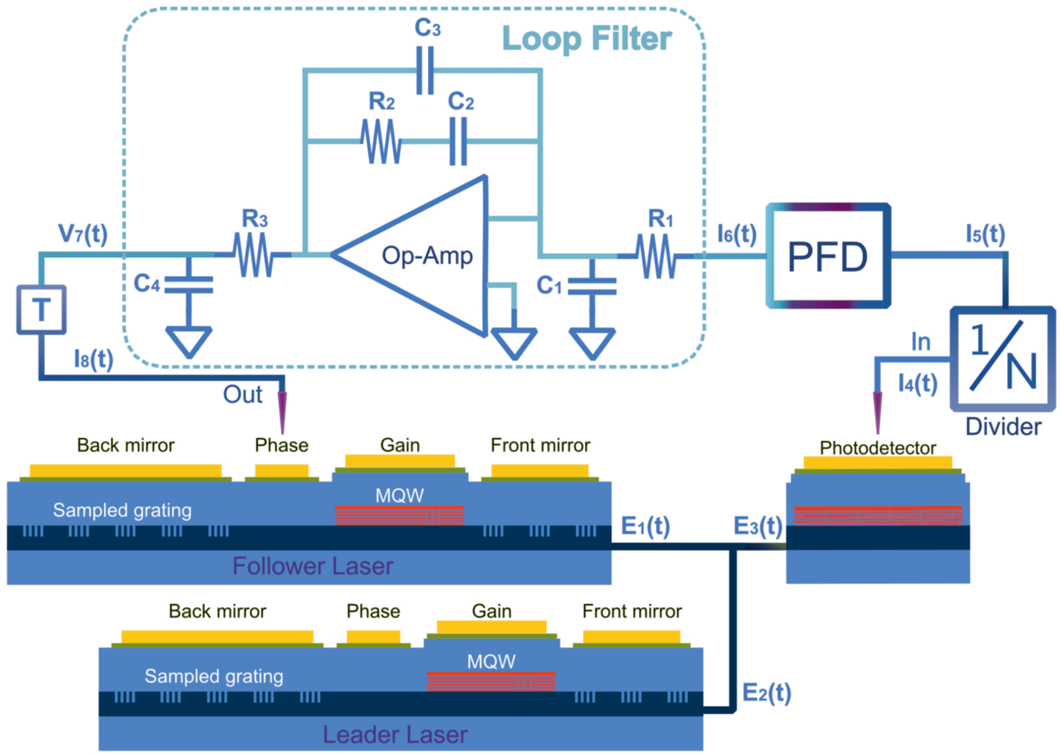

Figure 7.29: Functional block of follower laser offset phase locking mechanism.

$$E_3(t) = E_0\, e^{j(\omega_l t + \varphi_l)} + E_0'\, e^{j(\omega_f t + \varphi_f)} + c.c. \tag{7.23}$$

Using the square law, the detected current signal on the photodetector is Eq. 7.24, where the R is the responsivity of the PIN photodetector.

$$\begin{aligned} I_4(t) = R\, E_3(t)^2 = R\,\{&E_0^2 + E_0'^2 + E_0\, E_0'\, e^{j(\omega_l - \omega_f)t + j(\varphi_l - \varphi_f)} \\ &+ E_0\, E_0'\, e^{-j(\omega_l - \omega_f)t + j(\varphi_l - \varphi_f)}\} + c.c. \end{aligned} \tag{7.24}$$

By eliminating the DC term, only the intermediate frequency term is left, and I_4 becomes

Eq. 7.25

$$I_4(t) = R\left\{E_0\, E_0'\, e^{j(\omega_l-\omega_f)t+j(\varphi_l-\varphi_f)} + E_0\, E_0'\, e^{-j(\omega_l-\omega_f)t-j(\varphi_l-\varphi_f)}\right\} + c.c. \tag{7.25}$$

$$I_4(t) = R\, E_0\, E_0' cos[(\omega_l-\omega_f)t + (\varphi_l-\varphi_f)] \tag{7.26}$$

For convenience, we define the following parameters:

$$\Delta\omega = \omega_l - \omega_f \qquad \Delta\varphi = \varphi_l - \varphi_f \tag{7.27}$$

$$I_4(t) = R\, E_0\, E_0'\, cos(\Delta\omega t + \Delta\varphi) \tag{7.28}$$

The detected frequency is divided by N using a divider so the divided signal $I_5(t)$ is:

$$I_5(t) = R\, E_0\, E_0'\, cos(\frac{\Delta\omega}{N}t + \Delta\varphi) \tag{7.29}$$

The divided signal is compared with a reference signal in the phase frequency detector. The phase frequency detector (PFD) operates up to 250 MHz (integer N mode)/ 125 MHz (fractional-N mode). The integer N mode is used for a better phase noise performance of the PLL. Under the integer N mode, the PFD reference signal f_{PFD} can be expressed as Eq. 7.30 [9]:

$$f_{PFD} = REF_{IN}\, \frac{1+D}{R(1+T)} \tag{7.30}$$

Where D is the REF_{IN} doubler bit value (0 or 1), R is the preset divide ratio of the binary 5-bit programmable reference counter (1 to 32), and T is the REF_{IN} divide by 2 bit value (0 or 1). The REF_{IN} is 100 MHz provided by crystal oscillator on the EV-ADF41513SD1Z board. D, R,and T are controlled by the EVAL-SDP-CS1Z board.

$$RF_{out} = N\, f_{PFD} \tag{7.31}$$

The frequency and phase difference between the f_{PFD} and $I_5(t)$ are detected and sent to a charge pump which has a transfer function of $U(t)$. The output signal can be expressed as:

$$I_6(t) = I_0\,(\Delta\omega - \omega_{PFD})t\,U(t) \tag{7.32}$$

The loop filter is designed based on its transfer function and the details are introduced in the reference [10]. The transfer function of the loop filter is shown in Eq. 7.33

$$H_{loop} = \frac{V_7(t)}{I_6(t)} = \frac{1 + sR_2C_2}{sC_2(1 + sR_1C_1)(1 + sR_2C_3)(1 + sR_3C_4)} \tag{7.33}$$

The second order closed loop transfer function can be described by Eq. 7.34 where the K is the overall tuning sensitivity.

$$H_{loop}(s) = \frac{\frac{I_6K}{2\pi C_2}(1 + sR_2C_2)}{s^2 + s\frac{I_6KR_2}{2\pi N} + \frac{I_6K}{2\pi NC_2}} \tag{7.34}$$

The damping factor ζ and damped frequency ω_n are:

$$\zeta = \frac{R_2}{2}\sqrt{\frac{I_6C_2K}{2\pi N}} \tag{7.35}$$

$$\omega_n = \sqrt{\frac{I_6K}{2\pi NC_2}} \tag{7.36}$$

The corresponding capacitor and resistor values used in the loop filter and its zeros/poles are shown in Table. 7.3

Resistance	Capacitance	Zero/Pole
R1: 220 Ω	C1 : 100 pF	Pole: 7.23 MHz
R2 : 8 Ω	C2 : 460 pF	Zero: 43.2 KHz
R3 : 8 Ω	C3 : 10 pF	Pole: 2.03 MHz
R4 : 30 Ω	C4 : 3.3 pF	Pole: 1.61 MHz

Table 7.3: Values of resistors and capacitors used in the loop filter and corresponding poles and zeros.

Then the $V_7(t)$ can be expressed as:

$$V_7(t) = H_{loop}\, I_6(t) = H_{loop}\, [I_0\, (\Delta\omega - \omega_{PFD})t\, U(t)] \tag{7.37}$$

The feedback signal goes into the modulation channel of the current source connected to the follower laser's phase section, which has a transfer function T of 25mA/V. The final signal $I_8(t)$ going into the phase section is expressed as Eq. 7.38, where I_{DC} is the DC channel output which sets the initial current condition of the phase section.

$$I_8(t) = T\, H_{loop}\, [I_0\, (\Delta\omega - \omega_{PFD})t\, U(t)] + I_{DC} \tag{7.38}$$

7.2.2.2 Offset Phase Locking Performance

The performance of the follower laser offset phase locking is summarized in this section. The follower laser is successfully locked to the leader laser at various frequencies. The optical spectrum of the follower laser and leader laser is shown in Fig. 7.30, where the leader laser is locked to the CO_2 absorption peak and the follower laser is locked 2 GHz offset from the leader laser. Both locked lasers achieve a $\sim$ 42 dB SMSR.

The linewidth values when the system is locked and unlocked were measured and compared. The unlocked system linewidth from the follower side is shown in Fig. 7.31, where

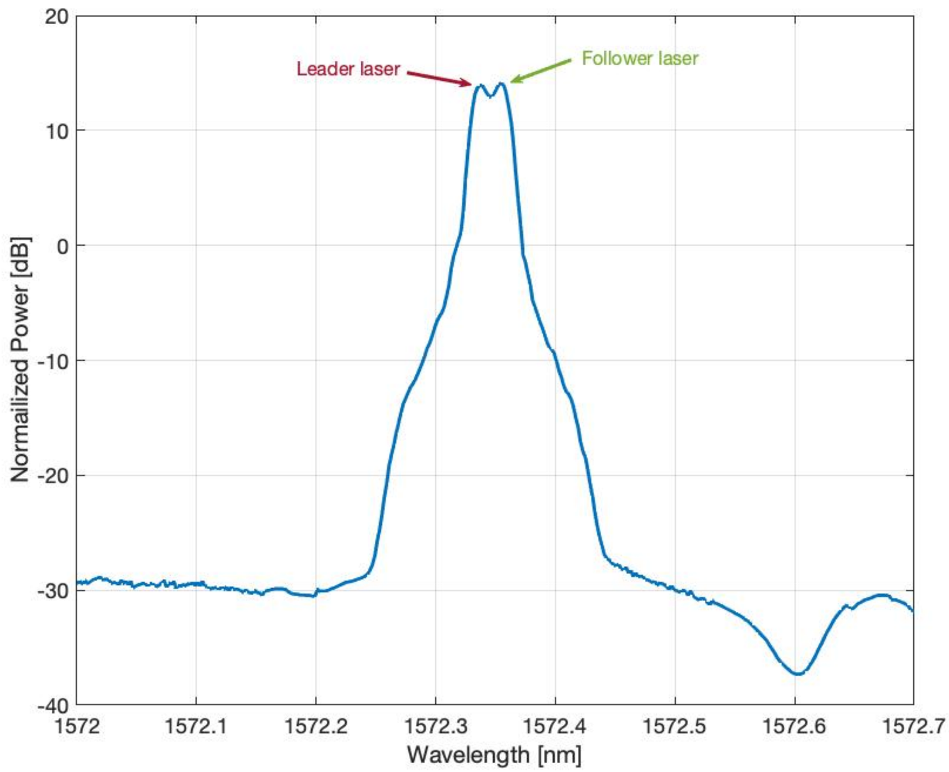

Figure 7.30: Optical spectrum of stabilized leader laser and follower laser.

it has a Lorentzian fitted 3 dB linewidth of 0.866 MHz. The locked system linewidth from the follower side is shown in Fig. 7.32, where it has a Lorentzian fitted 3 dB linewidth of 0.864 MHz. Both linewidths were measured using a 5 μs sweep time, a 2 MHz resolution bandwidth and a 20 KHz video bandwidth, and all the integrated components on PIC were set using the parameters shown in 7.2. Unlike the leader side, where a severe degradation is observed after the leader side stabilization system turns on, we do not observe a significant degradation of the linewidth performance when the follower side offset phase locking is enabled. Since this output is the output that will be sent into the next stage, it is very important to ensure there is no degradation caused by the OPLL system. This easily satisfies the minimum requirement from NASA for this application

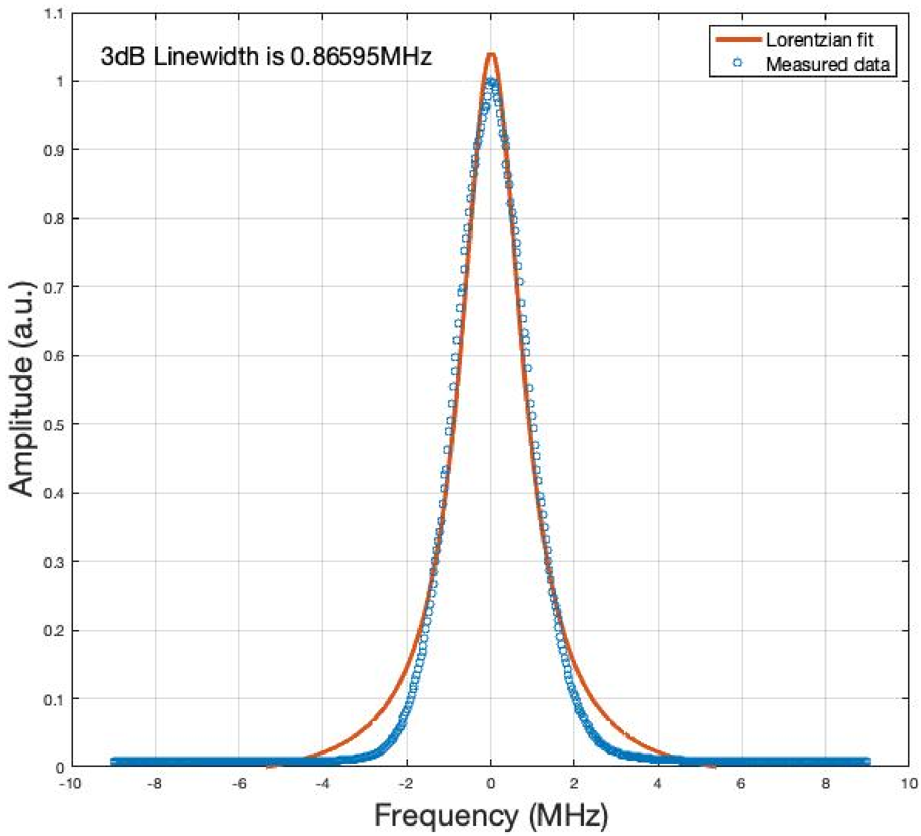

Figure 7.31: Unlocked follower side output linewidth with Lorentzian fit.

where the linewidth should be less than 50 MHz over a 15 μs sweep time [4–7].

The frequency stabilization at 2 GHz is characterized and shown below. The data was recorded using the same frequency counter above (which has the noise issue as discussed above) with a 1 s gate time. The locked leader laser and locked follower laser beat note signal from the on-chip photodiode was amplified using an external 10 GHz bandwidth driver amplifier with 26 dB gain and sent into the frequency counter.

Similar to the leader side CO_2 stabilization system, the follower side offset frequency locking was also able to continuously run for more than 24 hours. Data was recorded over two hours and eight hours. The two hour locking performance is shown in Fig. 7.33

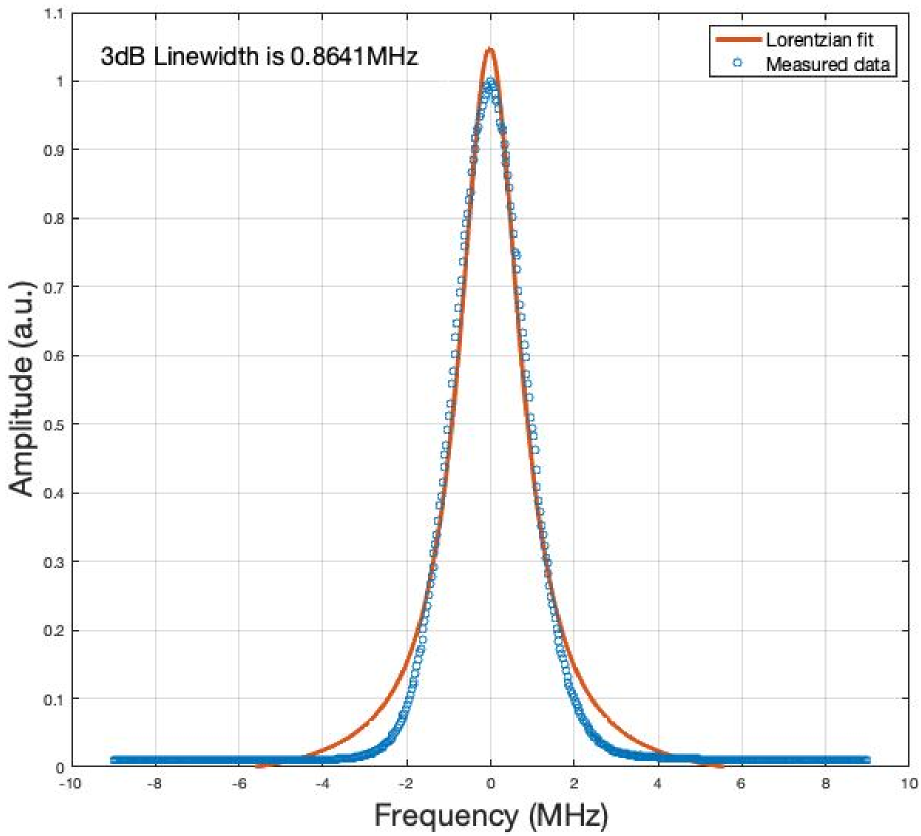

Figure 7.32: Locked follower side output linewidth with Lorentzian fit.

and Fig. 7.34. The eight hour locking performance is shown in Fig. 7.35 and Fig. 7.36. Similar to the leader side stabilization, a filter was used to remove the signal spikes in MATLAB. The filter is used to replace the data points that are below 0.6% and above 99.3% of the overall data range with a linear fit of its adjacent data point values. The same filter is also applied to all the locked and unlocked recorded data for follower side offset frequency locking stabilization.

In Fig. 7.33, the raw data and processed data are compared for a two hour time range. In Fig. 7.34, the processed locked and unlocked data are compared for a two hour range, where the peak-to-peak frequency drift is 7.0 KHz and 513.57 MHz when locked

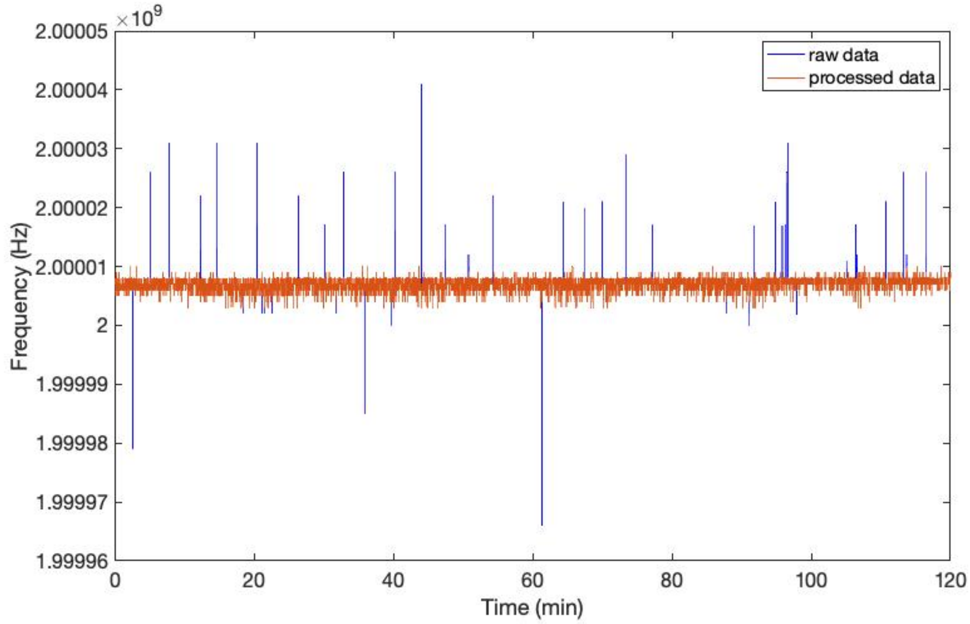

Figure 7.33: 2 hour follower side OPLL stabilization raw data vs. processed data.

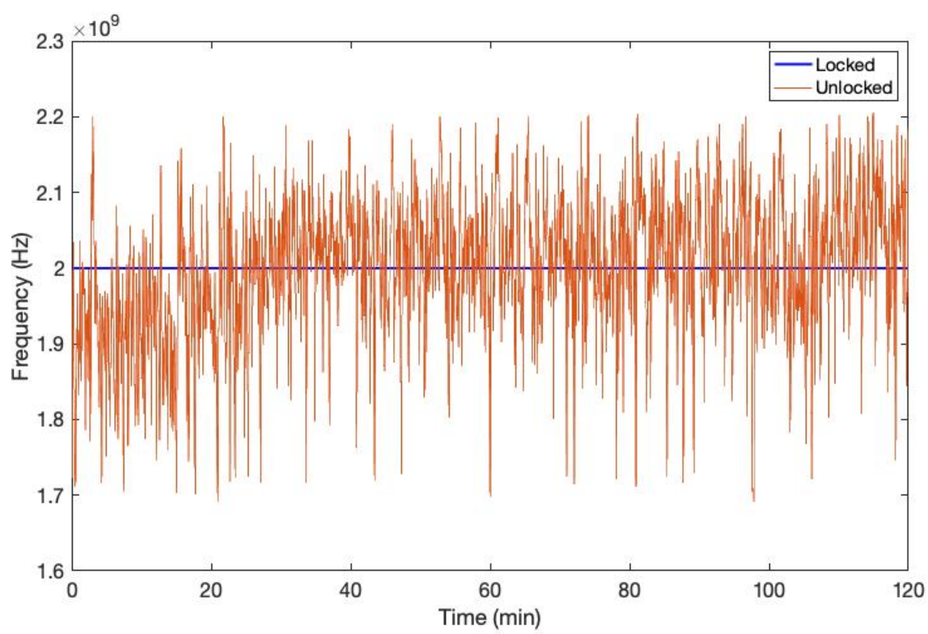

Figure 7.34: 2 hour follower side OPLL stabilization processed locked data vs. unlocked data.

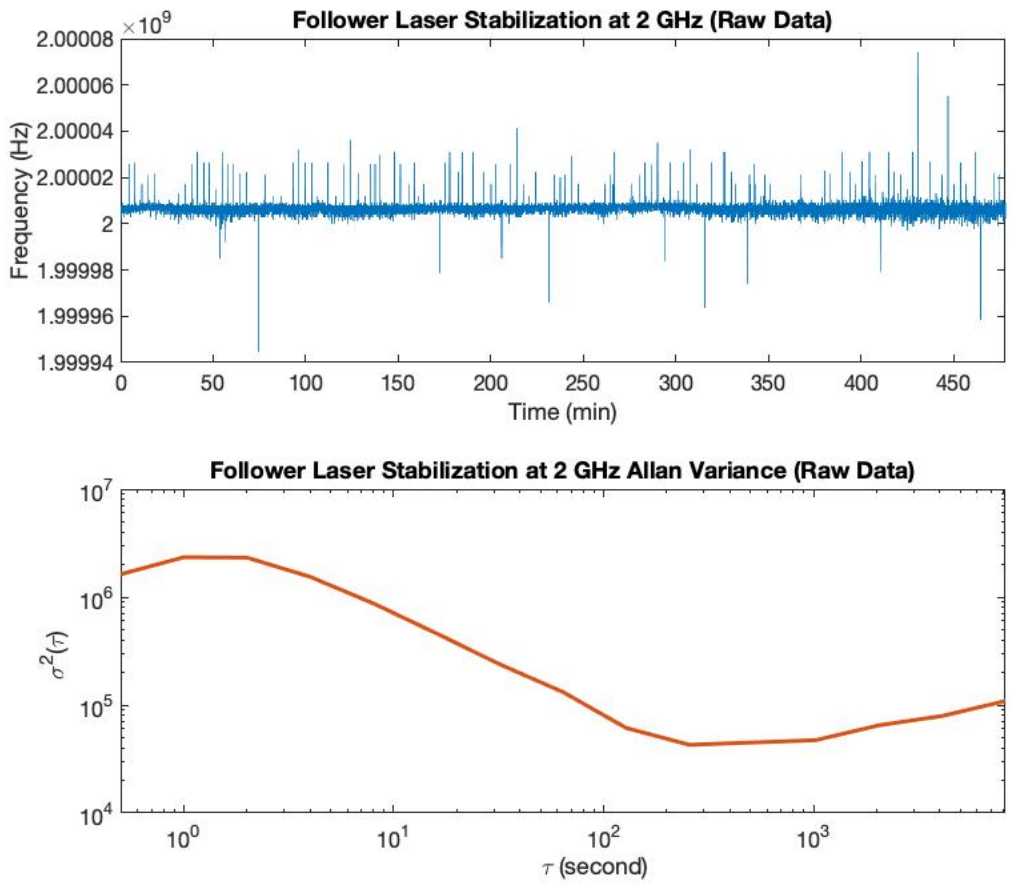

Figure 7.35: 8 hour follower side OPLL stabilization raw data with Allan variance.

and unlocked, respectively, and the standard deviation of the frequency drift is reduced from 92.51 MHz to 1.14 kHz with OPLL enabled. Overall, the peak-to-peak frequency drift improved by 73368 times (48.66 dB), and the standard deviation improved by 81174 times (49.09 dB).

The eight hour stabilization data and its Allan variance is shown in Fig. 7.35 and Fig. 7.36. The eight hour stabilization after filtering out the spikes shows a standard deviation of 1.34 kHz and peak-to-peak drift of 8 kHz. The Allan variance is much improved compared with the leader side stabilization, and the Allan deviation $\sigma(\tau)$ is in the kHz range instead of MHz range for the follower side stabilization.

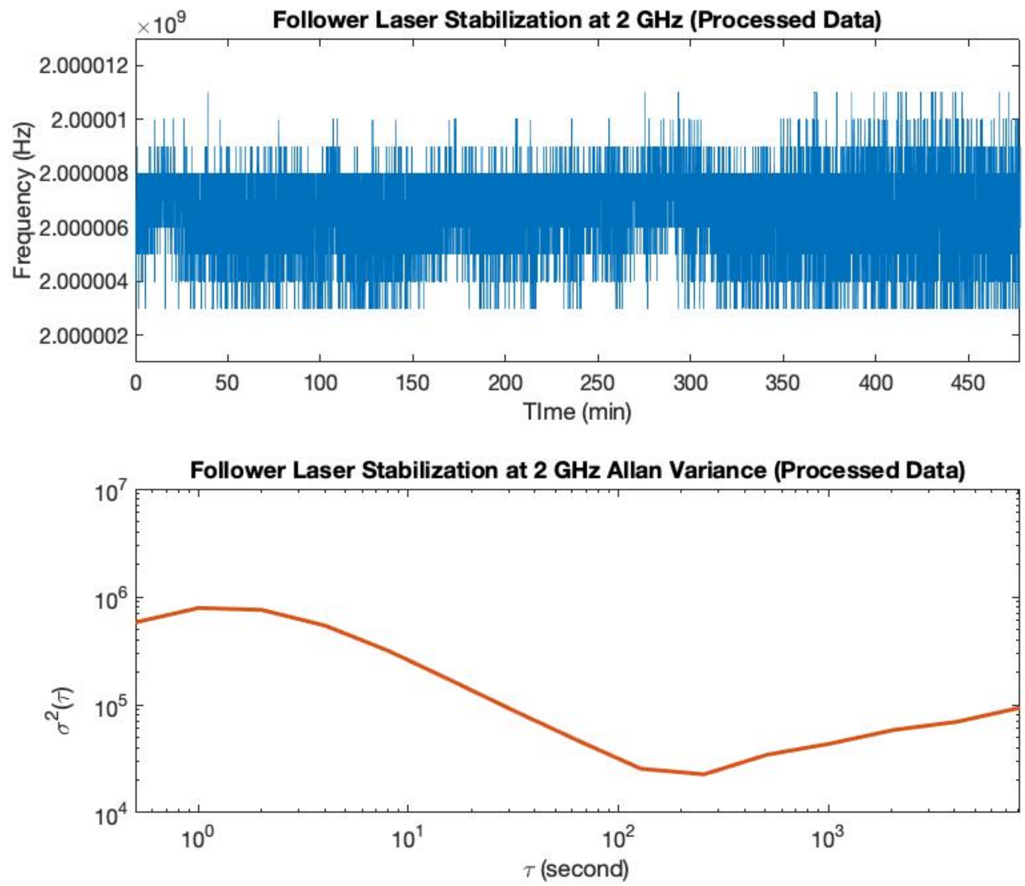

Figure 7.36: 8 hour follower side OPLL stabilization processed data with Allan variance.

7.3 Overall PIC Control

In the previous section, the subsystem PIC controls were discussed. In this section, the overall PIC control and CO_2 remote sensing are discussed. The overall PIC control requires scanning over a 20 GHz window centered at 1572.335 nm. The final output for the remote sensing needs to be performed with pulsed sampling with the specified pulse period of 133 μs and pulse width of 1 μs.

7.3.1 Overall PIC Control Architecture

The overall control architecture is shown in Fig. 7.37. The leader side frequency stabilization and follower side offset phase locking are included. In addition, the pulse carver and the CO_2 Herriott cell used for testing are also included, where the pulse carver generates the pulsed signal when driven by a pulse generator and a CW signal when a constant forward bias is applied to it.

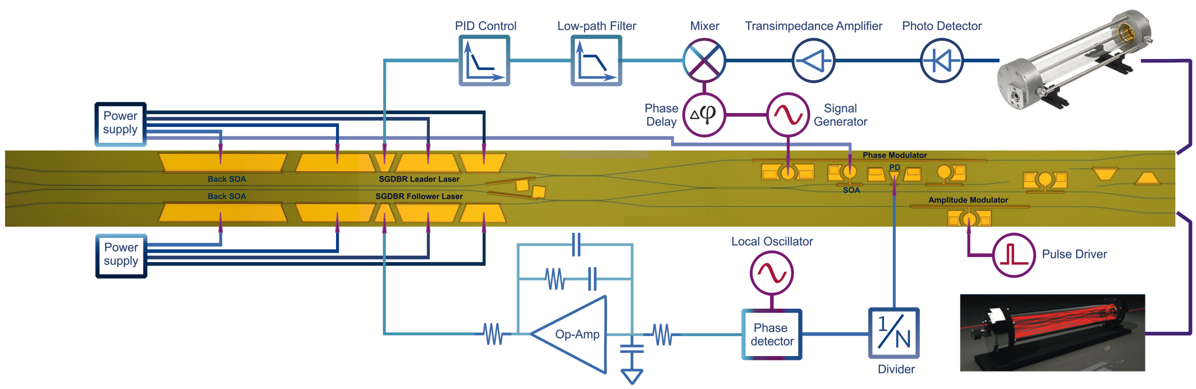

Figure 7.37: Overall remote sensing control setup block diagram.

The initial starting settings of all the components was shown earlier in Table 7.2. In order to improve the stability of the overall system and protect the device from the overshot of the feedback signals, the follower laser wavelength is tuned to the shortest wavelength needed. In this situation, the follower side OPLL feedback signal is always negative, which gets rid of the inaccuracy when the feedback signal switches signs. In addition, since the laser is tuned to the lowest wavelength, the phase section current is at the maximum level. The phase current level will only decrease when the laser is tuned to longer wavelengths. This protects our device from large current injection caused by the overshot of the feedback signal. The current source will turn off automatically if a negative output current is requested, so we do not need to worry about a negative current being injected into the device if the overshot feedback signal is larger than the DC bias signal. Based on the reasons outlined above, the follower laser frequency is tuned to 12 GHz ~ 15 GHz lower than the leader laser wavelength on purpose. This is achieved by only tuning the phase section current from 5.6 mA to 7.5 mA ~ 8.5 mA on the follower laser.

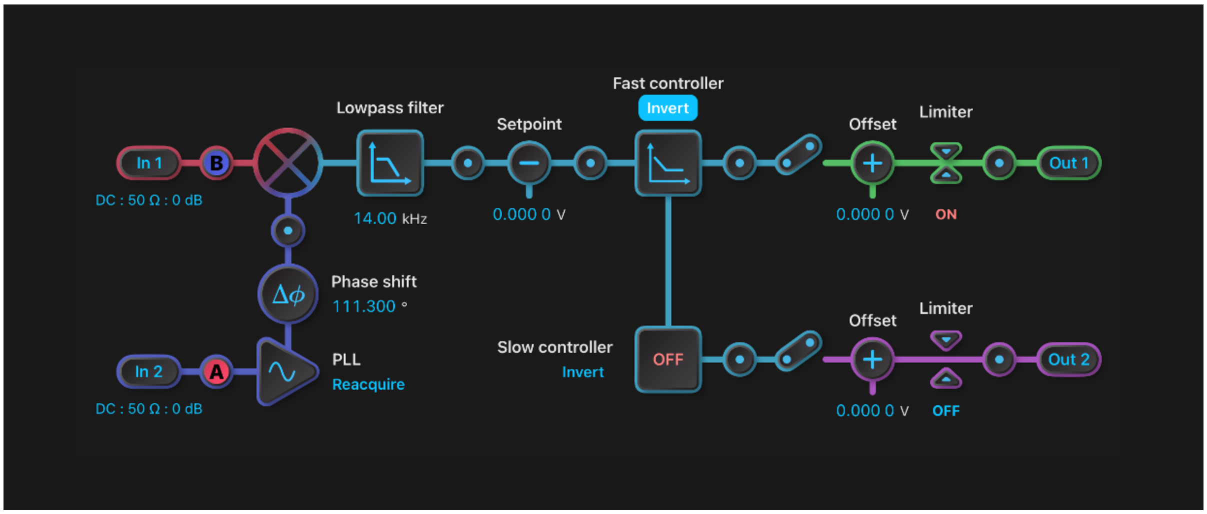

Figure 7.38: settings and interface of Moku:lab.

After all the settings mentioned above are set, the leader side frequency stabilization is turned on first. The leader side frequency stabilization system is fine tuned by controlling the Moku:lab equipment, the interface of which is shown in Fig. 7.38. For this measurement where the screen capture was taken, the phase shift between input 1, which is the 125 MHz signal from local oscillator, and input 2, which is the AC signal from the Herriott cell detector circuitry, is set to 113.3 degree to make the input 1 and input 2 signals in-phase with each other. Then, a 4th-order Butterworth low-pass filter with a corner frequency at 14 KHz and sampled at 31.25 MHz is applied to the signal. Then the Fast PID control is set to have -60.0 dB proportional gain, a 7.000 kHz integrator crossover, and disabled derivative gain. The limiter sets the output voltage range from -1V to 1V.

After optimizing the performance of the leader side frequency stabilization, the fol-

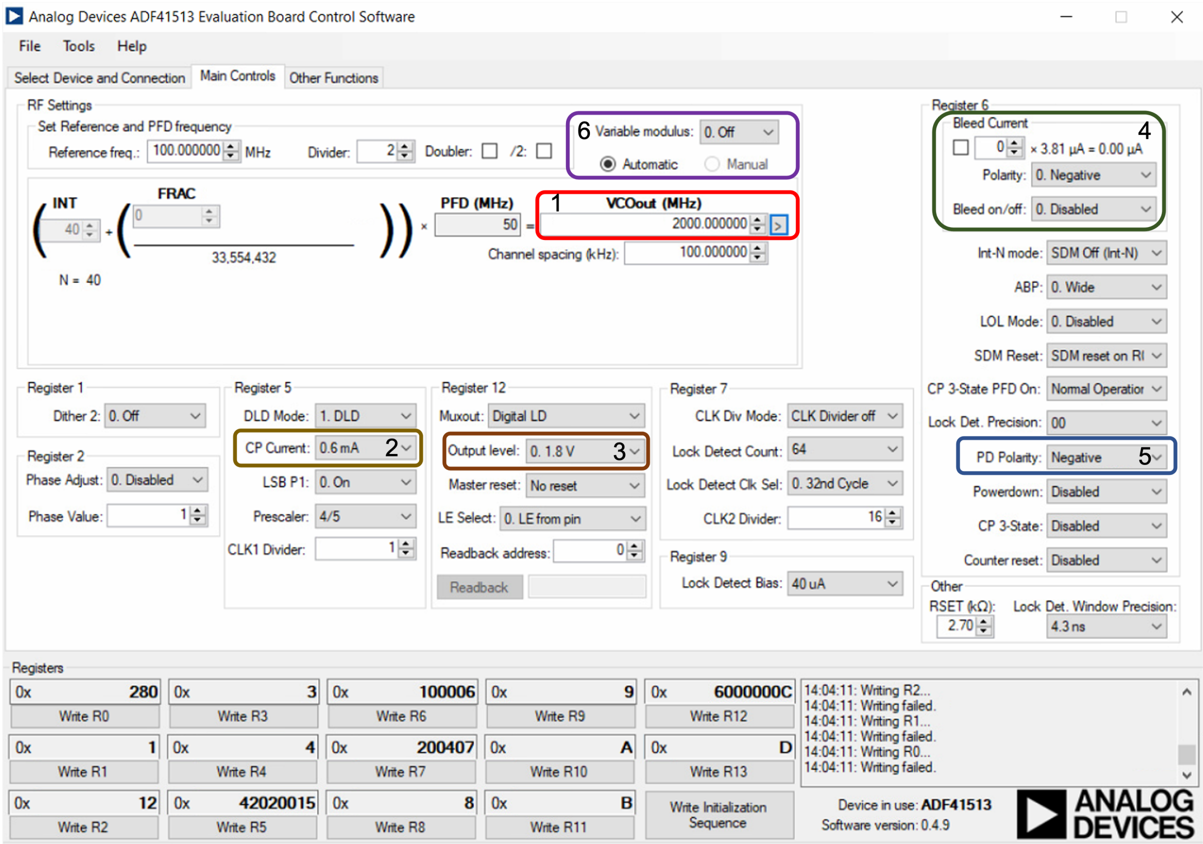

Figure 7.39: settings and interface of ADF41513 PLL synthesizer.

lower side offset phase locking was enabled by controlling the ADF41513 software to set the parameters from a computer. The computer interface of the ADF41513 software and corresponding settings are shown in Fig. 7.39. The setting uses a 25 bit fixed modulus instead of a 49 bit variable modulus by setting the variable modulus to OFF in box 6. The measurement also uses the integer N mode by setting all the parameters to zero in box 4. Then, the CP (current pump) current is set to 0.6 mA in box 2, and output level to 1.8 V in box 3. The locking frequency is control by VCO_{out} in box 1, which defines the absolute locking frequency between the two lasers. The polarity is controlled by the PD polarity in box 5, and for our experiment settings, negative PD polarity means that the follower laser is locked to the longer wavelength side and positive PD polarity means that the follower laser is locked to the shorter wavelength side. At last, since the EV-ADF41513SD1Z board and EVAL-SDP-CS1Z are both evaluation boards, which cannot be programmed externally, the follower laser frequency is controlled manually for tuning from -10 GHz to +10 GHz to perform the overall sensing experiment.

7.3.2 Overall PIC Control Performance

By using the setup mentioned above, the follower laser was successfully tuned from -10 GHz to +12 GHz by only controlling the ADF41513 software parameters. The optical spectra of both the leader and follower lasers at each tuning frequency with 1 GHz step

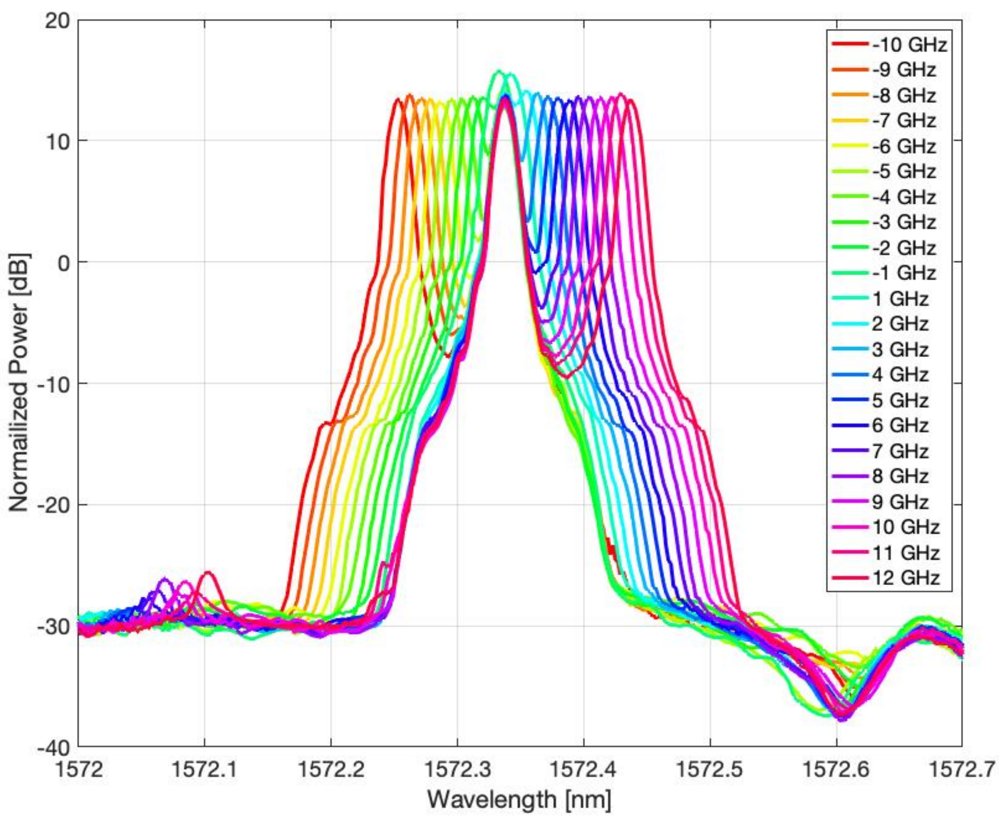

Figure 7.40: Optical spectra of leader and follower lasers locked from -10 GHz to +12GHz with step of 1 GHz.

are shown in Fig. 7.40. The follower laser has an SMSR of at least 39 dB over the entire tuning range. The beat note signal from the on-chip photodiode is also measured from 1 GHz to 9 GHz while the system is locked, as shown in Fig. 7.41. From the figure, we can estimate that the bandwidth of the integrated photodiode is about 6 GHz, because for frequency higher than 6 GHz the signal degrades quickly.

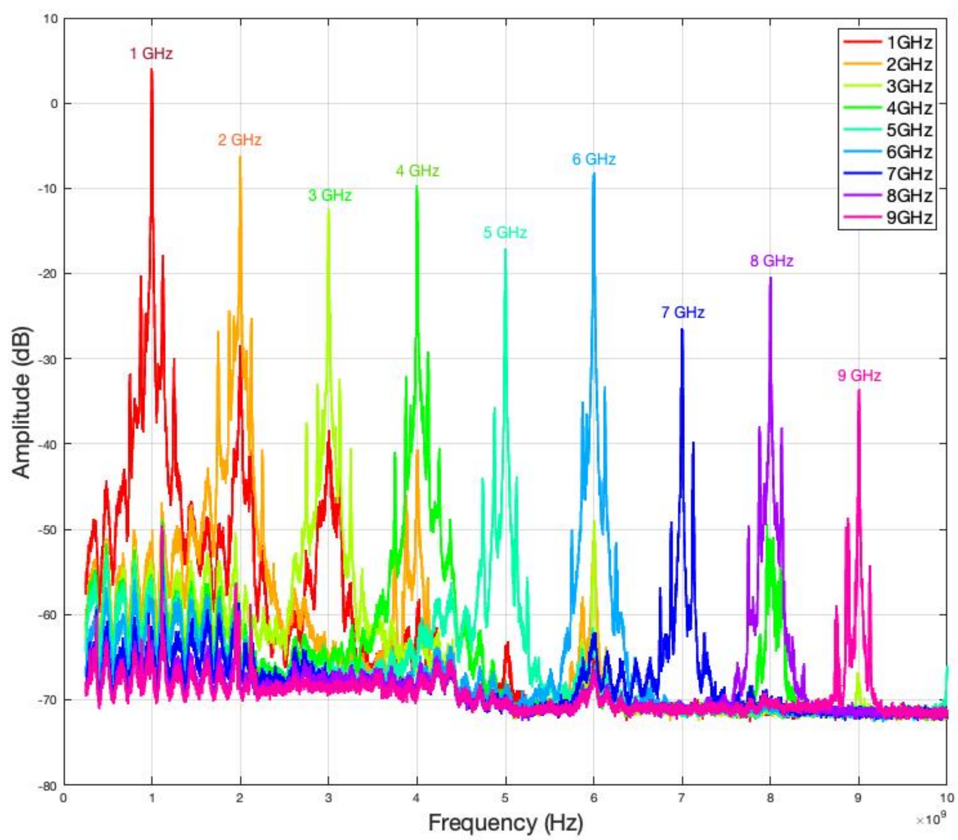

Figure 7.41: Electrical spectra of beatnote signal from 1 GHz to 9 GHz with 1 GHz step.

One thing we need to pay attention here is that the side-band at ±125 MHz can be observed on the electrical spectrum as a little ear near the IF band. Ideally, the phase modulation signal should not be seen here since it is modulated after splitting. But such a strong side band shows that the phase modulation on the output of the leader side is affecting the overall performance of the leader laser. This could be caused by reflection at each active/passive interface and/or substrate light coupling between the phase modulator and the photodiode since they are close to each other.

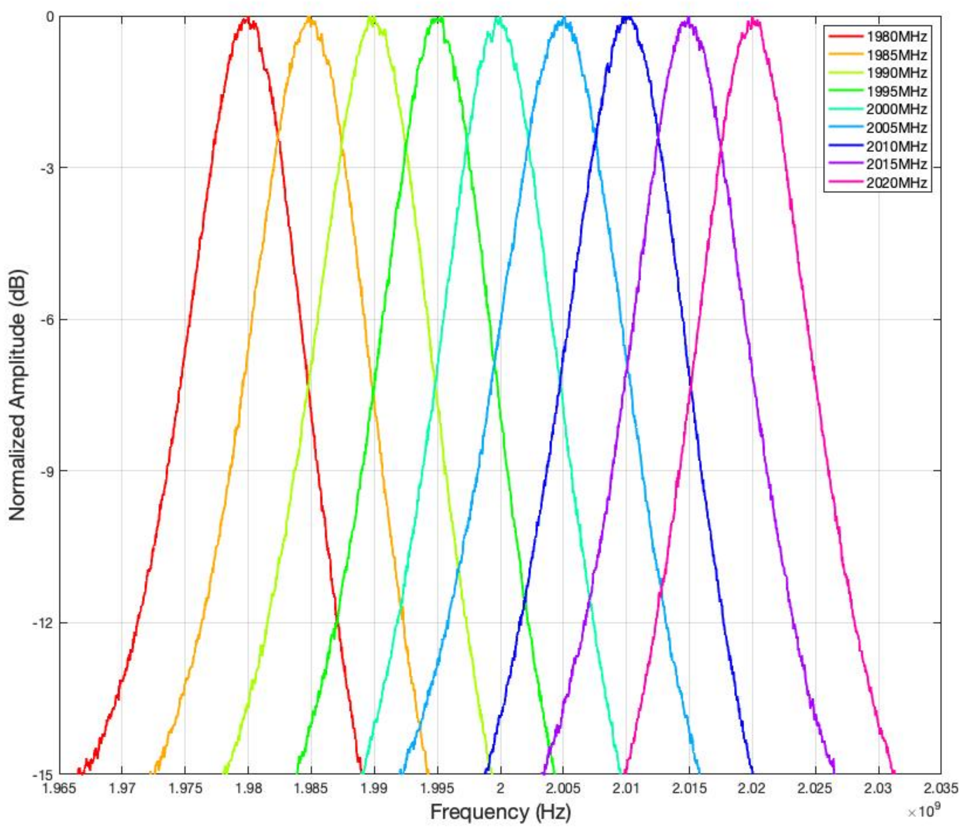

Figure 7.42: Electrical spectra of beatnote signal from 1980 MHz to 2020 MHz with 5 MHz step.

Then the locking resolution of the follower side output is characterized with the above system using the fractional N mode by enabling the bleed current in box 4 of Fig. 7.39. The reason for using the fractional N mode instead of the integer N mode is that, in the integer N mode, the frequency cannot be set to 1 MHz resolution since it has to be a multiple of the reference frequency which is 100 MHz in this case. From the characterization, the system can achieve a resolution of 1 MHz. The results are shown in Fig. 7.42 and Fig. 7.43.

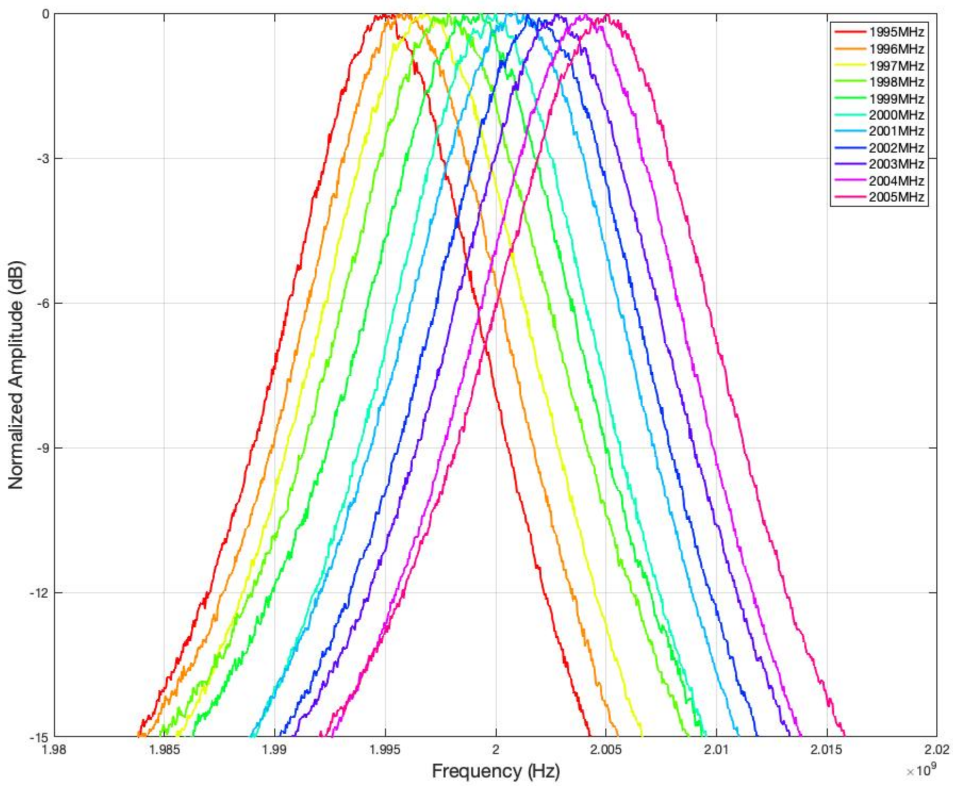

Figure 7.43: Electrical spectra of beatnote signal from 1995 MHz to 2005 MHz with 1 MHz step.

The 40 MHz tuning from 1980 MHz to 2020 MHz with a 5 MHz step is shown in Fig. 7.42. The cross point between the adjacent signals is around -2.5 dB relative to the peak power. The 10 MHz tuning from 1995 to 2005 MHz with 1 MHz step is shown in Fig. 7.43. The cross point between the adjacent signals is around -0.3 dB compared with the peak power. From both measurements, each signal can be separated clearly without mixing with each other.

Finally, the output power is characterized in the CW sampling, to see how much extinction ratio we can achieve using the SOA as an amplitude modulator, especially

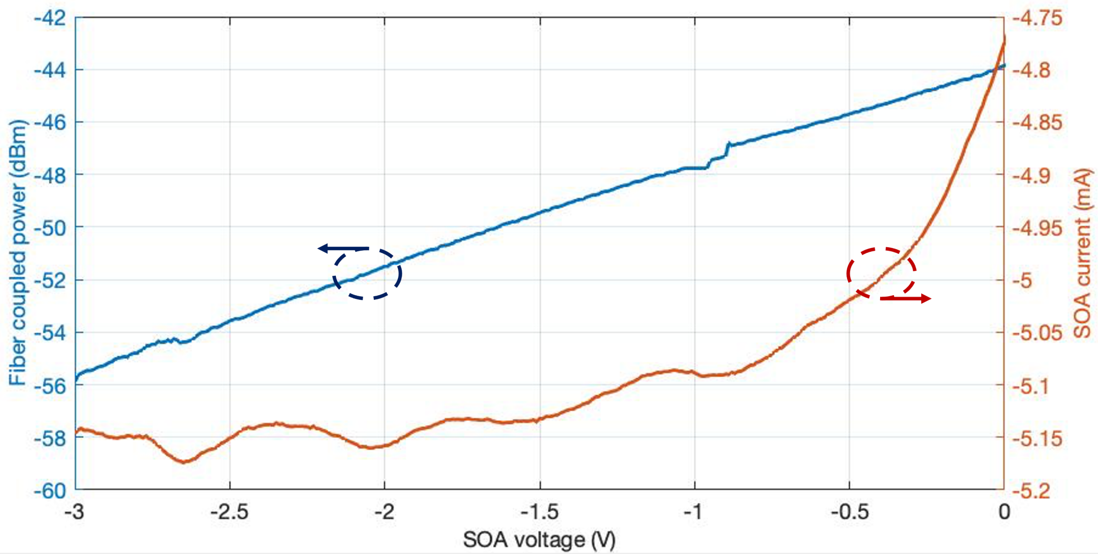

(a)

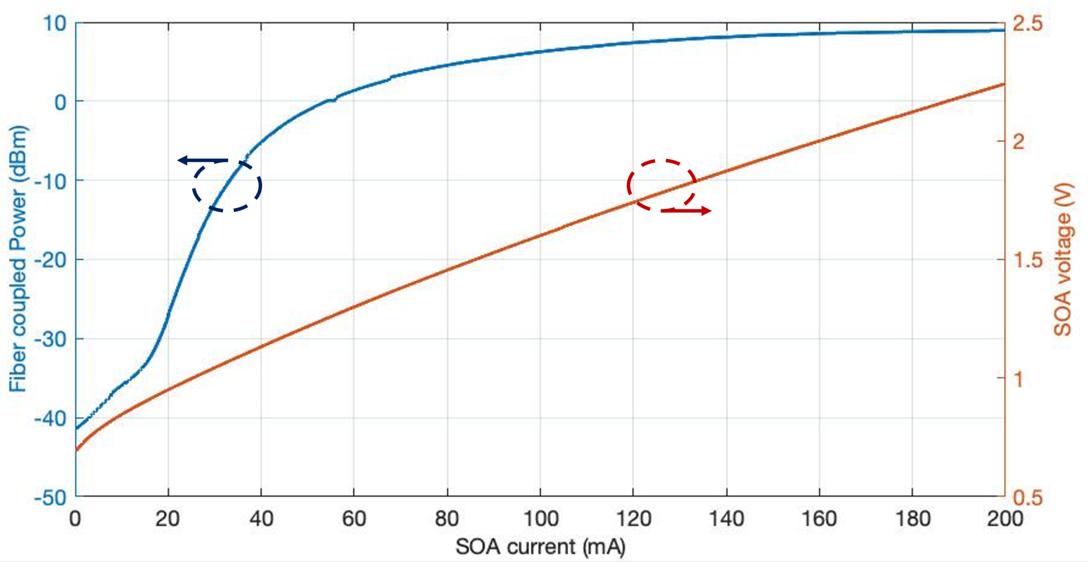

(b)

Figure 7.44: Light-current-voltage characterization of the output SOA with system locked at 2 GHz, (a) when it is reverse biased, and (b) when it is forward biased.

from reverse bias to forward bias. The amplitude modulator is swept from -3 V to 200 mA when the system is locked at 2 GHz. The characterization result is shown in Fig. 7.44. The amplitude modulator provides -55.90 dBm and 8.92 dBm fiber coupled output power when it is reverse biased at -3 V and forward biased at 200 mA, respectively. When the SOA is unbiased, the fiber coupled output power is around -42 dBm. Altogether, we can get an extinction ratio of 64.82 dB from -3 V to 200 mA, with 50.92 dB extinction from forward bias modulation and -13.9 dB from going into reverse bias.

In addition, the LIV also shows that the SOA power is almost saturated above 120 mA (7.4 dBm) where the gain becomes very small as the current increases, and finally achieves 8.92 dBm at 200 mA. Although the measured power does not exceed 10 dBm, it can easily exceed 10 dBm when the PIC is packaged with a better alignment technique. Usually the loss of fiber coupling is around 4 $\sim$ 5 dB when manually aligned in lab environment, but it can go below 2 dB easily with a better alignment technique with packaging.

7.3.3 $\mathbf{CO_2}$ remote sensing

The CO_2 remote sensing is performed in CW sampling and pulse sampling. For the remote sensing, we target to sweep over a 20 GHz window centered at 1572.335 nm. Another CO_2 Herriott cell is used as the testing cell for the sensing measurement. The CO_2 concentration is related to the full width half maximum (FWHM) of the absorption line, where the higher the concentration, the wider the FWHM. An example is shown in Fig. 7.45, where the CO_2 data was measured by NASA on Dec. 07 2008 at Ponca City. Many measurements were performed at different altitudes [11], and as the altitude increased the measured absorption line's FWHM also increased.

The difference between the CW sampling and pulsed sampling is how the amplitude modulator is biased. In the CW sampling, the amplitude modulator is forward biased constantly at 120 mA. In the pulse sampling, the amplitude modulator is driven by a current pulse driver with a 133 μs period and a pulse width of 1 μs. From the receiver

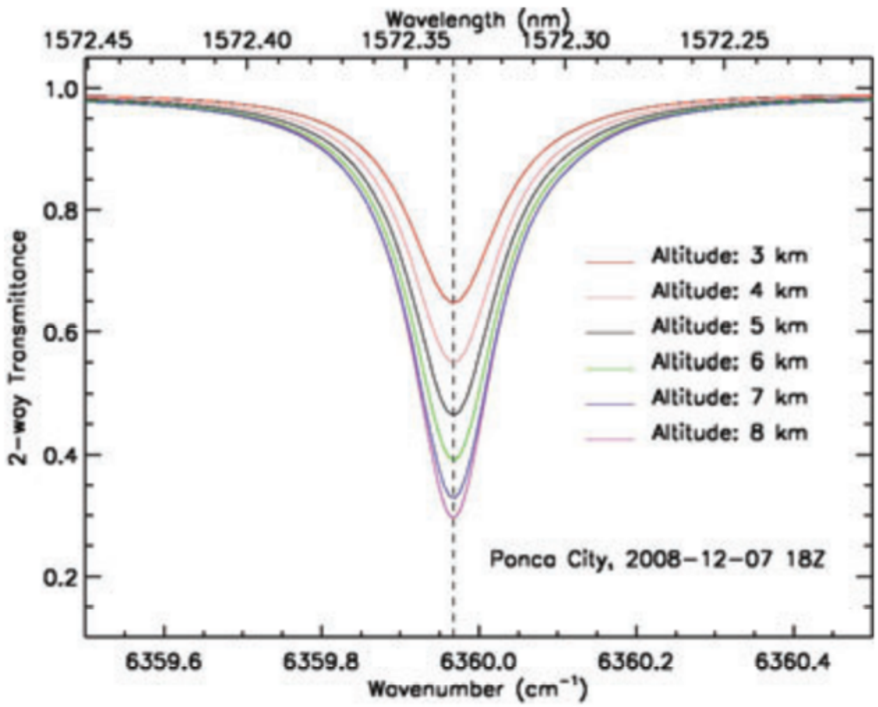

Figure 7.45: The two-way optical transmittance of the 1572.335 nm CO2 line as a function of flight altitude for December 7, 2008 computed from the radiosonde and Cessna readings.(© Taylor & Francis, [11].)

side, the details are shown in Fig. 7.46. The optical signal after the testing CO_2 Herriott cell is captured using the detection PCB with a high speed InGaAs PIN diode mounted.

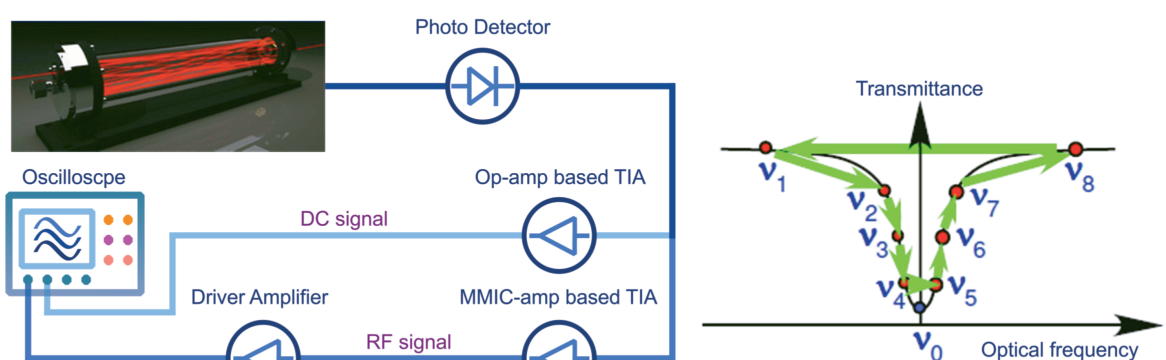

Figure 7.46: Sensing receiver block diagram.

On the detection PCB, the signal is first detected using the InGaAs PIN diode, and then separated into a DC signal and a RF signal. An op-amp based TIA is used to convert the current DC signal into a voltage DC signal and amplify the converted DC signal. A high-speed MMIC-amp based TIA is used to achieve the similar function for the RF signal. In addition, a driver amplifier is used to further amplify the RF signal for oscilloscope detection. At last, both signals are observed and captured using the oscilloscope, and the data is further processed in MATLAB.

7.3.3.1 CO_2 remote sensing under CW sampling

Finally, the transmittance was calculated by dividing the data shown in Fig. 7.47 and Fig. 7.48. Due to the different electrical TIA and amplifiers used in the CO_2 detection system and power monitoring system, the electrical signal gains are different, making it hard to calibrate the transmittance. So, it is normalized to the absorption flat and

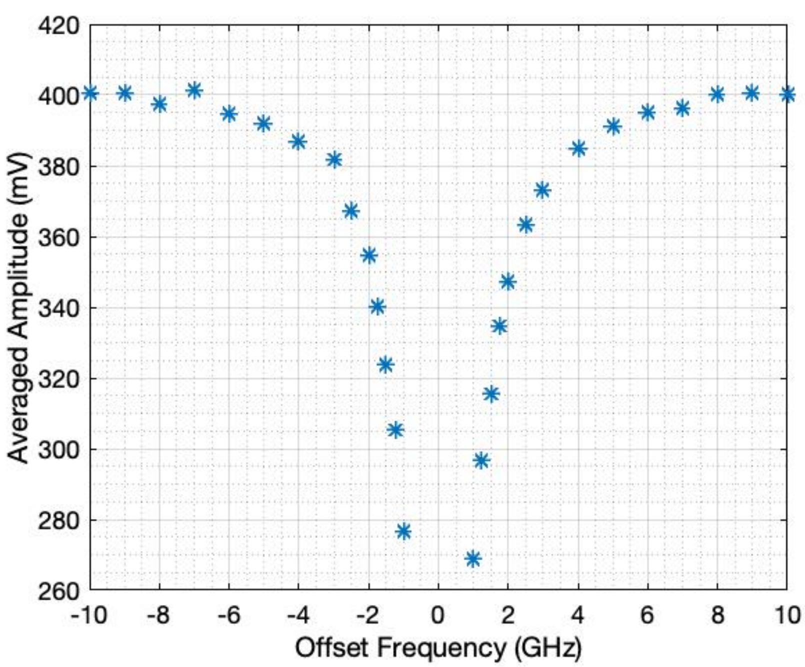

Figure 7.47: CW sampling measured CO_2 absorption line centered at 1572.335 nm.

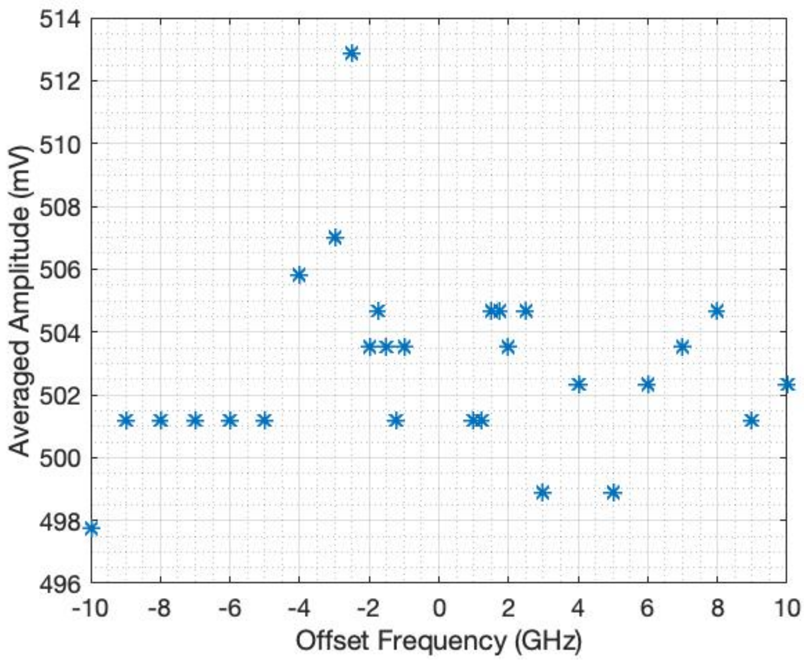

Figure 7.48: Monitored output power at different frequencies for CW sampling measurement.

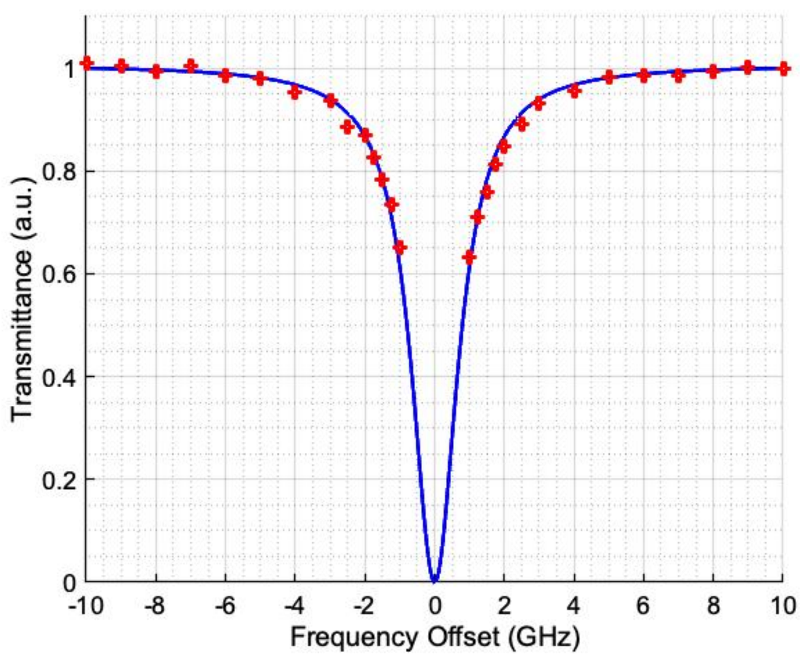

Figure 7.49: Normalized CW Measured transmittance with Lorentzian fit with FWHM of 1600 MHz.

peak, and fitted with a Lorentzian fit in MATLAB. The processed and fitted normalized transmittance is shown in Fig. 7.49.

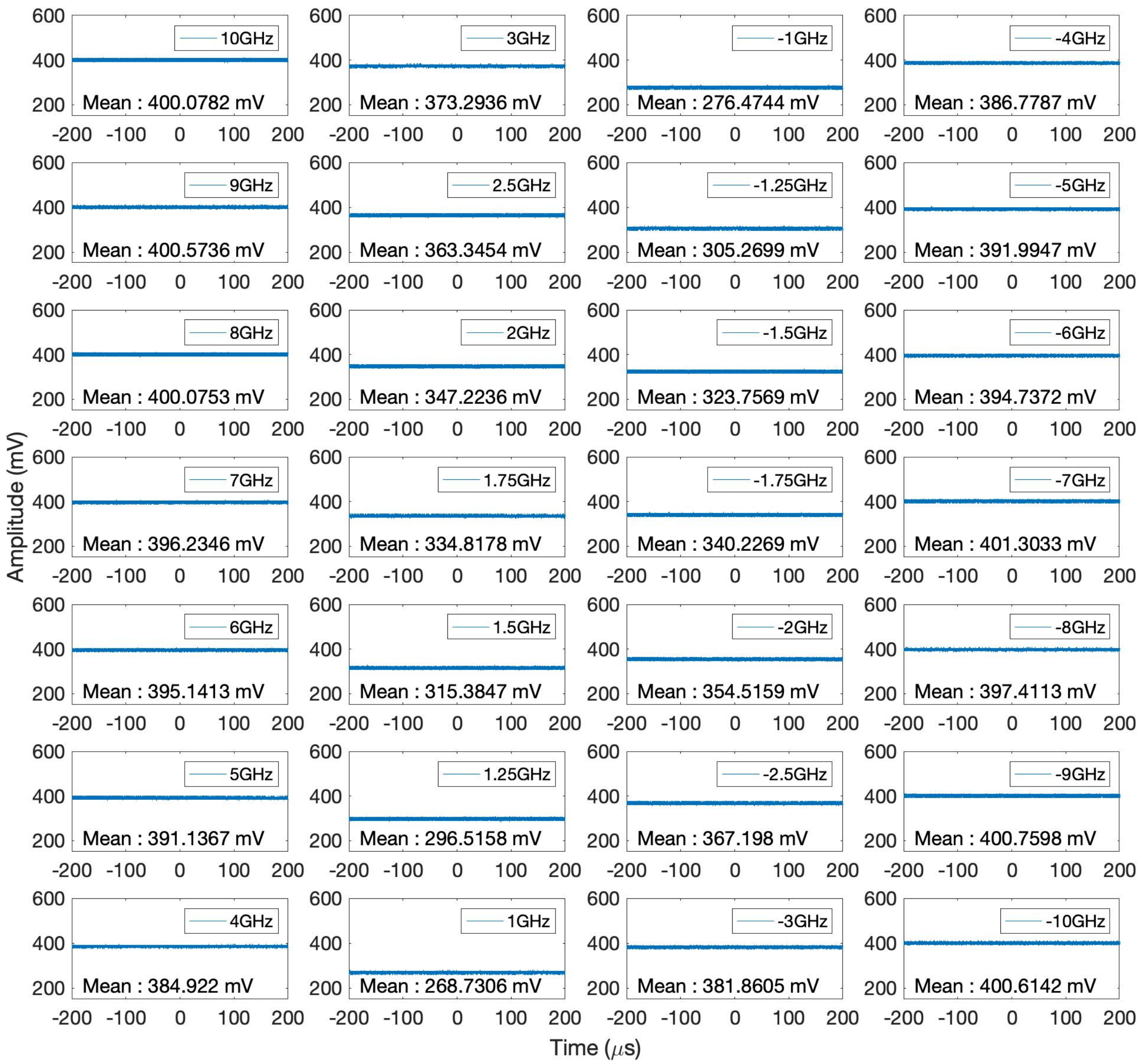

Figure 7.50: CW sensing DC signal at different sensing frequencies.

7.3.3.2 CO_2 remote sensing under pulse sampling

Then, the remote sensing for pulsed sampling was demonstrated for the PIC-based system. Under the pulsed sampling, the amplitude modulator is driven by a current pulse with a period of 133 μs and a pulse width of 1 μs. The electrical pulse and corresponding optical pulse output are shown earlier in Fig. 7.13. For the pulse sensing measurement, the outputs are also monitored and each pulse signal from RF and DC port was captured using an oscilloscope. The DC port pulse signals detected at different frequencies are shown in Fig. 7.51, and the RF port pulse signals detected at different frequencies are shown in Fig. 7.52.

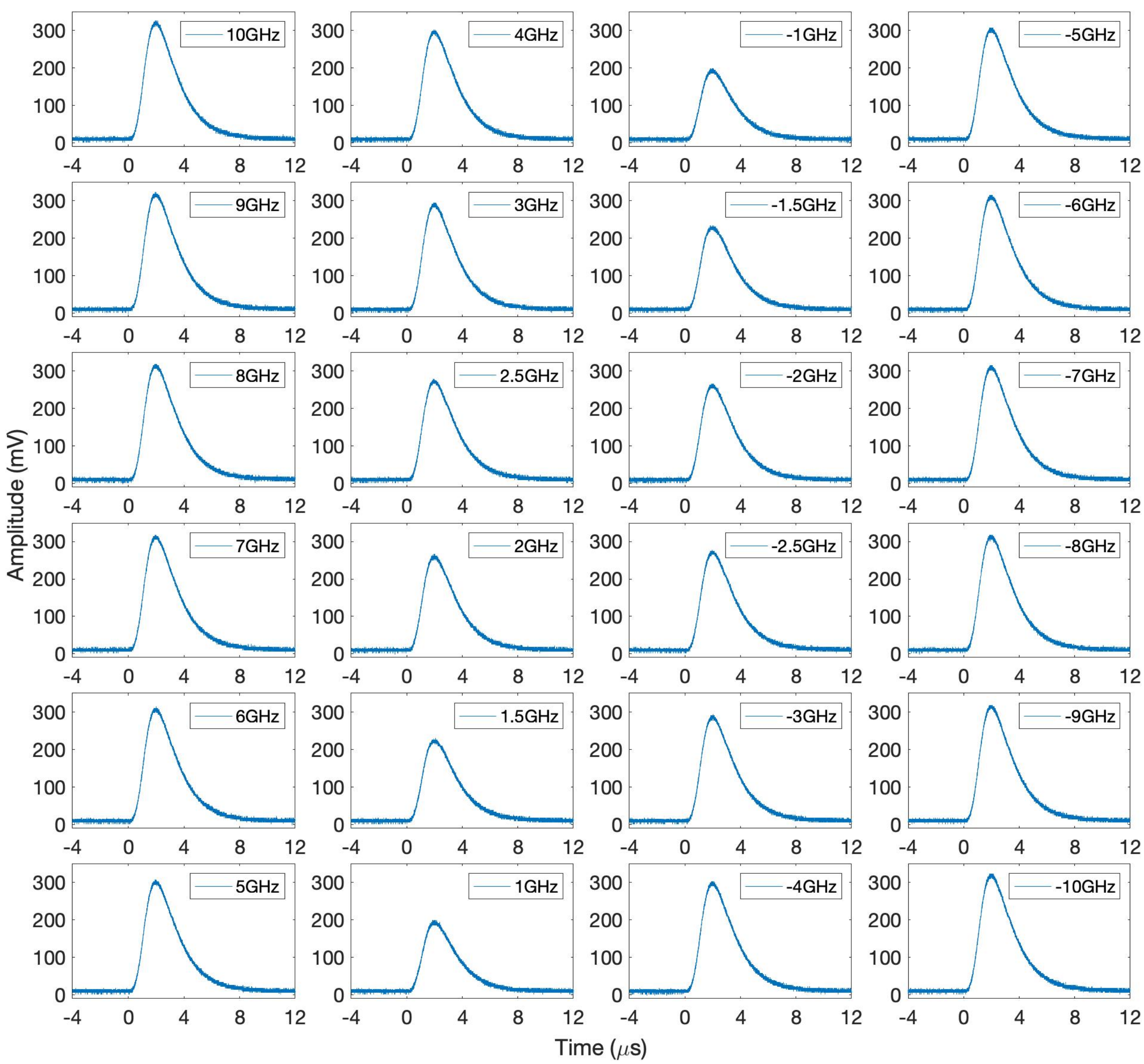

Figure 7.51: Pulse sensing DC signal at different sensing frequencies.

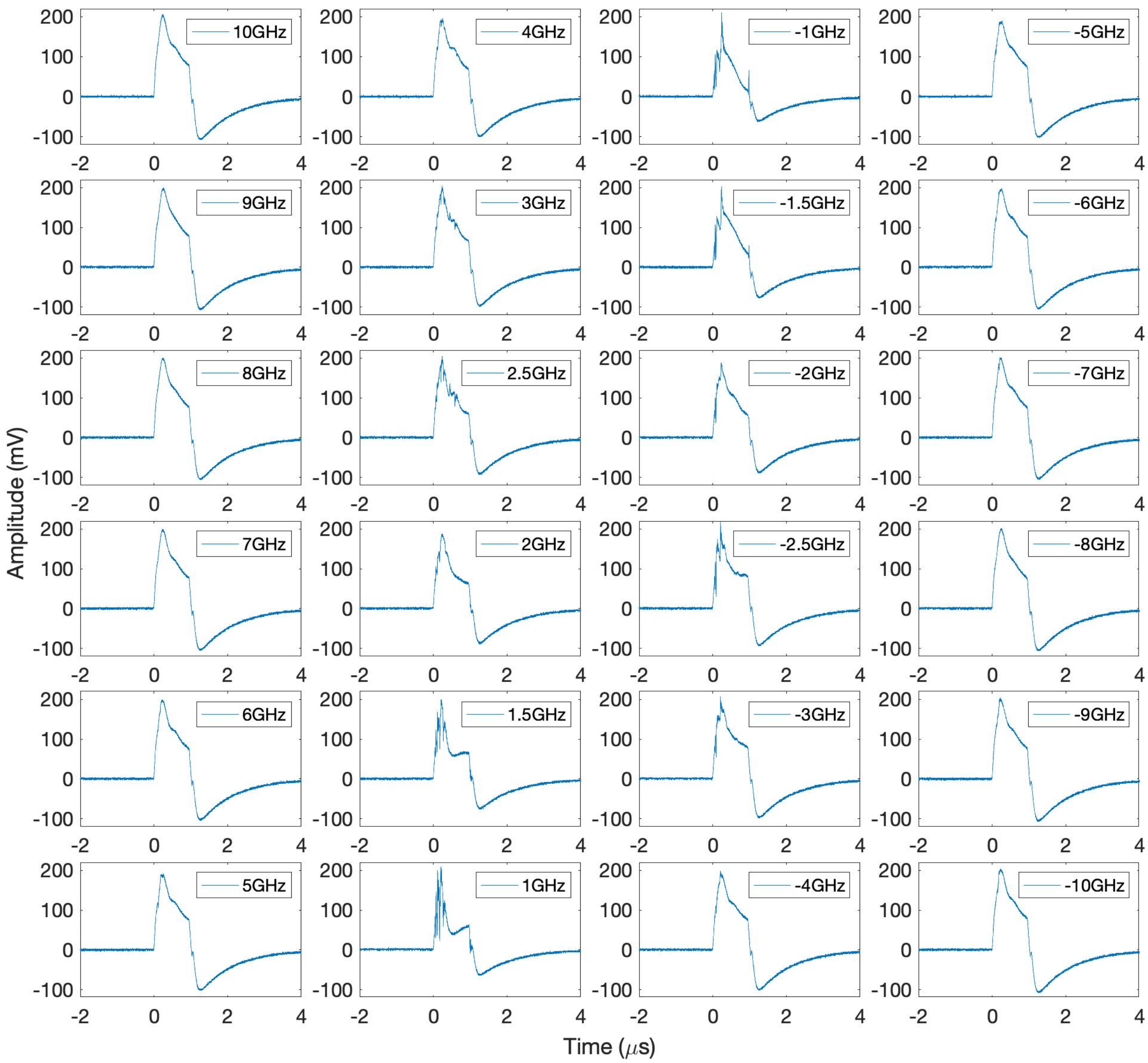

Figure 7.52: Pulse sensing RF signal at different sensing frequencies.

For the DC port signal, the pulse signal and corresponding amplitude change are observed. But, since the high frequency signal is separated from the DC port, only low frequency components are observed, which results in a slow time response. For the RF port signal, which only contains the high frequency signal of the pulse, the 1 μs signals at different frequencies are observed clearly, and the corresponding amplitude changes are also observed. However, some spikes are observed in the RF signals as the sweeping frequency becomes closer to the absorption peak, especially in the -1.5 GHz to 1.5 GHz range. From analysis, the spikes are caused by the phase noise and laser instability from the pulsed output. As the sweeping frequency moves towards the absorption peak, the slope of the absorption line becomes steeper. The absorption line at that region works as a more sensitive frequency discriminator. It converts the phase noise and frequency instability to amplitude noise, which is presented as spikes on the oscilloscope.

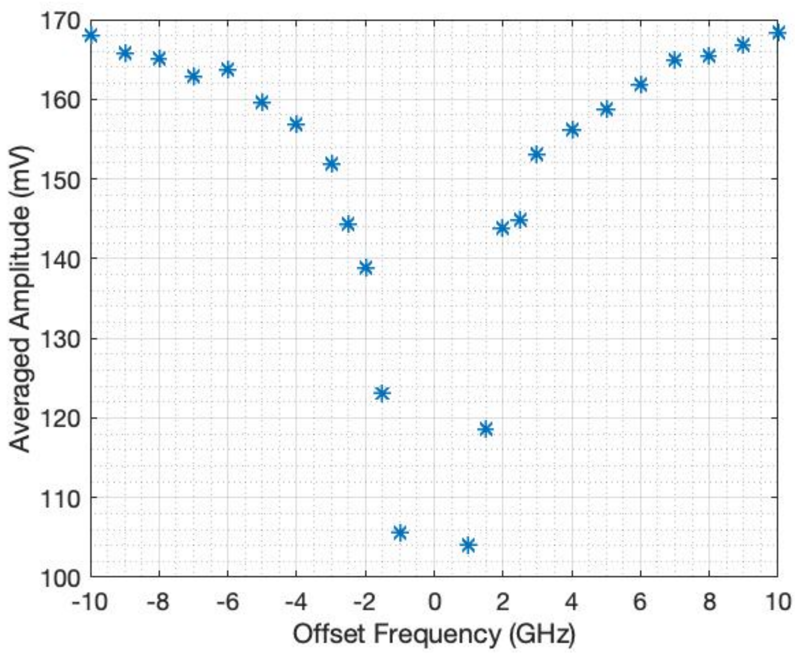

Figure 7.53: Pulse sampling RF signal measured CO_2 absorption line centered at 1572.335 nm.

The RF signal outputs are used for sensing analysis. The average power of each pulsed sensing signal and power monitoring signal were measured and are shown in Fig. 7.53 and Fig. 7.54. As mentioned above, due to the different electrical gain between the sensing signal and power monitoring signal, the averaged monitoring signals are around 1 order of magnitude smaller than the averaged sensing signals.

Finally, the transmittance is calculated by dividing the averaged pulsed sensing signal by its corresponding averaged monitoring signal at each frequency. The calculated

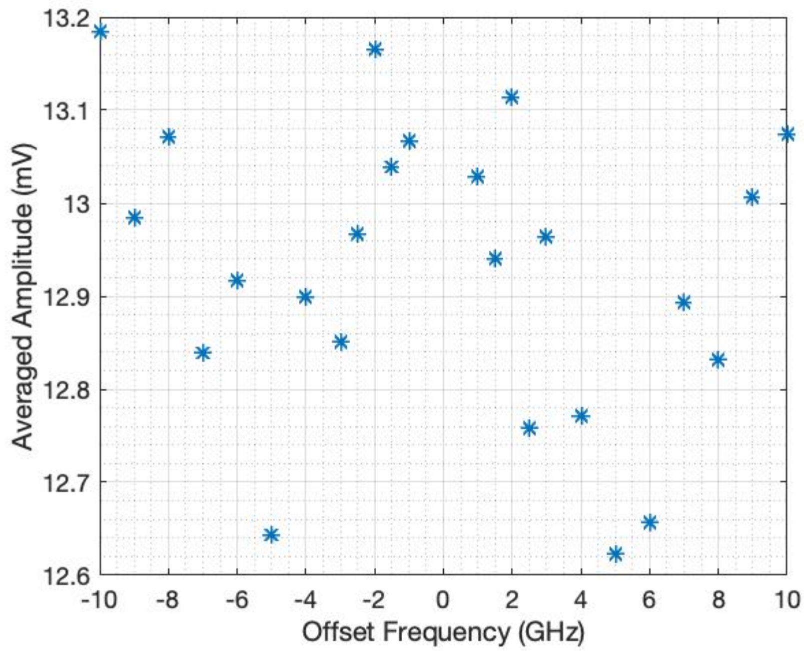

Figure 7.54: Monitored output power at different frequencies for pulse sampling measurement.

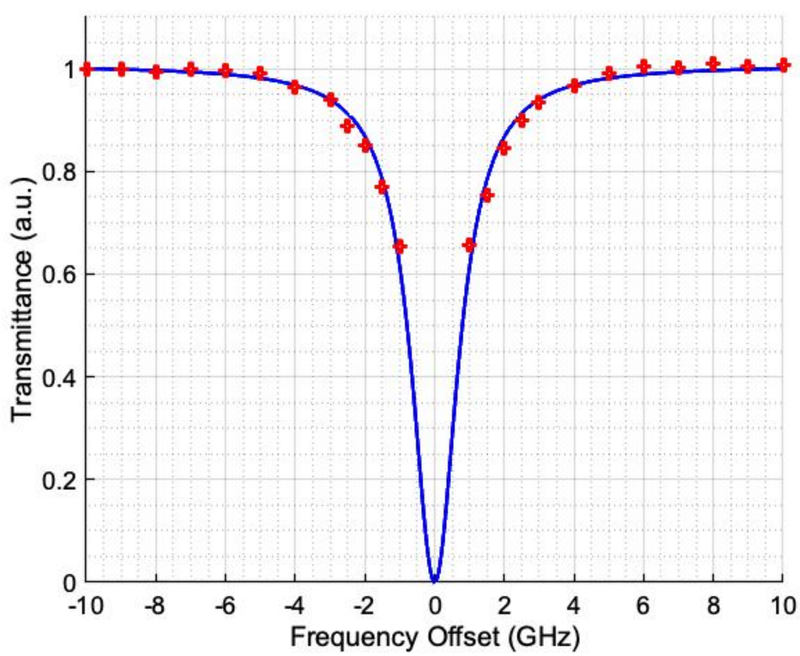

Figure 7.55: Normalized transmittance with Lorentzian fit with FWHM of 1600 MHz.

transmittance is also normalized, and fitted with Lorentzian shape, and it is shown in Fig. 7.55. The fitted Lorentzian shape also has a FWHM of 1600 MHz, which matches the FWHM measured under the CW sampling.

7.4 Conclusion

In this chapter, the details of the device level characterization and PIC level measurement were discussed. Overall, for the device level characterization, the device performance has satisfied the requirement to perform subsystem and system level measurement. For the PIC level measurement, we have successfully demonstrated the subsystem level and system level CO_2 sensing measurement under CW and pulse sampling in lab [7, 12].

For the leader laser stabilization subsystem, the modulation frequency and modulation depth of the phase modulator are optimized to improve the RAM and modulation efficiency. After analysing the characteristics of the phase modulator, a 125 MHz modulation signal with -7 dBm modulation power was used. In addition, a 14 kHz low-pass filter is used to further filter out the RAM noise and phase noise at higher frequencies to improve the stabilization performance.

For the follower laser offset locking subsystem, the loop filter of the OPLL is designed carefully [10]. The OPLL acts as a high-pass filter for the laser phase noise, and a low-pass filter for other noise including ASE noise, shot noise, RIN noise, and thermal noise [13]. A carefully designed OPLL loop filter can minimize the phase error and improve the overall subsystem functionality and reliability.

For the overall CO_2 sensing measurement, in order to achieve the best performance, the crosstalk and reflection between different components on the PIC need to be addressed carefully. They mainly include the thermal crosstalk between active components, the modulation crosstalk between modulators and lasers, reflections going back into the lasers, and reflections between other components. To minimize the crosstalk and reflection, a proper PIC design is required, a reliable fabrication process is needed, and a fine-tuned control system is also necessary.

Bibliography

[1] P. Kozodoy, T. A. Strand, Y. A. Akulova, G. Fish, C. Schow, P.-C. Koh, Z. Bian, J. Christofferson, and A. Shakouri, *Thermal effects in monolithically integrated tunable laser transmitters*, *IEEE Transactions on Components and Packaging Technologies* **28** (2005), no. 4 651–657.

[2] L. A. Coldren, S. W. Corzine, and M. L. Mashanovitch, *Diode lasers and photonic integrated circuits*, vol. 218. John Wiley & Sons, 2012.

[3] K. J. Åström, T. Hägglund, and K. J. Astrom, *Advanced PID control*, vol. 461. ISA-The Instrumentation, Systems, and Automation Society Research Triangle , 2006.

[4] K. Numata, J. R. Chen, and S. T. Wu, *Precision and fast wavelength tuning of a dynamically phase-locked widely-tunable laser*, *Optics express* **20** (2012), no. 13 14234–14243.

[5] K. Numata, J. R. Chen, S. T. Wu, J. B. Abshire, and M. A. Krainak, *Frequency stabilization of distributed-feedback laser diodes at 1572 nm for lidar measurements of atmospheric carbon dioxide*, *Applied optics* **50** (2011), no. 7 1047–1056.

[6] J. R. Chen, K. Numata, and S. T. Wu, *Error analysis for lidar retrievals of*

atmospheric species from absorption spectra, *Optics express* **27** (2019), no. 25 36487–36504.

[7] J. Fridlander, F. Sang, V. Rosborough, F. Gambini, S. T. S. Brunelli, J. R. Chen, K. Numata, M. Stephen, L. A. Coldren, and J. Klamkin, *Dual laser indium phosphide photonic integrated circuit for integrated path differential absorption lidar*, *IEEE Journal of Selected Topics in Quantum Electronics* (2021).

[8] Analog Devices, *EV-ADF41513SD1Z/EV-ADF41513SD2Z User Guide*, 2019. Rev. 0.

[9] Analog Devices, *ADF41513 - 6.5 GHz, Integer N/Fractional-N,PLL Synthesizer*, 2019. Rev. 0.

[10] J. M. Fridlander, *Photonic Integrated Circuits for Remote Sensing Lidar.* PhD thesis, University of California, Santa Barbara, 2021.

[11] J. B. Abshire, H. Riris, G. R. Allan, C. J. Weaver, J. Mao, X. Sun, W. E. Hasselbrack, S. R. Kawa, and S. Biraud, *Pulsed airborne lidar measurements of atmospheric co2 column absorption*, *Tellus B: Chemical and Physical Meteorology* **62** (2010), no. 5 770–783.

[12] F. Sang, J. Fridlander, V. Rosborough, S. T. Š. Brunelli, L. Coldren, J. Klamkin, J. Chen, K. Numata, R. Kawa, and M. Stephen, *Integrated photonics technology for earth science remote-sensing lidar*, in *2021 IEEE International Geoscience and Remote Sensing Symposium IGARSS*, pp. 7708–7711, IEEE, 2021.

[13] M. Lu, *Integrated optical phase-locked loops.* University of California, Santa Barbara, 2013.

Chapter 8

Summary and Future Work

In this work a novel InP photonic integrated circuit based on an OQW platform for CO_2 remote active sensing at 1572.335 nm was developed. The focus of this work can be categorized into two parts. The first part was the design and fabrication of the PIC, where three generations of PICs were designed and fabricated. The second part was the electronics design and development of the testing environment, where a custom pulse generator was designed for the SOA pulse carver and a CO_2 sensing testing environment was built with lab equipment.

We successfully demonstrated CO_2 sensing using the PIC based system in a lab environment [1–4]. This proves that the PIC based system can be utilized to perform CO_2 sensing and opens the possibility of deploying the PIC based system for future active CO_2 remote sensing. A PIC based system would dramatically reduce the size and weight of an active sensing optical module. To reduce the size of the entire system, closely integrated and power efficient electronics can be designed. This would enable the possibility of performing active sensing on smaller platforms, such as ESPA satellite and even CubeSats.

8.1 Summary of Accomplishments

The PIC designed, fabricated, and characterized in this work incorporated the functions of laser light generation, light combining and splitting, phase modulation, photodetection, and pulse generation. These were accomplished using SGDBR lasers, MMI and directional couplers, straight and MZM phase modulators, PIN photodiodes, and SOA and MZM pulse generators.

The PIC was designed based on an IPDA architecture [5] and the PIC-based system can be divided into two main parts: the leader laser stabilization and the follower laser offset locking. The leader and follower lasers both use SGDBR lasers. The leader laser functions as an absolute optical reference for the follower laser. The leader laser is locked to the center of the CO_2 absorption line through a CO_2 reference cell using a frequency modulation technique [5–7]. The follower laser is offset locked to the leader laser using an OPLL. A sensing experiment was demonstrated by operating both systems together to sweep over the target CO_2 absorption line centered at 1572.335 nm.

The designed and fabricated SGDBR laser demonstrated a 3 dB linewidth of $\sim$ 0.92 MHz with a 45 nm tuning range. For the leader laser stabilization, a $\sim$ 23 dB improvement was achieved while locking was enabled compared with when the locking was disabled. For the follower laser offset locking, a $\sim$ 48 dB improvement was achieved while the OPLL was engaged compared with when the OPLL was not engaged. In addition, the follower laser was successfully offset locked to the leader laser from -10 GHz to 12 GHz with a minimum locking resolution of 1 MHz centered at 2 GHz offset locking frequency. At last, sensing experiments were successfully demonstrated in both CW and pulsed mode with similar results and the measured absorption lines both had a Lorentzian fitted FWHM of 1600 MHz. In CW mode, 8.92 dBm of fiber-coupled power was measured. In pulsed mode, a 45 dB extinction ratio was achieved using only current injection. The extinction ratio can be further improved by using the custom designed pulse generator to sweep the bias on the SOA from reverse to forward. An extra 10 dB improvement is expected based on our experimental data.

8.2 Future Work

There are two parts that can be optimized in the future in order to improve the performance of this work. The first part is the PIC design and fabrication optimization. The second part is the PIC packaging and electronics & photonics integration.

For the PIC design and fabrication optimization, there are two main components that need to be improved. They are the phase modulator and photodiode. For the phase modulator, the PIC that achieved the sensing measurement results used the straight phase modulator discussed in chapter 4.2, which has a relatively high RAM. This limits the leader laser stabilization performance, which is also the main limitation of the stabilization of the overall system. As discussed in chapter 6.2, some PICs included an MZM low-RAM phase modulator, which was designed to improve the RAM performance of the leader laser side output. If those PICs work properly, the locking performance can be further improved. Another limitation of the sensing experiment was the integrated photodiode bandwidth. Unfortunately, the photodiode tested did not have a BCB layer to further enhance its bandwidth performance. The BCB layer was left out to simplify the fabrication process and improve the yield of the PICs in the later fabrication rounds. This caused the system to only achieve a $\pm$ 10 GHz offset sensing range. But, after three iterations of the fabrication process, the fabrication recipes are already optimized for the designed PICs. One fabrication generation included a BCB layer, so it would not be difficult to add a BCB layer while not affecting the yield and performance of the PIC significantly. With the BCB layer added, the 3 dB bandwidth of the photodiode can increase to more than 15 GHz and the sensing can be performed for over a $\pm$ 20 GHz range as estimated based on our current experiment data.

In addition, the PIC packaging and electronic & photonic integration is also an important aspect that needs to be improved. As discussed in chapter 7.3.2, the sensing measurement was performed in the lab without PIC packaging, and using individual benchtop instruments to control it. The instability from the temperature variation and vibration in a lab environment degrades the performance of the sensing measurement, especially for long time stability testing. The alignment of the fiber and the fine-tuning of the temperature controller need to be adjusted every 3 - 4 hours in order to achieve the best performance. If the PIC is packaged into a hermetically sealed environment, the stability of the PIC's environment can be significantly improved. In addition, a mature fiber attachment technology would also reduce the fiber coupling loss and therefore improve the final fiber coupled output power. After packaging, the PIC could be sent to NASA for sensing experiments in their test bed and launching qualification tests. Without these tests, it is hard make a conclusion about the readiness level of the PIC-based system for deployment, but we are sure that it satisfies the device level requirements provided by NASA. Additionally, designing a PCB board to integrate the functionality of all the electronic equipment would reduce the size of the overall system. We could also optimize the PCB board to add extra functions that off-the-shelf equipment cannot provide, such as the pulse generator for SOA pulse generation discussed in chapter 5. This will not only further improve the performance of the overall system, but also pave the way for real world implementation of small platform remote sensing.

Bibliography

[1] J. Fridlander, F. Sang, V. Rosborough, F. Gambini, S. T. S. Brunelli, J. R. Chen, K. Numata, M. Stephen, L. A. Coldren, and J. Klamkin, *Dual laser indium phosphide photonic integrated circuit for integrated path differential absorption lidar*, *IEEE Journal of Selected Topics in Quantum Electronics* (2021).

[2] J. Fridlander, F. Sang, V. Rosborough, S. T. Š. Brunelli, J. Chen, K. Numata, S. Kawa, M. Stephen, L. Coldren, and J. Klamkin, *Monolithic indium phosphide dual laser photonic integrated circuit for remote sensing lidar*, in *2021 Conference on Lasers and Electro-Optics (CLEO)*, pp. 1–2, IEEE, 2021.

[3] J. Klamkin, F. Sang, J. Fridlander, V. Rosborough, F. Gambini, S. T. Š. Brunelli, L. Coldren, J. R. Chen, S. Kawa, K. Numata, *et. al.*, *Integrated phase-locked lasers and photonic integrated circuits for remote gas sensing*, in *2021 27th International Semiconductor Laser Conference (ISLC)*, pp. 1–2, IEEE, 2021.

[4] F. Sang, J. Fridlander, V. Rosborough, S. T. Š. Brunelli, L. Coldren, J. Klamkin, J. Chen, K. Numata, R. Kawa, and M. Stephen, *Integrated photonics technology for earth science remote-sensing lidar*, in *2021 IEEE International Geoscience and Remote Sensing Symposium IGARSS*, pp. 7708–7711, IEEE, 2021.

[5] G. C. Bjorklund, *Frequency-modulation spectroscopy: a new method for measuring weak absorptions and dispersions*, Optics letters **5** (1980), no. 1 15–17.

[6] K. Numata, J. R. Chen, S. T. Wu, J. B. Abshire, and M. A. Krainak, *Frequency stabilization of distributed-feedback laser diodes at 1572 nm for lidar measurements of atmospheric carbon dioxide*, Applied optics **50** (2011), no. 7 1047–1056.

[7] K. Numata, J. R. Chen, and S. T. Wu, *Precision and fast wavelength tuning of a dynamically phase-locked widely-tunable laser*, Optics express **20** (2012), no. 13 14234–14243.